

APPLIED COMPUTATIONAL ELECTROMAGNETICS SOCIETY JOURNAL

Special Issue on CSQRWC 2018

Guest Editors:

Lei Zhao, China University of Mining and Technology

Long Li, Xidian University

Sheng Sun, University of Electronic Science and
Technology of China

Wenhua Yu, Jiangsu Normal University

March 2019

Vol. 34 No. 3

ISSN 1054-4887

The ACES Journal is abstracted in INSPEC, in Engineering Index, DTIC, Science Citation Index Expanded, the Research Alert, and to Current Contents/Engineering, Computing & Technology.

The illustrations on the front cover have been obtained from the research groups at the Department of Electrical Engineering, The University of Mississippi.

THE APPLIED COMPUTATIONAL ELECTROMAGNETICS SOCIETY

<http://aces-society.org>

EDITORS-IN-CHIEF

Atef Elsherbeni

Colorado School of Mines, EE Dept.
Golden, CO 80401, USA

Sami Barmada

University of Pisa, ESE Dept.
56122 Pisa, Italy

ASSOCIATE EDITORS: REGULAR PAPERS

Mohammed Hadi

Kuwait University, EE Dept.
Safat, Kuwait

Alistair Duffy

De Montfort University
Leicester, UK

Wenxing Li

Harbin Engineering University
Harbin 150001, China

Maokun Li

Tsinghua University
Beijing 100084, China

Mauro Parise

University Campus Bio-Medico of Rome
00128 Rome, Italy

Yingsong Li

Harbin Engineering University
Harbin 150001, China

Riyadh Mansoor

Al-Muthanna University
Samawa, Al-Muthanna, Iraq

Antonio Musolino

University of Pisa
56126 Pisa, Italy

Abdul A. Arkadan

Colorado School of Mines, EE Dept.
Golden, CO 80401, USA

Salvatore Campione

Sandia National Laboratories
Albuquerque, NM 87185, USA

Wei-Chung Weng

National Chi Nan University, EE Dept.
Puli, Nantou 54561, Taiwan

Alessandro Formisano

Seconda Università di Napoli
81031 CE, Italy

Piotr Gas

AGH University of Science and Technology
30-059 Krakow, Poland

Marco Arjona López

La Laguna Institute of Technology
Torreón, Coahuila 27266, Mexico

Paolo Mezzanotte

University of Perugia
I-06125 Perugia, Italy

Luca Di Rienzo

Politecnico di Milano
20133 Milano, Italy

Rocco Rizzo

University of Pisa
56123 Pisa, Italy

Lei Zhao

Jiangsu Normal University
Jiangsu 221116, China

Sima Noghianian

University of North Dakota
Grand Forks, ND 58202, USA

Qiang Ren

Beihang University
Beijing 100191, China

ASSOCIATE EDITORS: EXPRESS PAPERS

Lijun Jiang

University of Hong Kong, EEE Dept.
Hong Kong

Shinichiro Ohnuki

Nihon University
Tokyo, Japan

Kubilay Sertel

The Ohio State University
Columbus, OH 43210, USA

Steve J. Weiss

US Army Research Laboratory
Adelphi Laboratory Center (RDRL-SER-M)
Adelphi, MD 20783, USA

Jiming Song

Iowa State University, ECE Dept.
Ames, IA 50011, USA

Amedeo Capozzoli

Univerita di Napoli Federico II, DIETI
I-80125 Napoli, Italy

Yu Mao Wu

Fudan University
Shanghai 200433, China

Maokun Li

Tsinghua University, EE Dept.
Beijing 100084, China

EDITORIAL ASSISTANTS

Matthew J. Inman

University of Mississippi, EE Dept.
University, MS 38677, USA

Kyle Patel

Colorado School of Mines, EE Dept.
Golden, CO 80401, USA

Madison Le

Colorado School of Mines, EE Dept.
Golden, CO 80401, USA

Shanell Lopez

Colorado School of Mines, EE Dept.
Golden, CO 80401, USA

Allison Tanner

Colorado School of Mines, EE Dept.
Golden, CO 80401, USA

EMERITUS EDITORS-IN-CHIEF

Duncan C. Baker
EE Dept. U. of Pretoria
0002 Pretoria, South Africa

Allen Glisson
University of Mississippi, EE Dept.
University, MS 38677, USA

Ahmed Kishk
Concordia University, ECS Dept.
Montreal, QC H3G 1M8, Canada

Robert M. Bevensee
Box 812
Alamo, CA 94507-0516, USA

Ozlem Kilic
Catholic University of America
Washington, DC 20064, USA

David E. Stein
USAF Scientific Advisory Board
Washington, DC 20330, USA

EMERITUS ASSOCIATE EDITORS

Yasushi Kanai
Niigata Inst. of Technology
Kashiwazaki, Japan

Mohamed Abouzahra
MIT Lincoln Laboratory
Lexington, MA, USA

Alexander Yakovlev
University of Mississippi, EE Dept.
University, MS 38677, USA

Levent Gurel
Bilkent University
Ankara, Turkey

Sami Barmada
University of Pisa, ESE Dept.
56122 Pisa, Italy

Ozlem Kilic
Catholic University of America
Washington, DC 20064, USA

Erdem Topsakal
Mississippi State University, EE Dept.
Mississippi State, MS 39762, USA

William O'Keefe Coburn
US Army Research Laboratory
Adelphi, MD 20783, USA

Fan Yang
Tsinghua University, EE Dept.
Beijing 100084, China

EMERITUS EDITORIAL ASSISTANTS

Khaled ElMaghoub
Trimble Navigation/MIT
Boston, MA 02125, USA

Christina Bonnington
University of Mississippi, EE Dept.
University, MS 38677, USA

Anne Graham
University of Mississippi, EE Dept.
University, MS 38677, USA

Mohamed Al Sharkawy
Arab Academy for Science and Technology, ECE Dept.
Alexandria, Egypt

MARCH 2019 REVIEWERS: REGULAR PAPERS

Kiran Ajetroa
Nicola Anselmi
Chia-Chan Chang
Lu Guo
Yong Mao Huang
Michael Johnson
F. Las-Heras
Yingsong Li
Yue Li
Haiwen Liu
Mohammad Neshati
Xiao-Min Pan
Zhengyu Peng
Mohammd Pourbagher
Qiang Ren

Thenarasan Sabapathy
Albert Sabban
Wei E. I. Sha
Guo Shuai
Sheng Sun
Marsellas Waller
Jun Wang
Yongle Wu
Lixia Yang
Wenhua Yu
Huapeng Zhao
Hong-Xing Zheng
Liang Zhou
Yuanguo Zhou

SPECIAL ISSUE ON CSQRWC 2018

Dual-Band and Dual-Polarized Electrically Tunable Reconfigurable Reflectarray Antenna Shuncheng Tian, Haixia Liu, and Long Li	391
Gain-Enhanced Compact Circularly Polarized Array Microstrip Antenna Zhaoneng Jiang, Hongzhi Zhao, Xiaoyan Zhao, Jian Liu, Mingyue Shui, Ting Wan, and Xuguang Qiao.....	397
Mutual Coupling Reduction of a Dual-Band Antenna Array Using Dual-Frequency Metamaterial Structure Shengyuan Luo, Yingsong Li, Yinfeng Xia, Guohui Yang, Laijun Sun, and Lei Zhao	403
A Low Mutual Coupling Antenna Array with Gain Enhancement Using Metamaterial Loading and Neutralization Line Structure Shengyuan Luo, Yingsong Li, Yinfeng Xia, and Liang Zhang	411
Improved Constraint NLMS Algorithm for Sparse Adaptive Array Beamforming Control Applications Wanlu Shi, Yingsong Li, and Jingwei Yin.....	419
Accurate Analysis of JEM Interference in Airborne Array using Parallel HO-IE-DDM Yingyu Liu, Qin Su, Xunwang Zhao, Yu Zhang, Zhongchao Lin, Chang Zhai, and Qi Zhang	425
Direction Finding Using Uniform Circular Array of Horizontal Log-Periodic Dipole Antennas Xiaofei Ren, Shuai Zhang, Hu Li, and Shuxi Gong	434
On the Approximate Calculation of Half-Power Beam Width for Uniform Circular Arrays Hua Tang, Xianzheng Zong, and Zaiping Nie	444
Dual-polarized Grid-slotted Microstrip Antenna with Enhanced Bandwidth and Low Profile Wangyu Sun and Yue Li	451
Mm-wave Radar Based Micro-Deformation Monitoring for Highway and Freight Railway Bridges Yingsong Li, Zelong Shao, Xiangkun Zhang, and Jingshan Jiang	457

Ungrounded Lightning Surge Protection Device for Wireless Sensor Networks Node in the Wilderness Qinghua Cao, Lixia Yang, and Shu Yan	463
High Selectivity Bandpass Filter Using Three Pairs of Coupled Lines Loaded with Shorted Stubs Kai-Da Xu and Fengyu Zhang	469
Three-Dimensional Spherical-Shaped UPML for FDTD with Cubic Lattices Lu Wang, Mengjun Wang, Kanglong Zhang, Wenjie Cui, Hongxing Zheng, and Erping Li.....	475
Double-layer Metal Wire Based Artificial Electromagnetic Surface and its Application for Bessel Beam Microwave Lens He Yu, Guo-Hui Yang, Kuang Zhang, Fan-Yi Meng, and Yingsong Li	483
A Novel Query Tree Anti-collision Algorithm for RFID Fan Yang, Lei Zhao, Hu Chen, and Shuixia Hao	490
Design and Evaluation of Typical Antennas for Monitoring Vital Signs Ramadhani Selemani Mpanda, Lin Qi, Qiancheng Liang, Lisheng Xu, Jingjing Shi, and Lei Zhao	497

Dual-Band and Dual-Polarized Electrically Tunable Reconfigurable Reflectarray Antenna

Shuncheng Tian, Haixia Liu*, and Long Li**

Key Laboratory of High Speed Circuit Design and EMC of Ministry of Education
School of Electronic Engineering,
Xidian University, Xi'an, 710071, China

*hxliu@xidian.edu.cn, **lilong@mail.xidian.edu.cn

Abstract — In this paper, a dual-band and dual-polarized electrically tunable reconfigurable reflectarray antenna (RRA) is proposed, fabricated and measured for the beam-scanning performance. The RRA element, a single layer structure with two split-rings and a pair of varactor diodes, can be electrically tuned to work at the two orthogonal polarization modes of the incident electric field at 4.2GHz and 6.5GHz, respectively. Besides, the range of the phase compensation of the element is over 300° at the two polarization modes. Then, a RRA with 15×15 elements is designed, fabricated and measured to prove the validity. The main beam direction can be controlled by tuning these varactor diodes of the RRA and the beam-scanning range is from -60° to 60° . The experimental results and simulation results are in good agreement to prove the correctness and feasibility of the design of the novel dual-band and dual-polarized electrically tunable RRA.

Index Terms — Beam-scanning, electrically tunable, reconfigurable reflectarray antenna, varactor diodes.

I. INTRODUCTION

Microstrip reflectarray antennas, with the merits of low profile, low cost, small volume, high gain and accurate main beam direction, etc., are rapidly becoming an attractive alternative in the modern radar and satellite communication system. Some researchers alter the main beam direction by changing the size of reflectarray antenna unit, changing the length of phase delay line and so on [1].

However, these methods have an obvious shortcoming that it is not possible to achieve beam-scanning adaptively in the actually needed direction [2]. Furthermore, the conventional microstrip reflectarray antennas always only radiate in a fixed direction after fabricated. In order to meet the increasing demand of the antenna system, more reconfiguration properties are obviously studied to reduce the amount of antennas and improve the utilization ratio of antenna [3-4].

Besides, everyone knows, the base station antenna has radiation blind area of the communication system. One solution is to add antennas but the cost of the whole system is greatly increasing. The RRA may be a better choice to solve the signal coverage problem. However, it is still a challenge to design a RRA with much wider beam-scanning range and higher antenna efficiency [5-6]. There has been a series of researches and developments on the novel reconfigurable elements and RRAs. Some researchers utilize the electronically tunable materials, such as liquid crystal, graphene and other new functional materials, to obtain the beam-scanning characteristic.

Thus, it can be seen that the RRA has attracted more considerable attentions [7]. The RRA, just by changing the voltage of the external active devices, can achieve adaptive, flexible beam-scanning and reconfiguration properties [8-9]. Recently, the lumped switches are widely used in most of the design of the RRA, especially the PIN diode and the varactor diode because they are simple and don't need special process technology. Hence, the multifunctional RRA has emerged as an up-and-coming alternative in more areas in the future. But most of these studies only concentrate on single working frequency or single polarization mode [10-12].

In our work, a dual-band and dual-polarized electrically tunable RRA is proposed to obtain continuous controllable beam-scanning performance. The RRA consists of 15×15 elements etched on the dielectric substrate. Section II briefly describes the working principles of the reflectarray antenna. In Section III, a dual-band and dual-polarized RRA element is proposed working at two orthogonal polarization modes of the incident electric field at 4.2GHz and 6.5GHz, respectively. Specifically, in Section IV, a dual-band and dual-polarized RRA is simulated, fabricated and tested. The simulation results and measurement results are in good agreement to verify the effectiveness of the design of the novel RRA. Finally, Section V concludes this work.

II. PRINCIPLES OF REFLECTARRAY ANTENNA

For the microstrip reflectarray antenna, the key is the design of the element [13]. Once the determination of feed's position, the phase caused by the distance of the feed between the reflecting antenna unit is determined. While the element of the reflectarray antenna meets the certain amplitude and phase conditions, the reflected beam can radiate in the specified direction. In order to obtain the needed main beam direction, the key is to calculate the phase compensation for every element.

As shown in Fig. 1, the antenna contains $M \times N$ units, \vec{r}_f is the position of the feed and \hat{u}_0 is the main beam direction. The reradiated electromagnetic wave in an arbitrary direction can be calculated by:

$$E(\hat{u}) = \sum_{m=1}^M \sum_{n=1}^N F(\vec{r}_{mm} \cdot \vec{r}_f) A(\vec{r}_{mm} \cdot \hat{u}_0) A(\hat{u}_0 \cdot \hat{u}) \cdot \exp \phi, \quad (1)$$

$$\phi = -jk_0(|\vec{r}_{mm} - \vec{r}_f| - \vec{r}_{mm} \cdot \hat{u}) + j\alpha_{mm}, \quad (2)$$

where F is the function of the radiation pattern of the feed. A is the function of the radiation pattern of the array unit. \vec{r}_{mm} is the position of every element and α_{mm} is the phase compensation of the i^{th} cell. Based on the analyses above, the specific calculation process is given as below.

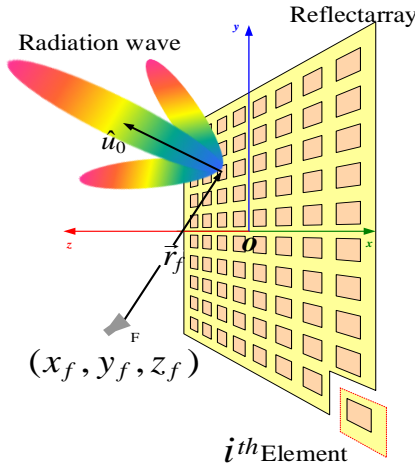


Fig. 1. Coordinate of the reflectarray.

If the antenna radiates in the desired direction, the cells must meet the equal phase delay path from the feed to the equiphase surface in Fig. 2. In other words, the phase compensation from the feed to each cell ϕ_f , the phase compensation of every cell ϕ_{mm} and the phase compensation from every cell to the equiphase surface ϕ_r should meet:

$$\phi_f + \phi_{mm} + \phi_r = 2n\pi \quad (n=1,2,3\dots). \quad (3)$$

In order to calculate ϕ_{mm} , we firstly have to calculate ϕ_f and ϕ_r . (x_f, y_f, z_f) and (x_{mm}, y_{mm}, z_{mm}) represent the coordinates of the feed and the element, respectively. d_{mm} , the distance between the feed and the element, is given by:

$$d_{mm} = \sqrt{(x_{mm} - x_f)^2 + (y_{mm} - y_f)^2 + (z_{mm} - z_f)^2}, \quad (4)$$

so ϕ_f can be calculated by:

$$\phi_f = k_0 d_{mm}, \quad (5)$$

where $k_0 = 2\pi / \lambda_0 = 2\pi f / c$ is the propagation constant in vacuum; λ_0 is the wavelength in vacuum; c is the speed of light in vacuum; f is the working frequency of the antenna; (θ_0, φ_0) represents the main beam direction. Based on the theory of array antenna, ϕ_r is reckoned by:

$$\phi_r = -k_0 \sin \theta_0 \cos \varphi_0 x_{mm} - k_0 \sin \theta_0 \sin \varphi_0 y_{mm}. \quad (6)$$

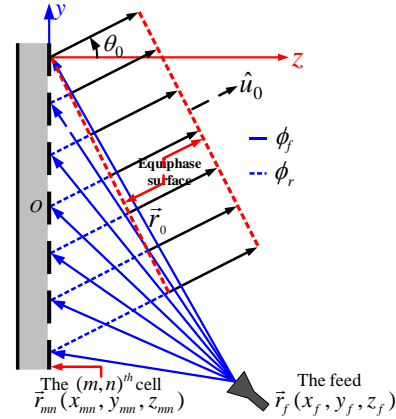


Fig. 2. Phase delay path of the reflectarray.

In the end, we can get the phase compensation ϕ_{mm} by taking Equations (4), (5) and (6) into Equation (3). Up to now, if we already know the operating frequency f , the main beam direction (θ_0, φ_0) , the coordinate of the feed (x_f, y_f, z_f) , and the coordinate of the cell (x_{mm}, y_{mm}, z_{mm}) , the phase compensation ϕ_{mm} of each cell will be computed and the reflectarray antenna can form the main beam in the desired direction.

III. DUAL-BAND AND DUAL-POLARIZED RRA ELEMENT

In this part, a dual-band and dual-polarized RRA element is presented, as Fig. 3 shows, which mainly consists of two split-rings and two varactor diodes. The direction of the opening of the inner ring is rotated by 90° compared with the outer one. The unit is etched on the dielectric substrate and the bottom is the metal ground. The permittivity of the dielectric substrate is 2.65 and other geometrical parameters of the element are given in Table 1. Numerical analyses and optimizations of this unit have been done in HFSS 15.0. The Floquet port and the infinite periodic boundary condition are adopted.

The element makes the point, dual-band and dual-polarized electrically tunable and beam-scanning performances, by adjusting the capacitance of varactor diodes not changing the structural parameters. When the polarization direction of the electric field of the incident

wave is along the X axis and the Y axis, the operating frequencies are at 4.2GHz and 6.5GHz, respectively.

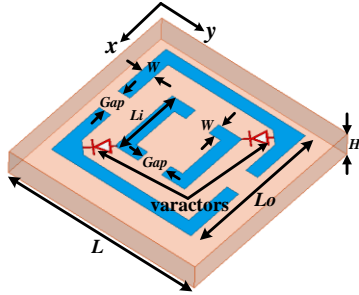


Fig. 3. Geometry of the dual-band and dual-polarized RRA element.

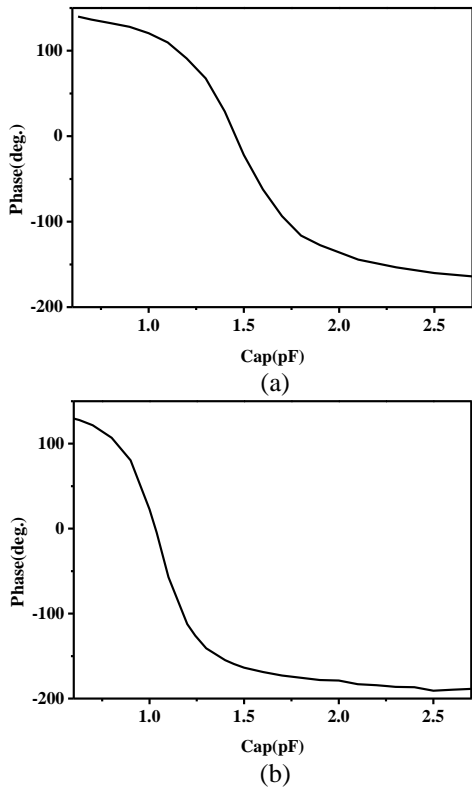


Fig. 4. Phase compensation curve: (a) at 4.2 GHz and (b) at 6.5GHz.

As seen in Fig. 4, it can be found that the range of the phase compensation is over 304° and 318° for each polarization mode. It is worthwhile to point out that the phase compensation of the cell can be changed through adjusting the capacitance of varactor diodes.

As we expected, the dual-band and dual-polarized element can work at different polarization modes at different operating frequencies. All in all, the unit is a crucial role in the design of the dual-band and dual-

polarized RRA.

Table 1: Parameters of the RRA element

Parameter	Size (mm)	Parameter	Size (mm)
L	20	W	1.8
Lo	14	Gap	0.2
Li	10	H	0.5
h	0.25		

IV. DESIGN AND ANALYSIS OF THE RRA

Based on the simulations of the dual-band and dual-polarized element, a RRA is designed in this section, given in Fig. 5, which works at two polarization modes at different frequencies. The dual-band and dual-polarized RRA is composed of 15×15 cells. The size of the antenna is $300 \times 300 \text{mm}$. The incident wave is in the xoz plane; the reflection wave is in the $yo z$ plane. The direction of the incidence wave $(\theta_i, \varphi_i) = (20^\circ, 0^\circ)$ and the direction of the reflection wave $(\theta_r, \varphi_r) = (\theta_r, 270^\circ)$.

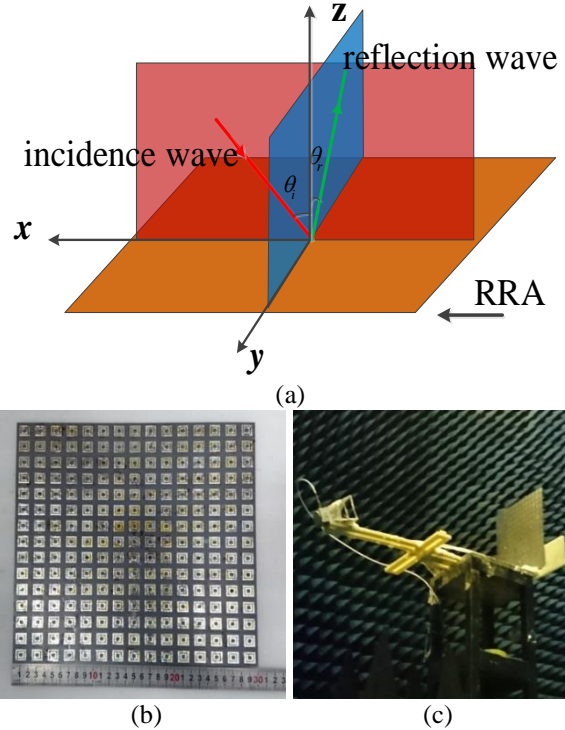


Fig. 5. (a) The coordinate of the simulation, (b) the fabricated RRA, and (c) the experimental scene.

According to the theories of the reflectarray antenna mentioned in Sec. II, we only need to determine the capacitance of each unit to acquire different main beam directions due to the relationship between the capacitance of the varactor diodes and the phase compensation. The angle of the beam-scanning θ_r is supposed from -60° to 60° .

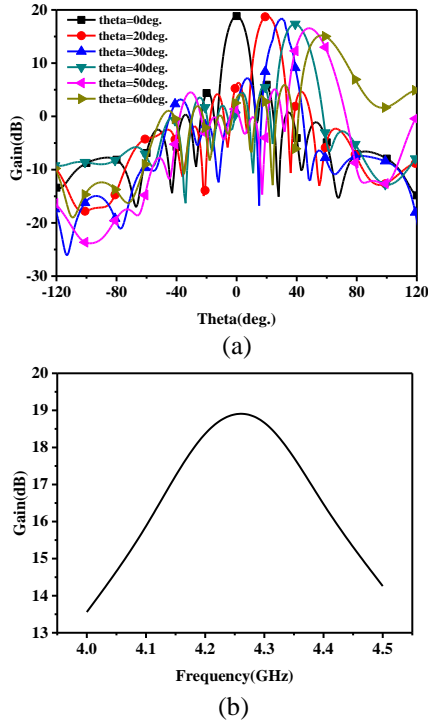


Fig. 6. (a) The gain of the RRA at 4.2GHz, and (b) the gain of the RRA when $(\theta_r, \varphi_r) = (20^\circ, 270^\circ)$.

Table 2: Characteristics of the RRA at 4.2GHz

Direction	Gain (dB)	FSSL (dB)	Error
$(0^\circ, 270^\circ)$	20.94	7.51	0°
$(20^\circ, 270^\circ)$	20.12	4.62	0°
$(30^\circ, 270^\circ)$	19.25	3.11	0°
$(40^\circ, 270^\circ)$	19.00	3.54	0°
$(50^\circ, 270^\circ)$	18.67	1.58	0°
$(60^\circ, 270^\circ)$	18.03	7.25	0°

The dual-band and dual-polarized RRA can work at the horizontal polarization mode and the perpendicular polarization mode. When the incident wave is at the horizontal polarization mode, the direction of the electric field of the incident wave and the incident plane are in the same plane, the operating frequency is 4.2GHz. The reflection angle θ_r is from 0° to 60° and the 3dB relative bandwidth is approximately 4.8% while $\theta_r = 20^\circ$ in Fig. 6. In order to compare the characteristics of the reflectarray more intuitively, Table 2 gives the characteristics in different radiation directions when the operating frequency is 4.2GHz. The gain of the RRA decreases slowly at horizontal polarization mode.

Besides, when the incident wave is at the perpendicular polarization mode, the direction of the electric field of the incident wave is perpendicular to the incident plane, the operating frequency is 6.5GHz. The reflection angle θ_r varies from 0° to 60° and the 3dB

relative bandwidth is approximately 6.7% while $\theta_r = 20^\circ$, as shown in Fig. 7. From Table 3, the gain of the RRA also decreases slowly at the perpendicular polarization mode. It is clear to see that the RRA can provide two selectable states, at two orthogonal polarization modes at 4.2GHz and 6.5GHz. The beam directions of the RRA are consistent with the presented directions and these simulations confirm the feasibility of the design. The RRA in this section can achieve the frequency agility and polarization reconfigurable feature. Furthermore, it can achieve beam-scanning through controlling the capacitances of varactor diodes.

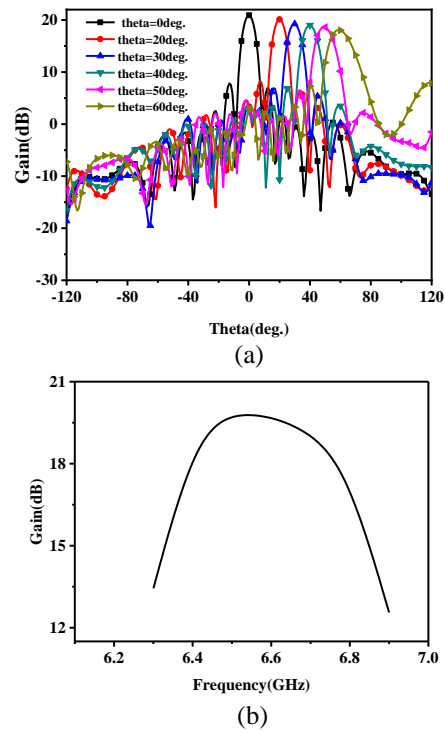


Fig. 7. (a) The gain of the RRA at 6.5GHz, and (b) the gain of the RRA when $(\theta_r, \varphi_r) = (20^\circ, 270^\circ)$.

Table 3: Characteristics of the RRA at 6.5GHz

Direction	Gain (dB)	FSSL (dB)	Error
$(0^\circ, 270^\circ)$	18.90	6.02	0°
$(20^\circ, 270^\circ)$	18.82	6.35	0°
$(30^\circ, 270^\circ)$	18.43	7.19	0°
$(40^\circ, 270^\circ)$	17.37	5.72	0°
$(50^\circ, 270^\circ)$	16.55	5.11	1°
$(60^\circ, 270^\circ)$	15.19	5.93	2°

In order to verify our design, the dual-band and dual-polarized RRA prototype is fabricated and experimentally tested for proof of principle. The incident wave are set in the xoz plane, the direction of the incident wave $(\theta_i, \varphi_i) = (20^\circ, 0^\circ)$, and the direction of the reflection

wave $(\theta_r, \varphi_r) = (20^\circ, 270^\circ)$. From Fig. 8 and Fig. 9, the main beam direction is a bit inconsistent between the simulation result and the measured result. The measured gain is less than the simulated result in Fig. 10 and Fig. 11. The reason may be the deviation in physical processing. It is believed that the design of the dual-band and dual-polarized RRA is reasonable and valid.

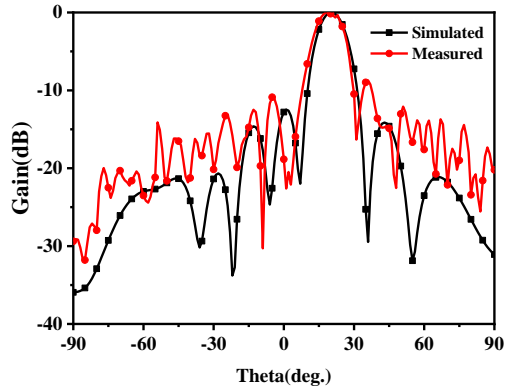


Fig. 8. The gain of the RRA at 4.2GHz.

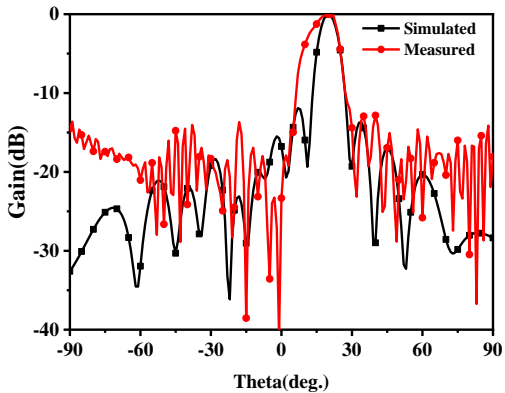


Fig. 9. The gain of the RRA at 6.5GHz.

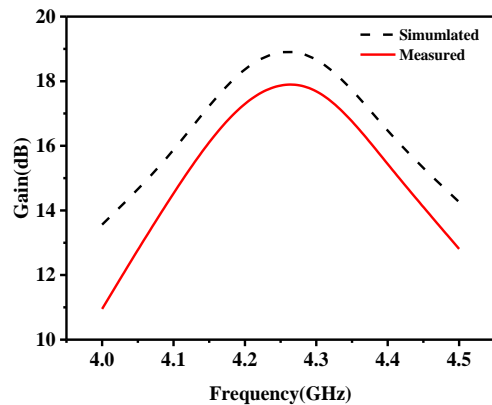


Fig. 10. The gain when at perpendicular polarization mode and $(\theta_r, \varphi_r) = (20^\circ, 270^\circ)$.

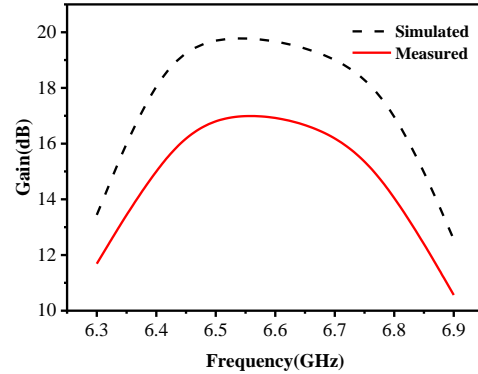


Fig. 11. The gain when at perpendicular polarization mode and $(\theta_r, \varphi_r) = (20^\circ, 270^\circ)$.

V. CONCLUSION

A dual-band and dual-polarized electrically tunable RRA is thoroughly investigated in our work. At dual-band, 4.2GHz and 6.5GHz, the polarization mode is also different. The dual-band and dual-polarized RRA is designed by utilizing the novel element to achieve continuous beam-scanning feature. In Sec. IV, the dual-band and dual-polarized RRA is fabricated. The simulated results and measured results are in good consistence to testify the good properties of the proposed antenna. The multifunctional RRA, which has notable potentials in offering interesting functionalities, may be given special attention in the radar and communication system to reduce the amount of antennas and the decrease of the complexity of the system.

ACKNOWLEDGMENT

This work is supported by Shaanxi Outstanding Youth Science Foundation and National Key R&D Program of China, and supported by the Science and Technology Project of State Grid Corporation of China “Research on Ten-meter level Microwave Radio wireless power Transmission Technology”.

REFERENCES

- [1] J. Perruisseau-Carrier and A. K. Skrivervik, “Monolithic MEMS-based reflectarray cell digitally reconfigurable over a 360 phase range,” *IEEE Antennas Wireless Propag. Lett.*, vol. 7, pp. 138-141, Feb. 2008.
- [2] J. Rodriguez-Zamudio, J. Martinez-Lopez, J. Rodriguez-Cuevas, and A. E. Martynyuk, “Design of an electronically beam scanning reflectarray using aperture-coupled elements,” *IEEE Trans. Antennas Propag.*, vol. 60, no. 4, pp. 1821-1830, Apr. 2012.
- [3] H. Kamoda, T. Iwasaki, J. Tsumochi, T. Kuki, and O. Hashimoto, “Design of an electronically beam scanning reflectarray using aperture-coupled elements,” *IEEE Trans. Antennas Propag.*, vol.

- 59, no. 6, pp. 2524-2531, July 2011.
- [4] J. Huang, and J. A. Encinar, *Reflectarray Antennas*. Singapore: Springer, 2016.
- [5] Y. J. Li, L. Li, Y. Zhang, and C. Zhao, "Design and synthesis of multilayer frequency selective surface based on antenna-filter-antenna using Minkowski fractal structures," *IEEE Trans. Antennas Propagat.*, vol. 63, no. 1, pp. 133-141, Nov. 2014.
- [6] S. Yu, L. Li, and N. Kou, "One-bit digital coding broadband reflectarray based on fuzzy phase control," *IEEE Antennas Wireless Propag. Lett.*, vol. 16, pp. 1524-1527, Jan. 2017.
- [7] S. C. Tian, H. X. Liu, and L. Li, "Design of 1-bit digital reconfigurable reflective metasurface for beam-scanning," *Appl. Sci.*, vol. 7, no. 9, 882, Sep. 2017.
- [8] J. L. T. Ethier, D. A. McNamara, M. R. Chaharmir, and J. Shaker, "Reflectarray design with similarity-shaped fragmented sub-wavelength elements," *IEEE Trans. Antennas Propagat.*, vol. 62, no. 9, pp. 4498-4509, Sep. 2014.
- [9] S. V. Hum and J. Perruisseau-Carrier, "Reconfigurable reflectarrays and array lenses for dynamic antenna beam control: A review," *IEEE Trans. Antennas Propagat.*, vol. 62, no. 1, pp. 183-198, Jan. 2014.
- [10] L. Li, Q. Chen, and Q. W. Yuan, "Frequency selective reflectarray using crossed-dipole elements with square loops for wireless communication applications," *IEEE Trans. Antennas Propagat.*, vol. 59, no. 1, pp. 89-99, Jan. 2011.
- [11] M. Y. Wang, N. Yang, S. C. Ye, H. L. Li, J. Xu, C. L. Zhong, and H. Zheng, "Scattering by a metallic sphere coated with chiral metamaterials," *Applied Computational Electromagnetics Society Journal*, vol. 28, no. 6, pp. 494-500, June 2013.
- [12] K. Yu, Y. Li, and X. Liu, "Mutual coupling reduction of a MIMO antenna array using 3-D novel meta-material structures," *Applied Computational Electromagnetics Society Journal*, vol. 33, no. 7, pp. 758-763, July 2018.
- [13] H.-T. Chen, R. Pan, W.-Z. Sun, and S.-Y. He, "Microstrip reflectarray for generation of electromagnetic waves with beam vorticity," *Applied Computational Electromagnetics Society Journal*, vol. 33, no. 5, pp. 488-493, Jan. 2018.



Shuncheng Tian was born in Tianjin, China, in 1990. He received the B.E. degree from Xidian University, Xi'an, China, in 2013. He is currently pursuing the Ph.D. degree in Electromagnetic Fields and Microwave Technology at Xidian University, Xi'an, China.

His research interests include reflectarray analysis, frequency-selective surface analysis and design, automated neural network model generation algorithm, and electromagnetic field simulation and optimization. He is an associate member of URSI.



Haixia Liu (M'13) was born in Hebei Province, China, in 1976. She received the B.S. degree and the M.S. degree in Test and Measurement Technique and Instrumentation from Xidian University, Xi'an, China, in 1998 and 2001, respectively. She studied at Shizuoka University, Shizuoka, Japan, as a cooperative graduate in 2001. From 2002, she worked at Xidian University. She received the Ph.D. degrees in Electromagnetic Fields and Microwave Technology from Xidian University, Xi'an, China, in 2014.

Her research interests include circuit analysis, frequency measurement and control, wireless power transfer, antennas, and electromagnetic compatibility.



Long Li (M'06-SM'11) was born in Guizhou province, China. He received the B.E. and Ph.D. degrees in Electromagnetic Fields and Microwave Technology from Xidian University, Xi'an, China, in 1998 and 2005, respectively.

He was a Senior Research Associate with City University of Hong Kong, in 2006. He received the Japan Society for Promotion of Science (JSPS) Postdoctoral Fellowship and visited Tohoku University, Sendai, Japan, as a JSPS Fellow from November 2006 to November 2008. He was a Senior Visiting Scholar with the Pennsylvania State University, State College, PA, USA, from December 2013 to July 2014. He is currently a Professor with the School of Electronic Engineering, Xidian University. He is the Director of Key Lab of High Speed Circuit Design and EMC, Ministry of Education, China. His research interests include metamaterials, electromagnetic compatibility, novel antennas, OAM, and wireless power transfer and harvesting technology.

Li was the recipient of the Nomination Award of National Excellent Doctoral Dissertation of China in 2007. He was also the recipient of the Program for New Century Excellent Talents in the University of the Ministry of Education of China in 2010, the First Prize of Awards for Scientific Research Results offered by Shaanxi Provincial Department of Education, China, in 2013, the IEEE APS Raj Mittra Travel Grant Senior Researcher Award in 2015, and the Shaanxi Youth Science and Technology Award in 2016.

Gain-Enhanced Compact Circularly Polarized Array Microstrip Antenna

Zhaoneng Jiang¹, Hongzhi Zhao¹, Xiaoyan Zhao¹, Jian Liu^{1*}, Mingyue Shui¹, Ting Wan²,
and Xuguang Qiao¹

¹ HeFei University of Technology, Hefei, 230009
jianliu@hfut.edu.cn

² Nanjing University of Posts and Telecommunications, Nanjing 210003
want@njupt.edu.cn

Abstract — A miniaturized circularly polarized microstrip antenna array with sequential-phase (SP) feed is presented. Attributed to the slotted metal walls surrounding the SP feed and the internally slotted patch array with parasitic rectangular patches, the key performance indicators of antennas are greatly improved, such as gain and impedance bandwidth. The numerical results of designed antenna simulated by ANSYS HFSS show that the impedance bandwidth is about 11.89% (5.41-6.09GHz) for the $S_{11} = -10$ dB matching criterion, the 3-dB Axial Ratio (AR) bandwidth is about 13.26% (5.64-6.44GHz), and the peak gain can reach to 11.86 dBi at 6.09GHz. When the center frequency of proposed antenna is operated at 5.87GHz, the available bandwidth is 7.71% (5.64-6.09GHz). Based on this, the AR bandwidth is about 450MHz.

Index Terms — Antenna array, circular polarization, microstrip, sequential-phase.

I. INTRODUCTION

With the development of microstrip technology in the field of modern wireless radio, the performance of circularly polarized antennas has become increasingly demanding. In this paper, a circularly polarized microstrip antenna arrays with enhanced gain has been proposed. Because of its compact structure, light weight, strong anti-jamming capability, and easy circuit integration, the circularly polarized microstrip antenna arrays exhibit important application prospects in modern radio fields, especially for electronic countermeasures and wireless communications.

At present, two common ways are used to constitute circularly polarized microstrip antenna array: (1) Uniformly feed each circularly polarized antenna to form an array [1]; (2) Construct a circularly polarized antenna array using a continuous phase rotation feed excitation microstrip antenna [2]. In general, by using two spatially orthogonal linearly polarized electric field components with equal amplitude and 90 degree heterogeneity, a

circularly polarized antenna can be achieved. This property determines that the antenna structure in the form of sequential phase rotation can better suppress cross polarization and extend the antenna bandwidth. On the other hand, the sequential phase rotation method can well reduce the coordination of feeders through reasonable layout improving the performance of the antenna [3-4]. Therefore, the AR bandwidth of the circular polarization array antenna can be effectively improved. At the same time, the gain performance of the antenna can be increased. Due to the expansibility of the antenna array, the general research is focus on microstrip patch antenna array that can generate circular polarized waves on the sequential phase rotation [5]. Reference [6] introduces a cross-dipole sub-circular polarized antenna with a parasitic loop resonator and its array. By using the sequential phase of the four branches, cross-dipoles can produce broadband circular polarization performance. In order to achieve a wider circular polarization bandwidth, the literature uses a parasitic open-loop resonator. Attributed to the half-wavelength resonator, the proposed antenna can achieve a 3-dB AR bandwidth of about 28.6% (0.75GHz, 2.25-3.0GHz) through the two orthogonal branches coupling with the resonator. Reference [7] proposed a circularly polarized microstrip antenna array with double-layered feed structure. Meanwhile, a thicker substrate is used to reduce the inherent quality factor, thereby increasing the bandwidth of the antenna. Generally speaking, the design of a multi-layer patch can lead to excessive antenna size and possible shortcomings, such as distorted patches and inconvenience handling. In addition, thicker substrates are also prone to increase the difficulty of antenna coupling. In this case, the article used a H-type coupling feeder as impedance matching network to improve antenna coupling. A slotted metal wall structure around the feed is proposed in Ref. [8] to improve the antenna's radiated gain. Reference [9] proposes a 2×2 antenna array with broadband circular polarization performance composed of four parasitic rectangular patches. The feed structure of this antenna is

consist of circular strips. Then the array elements are capacitively coupled with the four strips connected to the feed network. Finally, four parasitic patches are introduced to improve gain flatness.

In [10-11], a reflector structure is added below the radiation piece of the circularly polarized antenna to increase the gain. Compared with other antenna structures described above, the use of reflector can greatly reduce the sizes of antenna, that is, the gain can be enhanced by using a single radiating element. In addition, Ref. [11] also uses a short-circuit pin structure to optimize the bandwidth. In [12], a single-feed method is used to excite the radiation patch, and a phase-shifted network is used to construct a circularly-polarized antenna array. According to the chamber mode theory, the microstrip antenna that is excited by a single feed can produce two degenerate modes of equal amplitude and perpendicular to each other. On this basis, the perturbation unit is introduced by a rectangular chamfering angle to separate the resonance frequency, forming a circular polarization. The article uses a SP network as the power splitter to radiate patch arrays, effectively improving the antenna gain. However, such a splitter structure greatly reduces the bandwidth of the antenna, and makes the antenna size larger. Therefore, the Ref. [13] adds parasitic patches to optimize the antenna bandwidth, but the sizes of antenna have not changed much.

Inspired by the above progresses, a circularly polarized antenna with four radiating patches with parasitic patch is designed. The antenna is excited by a probe, and the feed section directly contacts the feed network. Besides, most of the feed network is isolated from the patch. Ultimately, it minimizes the parasitic radiation. In the optimization of proposed antenna, the bandwidth of the antenna can be improved by changing the structures of the patch. By cross-grooving the circular radiating patch, not only the current of the guiding patch is bent, but also the effective length of the current path is increased, and the resonant frequency is reduced. In addition, the outer circle is chamfered so that the array element is capacitively coupled with the four strips. At the same time, during the optimization process, it was found that by adding a parasitic patch next to the radiating patch, the impedance bandwidth of the antenna can be effectively increased. Finally, the available bandwidth of 450MHz can be achieved.

II. ANTENNA DESIGN

The configuration of the antenna array proposed in this paper is shown in Fig. 1. A 1.75mm thick Rogers RT/duroid 5880 (tm) dielectric plate ($\epsilon_r = 2.2$, loss tangent = 0.0009) is adopted. The size of the dielectric board is $L \times L$. A square loop is truncated from an angle of 1×1 on the inner side of a circle to realize SP rotation. A slotted metal wall surrounding the feed structure is introduced to improve the gain characteristics of the

antenna. The radiating patch of the antenna is a square structure of $L5 \times L5$, and located on the center of the square diagonal line, and the half diagonal is the radius $R1$ on the upper and lower sides of the square. Based on the simulation optimization, the final dimensions of the antenna are shown in Table 1.

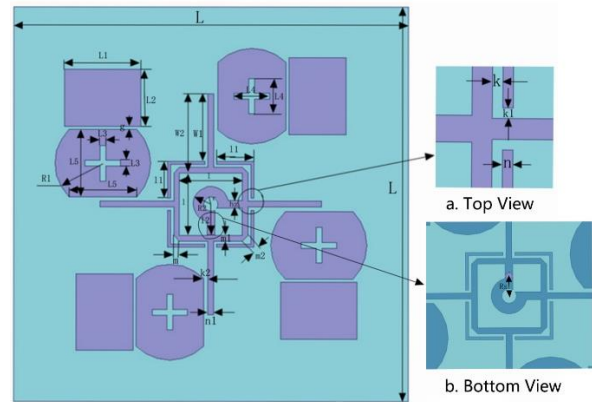


Fig. 1. Geometry and dimensions of the proposed antenna array.

Table 1: Detailed dimensions (unit: mm)

L	L1	L2	L3	L4
67	13	9.7	1	6
L5	1	l1	l2	m
11.5	10.64	6.3	5.32	0.98
m1	m2	W1	W2	hz
0.98	1.38	11.48	13.46	1.3
n1	g	r	R2	Rs
1	0.5	1.2	3	3.3
k	k1	k2	n	
0.5	0.5	0.5	0.7	

III. EXPERIMENTAL RESULTS

Through the strips protruding from the SP loop and the capacitors placed beside them, the antenna array excites the radiating patch in the form of a single feed point coupling, and the center cross-shaped slot acts as a perturbation unit to separate the antenna resonant frequencies. When the degenerate mode separation unit is properly selected, for the operating frequency of the antenna, the equivalent impedance phase of one mode leads the phase, and the equivalent impedance phase of the other mode lags behind, resulting in a phase difference of 90° , thereby forming circular polarization. According to the cavity mode theory, it is generally known that an antenna in the form of a rectangular patch can be understood as a cavity in which all the patches are open, and the corresponding equation is:

$$\nabla^2 \phi_{nm} + k^2 \phi_{nm} = 0, \quad (1)$$

$$\frac{\partial \phi_{nm}}{\partial n} = 0. \quad (2)$$

Based on the analysis of rectangular radiating patch, it is assumed that the rectangular structure of the microstrip antenna can only excite the working mode of the primary mode. When it is added to the perturbation unit Δs , a pair of characteristic modes can be obtained, and a pair of characteristic function ϕ' can also be obtained. Corresponding to the wave number k' , which ϕ' is satisfied:

$$\phi' = P\phi_{01} + \phi_{10}. \tag{3}$$

According to the orthogonality of characteristic function, the separation unit of ϕ' is a pair of modes whose polarization directions are perpendicular to each other and have the same amplitude. CP radiation is obtained when the phase between the two modes is $\pm 90^\circ$. As shown in the Figs. 2 and 3, it can be found that the AR bandwidth varies greatly by optimizing the distance g from stripe to patches in the ANSYS HFSS optimization process. By studying the current distribution, it is considered that the electric field generated by the induced current on the parasitic patch is the same as that on the original radiation patch. Comparing the array with or without parasitic patches, it was found that the electric field distribution was affected. Since the added parasitic patches are not connected to the original feed structure, two or more modes can be excited, and these modes can be approached by adjusting the geometric parameters of the parasitic patches to increase the bandwidth. Therefore, according to the Figs. 4 and 6, compared with a single array, the parasitic patch not only affects the return loss, but also controls the direction of antenna radiation. Figure 5 shows that the AR bandwidth of the antenna is improved when the antenna is attached with metal wall and parasitic patch. It is found that the influence of metal wall on heat sink varies with the thickness and position of metal wall.

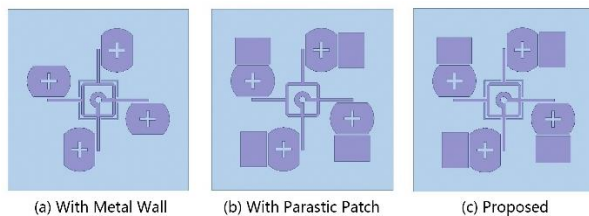


Fig. 2. Stages of antenna development: (a) with metal wall, (b) with parasitic patch, and (c) proposed antenna.

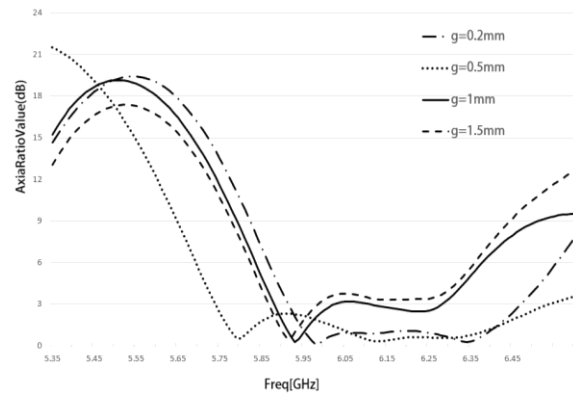


Fig. 3. Simulated AR of the 2×2 array with different g .

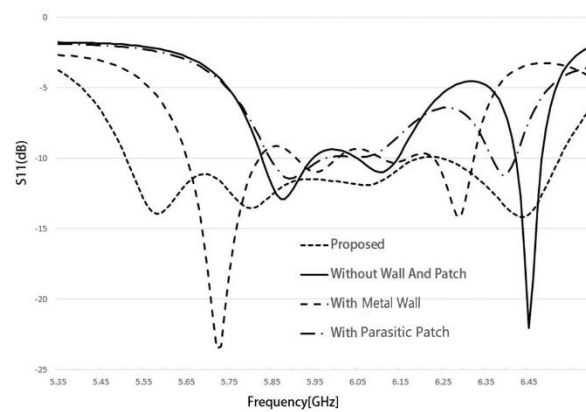


Fig. 4. Simulated return loss of the 2×2 array.

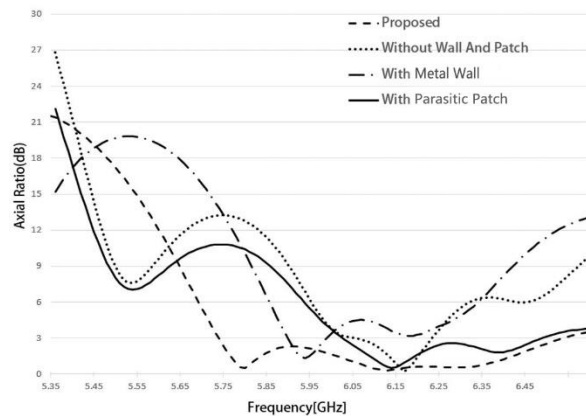


Fig. 5. Simulated AR of the 2×2 array.

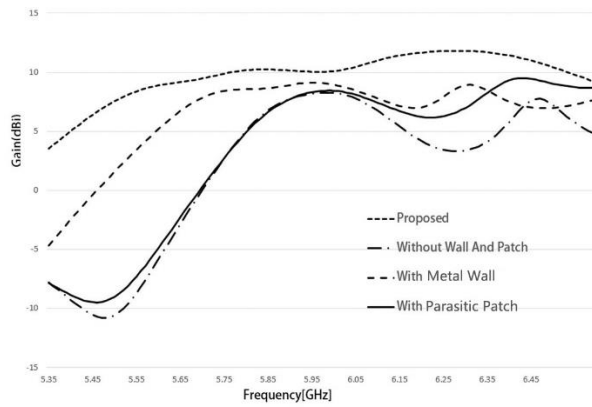


Fig. 6. Simulated gains of the 2×2 array.

According to the Fig. 6, it can be found that the gain of lower frequency band is significantly reduced without metal walls and parasitic patches. In order to analyze the influence of parasitic patch and metal wall on the gain and the impedance bandwidth, the electric field distribution of different antennas at 5.87GHz are shown in Fig. 7. Compared with the un-added metal wall, the placement of metal wall contributes to the quasi-traveling wave propagation, thereby achieving impedance matching of the antenna and increasing the antenna bandwidth. Figures 8 and 9 show the the current vector direction of different antennas at 5.87GHz. The induced current on the rectangular parasitic patch contributes to the original patch coupling energy, and the direction of electric field vector excited on the parasitic patch is the same as that of original patch. Therefore, the antenna gain is improved due to the disturbing effect of parasitic patch on the surface current of original patch. Meanwhile, by analyzing the electric field distribution of different phases, the electric field component is rotated counterclockwise to achieve a right circular polarization (RHCP) wave in the $+z$ direction. The electric field distribution was found to be slightly affected by comparing the presence or absence of parasitic patches of the array elements. Therefore, the application of parasitic patches not only improves the gain of low frequency band, but also maintains the performance of the CP. Figure 10 shows the effect of parasitic patches and metal walls on the performance of antenna array at 5.87GHz. It can be seen that after the addition of the metal wall, the 3 dB beamwidth is significantly narrowed in the xoz plane. The peak gain of antennas with or without metal walls are 10.5 and 9.5 dBi, respectively. Moreover, the gain difference is more obvious in the low frequency band.

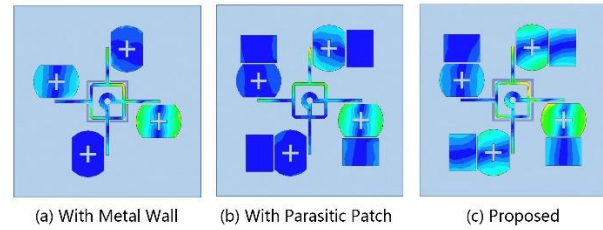


Fig. 7. Simulated vector electric field distributions at 0° , 5.87GHz: (a) with metal wall, (b) with parasitic patch, and (c) proposed.

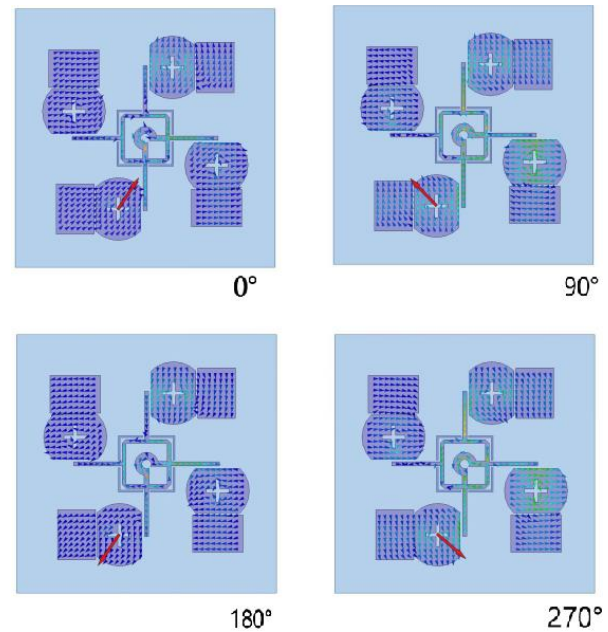


Fig. 8. Simulated current distributions at 5.87GHz.

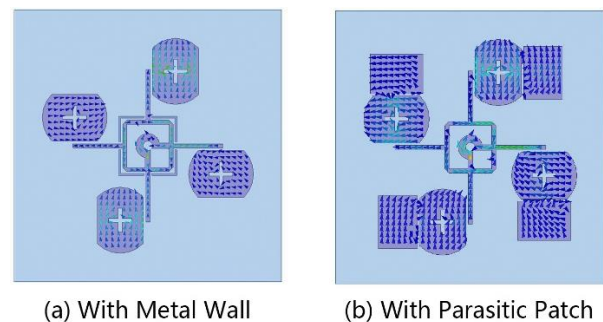


Fig. 9. Simulated current distributions at 0° , 5.87GHz: (a) with metal wall and (b) with parasitic patch.

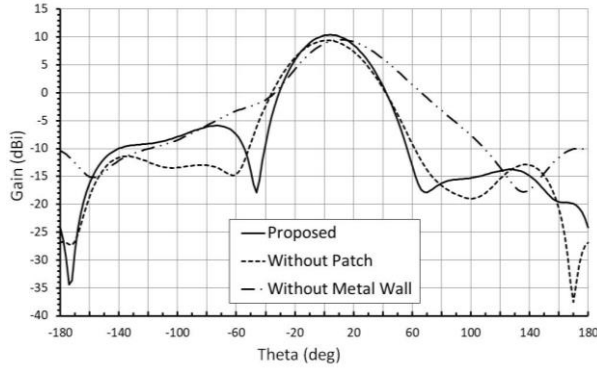


Fig. 10. Pattern comparisons of the proposed antenna at 5.87GHz (xoz-plane).

The normalized far field radiation pattern is shown in Fig. 11. Good RHCP radiation can be observed. Besides, in the CP band, the 3dB beam-width measured on the xoz plane is 54.2° (5.65GHz), 50.3° (5.87GHz), and 40.2° (6.09GHz). The performance of beam-width is desirable for radar and wireless communication systems. Table 2 shows the performance of the proposed antenna compared with that of the references. The results show that the proposed antenna has relatively small size and high gain.

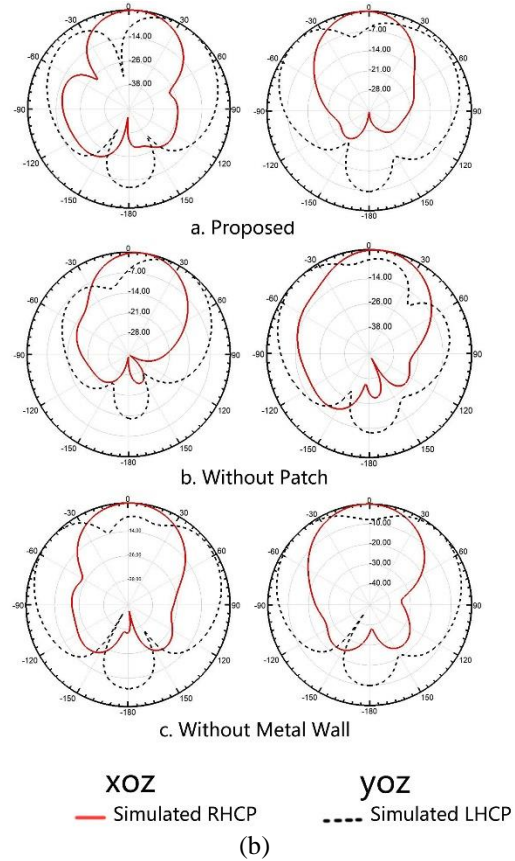
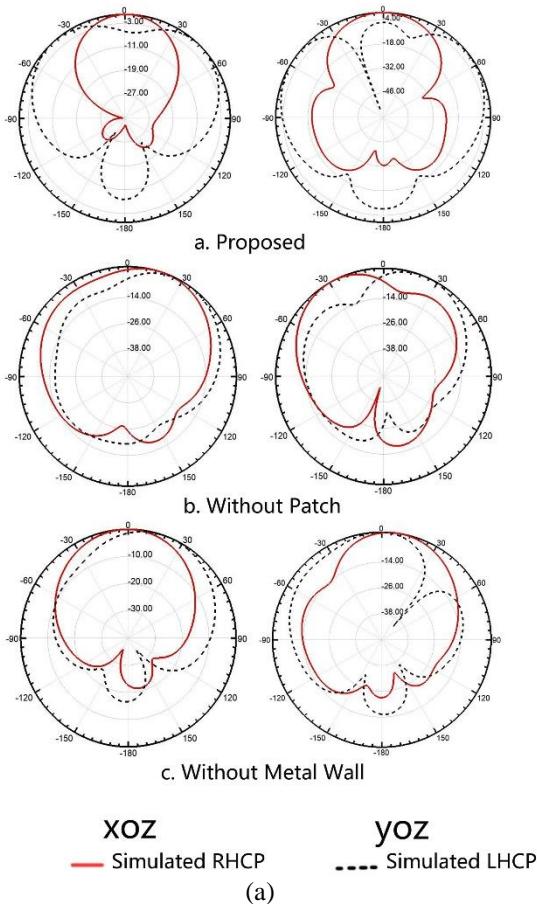


Fig. 11. Simulated and measured normalized radiation patterns in different planes: (a) 5.65 and (b) 5.87GHz.

Table 2: The comparison on the performance of the proposed CP antenna with other works

Ref.	CP Center Frequency (GHz)	10dB Return Loss BW (GHz/%)	3-dB ARBW (GHz/%)	Gain (dBi)	Dimension (mm×mm×mm)
[8]	4.99	0.3/6	0.29/5.8	10.05	100×100×3.5
[11]	5.50	1.03/18	0.7/12.5	12	75×75×1.5
Pro.	5.87	0.68/11.9	0.8/13.3	11.86	67×67×1.75

IV. CONCLUSION

This paper presents a compact circular polarized antenna array. According to the simulation results of ANSYS HFSS, the antenna can obtain flat antenna gain in the effective bandwidth of 450MHz (5.64-6.09GHz) with small size. Moreover, at the CP center frequency of 5.87GHz, the antenna gain is 10.04dBi. This designed antenna has the characteristics of small size, flat gain, wide impedance and AR bandwidth, which can satisfy the requirements of current miniaturized development of military and civilian circular polarized antenna arrays.

REFERENCES

[1] Nasimuddin and K. P. Esselle, “New feed system for wideband circularly polarised stacked micro-

- strip antennas,” *IET Microwaves, Antennas & Propagation*, vol. 1, no. 5, pp. 1086-1091, 2007.
- [2] C. W. Su and J. S. Row, “Slot-coupled microstrip antenna for broadband circular polarisation,” *Electronics Letters*, vol. 3, pp. 318-319, 2006.
- [3] P. N. Rao and N. V S. N. Sarma, “Fractal boundary circularly polarised single feed microstrip antenna,” *Electronics Letters*, vol. 12, pp. 713-714, 2008.
- [4] F. Ferrero, C. Luxey, G Jacquemod, and R. Staraj, “Dual-band circularly polarized microstrip antenna for satellite applications,” *IEEE Antennas and Wireless Propagation Letters*, vol. 4, pp. 13-15, 2005.
- [5] J. Huang, “A technique for an array to generate circular polarization with linearly polarized elements,” *IEEE Transactions on Antennas and Propagation*, vol. 34, no. 9, pp. 1113-1124, 1986.
- [6] J.-W. Bai, T.-H. Lee, S. Pyo, S.-M. Han, J. Jeong, and Y.-S. Kim, “Broadband circularly polarized crossed dipole with parasitic loop resonators and its arrays,” *IEEE Transactions on Antennas and Propagation*, vol. 1, pp. 80-88, 2011.
- [7] Y. Li, Z. Zhang, and Z. Feng, “A sequential-phase feed using a circularly polarized shorted loop structure,” *IEEE Transactions on Antennas and Propagation*, vol. 61, pp. 1443-1447, 2013.
- [8] W. Yang, J. Zhou, Z. Yu, and L. Li, “Bandwidth- and gain-enhanced circularly polarized antenna array using sequential phase feed,” *IEEE Antennas & Wireless Propagation Letters*, vol. 13, no. 13, pp. 1215-1218, 2014.
- [9] K. Ding, C. Gao, T. Yu, D. Qu, and B. Zhang, “Gain-improved broadband circularly polarized antenna array with parasitic patches,” *IEEE Antennas & Wireless Propagation Letters*, vol. 16, no. 99, pp. 1468-1471, 2017.
- [10] F. S. Chang, K. L. Wong, and T. W. Chiou, “Low-cost broadband circularly polarized patch antenna,” *IEEE Transactions on Antennas and Propagation*, vol. 10, pp. 3006-3009, 2003.
- [11] S. S. L. Yang, A. A. Kishk, and K. F. Lee, “Wideband circularly polarized antenna with L-shaped slot,” *IEEE Transactions on Antennas and Propagation*, vol. 6, pp. 1780-1783, 2008.
- [12] C. Deng, Y. Li, Z. Zhang, and Z. Feng, “A wideband sequential-phase fed circularly polarized patch array,” *IEEE Transactions on Antennas and Propagation*, vol. 62, pp. 3890-3893, 2014.
- [13] S. Mohammadi-Asl and J. Nourinia, “Wideband compact circularly polarized sequentially rotated array antenna with sequential-phase feed network,” *IEEE Transactions on Antennas and Propagation*, vol. 16, pp. 3176-3179, 2017.

Mutual Coupling Reduction of a Dual-Band Antenna Array Using Dual-Frequency Metamaterial Structure

Shengyuan Luo¹, Yingsong Li^{1,2,*}, Yinfeng Xia¹, Guohui Yang³, Laijun Sun⁴,
and Lei Zhao⁵

¹ College of Information and Communication Engineering
Harbin Engineering University, Harbin, Heilongjiang 150001, China

² National Space Science Center, Chinese Academy of Sciences, Beijing 100190, China
*liyingsong@ieee.org

³ School of Electronics and Information Engineering, Harbin Institute of Technology, Harbin 150001, China

⁴ College of Electronic Engineering, Heilongjiang University, Harbin, 150080

⁵ Center for Computational Science and Engineering, School of Mathematics and Statistics
Jiangsu Normal University, Xuzhou, China

Abstract — Dual-band antenna is an enabling component for wireless local area network (WLAN) communication systems. One of the challenges for improving the communication quality in dual-band multiple-input multiple-output (MIMO) system is to develop low coupling MIMO antenna array with compact size. In this paper, an isolation enhanced two-element MIMO antenna array with dual-frequency decoupling structure is proposed for operating at the upper and lower WLAN bands. The proposed dual-frequency decoupling structure is realized by an array of two columns of metamaterial structures with unique electromagnetic resonance characteristic. The property of the designed metamaterial array is analyzed and integrated between the elements of a two-element patch antenna array to reduce the mutual coupling. The performance of the dual-frequency patch antenna array is verified by the simulation and measurement, respectively. The experimental results show that the proposed dual-frequency MIMO antenna array has an isolation enhancement about 15dB at 2.4GHz and 9dB at 5.25GHz, respectively. Moreover, the proposed dual-band MIMO antenna has a smaller size and good directional radiation patterns, making it promising for WLAN applications.

Index Terms — Dual-band, MIMO, mutual decoupling, WLAN.

I. INTRODUCTION

With the development of wireless communication technologies, the antenna design carts an increasing

demand since it is required to transmit and receive the electromagnetic signals [1]. In order to improve the communication quality, multiple-input multiple-output (MIMO) technique has been applied for wireless communications and it is also considered as a technique for construct massive MIMO system in next generation communication systems [2]. Furthermore, the wireless local area network (WLAN) has been used for a long time, which needs to operate at dual frequency mode to incorporate 802.11 a/b/g/n/ac/ax standards. The antennas mentioned in [1-2] is printed on low cost substrate to utilize the characteristics like light weight, small volume and easy fabrication.

As for MIMO WLAN communication system, the design of the dual-band MIMO antenna has been applied to practical applications. So far, many methods have been exploited to design MIMO multi-band antennas that contain the WLAN band [3-11]. For the small dual-band antenna designs, the most mature technologies to obtain multi-band characteristics includes exciting multiple-mode [12-14] and engraving a groove on the microstrip patch [15-16], using multilayer structure or multi-stubs to form resonators and use multiple patches technology [17-20].

For the small dual-band antenna designs, the most mature technologies to obtain multi-band characteristics includes exciting multiple-mode and engraving a groove on the microstrip patch [15-16], using multilayer structure and multiple patches technology [17-19]. The dual-mode excitation technology may have two narrow operating bands for WLAN communication, but it has

advantages to provide multiple bands without changing the structure of the patch antenna and the radiation patterns.

On the other hand, the channel capacity and the throughput of the MIMO communication system might be reduced when the received signals at multiple receiving antennas are correlated [2]. Therefore, the mutual coupling (MC) from the adjacent antenna elements in the MIMO antenna array may degrade the efficiency, correlation and eventually deteriorate the communication quality of the entire MIMO system [20-21]. Some of the researchers paid much efforts to optimize the precoding strategies on both the receiver and transmitter sides to reduce the MC to design a compact large-scale MIMO system [22-23]. Recently, the compact device will limit the size of the components, which makes the MIMO antenna array smaller and smaller. Thus, the MC issue in the compact MIMO antenna array is an inevitable factor that seriously affects the MIMO antenna performance in small terminals. How to reduce the MC in the MIMO array becomes to be a hot topic which attracts more and more attention in recent years [20-23]. Especially for the compact dual-band MIMO antenna array that is used for dual-band WLAN communication and the MC problem becomes a key issue that should be resolved simultaneously at the lower and upper WLAN bands.

In general, the MC is serious when the antenna elements are placed less than half-wavelength, which will deteriorate the radiating performance and reduce the channel capacity. Thus, it is very useful to design decoupling structure to reduce the MC between the antenna elements [24]. Currently, many amazing mutual decoupling structures such as decoupling network, defected ground structure (DGS), electromagnetic band gap (EBG) and metamaterial are used in MIMO antenna array [25-38]. For the decoupling network, the typical decoupling structure is to use a stub in the ground plane of a MIMO antenna array, such as the T-shaped stub [25-27], which will affect the radiation patterns of the antenna array. Recently, an improved decoupling network has been proposed in [28]. It demonstrated that the coupled decoupling structure can reduce the MC over two bands, which is still realized based on stub technologies. Also, the periodic DGS has been developed to improve the isolation in the MIMO antenna array [29-31]. However, the DGS destroys the integrity of the ground plane, which may leak electromagnetic wave and affect the radiation patterns. Another effective method to enhance the isolation of antenna array is to use the EBG structure in antenna array [32-36]. Unlike the previous decoupling technologies, the EBG structure has been introduced into the middle of the antenna elements, and it can prohibit the microwave propagation between antenna elements because of its high impedance property. The resonance of the EBG is caused by the inductance of the EBG cell structure itself and the

capacitance between the EBG units.

In the past decades, the metamaterial decoupling techniques have attracted more attention because of its unique property, and it can perform high impedance, negative permittivity and negative permeability, negative refractive index. Moreover, the metamaterial decoupling has some advantages such as small size, easy fabrication. The resonance of the metamaterial is caused by the capacitance and inductance of the metamaterial cell itself. Therefore, although the structure of the EBG and metamaterial is similar, the basic resonance principle is different. For the decoupling network, DGS, EBGs, they are not easy to obtain a dual-band property because they need to redesign the entire structures. But, it is easy to achieve a dual-band negative permittivity by integrating two conventional SRRs into the same metamaterial structure, and the designed dual-band meta-material has been used for reducing the MC between the MIMO antenna elements by adjusting the dimensions of the two SRRs. [37-39]. However, these MIMO antennas only have one band by using the metamaterial decoupling structure. Currently, the dual-band antenna array becomes more and more useful because of its potential applications in modern wireless communication systems. Thus, how to reduce the MC between the dual-band antenna array elements becomes an urgent issue.

Based on the advantages of the planar metamaterial, a high isolation dual-band MIMO antenna array is proposed by using dual-frequency metamaterial structure operating at WLAN bands. Compared to existing technologies, our proposed method has the following unique features:

- (1) The designed MIMO antenna array with high isolation covers the lower and upper WLAN bands.
- (2) Dual-frequency metamaterial is used to reduce the MC of the dual-band WLAN MIMO antenna array.
- (3) The designed planar dual-band metamaterial can be independently adjusted to achieve a good match with the desired dual-band MIMO antenna array without affecting the performance of the MIMO array.

II. DESIGN OF THE PROPOSED DUAL-BAND WLAN MIMO ARRAY

A. Dual-band microstrip antenna

According to the rectangular microstrip antenna theory and the multiple mode excitation scheme, a dual-band microstrip antenna is developed with only one feeding, which is shown in Fig. 1. The proposed antenna has a simple rectangle patch printed on a FR4 substrate with a relative permittivity of 4.4 and a loss tangent of 0.02, and there is a ground plane set at the bottom of the FR4. Then, a coaxial probe feeding is used to excite the two modes. The longer side excites the TM_{10} mode to generate the lower frequency, while the short side excites the TM_{01} mode to give the upper band.

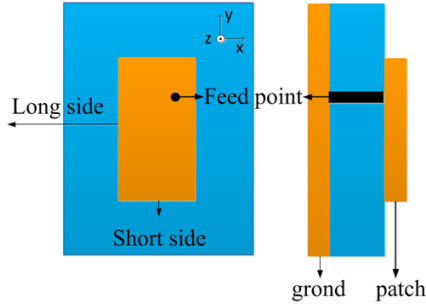


Fig. 1. The mechanism of dual-band patch antenna.

B. Principle of dual-band metamaterial

The schematic of a metamaterial comes from the resonance of the inductance in metal patch and the capacitance in the split ring resonator (SRR). For metamaterial structure, the resonance is caused by the inductance and capacitance of the SRR structure, while the dual-band metamaterial proposed in this paper is realized by the inductance and the two different capacitances. When two different SRRs are connected by a metal strip and placed on the same substrate, the inductance significantly increases while the capacitance does not change. Thus, two resonant frequencies are obtained. Comparing with the original single-band SRR, the proposed integrated SRR (ISRR) structure shown in Fig. 2 (a) has a more complicated design procedure. However, the ISRR can provide more bands, and the size is greatly reduced. Additionally, each band can be independently adjusted to match with the desired resonant frequency. Based on the theory of the metamaterial, a metamaterial based on the ISRR is designed and given in Fig. 2 (b). Figure 2 (c) shows the 3-demesion structure of the proposed metamaterial cell. Since the ISRR has an adjustable band, the proposed metamaterial cell can be flexibly designed to meet the desired resonance band requirements. To understand the performance of the proposed metamaterial cell, the perfect H, and perfect E boundaries, and wave port are used to analyze its characteristics.

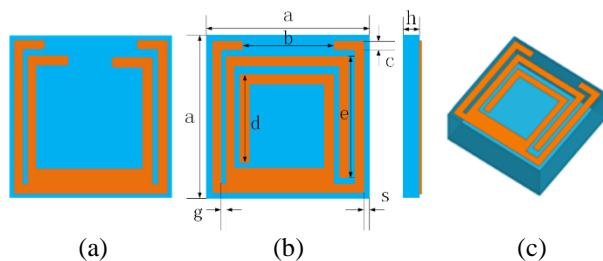


Fig. 2. Geometry of DBMC: (a) SRR structure, (b) proposed metamaterial cell, and (c) the 3-D structure of the DBMC.

Figure 3 presents the equivalent circuit of the proposed dual-band metamaterial cell. The split size controls the C_1 , the overall size of the outer SRR controls the L_1 , and the R_1 is the resistance of the outer SRR itself. C_2 is the capacitance between the two branches of the inner SRR. The R_2 and R_3 are the resistances of two branches of the inner SRR. Correspondingly, the L_2 and L_3 are the inductance of two branches of the inner SRR. Figure 4 presents the simulation model of the proposed dual-band metamaterial cell (DBMC), which is created in the HFSS. In fact, the gap between the SRRs and the length of the SRRs control the metamaterial property, which can be obtained by the numerical analysis. Figure 5 gives the transmission coefficient (S_{21}) and reflection coefficient (S_{11}) of the DBMC with different parameters. When b increases from 2mm to 4mm shown in Fig. 5 (a), the bandwidth of the center frequency of the upper band is changed while the bandwidth for the lower band remains same.

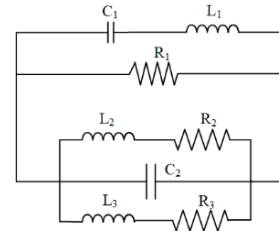


Fig. 3. The equivalent circuit of the proposed DBMC.

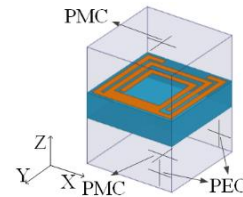


Fig. 4. Simulation model of the proposed dual-band metamaterial cell.

Figure 5 (b) presents the effects of various b on the phase difference of S_{11} and S_{21} . It is found that the phase at the upper band changes quickly with different parameter b . Then, the S-parameter method is utilized to retrieve the dielectric constant of designed DBMC, and the results are described in Fig. 5 (c). The negative permeability characteristics of the upper band move to higher frequency with the increment of parameter b . Then, the parameter e that gives important effects on the performance of the proposed DBMC is investigated in detail. Figure 6 (a) illustrates magnitude difference of S_{11} and S_{21} with different length e ranging from 2mm to 4mm of the ISRR. The frequency of the lower band

becomes to be smaller with an increasing e due to the coupling between the modified SRRs. The phase difference for different e is given in Fig. 6 (b). It is observed that the phase for both the upper band and lower band changes so fast with different parameter e . Then, the S-parameter method is considered to retrieve the dielectric constant of designed DBMC, and the results are presented in Fig. 6 (c). The negative permeability characteristics of the lower band shifts very quickly with various e .

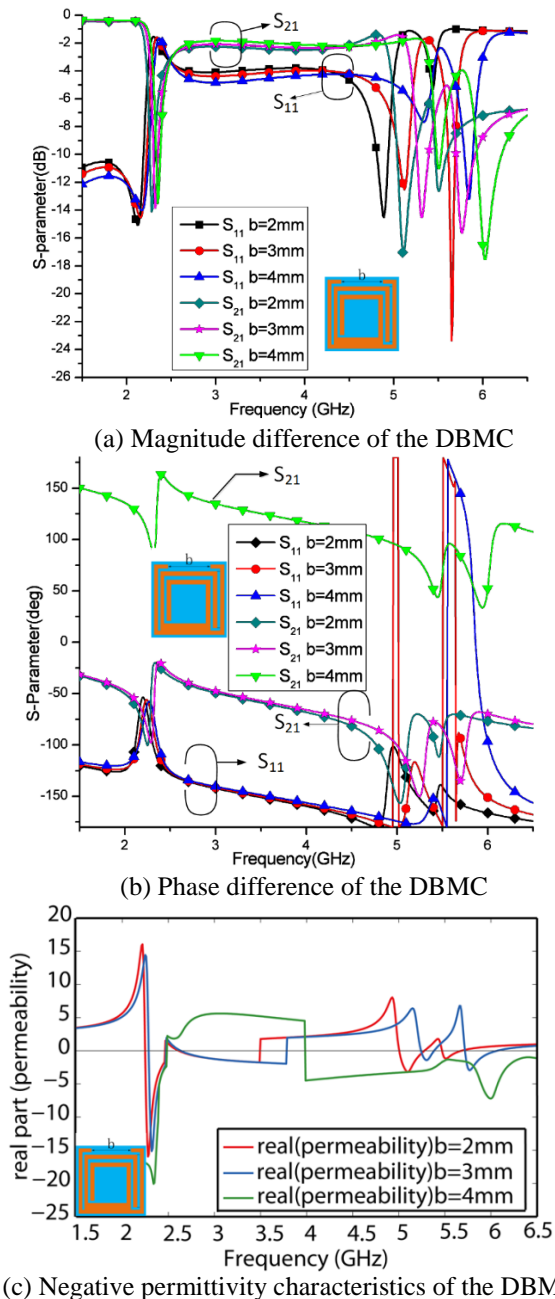


Fig. 5. Performance of the proposed DBMC with different b dual-band MIMO antenna array elements.

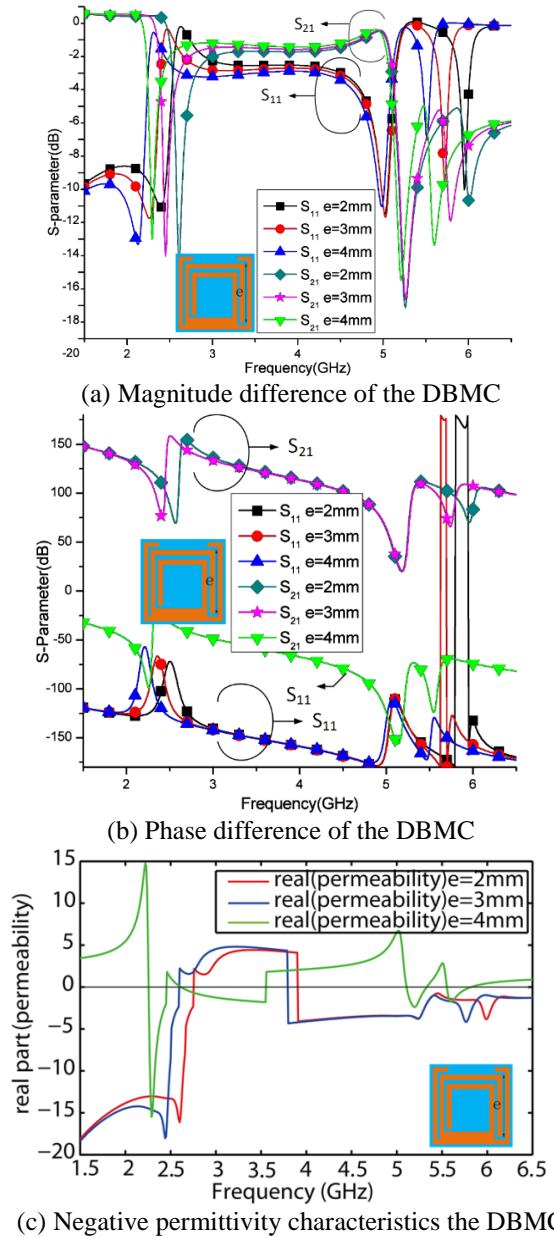


Fig. 6. Performance of the proposed DBMC with different e .

From the above discussions of the proposed DBMC, it is observed that the gap between the SRRs and the length of the SRRs decide the magnitude and phase of the transmission coefficient (S_{21}) and reflection coefficient (S_{11}) over the upper and lower operating bands of the DBMC. Then the upper and lower negative permeability bands of the proposed DBMC can be extracted from the magnitude and the phase of the S_{11} and S_{22} . Thus, the decoupling DBMC array composed of two columns of DBMC cells performs high impedance at the upper and lower negative permeability bands, which can be used to prohibit the propagation of the

electromagnetic wave between the dual-band MIMO antenna array elements. The upper permeability band can be properly also be properly adjusted, which make the negative permeability bands of the DBMC array match well with the dual-band MIMO antenna array.

III. DUAL-BAND DECOUPLING MIMO ANTENNA ARRAY BASED ON PERIODIC DBMCs

In this paper, the designed DBMC is used and periodically installed in the middle of the two antenna elements. The original dual-band MIMO antenna array is shown in Fig. 7. The MIMO array consists of two microstrip patch antennas and a common ground plane, which is printed on a FR4 substrate with a relative permittivity of 4.4 and a loss tangent of 0.02. For the rectangle-patch-antenna, dual modes are excited based on the mechanism in the Section 2 to obtain two resonance frequencies. By properly selecting the position of the feeding, TM_{10} and TM_{01} modes are excited. However, the dual-band rectangle-patch-antenna array has strong MC due to the propagation of surface waves between antenna array elements since the antenna elements are very close. The metamaterial cell has already been investigated to suppress surface waves owing to its high impedance characteristic in the negative permeability band [37]. Then, the proposed DBMC also has the ability to inhibit the surface waves in lower and upper negative permeability bands. The mutual decoupling can be realized by integrating the dual-band MIMO antenna array and the designed DBMC on a same substrate when the operating bands of the dual-band antenna array are same with the negative permeability bands of the DBMC. A decoupling array structure consists of two columns of DBMCs, which are symmetrically placed along the X-axis and Y-axis. Then, the designed decoupling array structure is set between the two patch antennas to relieve the MC. By using the proposed DBMC decoupling array structure (DBMC-DAS), a MIMO array with high isolation is achieved, whose geometry is shown in Fig. 8.

Then, the proposed MIMO array with DBMC-DAS is well optimized by the HFSS, and the finalized dimensions of the MIMO array are shown in Table 1.

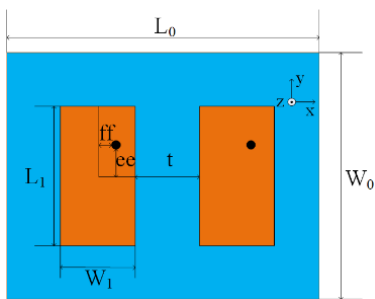


Fig. 7. Reference MIMO array.

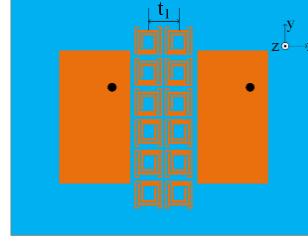


Fig. 8. Proposed MIMO array with DBMC-DAS.

Table 1: Parameters of the dual-band MIMO antenna array with high isolation (Unit: mm)

Parameters	h	W_0	ee	ff	b	g	L_0	L_1
Values	1.6	52	4.012	3.5	2.5	0.2	60	30
Parameters	e	t	t_1	a	c	s	d	W_1
Values	4	14	6	5.62	0.3	0.1	3.5	12

The optimized dual-band MIMO antenna array with proposed DBMC-DAS is fabricated, and the photograph of the fabricated MIMO array is shown in Fig. 9. Then, the fabricated MIMO antenna is measured by using Agilent N9923A in a chamber. The S_{11} and S_{21} of the MIMO array are compared in Fig. 10 for measurement and simulations. We can see that the MIMO antenna has two operating bands at the lower and upper WLAN frequencies. Additionally, the measured S_{11} meets the simulation one. The difference between the measurement and the simulation is attributed to the fabrication tolerance, the stability of the FR4 substrate and the soldering. From the coupling presented by the S_{21} , it is found that the MC between the two patch antennas is reduced by the DBMC-DAS at the expected operating bands, and its MC is reduced by 15dB and 9dB for the lower and upper operating bands, respectively. Thus, the DBMC-DAS can effectively improve the isolation between the two antenna elements. To better understand the MC reduction principle of the proposed MIMO array behind the S-parameter, the current distributions and radiation patterns are analyzed based on the HFSS, and its performance is presented in Figs. 11 and 12 respectively. From the surface current distributions of the MIMO array, we observed that the strong current distributed on both the patch antenna elements for the MIMO antenna without DBMC-DAS. In a word, there is MC effect between the two antenna elements. When the DBMC-DAS is inserted into the middle of the two antenna elements, the surface current on the adjacent patch antenna element is very small while the current on the DBMC-DAS is very strong. It is evident that the DBMC-DAS decoupling structure significantly interacts with the surface currents to block them from affecting adjacent radiation elements in the MIMO antenna array. Thus, the surface current from one antenna to another antenna is blocked by the DBMC-DAS, and hence, the isolation between the MIMO antenna elements are

improved.

Then, the radiation patterns of the MIMO antenna array are obtained in a chamber, which are shown in Fig. 12. We can see that the proposed MIMO antenna has a good radiation patterns at both 2.4GHz and 5.25GHz, which is useful for small station applications. The gains of the MIMO antenna array at the two band are 2dBi and 4.6dBi, respectively.

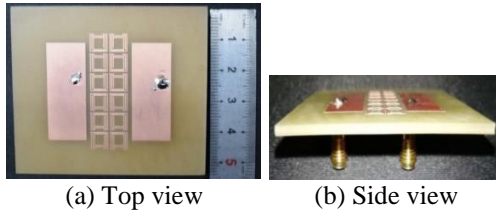


Fig. 9. Photograph of the fabricated dual-band MIMO antenna array.

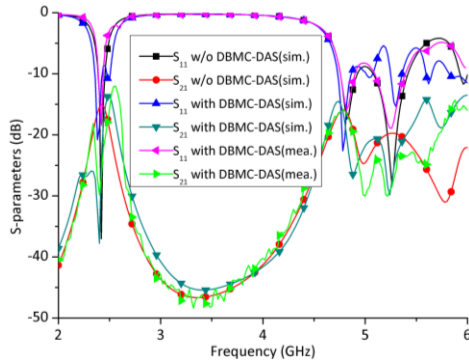


Fig. 10. S-parameter of the proposed MIMO array with DBMC-DAS.

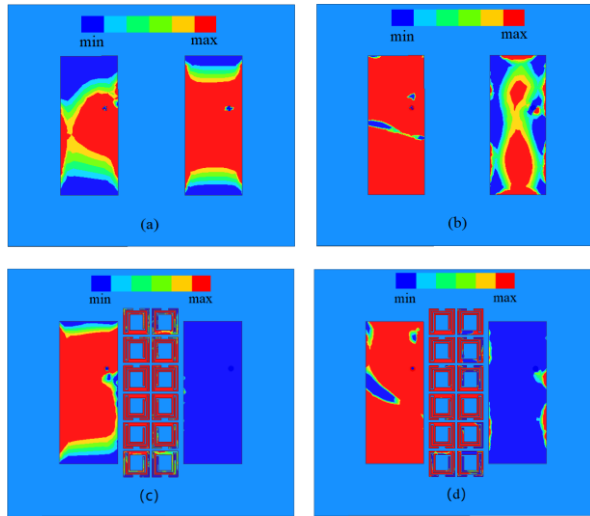


Fig. 11. Surface current distribution of the MIMO antenna: (a) 2.4GHz w/o DBMC-DAS, (b) 5.25GHz w/o DBMC-DAS, (c) 2.4GHz with DBMC-DAS, and (d) 5.25GHz with DBMC-DAS.

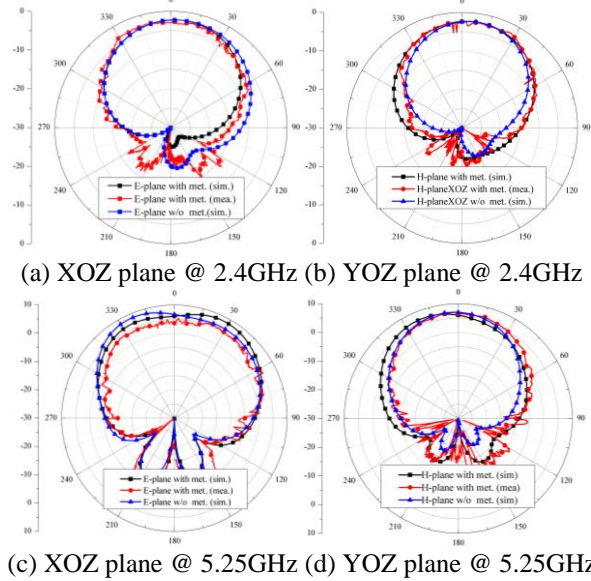


Fig. 12. Radiation patterns of the MIMO antenna array.

In order to show the priority of the high isolation dual-band antenna array in this paper, a comparison with the recent designs [40-44] is listed in Table 2. From the Table 2, it is found that the overall size of this high isolation antenna array is almost the smallest one, and its bandwidth covers the WLAN.

Table 2: Comparisons of proposed antennas with previous works

Refs.	10-dB BW (Low Band)	10-dB BW (High Band)	Isolation Enhancement at f_1 (dB)	Isolation Enhancement at f_2 (dB)	Total Size (λ_0 in GHz)
[40]	NA	NA	15.14	16.26	$1.14\lambda_{3.4} \times 0.68\lambda_{3.4}$
[41]	7.4%	5.7%	6	6	$1.26\lambda_{2.7} \times 0.63\lambda_{2.7}$
[28]	4.2%	3.8%	12	20	$0.88\lambda_{2.7} \times 0.44\lambda_{2.7}$
[42]	9.5%	12.2%	20	8	$1.23\lambda_{1.795} \times 0.42\lambda_{1.795}$
[43]	1.7%	0.75%	10.8	15.6	$0.41\lambda_{3.5} \times 0.41\lambda_{3.5}$
This work	4.2%	2.3%	15.5	9	$0.48\lambda_{3.5} \times 0.41\lambda_{3.5}$

IV. CONCLUSION

In this paper, a dual-band MIMO array with dual-frequency metamaterial decoupling structure is proposed and its performance is analyzed and discussed in detail. The DBMC-DAS consists of 6×2 dual-frequency metamaterial decoupling cells that are set in the middle of the two patch antenna elements. The proposed MIMO array with DBMC-DAS has been optimized, fabricated and measured. The results showed that the MC has been reduced by 15dB and 9dB for the lower and upper operating bands while the radiation patterns and the bandwidth of the MIMO array remain the same as that of the MIMO array without the DBMC-DAS. The proposed high isolation MIMO array with compact size can effectively reduce the mutual coupling without sacrificing

the radiation patterns. The advantage of the proposed technique is its simplicity and it can be easily retrofitted to existing antenna arrays quickly and at low cost.

ACKNOWLEDGMENT

This work was partially supported by the National Key Research and Development Program of China (2016YFE111100), Key Research and Development Program of Heilongjiang (GX17A016), the Science and Technology innovative Talents Foundation of Harbin (2016RAXXJ044), the Natural Science Foundation of Beijing (4182077), China Postdoctoral Science Foundation (2017M620918) and the Fundamental Research Funds for the Central University (HEUCFM180806).

REFERENCES

- [1] C. A. Balanis, *Antenna Theory, Analysis and Design*. John Wiley & Sons, Inc. 1982.
- [2] Y. Yang, Q. Chu, and C. Mao, "Multiband MIMO antenna for GSM, DCS, and LTE indoor application," *IEEE Antennas and Wireless Propag. Lett.*, vol. 15, pp. 1573-1576, 2016.
- [3] Y. Li, W. Li, and W. Yu, "A multi-band/UWB MIMO/diversity antenna with an enhance isolation using radial stub loaded resonator," *Applied Computational Electromagnetics Society Journal*, vol. 28, pp. 8-20, 2013.
- [4] S. Zhang, Z. Ying, J. Xiong, and S. He, "Ultra-wideband MIMO/diversity antennas with a tree-like structure to enhance wideband isolation," *IEEE Antennas and Wireless Propag. Lett.*, vol. 8, pp. 1279-1282, 2009.
- [5] Y. Li, T. Jiang, and R. Mittra, "A miniaturized dual-band antenna with toothbrush-shaped patch and meander line for WLAN applications," *Wireless Personal Communications*, vol. 91, pp. 595-602, 2016.
- [6] Y. Li, W. Li, and Q. Ye, "A reconfigurable triple notch band antenna integrated with defected microstrip structure band-stop filter for ultra-wideband cognitive radio applications," *International Journal of Antennas and Propagation*, vol. 2013, Article ID: 472645, pp. 1-13, 2013.
- [7] J. H. Chou, J. F. Chang, D. B. Lin, and T. L. Wu, "Dual-band WLAN MIMO antenna with a decoupling element for full-metallic bottom cover tablet computer applications," *Microwave and Optical Technology Letters*, vol. 60, no. 5, pp. 1245-1251, 2018.
- [8] Q. Luo, J. R. Pereira, and H. M. Salgado, "Reconfigurable dual-band C-shaped monopole antenna array with high isolation," *Electronics Letters*, vol. 46, no. 13, pp. 888-889, 2010.
- [9] Y. T. Wu, Q. X. Chu, and S. J. Yao, "A dual-band printed slot diversity antenna for wireless communication terminals," *2013 IEEE International Wireless Symposium (IWS)*, Beijing, China, 2013.
- [10] Q. L. Li, S. W. Cheung, D. Wu, and T. I. Yuk, "Optically transparent dual-band MIMO antenna using micro-metal mesh conductive film for WLAN system," *IEEE Antennas and Wireless Propag. Lett.*, vol. 16, pp. 920-923, 2016.
- [11] S. Shoaib, I. Shoaib, N. Shoaib, X. Chen, and C. Parini, "Design and performance study of a dual-element multiband printed monopole antenna array for MIMO terminals," *IEEE Antennas and Wireless Propag. Lett.*, vol. 13, pp. 329-332, 2014.
- [12] M. S. Khan, M. F. Shafique, A. Naqvi, et al., "A miniaturized dual-band MIMO antenna for WLAN applications," *IEEE Antennas and Wireless Propag. Lett.*, vol. 14, pp. 958-961, 2015.
- [13] E. Rajo-Iglesias, O. Quevedo-Teruel, and M. Sainchez-Ferflifldez, "Compact multimode patch antennas for MIMO applications," *IEEE Antennas and Propagation Magazine*, vol. 50, no. 2, pp. 197-205, 2008.
- [14] T. Zhang, W. Hong, Y. Zhang, and K. Wu, "Design and analysis of SIW cavity backed dual-band antennas with a dual-mode triangular-ring slot," *IEEE Trans. Antennas Propag.*, vol. 62, no. 10, pp. 5007-5016, 2014.
- [15] D. K. Karmokar and K. P. Esselle, "Periodic U-slot-loaded dual-band half-width microstrip leaky-wave antennas for forward and backward beam scanning," *IEEE Trans. Antennas Propag.*, vol. 63, no. 12, pp. 5372-5381, 2015.
- [16] U. Chakraborty, A. Kundu, S. K. Chowdhury, and A. K. Bhattacharjee, "Compact dual-band microstrip antenna for IEEE 802.11a WLAN application," *IEEE Antennas and Wireless Propag. Lett.*, vol. 13, pp. 407-410, 2014.
- [17] S. Liu, W. Wu, and D. Fang, "Single-feed dual-layer dual-band E-shaped and U-slot patch antenna for wireless communication application," *IEEE Antennas and Wireless Propag. Lett.*, vol. 15, pp. 468-471, 2016.
- [18] Q. Luo, S. Gao, and L. Zhang, "Wideband multi-layer dual circularly polarised antenna for array application," *Electronics Letters*, vol. 51, no. 25, pp. 2087-2089, 2015.
- [19] X. W. Dai, T. Zhou, and G. Cui, "Dual-band microstrip circular patch antenna with monopolar radiation pattern," *IEEE Antennas and Wireless Propag. Lett.*, vol. 15, pp. 1004-1007, 2016.
- [20] R. G. Vaughan and J. B. Andersen, "Antenna diversity in mobile communications," *IEEE Trans. Veh. Technol.*, vol. VT-36, no. 4, pp. 149-172, Nov. 1987.
- [21] M. Bouezzeddine and W. L. Schroeder, "Design of a wideband, tunable four-port MIMO antenna system with high isolation based on the theory of characteristic modes," *IEEE Trans. Antennas*

- Propag.*, vol. 64, no. 7, pp. 2679-2688, 2016.
- [22] B. Wang, Y. Chang, and Y. Sun, "Performance of the large-scale adaptive array antennas in the presence of mutual coupling," *IEEE Trans. Antennas Propag.*, vol. 64, no. 6, pp. 2236-2245, June 2016.
- [23] R. Janaswamy, "Effect of element mutual coupling on the capacity of fixed length linear arrays," *IEEE Antennas Wireless Propag. Lett.*, vol. 1, no. 1, pp. 157-160, 2002.
- [24] J. Sui and K.-L. Wu, "A general T-stub circuit for decoupling of two dual-band antennas," *IEEE Transactions on Microwave Theory and Techniques*, vol. 65, no. 6, pp. 2111-2121, 2017.
- [25] C. Wu, G. Zhou, Y. Wu, and T. Ma, "Stub-loaded reactive decoupling network for two-element array using even-odd analysis," *IEEE Antennas and Wireless Propag. Lett.*, vol. 12, pp. 452-455, 2013.
- [26] R. Xia, S. Qu, P. Li, D. Yang, S. Yang, and Z. Nie, "Wide-angle scanning phased array using an efficient decoupling network," *IEEE Trans. Antennas Propag.*, vol. 63, no. 11, pp. 5161-5165, 2015.
- [27] L. Zhao and K. Wu, "A dual-band coupled resonator decoupling network for two coupled antennas," *IEEE Trans. Antennas Propag.*, vol. 63, no. 7, pp. 2843-2850, 2015.
- [28] L. Zhao, F. Liu, X. Shen, G. Jing, Y. Cai, and Y. Li, "A high-pass antenna interference cancellation chip for mutual coupling reduction of antennas in contiguous frequency bands," *IEEE Access*, vol. 6, pp. 38097-38105, 2018.
- [29] A. Ghalib and M. S. Sharawi, "TCM analysis of defected ground structures for MIMO antenna designs in mobile terminals," *IEEE Access*, vol. 5, pp. 19680-19692, 2017.
- [30] K. Wei, J. Li, L. Wang, Z. Xing, and R. Xu, "S-shaped periodic defected ground structures to reduce microstrip antenna array mutual coupling," *Electronics Letters*, vol. 52, pp. 1288-1290, 2016.
- [31] K. Wei, J. Li, L. Wang, Z. Xing, and R. Xu, "Mutual coupling reduction by novel fractal defected ground structure bandgap filter," *IEEE Trans. Antennas Propag.*, vol. 64, pp. 4328-4335, 2016.
- [32] F. Yang and Y. Rahmat-Samii, "Microstrip antennas integrated with electromagnetic band-gap (EBG) structures: A low mutual coupling design for array applications," *IEEE Trans. Antennas Propag.*, vol. 51, pp. 2936-2946, 2003.
- [33] T. Jiang, T. Jiao, and Y. Li, "Array mutual coupling reduction using L-loading E-shaped electromagnetic band gap structures," *International Journal of Antennas and Propagation*, vol. 2016, Article ID 6731014, 9 pages, 2016.
- [34] T. Jiang, T. Jiao, and Y. Li, "A low mutual coupling MIMO antenna using periodic multi-layered electromagnetic band gap structures," *Applied Computational Electromagnetics Society Journal*, vol. 33, no. 3, 2018.
- [35] M. S. Alam, M. T. Islam, and N. Misran, "A novel compact split ring slotted electromagnetic bandgap structure for microstrip patch antenna performance enhancement," *Progress in Electromagnetics Research*, vol. 130, pp. 389-409, 2012.
- [36] H. N. B. Phuong, H. V. Phi, N. K. Kiem, and D. N. Dinh, "Design of compact EBG structure for array antenna application," *2015 International Conference on Advanced Technologies for Communications (ATC)*, Oct. 2015.
- [37] M. A. Abdalla and A. A. Ibrahim, "Compact and closely spaced metamaterial MIMO antenna with high isolation for wireless applications," *IEEE Antennas and Wireless Propag. Lett.*, vol. 12, pp. 1452-1455, 2013.
- [38] D. A. Ketzaki and T. V. Yioultis, "Metamaterial-based design of planar compact MIMO monopoles," *IEEE Transactions on Antennas and Propagation*, vol. 61, no. 5, pp. 2758-2766, 2013.
- [39] K. Yu, Y. Li, and X. Liu, "Mutual coupling reduction of a MIMO antenna array using 3-D novel meta-material structures," *Applied Computational Electromagnetics Society Journal*, vol. 33, no. 7, pp. 758-763, 2018.
- [40] B. L. Dhevi, K. S. Vishvakshnan, and K. Rajakani, "Isolation enhancement in dual-band microstrip antenna array using asymmetric loop resonator," *IEEE Antennas and Wireless Propagation Letters*, vol. 17, no. 2, pp. 238-241, 2018.
- [41] G. Li, H. Zhai, Z. Ma, C. Liang, R. Yu, and S. Liu, "Isolation-improved dual-band MIMO antenna array for LTE/WiMAX mobile terminals," *IEEE Antennas and Wireless Propagation Letters*, vol. 13, pp. 1128-1131, 2014.
- [42] Y. Zhang, X. Zhang, L. Ye, and Y. Pan, "Dual-band base station array using filtering antenna elements for mutual coupling suppression," *IEEE Trans. Antennas Propag.*, vol. 64, no. 8, pp. 3423-3429, 2016.
- [43] A. Boukarkar, X. Lin, Y. Jiang, L. Nie, P. Mei, and Y. Yu, "A miniaturized extremely close-spaced four-element dual-band MIMO antenna system with polarization and pattern diversity," *IEEE Antennas and Wireless Propagation Letters*, vol. 17, no. 1, pp. 134-137, 2018.
- [44] S. Luo, Y. Li, Y. Xia, G. Yang, L. Sun, and L. Zhao, "Mutual coupling reduction of a dual-band antenna array using dual-frequency metamaterial structure," *Applied Computational Electromagnetics Society Journal*, Accepted.

A Low Mutual Coupling Antenna Array with Gain Enhancement Using Metamaterial Loading and Neutralization Line Structure

Shengyuan Luo¹, Yingsong Li^{1,2,*}, Yinfeng Xia¹, and Liang Zhang³

¹ College of Information and Communication Engineering
Harbin Engineering University, Harbin, Heilongjiang 150001, China
liyingsong@ieee.org

² Key Laboratory of Microwave Sensing, National Space Science Center
Chinese Academy of Sciences, Beijing 100190, China

³ Anhui Province Key Laboratory of Simulation and Design for Electronic Information System, Hefei 230601, China

Abstract — A MIMO antenna array with high isolation and gain enhancement operating at 5.7 GHz is proposed by using a metamaterial and neutralization line for wireless local area network (WLAN) communication system. A suspended meta-surface consisted of periodic metamaterial cells is installed on the top of the MIMO antenna array to realize a gain enhancement, while the low correlation is implemented by using the neutralization line decoupling structure which is adopted on the feeding lines. The proposed MIMO array is modeled in the HFSS, and it is well analyzed, optimized, fabricated, and measured to discuss its performance. The obtained results demonstrate that the proposed MIMO antenna array can cover the upper WLAN band with a gain enhancement of 3dB and mutual decoupling of 30dB in the operating band with an efficiency of 68%.

Index Terms — Gain enhancement, MIMO antenna array, mutual decoupling, WLAN.

I. INTRODUCTION

The increment of the mobile terminal users has boosted the development of wireless communication technologies and systems, including the antennas. Especially for the next-generation communications which need multiple-input multiple-output (MIMO) antenna array to enhance the system performance, the MIMO antenna array requires not only high gain but also high isolation to satisfy the great demand of high communication quality with millions of users.

To improve the communication quality, MIMO technology is a good candidate to increase throughput of the system and to reduce the multi-path effects [1]. Moreover, the terminals of the modern portable communications become to be smaller and smaller. Since the space in these terminals are limited, the distance between the antenna array elements is only

a fraction of the wavelength in the operating band, which may cause a strong mutual coupling between these array elements [2]. The mutual coupling will seriously degrade the radiation performance of the antenna array. Additionally, if the MIMO antenna array does not have a high gain, it will result in a great waste of energy. Thus, how to improve the gain and the isolation of a MIMO antenna array has become to be an urgent problem. After that, many methods have been proposed and investigated to provide a high isolation since antenna array has been widely applied in military and industry.

To enhance the gain of the MIMO antenna array, numerous methods have been reported. The existing gain enhancement technologies include using reflectors, slotted metal wall, LTCC with a cavity inside the substrate, shorting pins, UC-EBG and near-zero refractive index metamaterial [3-12]. It is pointed out in [3] that both the gain and the frequency bandwidth of the antenna array have been improved simultaneously. In [4], the antenna array with several directors and a truncated ground plane acting as a reflector has been presented to maximize the antenna gain. Unlike the structure described in [4], a gain-enhanced circularly polarized antenna array is proposed by adding a slotted metal wall in [5]. In addition, low temperature co-fired ceramic (LTCC), as a multilayered technology, has been widely used in planner antenna design [6]. However, the radiation efficiency is severely reduced when the surface-wave power is increased in the antenna. Therefore, to maximize the radiation efficiency and antenna gain, low permittivity substrate is preferred and used for designing antenna arrays. But, the substrates with low permittivity are not currently available in LTCC technology. Thus, the cavity technology is used to improve the efficiency in [6-8]. Also, the LTCC technology is used to improve the antenna performance with low dielectric loss and low conductor losses while the fabrication cost is high. In [9],

a gain enhancement for a broadband symmetrical dual-loop antenna is presented, where a pair of shorting pins is symmetrically loaded beneath the radiator. Therefore, surface current crossing the center of the antenna can be significantly enhanced to improve its radiation directivity and gain. However, the increment in gain is not very high. The uniplanar-compact electro-magnetic band-gap (UC-EBG), referred in [10], is also an effective method to strengthen the gain of the antenna, where the antenna uses the periodic UC-EBG wrapped around the patch or placed under the radiation patch to implement as a reflector so that more energy is radiated toward a fixed direction. However, it needs more space to construct such a large reflector. Recently, the near zero refractive index metamaterial have been used and installed on the top of the patch antennas for achieving high gain [11-12].

On the other hand, the mutual coupling in the antenna array will also reduce the efficiency and peak gain. Thus, it is necessary to design a mutual decoupling structure to suppress the mutual coupling. In the past decades, many methods have been investigated for reducing the mutual decoupling between the antenna elements, and they have been proved to be effective, including spatial orthogonal current techniques, defected ground structure (DGS), electromagnetic band-gap (EBG), metamaterial and mutual decoupling networks [13-23]. The DGS has been developed to enhance the isolation between antenna array elements while it may destroy the integrity of the ground plane that may leak electromagnetic wave and deteriorate the radiation patterns [16-17]. Another effective method to reduce the mutual coupling of antenna array is implemented by loading the EBG structure between antenna array elements. The EBG can suppress the propagation of surface wave between array elements due to its high impedance property in the antenna operation frequency band. However, it can only reject the spread of surface waves rather than spatial waves [18-20]. Unlike EBG structure that requires shorting pins, metamaterial has been inserted between the antenna array elements, which is not suitable for the feed network design in massive antenna arrays [21-23]. For the mutual decoupling network referred in [24-25], it was only applied in mutual decoupling design of two-element antenna arrays.

Recently, the antenna array in base station needs a higher gain and isolation to serve dozens of mobile terminal users with more antenna elements over the upper WLAN work band. The mutual decoupling network has two features, the first feature is that it can be applied in mutual decoupling of massive MIMO antenna array with the feed network together, and the second feature is that it cannot only suppress the surface wave between MIMO array elements but also can prohibit the spatial waves over the patch. The metamaterial superstrate structure (MSS) has received growing interest because

of its potential advantages in wireless communication technology, including the characteristics of easily design and simply fabrication. An MSS consists of metamaterial cells which are installed on the top of the antenna array to form a Fabry-Perot cavity for gain enhancement. In this paper, a closely installed MIMO antenna array is considered rather than a standard antenna array. We aim to reduce the mutual coupling and enhance the gain in comparison with the MIMO array without the decoupling structure and MSS loading. In the design, the distance between the array elements is 2mm and the edge-to-edge distance between the two arrays is 5mm. According to the advantages of the MSS and mutual decoupling network, a high isolation MIMO antenna array with gain enhancement is proposed by using MSS and mutual decoupling network operating at upper WLAN band. Comparing with the existing technology of MIMO antenna array, the MIMO antenna array proposed in this paper has the following unique features:

- (1) The reported MIMO antenna array has a high gain and high isolation simultaneously.
- (2) The mutual decoupling network can be adjusted to match with the original MIMO antenna array for effectively reducing the coupling at the operating band.
- (3) The feed network and radiating patch are respectively located on both sides of the ground plane.

II. DESIGN OF THE PROPOSED MIMO ARRAY

A. Design of the MSS

The metamaterial is a favorable candidate for gain enhancement by properly adjusting its parameters, and it is also an artistic work to design a MSS which has a near zero refractive index property at the working frequency of four-element MIMO antenna array. The schematic of an MSS comes from the resonance of the inductance in the metal patch and the capacitance from the slots, which is shown in Fig. 1. Figure 1 (a) is the simulation model of the proposed MSS cell that is modified from a traditional split resonant ring (SRR). The boundaries are set to be PMC and PEC walls. The equivalent circuit of the design MSS cell is shown in Fig. 1 (a) at same time to illustrate the working mechanism of the metamaterial. To get the characteristics of the proposed MSS cell, the permittivity and permeability of the MSS are calculated and the results are shown in Fig. 1 (b). According to the metamaterial theory, Fabry-Perot cavity theory and the conventional cavity resonance condition, the dimensions of the metamaterial can be obtained. The conventional resonance cavity condition can be expressed as follow:

$$H + h\sqrt{\epsilon_r} = (\phi_{MS} + \phi_G) \frac{\lambda}{4\pi} \pm N \frac{\lambda}{2}, \quad (1)$$

where ϕ_{MS} is the reflected wave phase of the MSS, ϕ_G is the reflected wave phase of the metal ground plane. H is the distance between ground metal and the upper surface

of the coating metamaterial. The “N” is any integer value. When the parameter H is properly adjusted, a resonance cavity will be formed, where the electromagnetic waves will be reflected multiple times between metal ground plane and MSS. If the designed antenna meets the conventional resonance cavity condition, the reflected waves will pass through the MSS loading with same phase, which can strengthen the directionality of the MIMO antenna array, and the gain will be improved. The parameter has an important effect on the performance of the proposed MSS, and the reflected phase of the metamaterial cell with different a_1 is shown in detail in Fig. 1 (c). It is observed that the phase of the operating frequency shifts to lower frequency as the parameter a_1 increases from 3.5mm to 5.5mm.

B. High gain four –element antenna array design

The configuration of the proposed four-element MIMO antenna array without MSS is well designed and described in Fig. 2 (a). Aiming to compact the size and reduce the weight of the array, the proposed antenna array is realized based on the light weight and low profile microstrip antenna. The proposed antenna array has four microstrip patch antennas printed on the top of the FR4 substrate with a relative permittivity of 4.4 and a loss tangent of 0.02. A metal ground plane is placed on the bottom of the substrate. Because the distance of the inner-element is a small fraction of the wavelength, therefore, there is no enough space to locate a feed network. In this design, the feeding network is loaded on the bottom of the second substrate that is placed under the metal ground plane. The ground plane can reduce the interaction between feed network and antenna array. The antenna array and feed network are connected by metal probes to excite the antenna elements, which have some small holes on the metal ground plane. There is no gap between two substrates. It is to say that the MIMO antenna elements are designed on the top of the first substrate and the feeding network is printed on the bottom of the second substrate, while a common plane between the two substrates. The simulated S-parameters and radiation patterns of the original MIMO antenna array are described in Fig. 2 (b) and Fig. 2 (c), respectively. It can be found that the original MIMO antenna array has good impedance bandwidth ranging from 5.4-5.96 GHz, but the correlation coefficient between antenna array elements is high which might deteriorate the performance of the MIMO array. In this case, the gain of the antenna array is 5.3 dBi.

In previous engineering design of antenna array, the distance between the antenna array elements is half of the wavelength in substrate. But, when the four-element transmitting and receiving antenna are placed on the same substrate, the size of the antenna array is too large that cannot be easily integrated into a space-limited communication system. Therefore, it is an effective way

to design an antenna array that can be integrated with mobile terminal by reducing the distance between antenna array elements. Comparing with the normal antenna array, the gain of compact array antenna maybe seriously deteriorated, and therefore, the gain enhancement operation should be developed to improve the radiation characteristics of the antenna array.

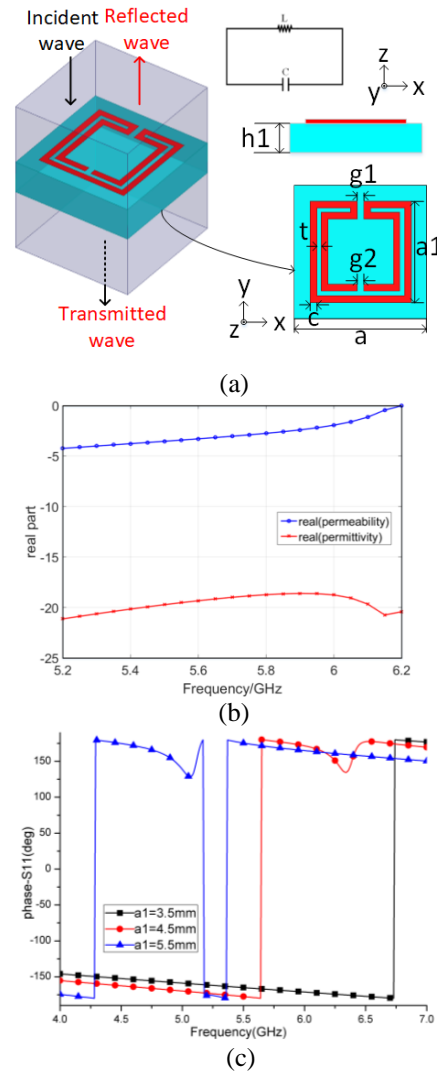


Fig. 1. (a) The electromagnetic simulation model of metamaterial cell, (b) the permittivity and permeability of the proposed metamaterial cell, and (c) the simulated phase of S11 of the metamaterial with different a_1 .

To further enhance the gain, a four-element microstrip MIMO antenna array with a cover layer consists of the MSS is proposed and is shown in Fig. 3 (a). The metamaterial is comprised of only one layer, which has 13 by 9 MSS cells, and it is illustrated in Fig. 3 (a). In this design, the metamaterial is printed on the FR4 substrate. The cover layer is fixed above the antenna

array by using four plastic bolts at each corner. The distance from patch antenna array to the bottom surface of the cover layer is $h_2=30\text{mm}$, which is large enough so that the near-field interaction is not obvious between the radiation of the antenna array and MSS. Therefore, the performance of the MIMO antenna array is basically unaffected by the cover layer that is comprised of MSS cells. The finalized model of the four-element MIMO antenna array with metamaterial cover layer is shown in Fig. 3 (b), and its physical dimensions are listed in Table 1. Since a portion of the electromagnetic waves radiate into space from the MSS, the remaining energy is reflected to the other antenna elements owing to the loading, which results in a space mutual coupling between transmitting antenna and receiving antenna.

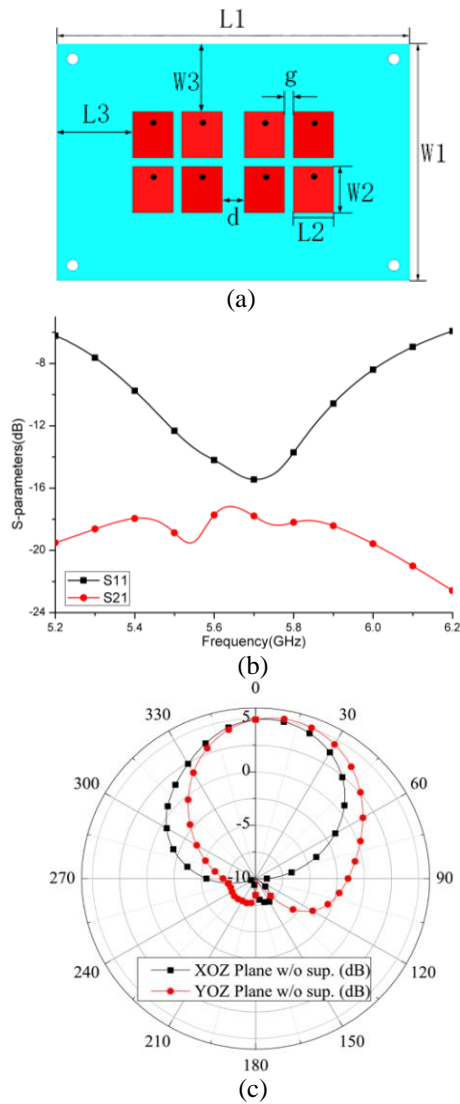


Fig. 2. (a) The configuration of the original four-element MIMO antenna, (b) simulated S-parameters, and (c) simulated radiation pattern.

C. High isolation antenna array with gain enhancement

In this paper, the gain of the proposed MIMO antenna array is enhanced by using loaded MSS, which might give some effects on its mutual coupling. To reduce the mutual decoupling in the designed MIMO antenna array, a mutual coupling network is utilized to implement the isolation enhancement. Fig. 4 (a) gives schematic of MIMO antenna array with the proposed mutual decoupling network. Figure 4 (b) shows the structure of the designed mutual decoupling network. From Fig. 4 (b), it is found that the mutual decoupling network is composed of two stage transmission line with electric length of θ , characteristic impedance of Z_0 , and a parallel reactance component with a value of jB . The decoupling mechanism is concluded as follows. By connecting the transmission lines with parallel reactance component, a partial input signal from Port 1 can be indirectly coupled to Port 2, which is named as indirect coupling hereafter. The magnitude of the indirect coupling can be controlled to reduce the mutual coupling caused by space waves and surface waves.

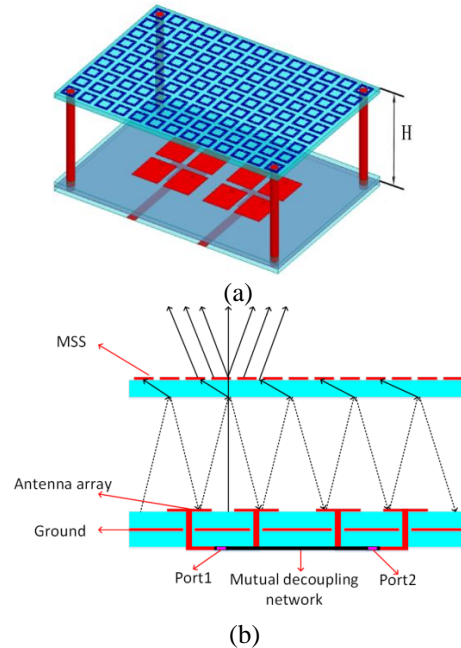


Fig. 3. (a) The configuration of the proposed four-element MIMO antenna with MSS loading, and (b) radiation model of the proposed four-element MIMO antenna with MSS loading.

Table 1: Parameters of the MIMO antenna array with metamaterial coating

Parameter	L1	L2	L3	g1	W1	W2	W3	A
Value (mm)	79	9	17	0.3	55	10.7	15.8	6
Parameter	g2	t	d	g	H	h1	c	a1
Value (mm)	0.3	0.2	5	2	34.8	1.6	0.3	4.55

Next, to better understand the effects of parameters θ , Z_0 , jB , and to optimize the performance of the design, parameters studies are carried out to give a good performance by totally considering the MIMO antenna array and mutual decoupling network. A symmetrical antenna array without decoupling network is characterized by a scattering matrix $[S^A]$, which can be expressed as:

$$[S^A] = \begin{bmatrix} 0 & \alpha e^{j\varphi} \\ \alpha e^{j\varphi} & 0 \end{bmatrix}. \quad (2)$$

The parameters α and φ are the amplitude and phase of the mutual coupling between the MIMO antenna array, respectively. We utilize the transmission lines with a characteristic impedance of Z_0 at the two ports of the MIMO antenna array, resulting in a phase delay of 2θ to the coupling coefficient. Therefore, the modified scattering matrix $[S^{A^1}]$ can be obtained, and it can be transformed into an admittance matrix of $[Y^{A^1}]$. In this paper, the matrix of $[S^{A^1}]$ is expressed as:

$$[S^{A^1}] = \begin{bmatrix} 0 & \alpha e^{j(\varphi-2\theta)} \\ \alpha e^{j(\varphi-2\theta)} & 0 \end{bmatrix}. \quad (3)$$

The transmission lines not only act as delay lines between the MIMO antenna array elements and parallel reactance component, but also it can transform the complex admittance matrix of the mutual coupling into a pure imaginary admittance matrix that can be canceled by the parallel reactance component. $[Y^b]$ is the scattering parameter of the two-port network consisting of the parallel reactive components, which can be expressed as:

$$[Y^b] = \begin{bmatrix} jB & -jB \\ -jB & jB \end{bmatrix}. \quad (4)$$

Thus, the admittance matrix after adding the parallel reactance component is:

$$[Y^B] = [Y^{A^1}] + [Y^b], \quad (5)$$

$$Y_{21}^B = Y_{12}^B = Y_0 \left(\frac{-2\alpha e^{j(\varphi-2\theta)}}{1 - \alpha^2 e^{j2(\varphi-2\theta)}} \right) - jB, \quad (6)$$

$$Y_{11}^B = Y_{22}^B = Y_0 \left(\frac{1 + \alpha^2 e^{j2(\varphi-2\theta)}}{1 - \alpha^2 e^{j2(\varphi-2\theta)}} \right) + jB, \quad (7)$$

$$Y = \frac{1}{Z_0}. \quad (8)$$

According to the conversion relationship between Y-parameter and S-parameter, the S-parameter after adding the parallel reactance element can be obtained:

$$S_{21}^B = \frac{-Y_{21}^B Y_0}{Y_0^2 + 2Y_{11}^B + (Y_{11}^B)^2 - (Y_{21}^B)^2}, \quad (9)$$

$$S_{11}^B = \frac{Y_0^2 - 2Y_{11}^B - (Y_{21}^B)^2}{Y_0^2 + 2Y_{11}^B + (Y_{11}^B)^2 - (Y_{21}^B)^2}. \quad (10)$$

To obtain the isolation enhancement after loading the mutual decoupling network, the parameter of S_{21}^B must be 0, which means that the Y_{21}^B should be set as 0.

Hence, a relationship can be obtained as follows:

$$\theta = \frac{1}{2} \left(\varphi \pm \frac{\pi}{2} \right), \quad (11)$$

$$B = \pm \frac{2\alpha}{1 + \alpha^2} Y_0. \quad (12)$$

In addition, the L-shaped branch is utilized to get a better match. The length and the width of the parallel reactance component that gives important effects on the mutual decoupling network are investigated in detail. Figure 5 (a) gives the S-parameter of the MIMO antenna array after adding the mutual decoupling with different length L ranging from 16mm to 20mm.

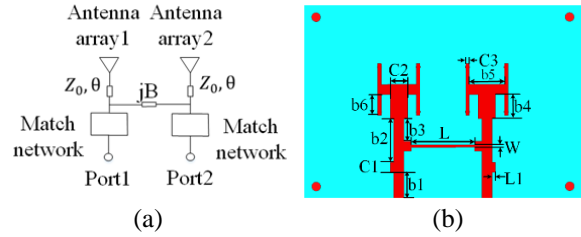


Fig. 4. (a) The schematic of the proposed mutual decoupling network in the MIMO antenna array, and (b) the mutual decoupling network.

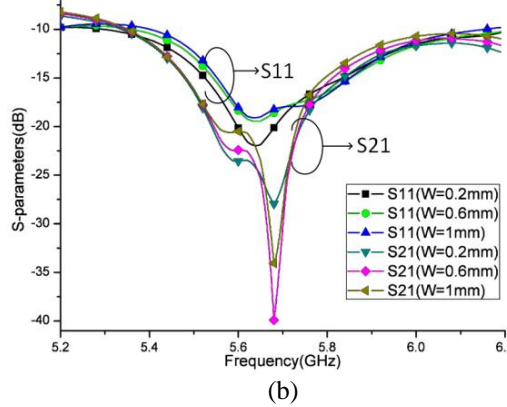
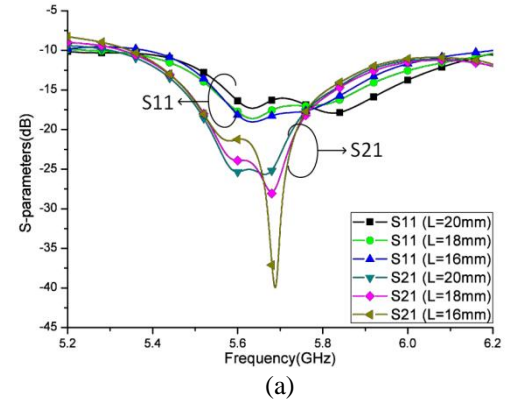


Fig. 5. (a) S-parameters of the MIMO antenna array with different L . (b) S-parameters of the MIMO antenna array with different W .

Figure 5 (b) shows the S-parameter of the MIMO antenna array after adding the mutual decoupling with different width W ranging from 0.2mm to 1mm. The isolation between antenna array elements becomes higher with an increasing L . And, it also can be seen that when W is 0.6mm, a higher isolation can be gotten. If W is getting larger than the 0.6mm, the isolation becomes worse. Then, the length of the L-shaped branch increasing from 1mm to 3mm is investigated to reach a good match. Figure 6 illustrates the effect with different length $L1$ on the S-parameter of the MIMO antenna array.

The center frequency of the S11 moves to higher frequency with an increasing of $L1$. The optimized parameters for the mutual decoupling network of the MIMO antenna array are listed in Table 2.

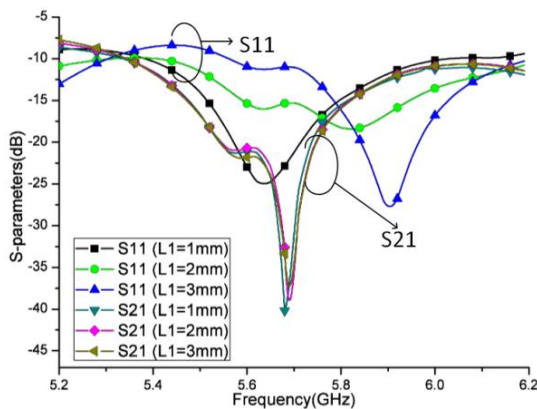


Fig. 6. S-parameters of the MIMO antenna array with different $L1$.

Table 2: The optimized parameters of the mutual decoupling network of the MIMO antenna array

Parameters	b1	b2	b3	b4	b5	b6
Value (mm)	7.5	12.39	6.39	6.82	10	5.92
Parameter	C1	C2	C3	L	W	L1
Value (mm)	2.86	4.87	1	18	0.63	1

III. PERFORMANCE OF THE PROPOSED MIMO ANTENNA ARRAY

In this paper, a high isolation MIMO antenna array with metamaterial loading and mutual decoupling network and gain enhancement is proposed and analyzed by using the HFSS. Herein, a mutual decoupling network is utilized to cancel the surface waves and space waves between antenna array elements since the metamaterial loading might also give some interferences from the adjacent antenna elements. The designed high isolation MIMO antenna array with gain enhancement is optimized, fabricated and measured. The photograph of the fabricated MIMO array is shown in Fig. 7. The S-parameter, radiation patterns, surface current distribution, and vector magnetic, and electric fields in the XOZ-plane are

presented when one antenna array is excited while another antenna array is terminated by 50-Ohm.



Fig. 7. The photograph of the fabricated MIMO antenna array.

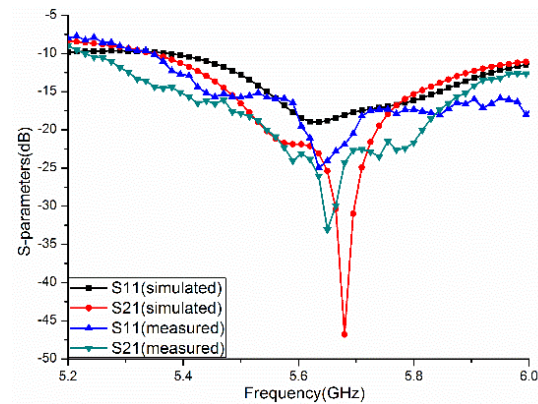


Fig. 8. S-Parameters of the proposed MIMO antenna array.

First, the S-parameters of the fabricated MIMO antenna array with loading MSS and mutual decoupling network are shown in Fig. 8. It can be seen that the proposed MIMO antenna array operates at 5.42-5.95 GHz covering the 5.8GHz WLAN band. The isolation of the MIMO antenna array is improved by about 30dB by using the proposed decoupling network and the MSS loading. Then the radiation patterns of the MIMO antenna array are measured in a chamber with NSI measurement system, which are shown in Fig. 9. From Fig. 2 (a), we can see that the peak gain of the developed MIMO antenna array without the MSS loading and the neutralization line structure is 5.3dB. By using the MSS and the neutralization line structure, our developed MIMO antenna array has a gain of 8.3 dB, which is shown in Fig. 9 (a). Thus, the proposed techniques can achieve a gain enhancement of 3dB.

To explain the mechanism of the mutual decoupling and gain enhancement for the space waves, the simulated vector magnetic field distribution and electric field contours are investigated and presented in Fig. 10. Without the mutual decoupling structure, the magnetic-field vector along the substrate of the MIMO antenna array propagates to the right direction while the

magnetic-field vector returned to the left direction of by using the decoupling network, which can reduce the mutual coupling. The electric field of the MIMO antenna array without and with the designed mutual decoupling are shown in Figs. 10 (c) and (d) respectively. The left antenna array is excited, while the right antenna array is induction antenna array. It can be seen that large electric field energy is radiated to the space without mutual decoupling, while the electric field energy is concentrated on the normal direction of the antenna array with the help of the MSS loading. Compared with the electric field distribution, there are more energy is radiated in the target direction, which means that less energy is radiated to the right antenna array. Therefore, after loading the MSS, the mutual decoupling, a high isolation and gain enhancement can be obtained. The radiation efficiency of the designed high gain and isolation antenna array is 68%.

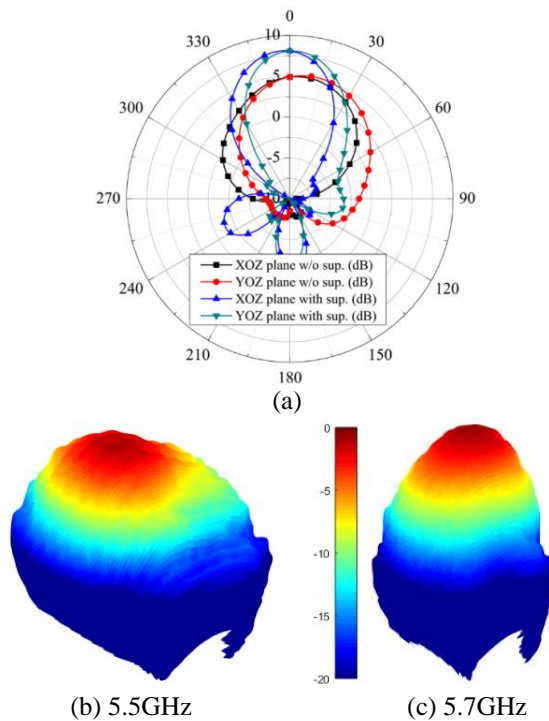


Fig. 9. (a) Simulated radiation patterns of the proposed antenna array with and without MSS loading. (b), (c) Measured radiation patterns of the proposed MIMO antenna array (unit: dB).

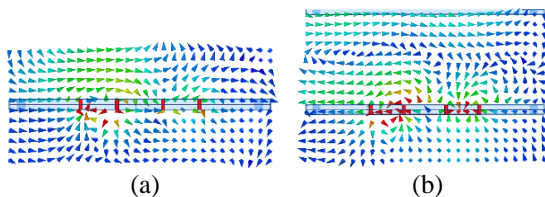


Fig. 10. (a) Simulated vector magnetic field distribution without mutual decoupling structure. (b) Simulated vector magnetic field distribution with mutual decoupling structure. (c) Simulated electric field contours without mutual decoupling structure. (d) Simulated electric field contours with mutual decoupling structure.

VI. CONCLUSION

In this paper, a high gain and high isolation MIMO antenna array has been proposed by using MSS loading and mutual decoupling structure, and its performance is analyzed and optimized by the use of both the simulations and measurements. The MSS loading consists of 13×9 metamaterial cells that are set above the MIMO antenna array to enhance the gain of the proposed antenna. The proposed antenna array has a gain and isolation enhancement about 3dB and 30dB, respectively, over the operating band within the upper WLAN communication band. The design of the MIMO antenna array with high performance has a great application prospect in based stations for WLAN communications.

ACKNOWLEDGMENT

This work was partially supported by the National Key Research and Development Program of China (2016YFE111100), Key Research and Development Program of Heilongjiang (GX17A016), the Science and Technology innovative Talents Foundation of Harbin (2016RAXXJ044), the Natural Science Foundation of Beijing (4182077), China Postdoctoral Science Foundation (2017M620918) and the Fundamental Research Funds for the Central University (HEUCFM180806).

REFERENCES

- [1] Y. Li, W. Li, and W. Yu, "A multi-band/UWB MIMO/diversity antenna with an enhance isolation using radial stub loaded resonator," *Applied Computational Electromagnetics Society Journal*, vol. 28, no. 1, pp. 8-20, 2013.
- [2] Z. Wang, G. Zhang, and Y. Yin, "Design of a dual-band high-gain antenna array for WLAN and WiMAX base station," *IEEE Antennas and Wireless Propag. Lett.*, vol. 13, pp. 1721-1724, 2014.
- [3] Y. Li, W. Li, and W. Yu, "A switchable UWB slot antenna using SIS-HSIR and SIS-SIR for multi-mode wireless communications applications," *Applied Computational Electromagnetics Society Journal*, vol. 27, no. 4, pp. 340-351, 2012.

- [4] R. A. Alhalabi and G. M. Rebeiz, "High-gain Yagi-Uda antennas for millimeter-wave switched-beam system," *IEEE Trans. Antennas Propag.*, vol. 57, no. 11, pp. 3672-3676, 2009.
- [5] W. Yang, J. Zhou, Z. Yu, and L. Li, "Bandwidth and gain-enhanced circularly polarized antenna array using sequential phase feed," *IEEE Antennas Wireless Propag. Lett.*, vol. 13, pp. 1215-1218, 2014.
- [6] A. E. I. Lamminen, J. Saily, and A. R. Vimpari, "60-GHz patch antennas and arrays on LTCC with embedded-cavity substrates," *IEEE Trans. Antennas Propag.*, vol. 56, no. 9, pp. 2865-2874, Sep. 2008.
- [7] S. Yeap, Z. Chen, and X. Qing, "Gain-enhanced 60-GHz LTCC antenna array with openair cavities," *IEEE Trans. Antennas Propag.*, vol. 59, no. 9, pp. 3470-3473, 2011.
- [8] B. Cao, H. Wang, Y. Huang, and J. Zheng, "High-gain L-probe excited substrate integrated cavity antenna array with LTCC-based gap waveguide feeding network for W-band application," *IEEE Trans. Antennas Propag.*, vol. 63, no. 12, pp. 5465-5474, 2015.
- [9] J. Liu, Z. Tang, Z. Wang, et al., "Gain enhancement of a broadband symmetrical dual-loop antenna using shorting pins," *IEEE Antennas Wireless Propag. Lett.*, vol. 17, no. 8, pp. 1369-1372, 2018.
- [10] A. E. I. Lamminen, A. R. Vimpari, and J. Saily, "UC-EBG on LTCC for 60-GHz frequency band antenna applications," *IEEE Trans. Antennas Propag.*, vol. 57, no. 10, pp. 2904-2912, 2009.
- [11] H. Zhou, Z. Pei, and S. Qu, "A novel high-directivity microstrip patch antenna based on zero-index metamaterial," *IEEE Antennas Wireless Propag. Lett.*, vol. 8, pp. 538-541, 2009.
- [12] D. Ramaccia, F. Scattoni, F. Bilotti, et al., "Broadband compact horn antennas by using EPS-ENZ metamaterial lens," *IEEE Trans. Antennas Propag.*, vol. 61, no. 6, pp. 2929-2937, 2013.
- [13] Y. Li, Z. Zhang, J. Zheng, and Z. Feng, "Compact azimuthal omnidirectional dual-polarized antenna using highly isolated co-located slots," *IEEE Trans. Antennas Propag.*, vol. 60, no. 9, pp. 4037-4045, 2012.
- [14] Y. Li, Z. Zhang, Z. Feng, and M. F. Iskander, "Design of omnidirectional dual-polarized antenna in slender and low-profile column," *IEEE Trans. Antennas Propag.*, vol. 62, no. 4, pp. 2323-2326, 2014.
- [15] Y. Li, W. Li, and Q. Ye, "A reconfigurable triple notch band antenna integrated with defected microstrip structure band-stop filter for ultra-wideband cognitive radio applications," *International Journal of Antennas and Propagation*, vol. 2013, Article ID: 472645, pp. 1-13, 2013.
- [16] K. Wei, J. Li, L. Wang, Z. Xing, and R. Xu, "S-shaped periodic defected ground structures to reduce microstrip antenna array mutual coupling," *Electronics Letters*, vol. 52, pp. 1288-1290, 2016.
- [17] K. Wei, J. Li, L. Wang, Z. Xing, and R. Xu, "Mutual coupling reduction by novel fractal defected ground structure bandgap filter," *IEEE Trans. Antennas Propag.*, vol. 64, pp. 4328-4335, 2016.
- [18] F. Yang and Y. Rahmat-Samii, "Microstrip antennas integrated with electromagnetic band-gap (EBG) structures: A low mutual coupling design for array applications," *IEEE Trans. Antennas Propag.*, vol. 51, no. 10, pp. 2936-2946, 2003.
- [19] T. Jiang, T. Jiao, and Y. Li, "Array mutual coupling reduction using L-loading E-shaped electromagnetic band gap structures," *International Journal of Antennas and Propagation*, vol. 2016, Article ID 6731014, 9 pages, 2016.
- [20] T. Jiang, T. Jiao, and Y. Li, "A low mutual coupling MIMO antenna using periodic multi-layered electromagnetic band gap structures," *Applied Computational Electromagnetics Society Journal*, vol. 33, no. 3, 2018.
- [21] M. A. Abdalla and A. A. Ibrahim, "Compact and closely spaced metamaterial MIMO antenna with high isolation for wireless applications," *IEEE Trans. Antennas Propag.*, vol. 12, pp. 1452-1455, 2013.
- [22] K. Yu, Y. Li, and X. Liu, "Mutual coupling reduction of a MIMO antenna array using 3-D novel meta-material structures," *Applied Computational Electromagnetic Society Journal*, vol. 33, no. 7, pp. 758-763, 2018.
- [23] D. A. Ketzaki and T. V. Yioultis, "Metamaterial-based design of planar compact MIMO monopoles," *IEEE Trans. Antennas Propag.*, vol. 61, no. 5, pp. 2758-2766, 2013.
- [24] L. Zhao, F. Liu, X. Shen, G. Jing, Y. Cai, and Y. Li, "A high-pass antenna interference cancellation chip for mutual coupling reduction of antennas in contiguous frequency bands," *IEEE Access*, vol. 6, pp. 38097-38105, 2018.
- [25] R. Xia, S. Qu, P. Li, D. Yang, S. Yang, and Z. Nie, "Wide-angle scanning phased array using an efficient decoupling network," *IEEE Trans. Antennas Propag.*, vol. 63, no. 11, 2015.

Improved Constraint NLMS Algorithm for Sparse Adaptive Array Beamforming Control Applications

Wanlu Shi¹, Yingsong Li^{1,2,*}, and Jingwei Yin³

¹ College of Information and Communication Engineering
Harbin Engineering University, Harbin, 150001, China
liyingsong@ieee.org

² Key Laboratory of Microwave Remote Sensing
National Space Science Center, Chinese Academy of Sciences, Beijing, 100190, China

³ Acoustic Science and Technology Laboratory
Harbin Engineering University, Harbin, 150001, China

Abstract — In this paper, a new reweighted l_1 -norm and an l_p -norm based normalized least mean square (NLMS) algorithms are developed for sparse adaptive array beamforming control applications. The proposed reweighted l_1 -norm constrained NLMS (RL₁-CNLMS) and l_p -norm constrained NLMS (L_p-CNLMS) algorithms use the l_1 -norm penalty and l_p -norm penalty to the conventional cost function of constrained normalized LMS (CLMS) algorithm to control the sparsity of the antenna array. What's more, in the derivation process, the gradient descent principle and Lagrange multiplier method are adopted to obtain the desired updating formulations. Computer simulations demonstrate that the superiority of proposed algorithms compared with other LMS based beamforming methods.

Index Terms — array beamforming, constrained LMS algorithm, l_1 -norm constraint, l_p -norm constraint, sparse adaptive beamforming.

I. INTRODUCTION

Adaptive beamforming has drawn lots of attention due to its good performance, and it has been widely developed for wireless communications, radio astronomy, mobile communications, radar, sonar and other fields [1-2]. Adaptive beamformer can generate a main lobe in the interested direction to get a high gain, meanwhile, to form nulls to attenuate the interferences to obtain better the signal-to-interference-plus-noise ratio (SINR) [3].

The principle of adaptive beamforming algorithms is to match the signals of interest (SOI) and adaptively suppress the interferences by dynamically adjusting the array weight vectors. The linearly constrained minimum variance (LCMV) algorithm proposed by Frost [3] is a famous beamforming method which can realize the mentioned properties. In [4], under the assumption that

array elements can be adjusted in real-time, the CLMS algorithm is developed as a normalized adaptive version of LCMV which can minimize the output power and reduce unwanted interferences with the object of keeping a maximum gain in the desired direction.

However, in some particular applications, especially in radar application, in order to realize the desired capacity, large arrays are always indispensable which attributes to the fact that big arrays are always restricted by the power supply and computation ability. Existing beamforming algorithms cannot solve this problem. Hence, as the development of sparse signal processing [5-14], and inspired by the Least Absolutely Shrinkage and Selection Operator [15] and Compressive Sensing [16], it is well worth to develop sparse adaptive beamforming algorithms to reduce the ratio of active elements in the antenna array, i.e., forcing the array weight vector towards sparsity [17-19].

Sparse signal processing technique can fully take advantage of the sparse characteristics existing in many situations, and it should have special advantages in both performance and convergence. In recent years, sparse signal processing has been widely studied. A great number of sparse LMS based algorithms have been developed for various sparse system identifications [5-8]. In these algorithms, it is no doubt that the zero-attracting LMS (ZA-LMS) which employs the l_1 -norm penalty is representative. The ZA-LMS algorithm creates a modified updating formulation with a zero-attractor on all filter taps so as to force the inactive coefficients to zero quickly. To further accelerate the convergence speed, the reweighted ZA-LMS (RZA-LMS) is presented to take account different zero attractors for different taps.

Motivated by the ideas of sparse signal processing, a l_1 -norm CNLMS (L₁-CNLMS) algorithm and weighted l_1 -norm CNLMS (L₁-WCNLMS) are proposed in [17].

Recently, many reweighted l_1 -norm penalties and l_p -norm penalties are proposed and considered in [5-8]. Thus, it is possible to introduce these penalties into the cost function of the basic CLMS algorithm for obtaining a new beamformer to get a better performance.

In this paper, we develop a reweighted L_1 -CNLMS (RL_1 -CNLMS) algorithm and an l_p -norm based CNLMS (L_p -CNLMS) algorithm for sparse adaptive beamforming control applications. Simulation results demonstrate the proposed algorithms can get a better beam performance and use less antenna array elements, while the output SINR are also better than the existing algorithm in [17].

II. THE ARRAY PROCESSING MODEL

As is depicted in Fig. 1, a model of a planar antenna array which is composed of N omnidirectional antenna elements with a spacing of $\lambda/2$ is considered for discussing the adaptive beamforming algorithm, where λ denotes the operating frequency wavelength. Assuming that we have $M+1$ narrowband signals received by the antenna array including the SOI and interferences with the direction of θ_s and θ_i ($i=1,2,\dots,M$). Then, receiving signals during k th snap can be written as:

$$\mathbf{x}(k) = \mathbf{a}_s \mathbf{s}(k) + \mathbf{a}_i \mathbf{i}(k) + \mathbf{n}(k). \quad (1)$$

In our notation, \mathbf{a} , $\mathbf{s}(k)$, $\mathbf{i}(k)$ and $\mathbf{n}(k)$ are the steering matrix associated with the SOI as well as interferences, complex signal envelope vector and zero-mean white Gaussian noise vector, respectively. Note that the SOI, interferences and the noise are assumed to be statistically independent.

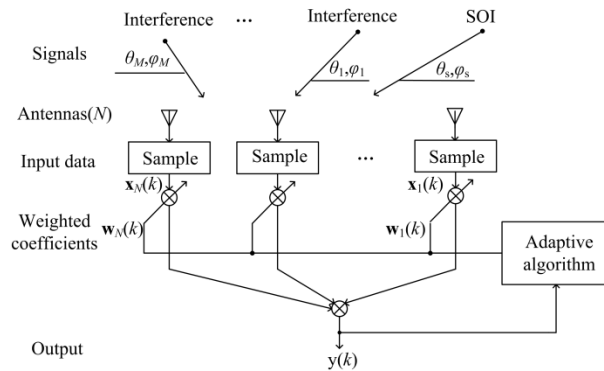


Fig. 1. Adaptive beamforming for planar antenna array.

In this case, one can write the SINR of the beamformer as:

$$\text{SINR} = \frac{p_s^2 |\mathbf{w}^H \mathbf{a}_s|^2}{\mathbf{w}^H \mathbf{R}_{n+i} \mathbf{w}}, \quad (2)$$

where p_s^2 is the power of SOI, \mathbf{w} is the weighted coefficient vector of the planar array with a dimension of $N \times 1$ and \mathbf{R}_{n+i} is the interference-plus-noise covariance matrix which can be written as:

$$\mathbf{R}_{n+i} = E \{ (\mathbf{i}(k) + \mathbf{n}(k))(\mathbf{i}(k) + \mathbf{n}(k))^H \}, \quad (3)$$

with $E\{\cdot\}$ representing the expectation operator and $(\cdot)^H$ stands for the Hermitian operator.

The output signal $y(k)$ at time index k is given by:

$$y(k) = \mathbf{w}^H \mathbf{x}(k). \quad (4)$$

III. THE CNLMS ALGORITHMS FOR BEAMFORMING

A. The CLMS algorithm

The solution to the LCMV algorithm presented in [1] is expressed as:

$$\mathbf{w}_{\text{opt}} = \mathbf{R}^{-1} \mathbf{C} (\mathbf{C}^H \mathbf{R}^{-1} \mathbf{C})^{-1} \mathbf{f}. \quad (5)$$

In (5), \mathbf{R} is the covariance matrix of the input data. \mathbf{C} and \mathbf{f} are the constrained matrix, and the constrained vector, respectively, of whom the elements are associated to the SOI and interferences. Compared with the LCMV solution, the CLMS algorithm can adaptively provide a high gain for the SOI and effectively attenuate the interferences, which is to solve:

$$\min_{\mathbf{w}} E [|e_k|^2] \quad \text{subject to} \quad \mathbf{C}^H \mathbf{w} = \mathbf{f}, \quad (6)$$

where $e_k = d_k - \mathbf{w}^H \mathbf{x}_k$ is the estimation error and d_k represents the expected output signal.

Make use of the Lagrange multiplier method, one can transform (6) into the following cost function:

$$L(k) = E [|e_k|^2] + \gamma_1^H (\mathbf{C}^H \mathbf{w}_k - \mathbf{f}), \quad (7)$$

where γ_1 is the Lagrange multiplier.

On the basis of the gradient descent principle, the update formulation can be constructed as:

$$\mathbf{w}_{k+1} = \mathbf{w}_k - \mu \mathbf{g}_w L(k), \quad (8)$$

where μ is the step size and $\mathbf{g}_w L(k)$ is the gradient vector.

In this paper, we use the instantaneous estimate of the gradient vector for simply, which can be written as:

$$\mathbf{g}_w L(k) = -2e_k^* \mathbf{x}_k + \mathbf{C} \gamma_1. \quad (9)$$

Using the constraint in (6) and several straightforward calculations, we can get the update function:

$$\mathbf{w}_{k+1} = \mathbf{P} [\mathbf{w}_k + \mu e_k^* \mathbf{x}_k] + \mathbf{f}_c, \quad (10)$$

where

$$\mathbf{P} = \mathbf{I}_{N \times N} - \mathbf{C} (\mathbf{C}^H \mathbf{C})^{-1} \mathbf{C}^H, \quad (11)$$

and

$$\mathbf{f}_c = \mathbf{C} (\mathbf{C}^H \mathbf{C})^{-1} \mathbf{f}. \quad (12)$$

B. The CNLMS algorithm

Note that the step size, also known as the convergence factor, is stationary in the CLMS algorithm. Hence, one can accelerate the convergence process by minimizing the instantaneous posteriori squared error with respect to the step size at snap k , which is to calculate [20]:

$$\frac{\partial [|e_{ap}(k)|^2]}{\partial \mu_k^*} = \frac{\partial [e_{ap}(k) e_{ap}^*(k)]}{\partial \mu_k^*} = 0, \quad (13)$$

where

$$e_{ap}(k) = e_k (1 - \mu_k \mathbf{x}_k^H \mathbf{P} \mathbf{x}_k). \quad (14)$$

Then, we can get:

$$\mu_k = \frac{\mu_0}{\mathbf{x}_k^H \mathbf{P} \mathbf{x}_k + \zeta_c}, \quad (15)$$

where $\zeta_c > 0$ is a small constant to prevent overflowing, and μ_0 is the step size used to implement this algorithm.

At last, we can get its updating equation:

$$\mathbf{w}_{k+1} = \mathbf{P}[\mathbf{w}_k + \mu_0 \frac{e_k \mathbf{x}_k}{\mathbf{x}_k^H \mathbf{P} \mathbf{x}_k + \zeta_c}] + \mathbf{f}_c. \quad (16)$$

C. The proposed new RL₁-CNLMS

In this paper, we develop a new RL₁-CNLMS algorithm for adaptive beamforming control application, which is to mimic:

$$\min_{\mathbf{w}} E[|e_k|^2] \quad \text{subject to} \quad \begin{cases} \mathbf{C}^H \mathbf{w}_k = \mathbf{f}; \\ \|\mathbf{h}_k \mathbf{w}_k\|_1 = t, \end{cases} \quad (17)$$

where t denotes the constraint factor, and \mathbf{h}_k is [6]:

$$[\mathbf{h}_k]_i = \frac{1}{\zeta_{r1} + |\mathbf{w}_{k-1}|_i}, \quad i = 1, \dots, N \quad (18)$$

where $\zeta_{r1} > 0$ is a small value similar with ζ_c in (15).

Similar to the basic CLMS algorithm, we can get the modified cost function applying the Lagrange multiplier method:

$$L_{r1}(k) = E[|e_k|^2] + \gamma_1^H (\mathbf{C}^H \mathbf{w}_k - \mathbf{f}) \quad (19)$$

$$+ \gamma_{r1} [\|\mathbf{h}_k \mathbf{w}_k\|_1 - t],$$

where γ_1 and γ_{r1} act as the Lagrange multipliers.

The instantaneous estimation for implementing the gradient of (19) is:

$$\mathbf{g}_w L_{r1}(k) = -2e_k^* \mathbf{x}_k + \mathbf{C} \gamma_1 + \gamma_{r1} \mathbf{J}_{r1}(k), \quad (20)$$

with

$$\mathbf{J}_{r1}(k) = \frac{\text{sgn}(\mathbf{w}_k)}{\zeta_{r1} + |\mathbf{w}_{k-1}|}, \quad (21)$$

where $\text{sgn}(\cdot)$ is an element-wise sign operator whose definition is:

$$\text{sgn}(x) = \begin{cases} \frac{x}{|x|} & x \neq 0; \\ 0 & \text{elsewhere.} \end{cases} \quad (22)$$

Based on the principle of gradient descent concepts shown in (8), we can get the final update equation that is written as:

$$\mathbf{w}_{k+1} = \mathbf{w}_k - \mu \mathbf{g}_w L_{r1}(k), \quad (23)$$

where $\mathbf{g}_w L_{r1}(k)$ is given in (20).

Now, it turns to solve the Lagrange multipliers. Under the circumstance that the algorithm has converged, we have $\mathbf{w}_{k+1} = \mathbf{w}_k$, then the constraints in (17) can be rewritten as:

$$\begin{cases} \mathbf{C}^H \mathbf{w}_{k+1} = \mathbf{C}^H \mathbf{w}_k = \mathbf{f}, \\ \mathbf{J}_{r1}(k) \mathbf{w}_{k+1} = \mathbf{J}_{r1}(k) \mathbf{w}_k = \|\mathbf{h}_k \mathbf{w}_k\|_1 = t. \end{cases} \quad (24)$$

After substituting (20) into (23), and pre-multiplying (23) by \mathbf{C}^H and \mathbf{J}_{r1} , we can get the expressions for γ_1 and γ_{r1} :

$$\begin{cases} \gamma_1 = \mathbf{G}(2e_k^* \mathbf{x}_k - \gamma_{r1} \mathbf{J}_{r1}(k)), \\ \gamma_{r1} = \left(\frac{-2}{n\mu}\right)(t - \mathbf{J}_{r1}^H(k) \mathbf{w}_k) + \frac{2e_k^* \mathbf{s}_k^H \mathbf{P} \mathbf{x}_k}{n}, \end{cases} \quad (25)$$

with

$$\begin{cases} \mathbf{G} = (\mathbf{C}^H \mathbf{C})^{-1} \mathbf{C}^H \\ n = \|\mathbf{P} \mathbf{s}_k\|_2^2. \end{cases} \quad (26)$$

Putting γ_1 and γ_{r1} into (23), and considering the normalizing method in [20], we can derive the final updating equation for the proposed RL₁-CNLMS:

$$\mathbf{w}_{k+1} = \mathbf{w}_k + \mu_k e_k^* \mathbf{V} + (t - \mathbf{J}_{r1}^H(k) \mathbf{w}_k) \left(\frac{\mathbf{P} \mathbf{J}_{r1}(k)}{m}\right), \quad (27)$$

where, for simply, we use the notations as below:

$$\begin{cases} q = \mathbf{J}_{r1}^H(k) \mathbf{P} \mathbf{x}_k, \\ m = \mathbf{J}_{r1}^H(k) \mathbf{P} \mathbf{J}_{r1}(k), \\ \mu_k = \frac{\left[e_k - (t - \mathbf{J}_{r1}^H(k) \mathbf{w}_k) \left(\frac{\mathbf{P} \mathbf{J}_{r1}(k)}{m}\right) \mathbf{x}_k \right]}{e_k \mathbf{V}^H \mathbf{x}_k + \zeta_{r1}}, \\ \mathbf{P} = \mathbf{I}_{N \times N} - \mathbf{C}(\mathbf{C}^H \mathbf{C})^{-1} \mathbf{C}^H, \\ \mathbf{V} = \mathbf{P} \left(\mathbf{x}_k - \frac{q \mathbf{J}_{r1}(k)}{m} \right). \end{cases} \quad (28)$$

IV. THE L_p-CNLMS ALGORITHM

To further improve the adaptive beamforming performance of the designed beamformer, we develop an L_p-CNLMS algorithm. Inspired by the fact for the corresponding sparse constraint, the more it is closer to l_0 -norm, the better result we will get. Thus, as we have known from the field of sparse system identification [6-9], the l_p -norm penalty which can obtain better results than l_1 -norm is considered as a new constraint in the CNLMS algorithm to further improve the estimation behavior of adaptive beamformers.

The cost function of the L_p-CNLMS algorithm with $0 < p < 1$ is presented [6]:

$$L_p(k) = E[|e_k|^2] + \gamma_1^H (\mathbf{C}^H \mathbf{w}_k - \mathbf{f}) \quad (29)$$

$$+ \gamma_{ip} [\|\mathbf{w}_k\|_{lp} - t].$$

One can get the gradient instantaneous estimation for $L_p(k)$ case, which is expressed as:

$$\mathbf{g}_w L_p(k) = -2e_k^* \mathbf{x}_k + \mathbf{C} \gamma_1 + \gamma_{ip} \mathbf{J}_{ip}(k), \quad (30)$$

where

$$\mathbf{J}_{ip}(k) = \frac{(\|\mathbf{w}_k\|_{lp})^{1-p} \text{sgn}(\mathbf{w}_k)}{\zeta_{ip} + \|\mathbf{w}_k\|^{1-p}}. \quad (31)$$

Note that the only difference between (20) and (30) are the \mathbf{J}_{r1} and \mathbf{J}_{ip} terms. In this case, one can easily obtain the final updating function of the L_p-CNLMS algorithm by considering the \mathbf{J}_{r1} term like the equation

(26) to obtain:

$$\mathbf{w}_{k+1} = \mathbf{w}_k + \mu_k \mathbf{e}_k^* \mathbf{V} + (t - \mathbf{J}_{lp}^H(k) \mathbf{w}_k) \left(\frac{\mathbf{P} \mathbf{J}_{lp}(k)}{m} \right), \quad (32)$$

where

$$\begin{cases} q = \mathbf{J}_{lp}^H(k) \mathbf{P} \mathbf{x}_k, \\ m = \mathbf{J}_{lp}^H(k) \mathbf{P} \mathbf{J}_{lp}(k), \\ \mu_k = \frac{e_k - (t - \mathbf{J}_{lp}^H(k) \mathbf{w}_k) \left(\frac{\mathbf{P} \mathbf{J}_{lp}(k)}{m} \right) \mathbf{x}_k}{e_k \mathbf{V}^H \mathbf{x}_k + \xi_{lp}}, \\ \mathbf{P} = \mathbf{I}_{N \times N} - \mathbf{C}(\mathbf{C}^H \mathbf{C})^{-1} \mathbf{C}^H, \\ \mathbf{V} = \mathbf{P} \left(\mathbf{x}_k - \frac{q \mathbf{J}_{lp}(k)}{m} \right). \end{cases} \quad (33)$$

V. SIMULATION RESULTS

In this section, experiments are set up to evaluate the effectiveness and improvement of the proposed algorithms. The SOI and interferences are QPSK signals from the azimuth of 90° , 22° , 62° , 120° and 147° , respectively, which are received by the 91-elements hexagonal array (HA). The interference-to-noise ratio (INR) is 30 dB and the initialized step size for L_1 -WCNLS, RL_1 -CNLS, CNLS and L_p -CNLS are 5×10^{-2} , 2×10^{-3} , 5×10^{-3} and 5×10^{-4} , respectively; while the constraint factor t is set to 0.8 uniformly. The iteration times are 1.2×10^{-4} , while the parameters γ and ζ are 5 and 5×10^{-3} .

Figure 2 illustrates the beam patterns of the proposed algorithms in comparison with the existing algorithms. It can be seen from the figure that our proposed algorithms can form nulls corresponding interferences while generate nearly identical main lobe in the direction of SOI. What's more, the side lobe level (SLL) is lower than the algorithm developed in [17], but a little higher against the non-sparse algorithm CNLS.

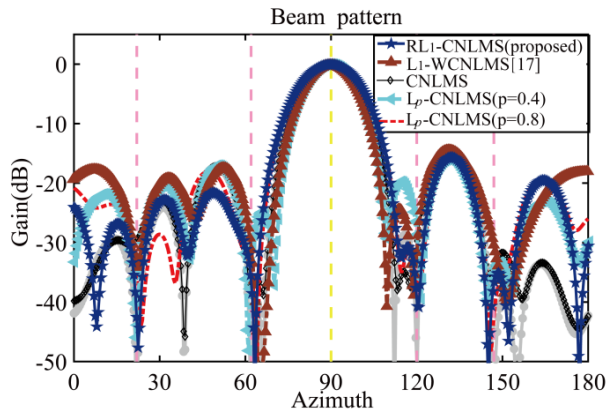


Fig. 2. Beam patterns of the proposed algorithms versus the CNLS algorithm and the existing algorithm in [17]. Yellow line stands for the SOI, pink lines are interferences.

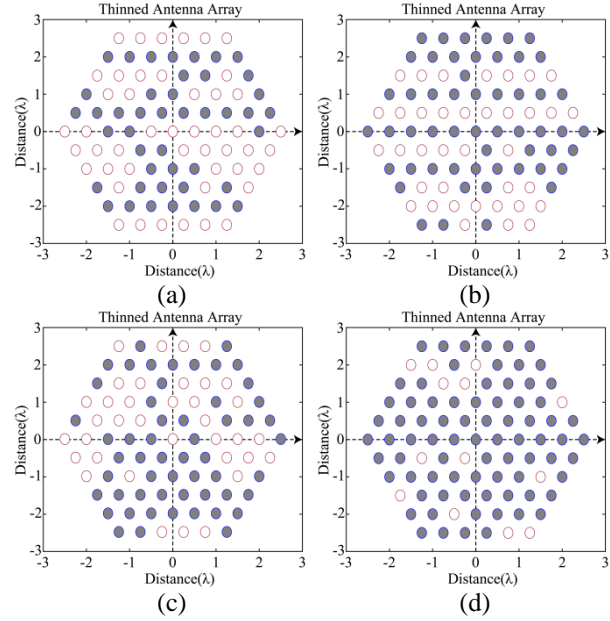


Fig. 3. Sparse arrays thinned by the proposed algorithms and the algorithm developed in [17]. (a) L_p -CNLS algorithm with $p=0.8$, (b) L_p -CNLS algorithm with $p=0.4$, (c) RL_1 -CNLS algorithm, and (d) algorithm in [17].

Figure 3 shows the sparse arrays thinned by using the proposed algorithms and the algorithm in [17]. As the figure indicates, all the algorithms can achieve sparse adaptive beamforming successfully. However, it is clearly that the beam patterns of the proposed algorithms turn off much more active antennas in comparison with the algorithm in [17] under the same iteration times. In addition, the L_p -CNLS has a better performance than that of the RL_1 -CNLS algorithm since it can effectively exploit the sparseness of the antenna array. Thus, our proposed adaptive beamformer can reduce the power supply via utilizing less antenna elements to get nearly same performance in the HA beamforming.

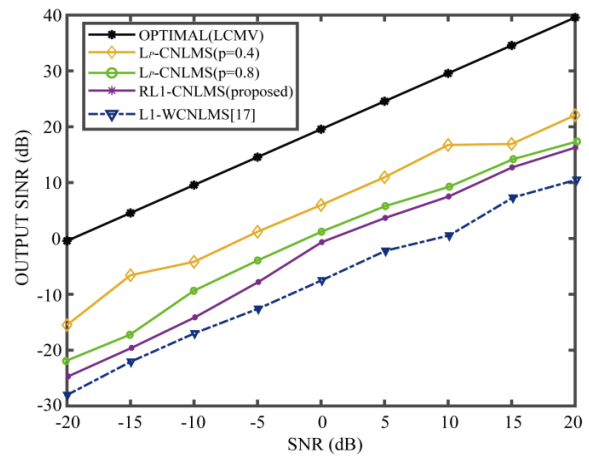


Fig. 4. Output SINR versus the input SNR.

In terms of the output SINR performance shown in Fig. 4, the proposed algorithms can obviously obtain a better SINR results with the same SNR. In addition, the L_p -CNLMS algorithm is superior to the RL_1 -CNLMS. What's more, if p goes closer to 0, we will get better SINR performance, but its beam is getting worse. Thus, it is a trade-off for practical applications. Moreover, since we aim to develop sparse antenna array, resulting in an inferior output SINR which should be improved in the future.

VI. CONCLUSION

In this paper, a RL_1 -CNLMS algorithm and an L_p -CNLMS algorithm have been proposed for sparse adaptive beamforming control applications. The proposed algorithms can reconstruct the main beam in the direction of SOI and provide nulls to reduce the influences from the interferences. Besides, they can achieve better performance than the existing sparse beamformer by using much less antenna elements. In terms of the output SINR, our proposed algorithms also have a good property. However, they still have some weaknesses that need for further study, such as the high SLL. Additionally, in the model, we neglect the influence of mutual coupling, which may lead to estimate error and need future investigate either. Also, we will consider the sparse beam scanning antenna arrays in the future studies in the MIMO antenna arrays [21-23].

ACKNOWLEDGMENT

This work was partially supported by the National Key Research and Development Program of China (2016YFE111100), Key Research and Development Program of Heilongjiang (GX17A016), the Science and Technology innovative Talents Foundation of Harbin (2016RAXXJ044), the Natural Science Foundation of Beijing (4182077), China Postdoctoral Science Foundation (2017M620918), the Fundamental Research Funds for the Central University (HEUCFM180806) and Opening Fund of Acoustics Science and Technology Laboratory (Grant No. SSKF2016001).

REFERENCES

- [1] H. L. Van, *Trees, Detection, Estimation, and Modulation Theory, Part IV: Optimum Array Processing*. John Wiley & Sons, New York, NY, 2002.
- [2] J. Li and P. Stoica (Eds.), *Robust Adaptive Beamforming*. John Wiley & Sons, New York, NY, 2005.
- [3] O. L. Frost III, "An algorithm for linearly constrained adaptive array processing," *Proc. IEEE*, vol. 60, no. 8, pp. 926-935, Aug. 1972.
- [4] J. A. Apolinário, Jr., S. Werner, P. S. R. Diniz, and T. I. Laakso, "Constrained normalized adaptive filtering for CDMA mobile communications," *IEEE Signal Processing Conference*, Rhodes, Greece, Sep. 1998.
- [5] Y. Chen, Y. Gu, and A. O. Hero, "Sparse LMS for system identification," *Proc. IEEE International Conference on Acoustic Speech and Signal Processing, (ICASSP'09)*, Taipei, Taiwan, pp. 3125-3128, Apr. 2009.
- [6] O. Taheri and S. A. Vorobyov, "Sparse channel estimation with L_p -norm and reweighted L_1 -norm penalized least mean squares," *IEEE International Conference on Acoustic Speech and Signal Processing (ICASSP'11)*, Prague, Czech Republic, pp. 2864-2867, May 2011.
- [7] Y. Wang, Y. Li, and Z. Jin, "An improved reweighted zero-attracting NLMS algorithm for broadband sparse channel estimation," *IEEE International Conference on Electronic Information and Communication Technology*, Harbin, China, Aug. 2016.
- [8] Y. Gu, J. Jin, and S. Mei, " l_0 -norm constraint LMS algorithm for sparse system identification," *IEEE Signal Process. Lett.*, vol. 16, no. 9, pp. 774-777, Sept. 2009. 10.1109/LSP.2009.2024736.
- [9] Y. Li, Y. Wang, R. Yang, et al., "A soft parameter function penalized normalized maximum correntropy criterion algorithm for sparse system identification," *Entropy*, vol. 19, no. 1, p. 45, Jan. 2017. 10.3390/e19010045.
- [10] Z. Jin, Y. Li, and J. Liu, "An improved set-membership proportionate adaptive algorithm for a block-sparse system," *Symmetry*, vol. 10, no. 3, p. 75, Mar. 2018. 10.3390/sym10030075.
- [11] D. Angelosante, J. A. Bazerque, and G. B. Giannakis, "Online adaptive estimation of sparse signals: Where RLS meets the l_1 -norm," *IEEE Transactions on Signal Processing*, vol. 58, no. 7, pp. 3436-3447, Mar. 2010. 10.1109/TSP.2010.2046897.
- [12] O. Taheri and S. A. Vorobyov, "Reweighted l_1 -norm penalized LMS for sparse channel estimation and its analysis," *Elsevier Signal Processing*, vol. 104, pp. 70-79, May 2014.
- [13] Y. Li, Y. Wang, and T. Jiang, "Sparse-aware set-membership NLMS algorithms and their application for sparse channel estimation and echo cancelation," *AEUE - International Journal of Electronics and Communications*, vol. 70, no. 7, pp. 895-902, 2016.
- [14] Y. Li, Y. Wang, and T. Jiang, "Norm-adaption penalized least mean square/fourth algorithm for sparse channel estimation," *Signal Processing*, 128:243-251, 2016.
- [15] R. Tibshirani, "Regression shrinkage and selection via the lasso," *J. R. Stat. Soc. Ser. B-Stat. Methodol.*, vol. 58, no. 1, pp. 267-288, Jan. 1996.

- [16] D. L. Donoho, "Compressed sensing," *IEEE Trans. Inf. Theory*, vol. 52, no. 4, pp. 1289-1306, Apr. 2006.
- [17] J. F. de Andrade, M. L. R. de Campos, and J. A. Apolinário, " L_1 -constrained normalized LMS algorithms for adaptive beamforming," *IEEE Transactions on Signal Processing*, vol. 63, no. 24, pp. 6524-6539, Dec. 2015. 10.1109/TSP.2015.2474302.
- [18] W. Shi, Y. Li, and S. Luo, "Adaptive antenna array beamforming based on norm penalized NLMS algorithm," *2018 IEEE International Symposium on Antennas and Propagation and USNC-URSI Radio Science Meeting*, in press, Boston, America, July 2018.
- [19] W. Shi and Y. Li, "Norm-constrained NLMS for sparse controllable adaptive array beamforming," *2018 International Applied Computational Electromagnetics Society Symposium*, in press, Beijing, China, July 2018.
- [20] P. S. R. Diniz, *Adaptive Filtering: Algorithms and Practical Implementation*. New York, USA: Springer, 2010.
- [21] K. Yu, Y. Li, and X. Liu, "Mutual coupling reduction of a MIMO antenna array using 3-D novel meta-material structures," *Applied Computational Electromagnetics Society Journal*, vol. 33, no. 7, pp. 758-763, 2018.
- [22] T. Jiang, T. Jiao, Y. Li, and W. Yu, "A low mutual coupling MIMO antenna using periodic multi-layered electromagnetic band gap structures," *Applied Computational Electromagnetics Society Journal*, vol. 33, no. 3, pp. 305-311, 2018.
- [23] Y. Li, W. Li, and W. Yu, "A multi-band/UWB MIMO/diversity antenna with an enhance isolation using radial stub loaded resonator," *Applied Computational Electromagnetics Society Journal*, vol. 28, no. 1, pp. 8-20.

Accurate Analysis of JEM Interference in Airborne Array using Parallel HO-IE-DDM

Yingyu Liu¹, Qin Su¹, Xunwang Zhao¹, Yu Zhang¹, Zhongchao Lin¹, Chang Zhai¹,
and Qi Zhang²

¹ Shaanxi Key Laboratory of Large Scale Electromagnetic Computing
Xidian University, Xi'an, Shaanxi 710071, China
xwzhao@mail.xidian.edu.cn

² Science and Technology on Electromagnetic Compatibility Laboratory
China Ship Development and Design Center, Wuhan 430064, China

Abstract — In this paper, we present a parallel integral equation solver based on domain decomposition method for the analysis of airborne array interference problems affected by jet engine modulation. The solver makes use of higher-order basis functions for the discretization of the problem. The paper proposes two main novelties: firstly, the radiation characteristics of the airborne array (interfered by multiple rotating blades) are analyzed using an integrated simulation technology; secondly, the computation during the analysis of JEM problem is significantly reduced, for only re-computing the changed parts of the model. Numerical examples using complex electrically large structures are presented in order to demonstrate the flexibility, accuracy, and efficiency of the proposed integral equation solver.

Index Terms — Airborne antenna array, domain decomposition method, higher-order MoM, Jet engine modulation, parallel.

I. INTRODUCTION

Radar is regarded as a powerful tool for detecting and tracking airborne targets. For a radar system, the antenna pattern provides input information. However, due to the nearfield scattering from the platform, the antenna radiation pattern can be distorted. This distorted pattern may seriously affect the detection performance of the radar [1]. For a common carrier platform, an airplane, there are some rotating parts of it like blades of turbofan engine and propeller-fan engine [1-3]. These rotating objects can cause a periodic modulation of electromagnetic (EM) wave radiated by antenna array, which is known as jet engine modulation (JEM). Thus, this effect can result in a miscomputation of radar prediction.

For a long time, researches about JEM issues are mainly limited in scattering characteristics [1-4]. For

more complex EM problem, the radiation patterns of the antenna affected by JEM effect, it was not until last decade to be carried out [5]. Usually, the antennas involved are simpler structures such as a dipole antenna at lower working frequency, and only one single rotor can be calculated. Due to the large electrical size of the whole targets and the complex EM environment, such electromagnetic compatibility (EMC) problem is extremely challenging. Scholars generally use high frequency algorithm like uniform geometrical theory of diffraction (UTD) [6] and physical optics (PO) to analyze JEM. However, such method fails to ensure sufficient accuracy. Using method of moment (MoM) to study JEM can get accurate results, but MoM usually requires very large computational resources [7].

It could be an effective way to solve the EM problems from electrically large structures combining the method of integral equations (IE) with the domain decomposition method (DDM). There are also some studies on IE-DDM [8-11]. However, they are mostly aimed at solving the scattering problem. Even if the radiating problem can be analyzed, it is difficult to analyze large complex issues such as the airborne antenna array. Let alone the JEM issues of the large airborne antenna arrays. Among these studies on IE-DDM, it is worthwhile to mention the work presented by Peng and Lee [9], which is able to address multi-scale issue with non-conformal meshes. It is possible to only re-mesh the changed portion of a target, but the whole problem still need to be re-computed.

A new solution scheme of integral equations based on domain decomposition method discretized by higher-order basis functions, called as HO-IE-DDM, is proposed in this paper. The advantages of the higher-order basis functions, which are used to approximate the current distribution [7,12,13], are that produce fewer unknowns than lower-order basis functions and increase the scale

of the problem to be solved. By bringing parallel computing technique in the HO-IE-DDM, the simulating capability of the method is further improved. The proposed parallelization scheme allows all the computer resources to be used to a single subdomain at a time, the advantage of which is that the imbalanced workload caused by the unevenly decomposed subdomains is reduced, and at the same time the scale of the problem to be solved is greatly enlarged. Moreover, the proposed solver provides unprecedented flexibility and convenience for analysis of JEM issues, since it is possible to only compute the changed part of the aircraft.

The remaining of this paper is organized as follows. In Section II, the algorithm of the HO-IE-DDM is presented. Section III provides two cases of JEM radiation problem are analyzed using parallel HO-IE-DDM, and the numerical examples to demonstrate the correctness, flexibility and high efficiency of the proposed method. Finally, some conclusions are given in Section IV.

II. THEORY OF HO-IE-DDM

A. Integral equations

Let us consider a finite large complex EM target containing multiple perfect electric conductors (PECs) and dielectric structures in free space. In the i th region ($i=1,2,\dots,n$), the permittivity and the permeability are ε_i and μ_i , and the incident electric and magnetic fields are \mathbf{E}_i^{inc} and \mathbf{H}_i^{inc} , respectively, as shown in Fig. 1 (a). Region 0 is for perfect electric conductors (PECs), in which the electromagnetic field is zero.

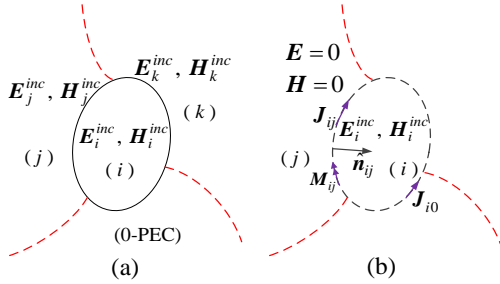


Fig. 1. Surface equivalence theorem: (a) the original problem, and (b) the equivalent problem of region i .

In general, we consider the i th region, as shown in Fig. 1 (b). According to the equivalence principle, the regions except the i th region are filled with the same medium as the i th region. At this time, the electric and magnetic fields in these regions (except the i th region) are $\mathbf{E}=0$ and $\mathbf{H}=0$. The equivalent current density at the boundary surface between region i and j can be expressed as:

$$\mathbf{J}_{ij} = \hat{\mathbf{n}}_{ij} \times \mathbf{H}_i, \mathbf{M}_{ik} = -\hat{\mathbf{n}}_{ij} \times \mathbf{E}_i, \quad (1)$$

where $\hat{\mathbf{n}}_{ij}$ is the unit normal vector. If we consider the

j th region, the equivalent current density at the boundary surface between region j and i can be expressed as:

$$\mathbf{J}_{ji} = \hat{\mathbf{n}}_{ji} \times \mathbf{H}_j, \mathbf{M}_{jk} = -\hat{\mathbf{n}}_{ji} \times \mathbf{E}_j. \quad (2)$$

The electromagnetic field satisfies the following boundary conditions:

$$\hat{\mathbf{n}}_{ij} \times (\mathbf{H}_i - \mathbf{H}_j) = 0, \hat{\mathbf{n}}_{ij} \times (\mathbf{E}_i - \mathbf{E}_j) = 0. \quad (3)$$

Here \mathbf{E}_i and \mathbf{H}_i , the total field in the i th region, are expressed as:

$$\mathbf{E}_i = \sum_{\substack{k=0 \\ k \neq i}}^n [\eta_i L_i(\mathbf{J}_{ik}) - K_i(\mathbf{M}_{ik})] + \mathbf{E}_i^{inc}, \quad (4)$$

$$\mathbf{H}_i = \sum_{\substack{k=0 \\ k \neq i}}^n \left[K_i(\mathbf{J}_{ik}) + \frac{L_i(\mathbf{M}_{ik})}{\eta_i} \right] + \mathbf{H}_i^{inc}, \quad (5)$$

where η_i is the intrinsic impedance of the i th region:

$$L_i(\mathbf{X}_{ik}) = -jk_i \int_{S_{ik}} \left(\mathbf{X}_{ik}(\mathbf{r}_{ik}) G_i(\mathbf{r}, \mathbf{r}') + \frac{1}{k_i^2} \nabla \mathbf{X}_{ik}(\mathbf{r}_{ik}) \nabla G_i(\mathbf{r}, \mathbf{r}') \right) dS_{ik}, \quad (6)$$

$$K_i(\mathbf{X}_{ik}) = -\int_{S_{ik}} (\mathbf{X}_{ik}(\mathbf{r}_{ik}) \times \nabla G_i(\mathbf{r}, \mathbf{r}')) dS_{ik}, \quad (7)$$

where $G_i(\mathbf{r}, \mathbf{r}') = e^{-jk_i R} / 4\pi R$, $R = |\mathbf{r} - \mathbf{r}'|$, $k_i = \omega \sqrt{\varepsilon_i \mu_i}$.

By substituting equations (4) and (5) into equation (3), the surface IE, called the PMCHWT formulation [12], at the boundary surface between region i and j can be obtained by:

$$\hat{\mathbf{n}}_{ij} \times \left\{ \sum_{\substack{k=0 \\ k \neq i}}^n [\eta_i L_i(\mathbf{J}_{ik}) - K_i(\mathbf{M}_{ik})] - \sum_{\substack{k=0 \\ k \neq j}}^n [\eta_j L_j(\mathbf{J}_{jk}) - K_j(\mathbf{M}_{jk})] \right\} = \hat{\mathbf{n}}_{ij} \times (\mathbf{E}_j^{inc} - \mathbf{E}_i^{inc}), \quad (8)$$

$$\hat{\mathbf{n}}_{ij} \times \left\{ \sum_{\substack{k=0 \\ k \neq i}}^n \left[K_i(\mathbf{J}_{ik}) + \frac{L_i(\mathbf{M}_{ik})}{\eta_i} \right] - \sum_{\substack{k=0 \\ k \neq j}}^n \left[K_j(\mathbf{J}_{jk}) + \frac{L_j(\mathbf{M}_{jk})}{\eta_j} \right] \right\} = \hat{\mathbf{n}}_{ij} \times (\mathbf{H}_j^{inc} - \mathbf{H}_i^{inc}). \quad (9)$$

At boundary surfaces between region i and region 0 (PECs), the magnetic currents vanish, so equation (9) is no longer established, and equation (8) degenerates into the electric field integral equation (EFIE) [14].

B. Domain decomposition method

As shown in Fig. 2, the simulation model is decomposed into several subdomains Ω_i ($i=1,2,\dots,n$). Generally, for the n subdomains case, the Galerkin test is performed to the weighted linear combination of equations (8-9) and the following matrix equation is obtained:

$$\begin{bmatrix} \mathbf{Z}_{11} & \mathbf{Z}_{12} & \cdots & \mathbf{Z}_{1n} \\ \mathbf{Z}_{21} & \mathbf{Z}_{22} & \cdots & \mathbf{Z}_{2n} \\ \vdots & \vdots & \ddots & \vdots \\ \mathbf{Z}_{n1} & \mathbf{Z}_{n2} & \cdots & \mathbf{Z}_{nn} \end{bmatrix} \begin{bmatrix} \mathbf{I}_1 \\ \mathbf{I}_2 \\ \vdots \\ \mathbf{I}_n \end{bmatrix} = \begin{bmatrix} \mathbf{V}_1 \\ \mathbf{V}_2 \\ \vdots \\ \mathbf{V}_n \end{bmatrix}, \quad (10)$$

where \mathbf{Z}_{ij} ($i=j$) is the self impedance matrix in Ω_i , \mathbf{Z}_{ij} ($i \neq j$) is the mutual impedance matrix between Ω_j and Ω_i , \mathbf{I}_i is the current coefficient vector in Ω_i and \mathbf{V}_i is the excitation vector in Ω_i .

Parallel out of core higher-order MoM (HOMoM) with the lower/upper decomposition (LU) solver is employed for each part. If the model is decomposed completely evenly, that each subdomain Ω_i contains $M=N/n$ unknowns, the memory requirement and the computing complexity of the LU solver is $O(M^2)$ and $O(M^3)$. If the division is uneven, the memory requirement and the computing complexity depend on the number of unknowns in the largest subdomain.

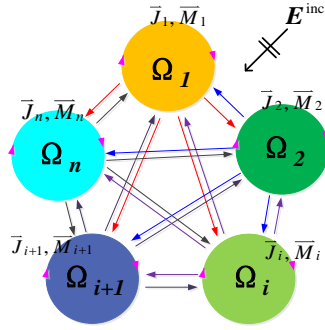


Fig. 2. Notations for domain decomposition.

Noting that the mutual impedance matrices in (10) are unnecessary to be stored, the coupling voltage vector ($\Delta \mathbf{V}_i = \mathbf{Z}_{ij} \mathbf{I}_j$) can be obtained using the near scattered field produced by the current ($\Delta \mathbf{V}_i(\mathbf{E}_{ij}, \mathbf{H}_{ij})$), and hence the memory requirement is reduced. The Gauss–Seidel method is adopted to calculate the interactions among domains allowing the use of all the computer resources in every subdomain problem at a time [15]. The vector of excitation \mathbf{V}_i of Ω_i is updated by other domains at each step:

$$\mathbf{Z}_{ii} \cdot \mathbf{I}_i = \mathbf{V}_i(\mathbf{E}^{\text{inc}}, \mathbf{H}^{\text{inc}}) + \sum_{j=1, j \neq i}^n \Delta \mathbf{V}_i(\mathbf{E}_{ij}, \mathbf{H}_{ij}). \quad (11)$$

Given the tolerance δ , at the initial step $k=0$, $\mathbf{I}_i^{(0)} = 0$ ($i = 1, 2, \dots, n$) and at the $k+1$ th step, the unknown surface current can be expressed as:

$$\mathbf{I}_i^{(k+1)} = \mathbf{Z}_{ii}^{-1} \left[\mathbf{V}_i(\mathbf{E}^{\text{inc}}, \mathbf{H}^{\text{inc}}) + \sum_{j>i} \Delta \mathbf{V}_i(\mathbf{E}_{ij}^{(k)}, \mathbf{H}_{ij}^{(k)}) + \sum_{j<i} \Delta \mathbf{V}_i(\mathbf{E}_{ij}^{(k+1)}, \mathbf{H}_{ij}^{(k+1)}) \right]. \quad (12)$$

The iterative steps continue and the residual error $\varepsilon_i = \|\mathbf{I}_i^{(k+1)} - \mathbf{I}_i^{(k)}\| / \|\mathbf{I}_i^{(k+1)}\|$ is calculated after each step. When $\max(\varepsilon_1, \varepsilon_2, \dots, \varepsilon_n) \leq \delta$ at the k th step, the iterative process stops and outputs \mathbf{I}^k ; otherwise, the process continues. If each subdomain Ω_i contains $M=N/n$

unknowns, the memory requirement and the computing complexity of the iterative process is $O(M)$ and $O(M^2)$. The flowchart of HO-IE-DDM is shown in Fig. 3.

Noting that the inverse matrices of self impedance in (12) is unnecessary to be re-computed, because they have been stored after the initial step. This provides a huge advantage for the analysis of JEM problems. When introducing quasi-stationary method to study how the rotating parts affect the airborne antenna performance, we need to compute the airplane with hundreds of different rotating blades stations. Considering the computing complexity of each subdomain is $O(M^3)$, if we decompose the rotating parts from the main part of the aircraft, the unchanged part can be computed only once. Thus the computing time can be reduced effectively.

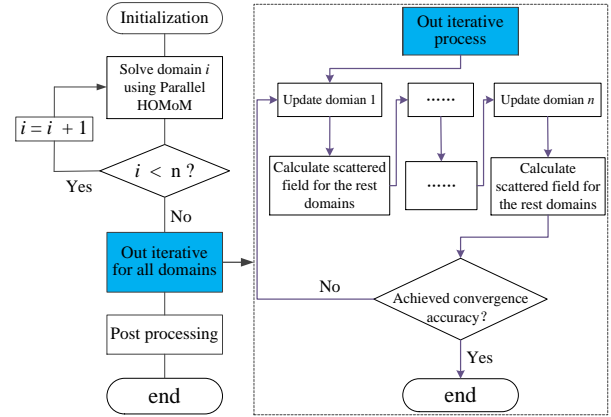


Fig. 3. Flowchart of HO-IE-DDM.

C. High-order basis functions

Different with the traditional RWGs which are defined on triangle patches, the higher-order basis functions (HOBs) employed by the proposed solver are defined on bilinear quadrilateral patches, as shown in Fig. 4. We refer the interested readers to [7,12] for details. The polynomial orders of the HOBs can be adjusted according to the electrical size of the geometric element. The main advantage of HOBs is that the size of the bilinear patch can be much bigger than that of the RWGs [14]. It means that the application of the HOBs can reduce the number of unknowns dramatically.

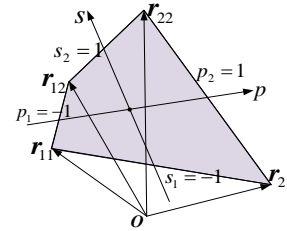


Fig. 4. Bilinear quadrilateral patch.

D. Parallelization

Based on DDM, the computing capability of HOMoM is improved. With the aid of parallel strategy, the computing speed of HO-IE-DDM can be further accelerated. For each subdomain, the large dense MoM matrix is divided into a number of smaller block matrices that are nearly equal in size and distributed among all participating processes. The distribution manner of the blocks is chosen appropriately according to the parallel LU direct solver to minimize the communication between processes.

The LU solver is a numerical accurate method in solving matrix equations, which can solve arbitrary geometric model problems, even if the matrix condition number is bad. For the parallel LU solver, the data should be distributed to multiple processes in a certain way and a load balanced approach called two-dimensional block-cyclic matrix distribution, which is similar to the ScaLAPACK, is adopted. It is important that the matrix filling schemes should be designed to avoid redundant calculation for better parallel efficiency.

Different from other parallel DDM strategy [16], which parallel computation occurs among subdomains, the parallel computation occurs both in and among every subdomains. The parallel strategy will not only simplify the modeling and meshing of subdomains to ensure their unknowns are even, but also save the waiting time to ensure each subdomain has been computed over.

III. COMPUTATIONAL ANALYSIS OF JEM ON AIRBORNE ANTENNA ARRAY

Two EM examples are presented to demonstrate the efficiency and accuracy of the proposed method. The residual error for outer iterative convergence is set to $3.0e-3$ without any specification. Two computational platforms are used in this paper:

Platform I: A workstation with two six-core 64 bit Intel Xeon E5-2620 2.0 GHz CPUs, 64GB RAM and 6TB disk.

Platform II: High-Performance Computing (HPC) cluster with 140 computing nodes. Each computing node has two 12-core bit Intel Xeon E5-2692 2.2 GHz CPUs, 64 GB RAM and 1.8TB disk.

A. Static airborne Yagi-Uda antenna array characteristic

First of all, to validate the accuracy and efficiency of the proposed HO-IE-DDM, the radiation characteristic of an airborne Yagi-Uda antenna array is calculated. The aircraft is $22.03m \times 17.16m \times 6.16m$ [17]. A Yagi-Uda antenna array [18] operated in 500MHz is mounted 2.5m above the middle part of the fuselage. The array consists of 36 units, and each unit has 8 directors. The aircraft model is shown in Fig. 5, which illustrates the relative location of the antenna array. Both sides of the wings are respectively equipped with a rotor. Each blade is

$1.77m \times 0.15m \times 0.03m$. The corresponding electrical size of that is about 2.77λ long, 0.23λ wide, 0.05λ thick. The patterns of antenna array before and after it is mounted on the airplane are shown in Fig. 6.

The model of the aircraft is decomposed into two subdomains as it is shown in Fig. 7. The 2D radiation patterns obtained by the proposed HO-IE-DDM are shown in Fig. 8. The patterns of overall solution using HOMoM and FEKO (a commercial software based on MoM) are also given for comparison.

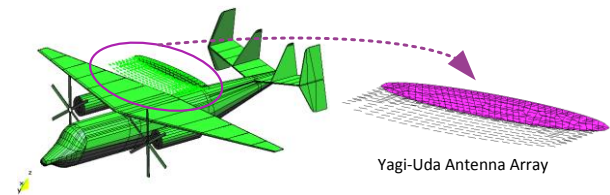


Fig. 5. Model of the double rotor aircraft mounting Yagi-Uda antenna array.

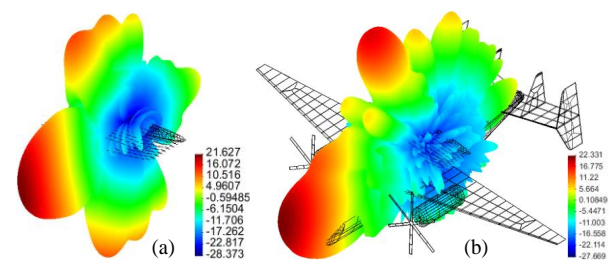


Fig. 6. Yagi-Uda array patterns: (a) array and (b) airborne array.

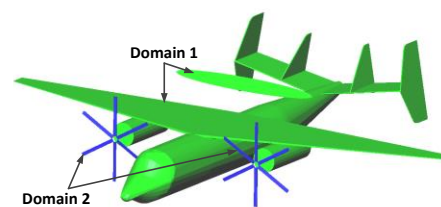


Fig. 7. Domain decomposition model (each color represents a subdomain).

The simulation is performed on Platform I, and the results obtained from HO-IE-DDM and HOMoM agree very well. The results obtained from HO-IE-DDM, HOMoM and FEKO (MoM) also agree well. Some difference between HOMoM and FEKO should result from the different meshes of the triangular meshes for RWGs and the quadrilateral meshes for HOBs. Computing information of radiation characteristics of the model analyzed by parallelized HO-IE-DDM and HOMoM is shown in Table 1. It can be seen that the computing time of HO-IE-DDM is not reduced compared with HOMoM (in core), but reduced compared with

HOMoM (out of core) and FEKO (MoM). For HOMoM (out of core), the computing time is saved owing to the reduction in I/O of hard disk, while for FEKO (MoM), the computing time is saved owing to the reduction in unknowns. We refer the interested readers to [7,8] for details between out of core HOMoM and in core HOMoM.

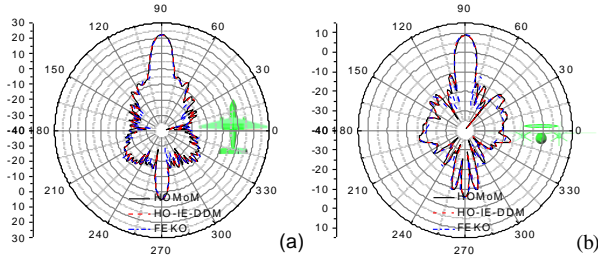


Fig. 8. 2D radiation patterns of the airborne Yagi-Uda array: (a) x-y and (b) x-z.

Table 1: Computational statistics of airborne Yagi-Uda array

Method	Unknowns	Storage (GB)	Time (s)
HO-IE-DDM	30324 (domain1)	13.70 (domain1)	1392.6
	1712 (domain2)	0.04 (domain2)	
HOMoM (out of core)	31716	14.99	1424.9
HOMoM (in core)	31716	14.99	1283.6
FEKO (MoM)	126902	120.23	60439.9

B. Dynamic airborne Yagi-Uda antenna array JEM characteristics

Based on quasi-stationary method, 1024 rotor orientations are included in the predictions of 0° to 360° to simulate rotor motion. For each of the fixed rotor orientations, the principal plane radiation pattern is predicted. The level of rotor modulation is calculated for each observation angle. For these comparisons, the level of rotor modulation is defined as the difference between the maximum and minimum magnitudes of the electric field that occur at a given observation angle among the rotor orientations (modulation level = $20\lg|\mathbf{E}_{\max}| - 20\lg|\mathbf{E}_{\min}|$). The accuracy of the proposed method has been proved in Fig. 8.

In order to compare with modulation level, we spread 3D radiation pattern contour plot along θ axis and ϕ axis in Fig. 9. Figure 10 shows the changeable intensity of the airborne array radiation pattern at every observation angles. JEM affects less when the receiving antenna is circularly polarized. Compared with Fig. 9, there is a complementary relationship before and after the

modulation. It shows that side-lobes and null depth levels of the airborne array are intensely changed.

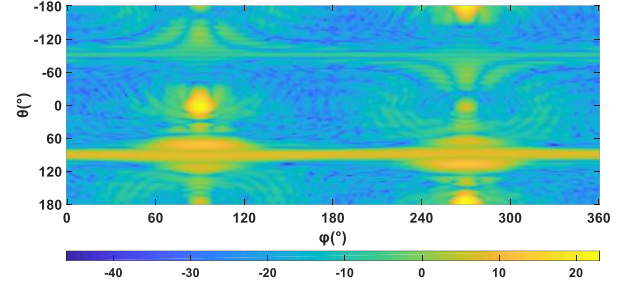


Fig. 9. Spreaded airborne Yagi-Uda array pattern.

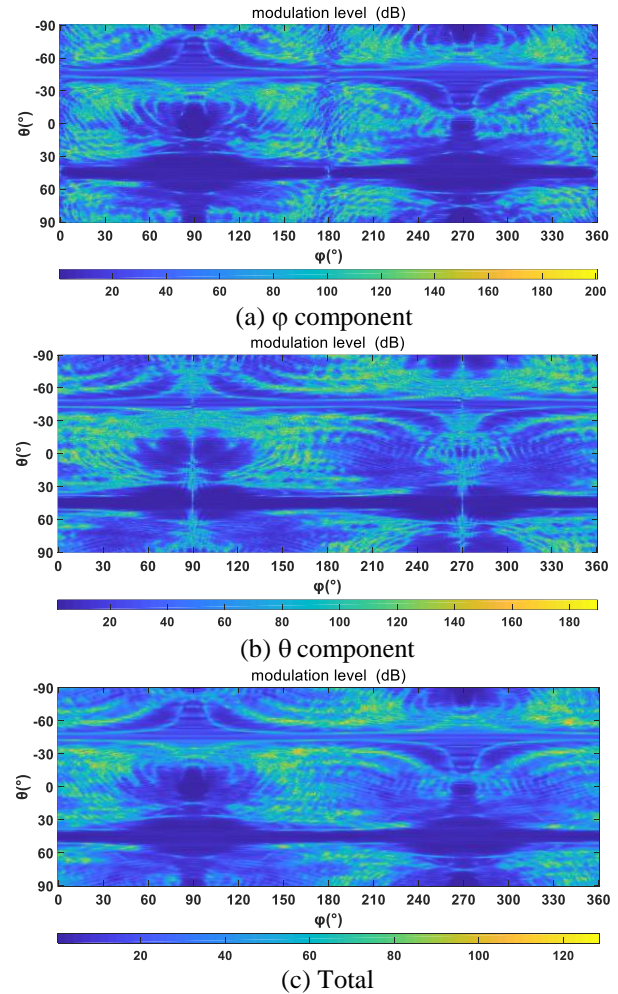


Fig. 10. Spreaded modulation level contour plots.

To save computing time, the modulation level is only computed by HO-IE-DDM. When the turbofans rotate, it needs to perform multiple simulations according to the changed position. For HOMoM (out of core), it needs at least 1024×1424.91 s to simulate the 1024 rotor orientations. As shown in Table 2, when solving the JEM

issues with repetitive similar simulations with changeable parts, HO-IE-DDM exhibits good performance for saving 92% of computation time compared to HOMoM. Because the computation of the main part of an aircraft is only need to do once, and the result of it is stored to be reused in the next 1024 iterations, the computing efficiency is significantly improved.

Table 2: Computational statistics of interfered Yagi-Uda array

Method	Unknowns	Storage (GB)	Time (s)
HO-IE-DDM	30324 (domain1)	13.70 (domain1)	897.5×1 (domain1) 9.8×1024 (domain2)
	1712×1024 (domain2)	0.04×1024 (domain2)	113542.7 (total)
HOMoM (out of core)	31716×1024	14.99×1024	-

C. Static airborne microstrip antenna array characteristics

Consider a rectangle patch microstrip array with 37×9 elements as shown in Fig. 11. The dimension of the dielectric substrate of a unit is $321.4\text{mm} \times 321.4\text{mm}$, and the dimension of the rectangle patch of a unit is $205.6\text{mm} \times 154.8\text{mm}$. The units are connected with each other. The thickness of the dielectric substrate is 18mm and $\epsilon_r=4.5$, the operating frequency is 700MHz . And the aircraft is $38.6\text{m} \times 36.5\text{m} \times 6.14\text{m}$ [8]. The array [14] is mounted 6.0m above the middle of the fuselage. The aircraft model is shown in Fig. 12, which illustrates the relative location of the antenna array. Both sides of the wings are respectively equipped with two rotors. Each blade is $1.5\text{m} \times 0.3\text{m} \times 0.05\text{m}$. The corresponding electrical size of that is about 2.25λ long, 0.51λ wide, 0.08λ thick. The patterns of antenna array before and after it is mounted on the airplane are shown in Fig. 13.

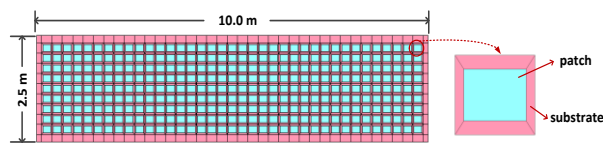


Fig. 11. Model of the microstrip antenna array.

The model is decomposed into four subdomains in this example, and the array is in an independent subdomain. The domain decomposition model of the aircraft for HO-IE-DDM is shown in Fig. 14. The simulation is performed on Platform II and 96 CPU cores are used in this example. The radiation patterns of the airborne antenna array obtained by HO-IE-DDM and the overall solution by HOMoM (out of core) are shown in Fig. 15. They are in good agreement with each other. The

overall solution can neither be obtained by HOMoM (in core) due to the limited computer memory, nor be obtained by FEKO (MoM) due to the limited computing power of commercial software.

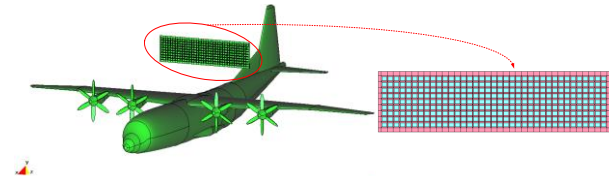


Fig. 12. Model of the four rotor aircraft mounting microstrip antenna array.

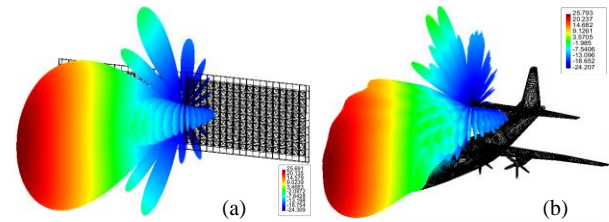


Fig. 13. Microstrip antenna array patterns: (a) array and (b) airborne array.

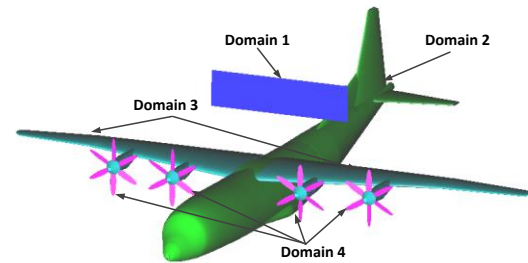


Fig. 14. Domain decomposition model (each color represents a subdomain).

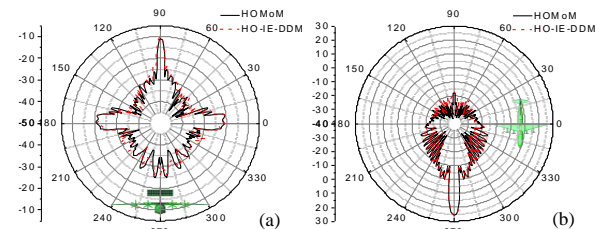


Fig. 15. 2D radiation patterns of the airborne microstrip array: (a) x-y and (b) x-z.

The computational statistics for solving each subdomain and entire problem are recorded in Table 3. It can be observed that the HO-IE-DDM leads to over 80% memory reduction compared with the overall solution for this example. Moreover, the speedup and parallel efficiency of the proposed parallel solver is evaluated

and shown in Fig. 16. The parallelized HO-IE-DDM performs well.

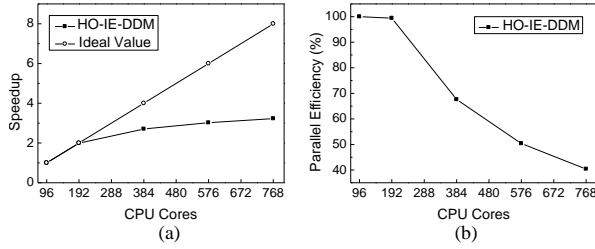


Fig. 16. Parallel performance of parallelized HO-IE-DDM for the airborne microstrip array: (a) speedup ratio and (b) parallel efficiency.

Table 3: Computational statistics of airborne microstrip array

Method	Unknowns	Storage (GB)	Time (min)
HO-IE-DDM	7568 (domain1)	0.85 (domain1)	259.14
	94692 (domain2)	133.61 (domain2)	
	110228 (domain3)	181.05 (domain3)	
	3648 (domain4)	0.20 (domain4)	
HOMoM (out of core)	250216	932.93	288.55

D. Airborne microstrip antenna array JEM characteristics

When airborne array is in an independent subdomain, the accuracy of the proposed method has been proved above. Based on quasi-stationary method, we calculate 360 rotor orientations of the four rotor wings in this example. In order to compare with modulation level, we spread the 3D radiation pattern of the rectangle patch microstrip array installed above a four-rotor aircraft along θ axis and ϕ axis in Fig. 17.

Table 4: Average modulation level (dB)

Receive \ Transmit	Phi Polarized	Theta Polarized	Circularly Polarized
	Yagi-Uda array	52.01	50.73
Microstrip array	21.98	23.09	11.58

Similar to the last two-rotor aircraft case, JEM affects less in this four-rotor aircraft when the receiving antenna is circularly polarized. In Table 4, we can confirm this rule more intuitively from the data in the two cases. Figure 18 shows the changeable intensity of the airborne array radiation pattern at every observation

angles. Compared with Fig. 17 there also is a complementary relationship before and after the modulation. It shows that side-lobes and null depth levels of the airborne array are intensely changed.

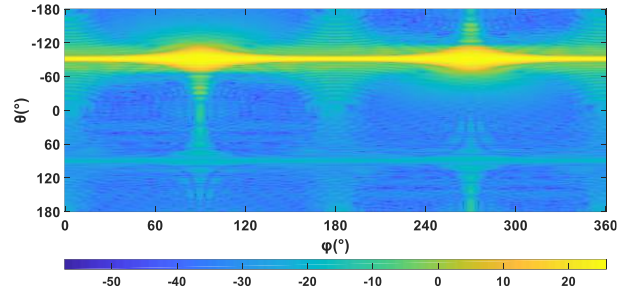


Fig. 17. Spreaded airborne microstrip array pattern.

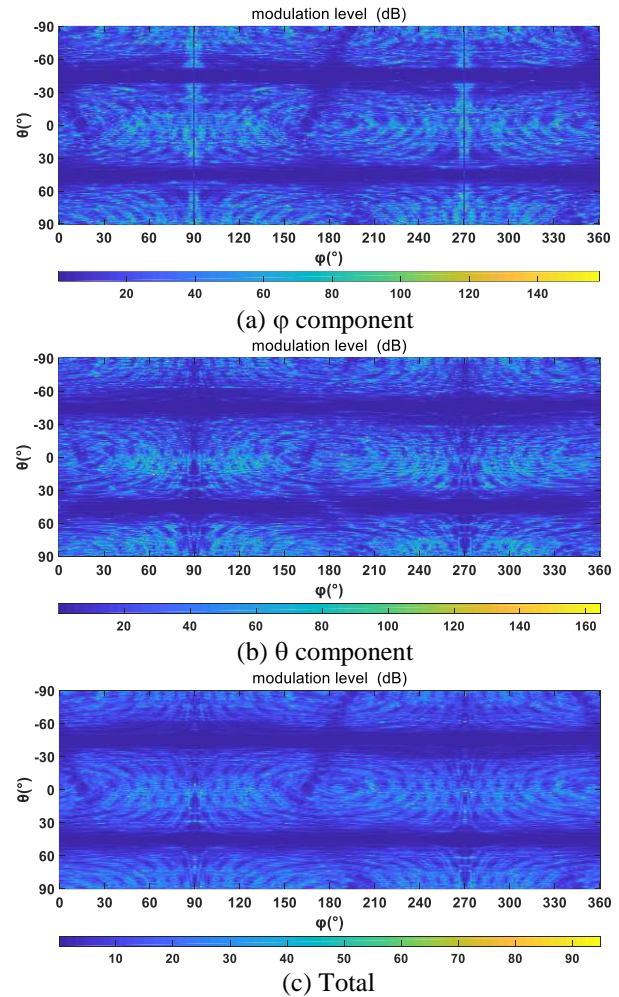


Fig. 18. Spreaded modulation level contour plots.

In Table 5, a comparison of the computational statistics between the HO-IE-DDM and HOMoM is shown. In the solution time, the computing time and the

iteration time for domain 4 is only 3.0 min totally. For the four rotor aircraft airborne antenna, the platform subdomains (domain 2-3) and the array part (domain 1) are unchanged and can be reused during the solution. Thus, the memory requirement and CPU time are greatly reduced. The proposed method is of great significance especially for the problems with changeable parts.

Table 5: Computational statistics of interfered microstrip array

Method	Unknowns	Storage (GB)	Time (min)
HO-IE-DDM	7568 (domain1)	0.85 (domain1)	254.5×1 (domain1-3) 3.0×360 (domain4) 1340.03 (total)
	94692 (domain2)	133.61 (domain2)	
	110228 (domain3)	181.05 (domain3)	
	3648×360 (domain4)	0.20×360 (domain4)	
HOMoM	250216×360	932.93×360	-

IV. CONCLUSION

An efficient HO-IE-DDM algorithm is developed to solve large complex EMC problem, such as airborne array JEM interference problem. The proposed method provides unprecedented flexibility and convenience for the object with changeable parts, since it just needs to re-compute the changed parts of the model during the design process. The modulation level of a double rotor aircraft and a four rotor aircraft loading large antenna array respectively has been successfully obtained. Numerical results verify the feasibility and versatility of this method, and also reveal the radiation characteristics of airborne antennas affected by JEM effects.

ACKNOWLEDGMENT

This work was supported in part by the National Key R&D Program of China under Grant 2017YFB0202102, in part by the China Postdoctoral Science Foundation funded project under Grant 2017M613068, in part by the National Key R&D Program of China under Grant 2016YFE0121600, and in part by the Special Program for Applied Research on Super Computation of the NSFC-Guangdong Joint Fund (the third phase) under Grant No. U150150.

REFERENCES

- [1] V. C. Chen, *The Micro-Doppler Effect in Radar*. USA: Artech House, 2011.
- [2] D. Gaglione, "MACHe-model-based algorithm for classification of helicopters," *IEEE A&E Systems Magazine*, vol. 1, pp. 38-40, 2016.
- [3] A. K. Singh and Y. H. Kim, "Automatic measurement of blade length and rotation rate of drone using W-band micro-Doppler radar," *IEEE Sensors Journal*, vol. 18, pp. 1895-1902, 2018.
- [4] T. Dogaru, K. Gallagher, and C. Le, "Doppler radar phenomenology in small commercial unmanned aerial systems," *U.S. Government Work*, pp. 205-206, 2017.
- [5] J. E. Richie and B. R. Koch, "The use of side-mounted loop antennas on platforms to obtain nearly omnidirectional radiation," *IEEE Trans. Antennas Propag.*, vol. 53, pp. 3915-3919, 2005.
- [6] C. R. Birtcher, C. A. Balanis, and D. Decarlo, "Rotor-blade modulation on antenna amplitude pattern and polarization: Predictions and measurements," *IEEE Trans. EMC*, vol. 41, pp. 384-393, Nov. 1999.
- [7] Y. Zhang, T. K. Sarkar, and X. Zhao, *Higher Order Basis Based Integral Equation Solver (HOBBIES)*. Hoboken, New York: John Wiley, 2012.
- [8] Y. Li, X. Zhao, and H. Zhang, "Out-of-core solver based DDM for solving large airborne array," *Applied Computational Electromagnetics Society*, vol. 31, pp. 509-519, 2016.
- [9] Z. Peng, X. C. Wang, and J. F. Lee, "Integral equation based domain decomposition method for solving electromagnetic wave scattering from non-penetrable objects," *IEEE Trans. Antennas and Propag.*, vol. 59, pp. 3328-3338, 2011.
- [10] W. Li, W. Hong, and H. Zhou, "An IE-ODDM-MLFMA scheme with DILU preconditioner for analysis of electromagnetic scattering from large complex objects," *IEEE Trans. Antennas and Propag.*, vol. 56, pp. 1368-1380, 2008.
- [11] L. Guo, Y. Chen, J. Hu, and R. Zhao, "A novel JMCIE-DDM for analysis of EM scattering and radiation by composite objects," *IEEE Antennas and Wireless Propag. Letters*, vol. 16, pp. 389-392, 2017.
- [12] Y. Zhang and T. K. Sarkar, *Parallel Solution of Integral Equation Based EM Problems in the Frequency Domain*. John Wiley & Sons, Hoboken, NJ, USA, 2009.
- [13] Y. Wang, X. Zhao, Y. Zhang, S. W. Ting, T. K. Sarkar, and C. H. Liang, "Higher order MoM analysis of traveling-wave waveguide antennas with matched waveports," *IEEE Trans. Antennas and Propag.*, vol. 63, pp. 3718-3721, 2015.
- [14] Z. Lin, Y. Chen, and Y. Zhang, "Study of the parallel higher-order MoM on a domestically-made CPU platform," *Journal of Xidian University (Natural Science)*, vol. 3, pp. 43-47, 2015.
- [15] Q. Su, Y. Liu, and X. Zhao, "Parallel integral equation-based nonoverlapping DDM for solving challenging electromagnetic scattering problems of two thousand wavelengths," *International Journal of Antennas and Propagation*, 2019.
- [16] Z. Peng and B. M. Mason, "High-performance surface integral equation solvers towards extreme-scale electromagnetic modeling and simulation,"

Proceedings of the 2016 IEEE/ACES International Conference on Wireless Information Technology and Systems and Applied Computational Electromagnetics, pp. 1-2, 2016.

- [17] SP Ltd, "NATOPS Flight Manual: Navy Model E-2C Plus Aircraft," US Navy: Navair 01-E2AAB-1, 1999.
- [18] V. Pan'ko, Y. Salomatov, and V. Ovechkin, "Software for designing of dipole antenna arrays, multi-frequency matching with wide band antennas," *Proceedings of the IEEE-Russia Conference*, vol. 4, pp. 36-38, 1999.



Yingyu Liu received the B.S. degrees from Xidian University, Xi'an, China, in 2013. Her current research interests include high performance electromagnetic computing based on supercomputer platforms.



Qin Su received the B.S. degree from Xidian University, Xi'an, China, in 2012, and is currently working toward the Ph.D. degree at Xidian University. His current research interests is computational electromagnetic.



Xunwang Zhao received the B.S., and Ph.D. degrees from Xidian University, Xi'an, China, in 2004, and 2008, respectively. He joined Xidian University as a Faculty Member in 2008. As Principal Investigator, he is doing or has completed some projects including project of NSFC.

Direction Finding Using Uniform Circular Array of Horizontal Log-Periodic Dipole Antennas

Xiaofei Ren^{1,2}, Shuai Zhang¹, Hu Li², and Shuxi Gong¹

¹National Key Laboratory of Antennas and Microwave Technology
Xidian University, Xi'an, Shaanxi 710071, China
renxf_1981@163.com

²China Research Institute of Radiowave Propagation
Qingdao Shandong 266107, China

Abstract — Direction finding (DF) using the uniform circular array composed of horizontal log-periodic dipole antennas (UCA-LPDA) is studied in this paper. One advantage of the UCA-LPDA is that it has a reasonable effective radius for broadband DF. Compared with the previous works which usually focused on isotropic antennas, the UCA-LPDA has higher gain and higher angular resolution for the direction of arrival estimation. The spatial response of the UCA-LPDA and the direction of arrival (DOA) estimation algorithms are discussed. The proposed polarized MUSIC (Pol-MUSIC) method can obtain the DOA of signals with any unknown polarizations while no search of the polarizations is required. Based on the theoretical analysis, the actual signal DF experiment which uses a UCA-LPDA with 24 elements was carried out. The DF experiments results demonstrate the effectiveness and accuracy of using UCA-LPDA with Pol-MUSIC method.

Index Terms — Log-periodic dipole antenna, multiple signal classification (MUSIC) algorithm, radio direction finding, uniform circular array.

I. INTRODUCTION

Most of the radio DF systems adopt several identical antennas (including amplitude, phase, polarization, etc.) to form linear array, circular array, or L-shaped array, and so on. Usually vertical monopole or dipole antenna is employed as the element in DF array antennas, and then a single-polarized antenna system can be formed for DF. According to the simple relationship of geometric phase between array elements, the DOA is estimated by means of related interferometer and MUSIC, which have been widely applied in many DF systems [1-3]. The DF algorithms of the circular arrays with directional array elements are considered in [4, 5]. The Cramer-Rao Lower Bound of the DOA estimation by using directional antenna is analyzed in [6]. These studies mainly focus on the radiation pattern of directional antenna and obtaining

good DF results. However, the polarization characteristics of the antenna are rarely discussed.

In order to estimate the DOA for unknown polarization of signals, the polarization-sensitive array is proposed [7-9]. These arrays are often composed of orthogonal dipole antennas, triad antennas and six dimensional electromagnetic vector sensors. These DF systems require at least two channels for each space sampling point, and the system equipment's are large in size and expensive in cost. Heterogeneous array with only one element at each point of the spatial sampling is proposed in [10]. The directions of arrival are estimated for two known polarized waves using active loop antennas with eight different polarized states. Furthermore in [11], the unknown polarized signal DF operated on six art ferrite load dipole with titled forward different direction, which constituted a heterogeneous array. Although, the heterogeneous array needs only one channel in each space sampling point, and it can be used to estimate the direction of arrival for unknown polarized signals. However, the gains of these elements are low, which make them difficult to be applied to high sensitivity DF system.

In order to implement high sensitivity direction-finding for HF wave signals in the range of 0-360 degrees, the direction finding using a novel UCA-LPDA is studied in this paper. 24 horizontal log-periodic dipole antennas (LPDA) are arranged in a circle with certain angle in the XOY plane to form a uniform circular array. The beam of each antenna points to the center of the circle. Because of the relationship between the phase center of the LPDA and the operating frequency [12], the effective radius of the UCA-LPDA is reasonable. The effective radius of the DF array is defined as the horizontal distance between the phase centre of the LPDA and the center of the circle. At lower frequency, the array has a long effective radius, and at high frequency, it has a short effective radius. This ensures a reasonable effective radius for broadband direction

finding using interferometer or MUSIC method [13].

In addition, the UCA-LPDA is a heterogeneous array, in which the elements have different polarized states. For the UCA-LPDA, a polarized MUSIC (Pol-MUSIC) method is proposed for unknown polarized signal while no search of the polarizations is required. Because of the polarization-sensitivity, the UCA-LPDA has lower spatial correlation than isotropic antennas and can obtain a higher angular resolution. The effectiveness and robustness of the DOA estimation for unknown polarized signals using UCA-LPDA are demonstrated by simulation and experiment in this paper.

II. DOA ESTIMATE WITH UCA-LPDA

A. Spatial response of LPDA

Log-periodic dipole antenna (LPDA) is composed of multiple dipoles arranged according to a certain scale factor. Current distributions on the antenna can be obtained by using computer simulations based on the method of moment (MOM). Once the current distributions are determined, it is easy to calculate the radiation vector \mathbf{a} of LPDAs in far area [14]. In spherical coordinate, the general expression is as follows:

$$\mathbf{a} = (|a_\theta|e^{j\delta}\hat{\boldsymbol{\theta}} + |a_\phi|e^{j\zeta}\hat{\boldsymbol{\phi}}), \quad (1)$$

where $|a_\theta|$ and $|a_\phi|$ represent the magnitude of the $\hat{\boldsymbol{\theta}}$ component and the $\hat{\boldsymbol{\phi}}$ component of the electric field, respectively. δ and ζ represent the phase.

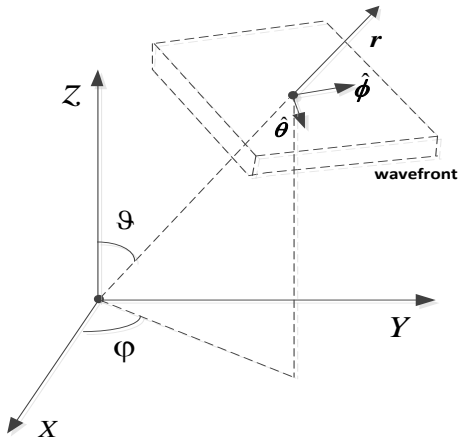


Fig. 1. The unified coordinate system.

Formula (1) can be further rewritten as follows:

$$\mathbf{a} = f(\vartheta, \varphi)e^{j\zeta(\vartheta, \varphi)}(\cos \gamma e^{j\eta}\hat{\boldsymbol{\theta}} + \sin \gamma \hat{\boldsymbol{\phi}}). \quad (2)$$

$$\cos \gamma = \frac{|a_\theta|}{\sqrt{|a_\theta|^2 + |a_\phi|^2}}, \quad \sin \gamma = \frac{|a_\phi|}{\sqrt{|a_\theta|^2 + |a_\phi|^2}}, \quad \eta = \delta - \zeta,$$

$$f(\vartheta, \varphi) = \sqrt{|a_\theta|^2 + |a_\phi|^2}.$$

Where $\gamma \in [0, \pi/2]$ and $\eta \in [-\pi, \pi]$ represent the magnitude

ratio and the phase between the two polarization components [15]. When $\gamma=0^\circ$, represents the vertical polarization, when $\gamma=90^\circ$, represents the horizontal polarization. For a horizontal LPDA, there is only horizontal components $\hat{\boldsymbol{\phi}}$ at pitch angle $\vartheta=90^\circ$; however, there are both the horizontal components $\hat{\boldsymbol{\phi}}$ and vertical components $\hat{\boldsymbol{\theta}}$ at other pitch angles. The definition of the coordinate system is shown in Fig. 1.

Let $\mathbf{U} = (\cos \gamma e^{j\eta}\hat{\boldsymbol{\theta}} + \sin \gamma \hat{\boldsymbol{\phi}})$, then

$$\mathbf{a} = f(\vartheta, \varphi)e^{j\zeta(\vartheta, \varphi)}\mathbf{U}. \quad (3)$$

Formula (3) represents the full spatial response of the LPDA, including amplitude, phase, and polarization. \mathbf{U} represents spatial polarization, which is a function of the angle of space observation (ϑ, φ) .

The LPDA with N elements are arranged into an "inward-looking" circular array with a certain angle in the XOY plane. The schematic diagram is shown in Fig. 2. The main radiation direction of each element is toward the center of the circle. So the array with small size is obtained. Besides, the DOA within the range of 0-360° can also be achieved and the electrical effective radius of the UCA-LPDA can be remained in a wide frequency range because of its phase center movement toward the center of the array.

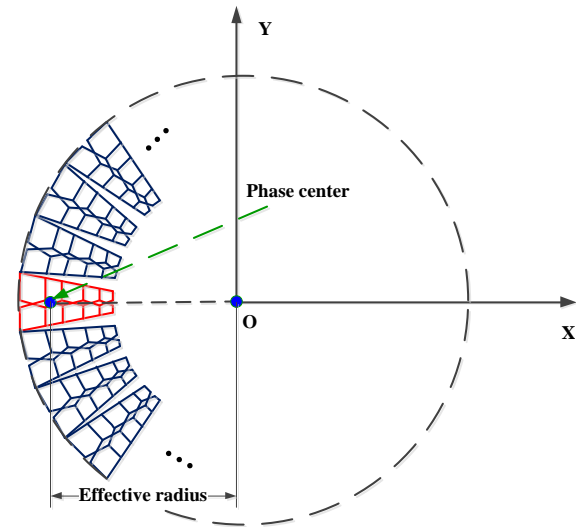


Fig. 2. The schematic diagram of the UCA-LPDA.

The spatial response of the array can be written as follows:

$$\mathbf{a}(\vartheta, \varphi) = [\mathbf{a}_\theta \quad \mathbf{a}_\phi] = \begin{bmatrix} a_1^0(\vartheta, \varphi) & a_1^\phi(\vartheta, \varphi) \\ a_2^0(\vartheta, \varphi) & a_2^\phi(\vartheta, \varphi) \\ \vdots & \vdots \\ a_N^0(\vartheta, \varphi) & a_N^\phi(\vartheta, \varphi) \end{bmatrix} = \begin{bmatrix} f_1(\vartheta, \varphi)e^{j\zeta_1(\vartheta, \varphi)}\mathbf{U}_1 \\ f_2(\vartheta, \varphi)e^{j\zeta_2(\vartheta, \varphi)}\mathbf{U}_2 \\ \vdots \\ f_N(\vartheta, \varphi)e^{j\zeta_N(\vartheta, \varphi)}\mathbf{U}_N \end{bmatrix}. \quad (4)$$

The spatial response of the array includes the amplitude, phase, and polarization, whose dimension is

$N \times 2$. Because the elements point to different orientations, $\mathbf{U}_1 \neq \mathbf{U}_2 \neq \dots \neq \mathbf{U}_N$, the UCA-LPDA is a heterogeneous array.

Considering that the incoming wave of signal is a fully polarized wave, the polarization state is $\hat{\mathbf{u}}$. $\hat{\mathbf{u}} = \hat{\boldsymbol{\theta}} \cos \gamma_0 + \hat{\boldsymbol{\phi}} \sin \gamma_0 e^{j\eta_0}$, $\gamma \in [0, \pi/2]$ and $\eta \in [-\pi, \pi]$ represent the magnitude ratio and the phase between the two polarization components. $\gamma=0^\circ$ represents the vertical polarization while $\gamma=90^\circ$ the horizontal polarization. According to the antenna receiving theory, the amplitude of the i th element receiving the unit field strength is:

$$V_i = \mathbf{a}_i \cdot \hat{\mathbf{u}}^*$$

Where the sign (*) represents conjugate. Then the manifold of the UCA-LPDA is:

$$\mathbf{A}(\vartheta, \varphi, \gamma_0, \eta_0) = \underbrace{\begin{bmatrix} f_1(\vartheta, \varphi) e^{j\zeta_1(\vartheta, \varphi)} \\ f_2(\vartheta, \varphi) e^{j\zeta_2(\vartheta, \varphi)} \\ \vdots \\ f_N(\vartheta, \varphi) e^{j\zeta_N(\vartheta, \varphi)} \end{bmatrix}}_{N \times 1} \odot \underbrace{\begin{bmatrix} \mathbf{U}_1 \\ \mathbf{U}_2 \\ \vdots \\ \mathbf{U}_N \end{bmatrix}}_{N \times 2} \underbrace{\begin{bmatrix} \cos \gamma_0 \\ \sin \gamma_0 e^{-j\eta_0} \end{bmatrix}}_{u^H: 2 \times 1}. \quad (5)$$

Where the sign (\odot) represents the Schur-Hadamard.

From formula (5), it can be seen that the manifold of the UCA-LPDA is relation to the polarization state of the incoming wave because of the different polarization states of the LPDAs.

Now, we consider the spatial correlation coefficient of two incident waves impinging upon the UCA-LPDA. Let the directions of the two incoming waves in space are $\psi_1 = (\vartheta_1, \varphi_1)$ and $\psi_2 = (\vartheta_2, \varphi_2)$, respectively, and the corresponding polarized states are respectively $\mathbf{u}_1, \mathbf{u}_2$ respectively. Then, the spatial correlation coefficient of the two incident waves is:

$$\rho = \frac{[\mathbf{a}(\psi_1) \mathbf{u}_1^H]^H [\mathbf{a}(\psi_2) \mathbf{u}_2^H]}{\|[\mathbf{a}(\psi_1) \mathbf{u}_1]\| \cdot \|[\mathbf{a}(\psi_2) \mathbf{u}_2]\|} \\ = \frac{\sum_{i=1}^N f_i(\psi_1) f_i(\psi_2) e^{j[\zeta_i(\psi_1) - \zeta_i(\psi_2)]} [\mathbf{u}_1 \mathbf{U}_i^H(\psi_1) \mathbf{U}_i(\psi_2) \mathbf{u}_2^H]}{\sqrt{\sum_{i=1}^N |f_i(\psi_1) \mathbf{u}_1 \mathbf{U}_i^H(\psi_1)|^2} \cdot \sqrt{\sum_{i=1}^N |f_i(\psi_2) \mathbf{u}_2 \mathbf{U}_i^H(\psi_2)|^2}}. \quad (6)$$

When the antennas are omni-directional and have same polarized states (such as vertical dipoles), the spatial correlation coefficient is:

$$\rho = \frac{\sum_{i=1}^N e^{j[\varphi_i(\psi_1) - \varphi_i(\psi_2)]}}{N}. \quad (7)$$

Obviously, for UCA-LPDA, the correlation coefficients are related to wave polarized state. Two waves have different polarized states and their spatial angles are close to each other, the correlation coefficient is less than 1 according to Schwartz inequality. However, for the isotropic antenna, its correlation coefficient is approximately equal to 1. The spatial correlation decreases

in the UCA-LPDA, which provides favorable conditions for distinguishing two signals in space. The smaller the spatial correlation coefficient, the more favorable distinguishing signals will be [16].

The spatial response of UCA-LPDA is more complex than the isotropic antenna. Usually it is not an analytical expression. A feasible method is that spatial response of the element in the whole array including mutual coupling is calculated using MOM, or measured accurately. The spatial response obtained is stored into the direction-finding receiver in the term of tables.

B. DOA estimation algorithms

Considering that the UCA is composed of N LPDAs with the same parameters in the XOY plane. Assuming that there are D signals illuminating upon, and the signal is narrow-band, and the noise obeys Gaussian white noise distribution. Then the time domain signal received by the elements can be written as follows:

$$\mathbf{X} = \mathbf{A} \mathbf{S}(\mathbf{t}) + \mathbf{N}(\mathbf{t}), \quad (8)$$

where $\mathbf{N}(\mathbf{t})$ is Gaussian white noise. $\mathbf{A} = [\mathbf{a}(\psi_1) \mathbf{u}_1^H, \mathbf{a}(\psi_2) \mathbf{u}_2^H, \dots, \mathbf{a}(\psi_D) \mathbf{u}_D^H]$ is the manifold [17]. $\mathbf{S} = [s_1(\mathbf{t}), s_2(\mathbf{t}), \dots, s_D(\mathbf{t})]^T \cdot \psi_1, \psi_2, \dots, \psi_D$ are the directions of the D signals, respectively, which including the two dimension direction (ϑ, φ) . $\mathbf{u}_1, \mathbf{u}_2 \dots \mathbf{u}_D$ are the polarization of the D signals.

Then the covariance matrix of the receiving data is:

$$\mathbf{R}_{xx} = \mathbf{A} \mathbf{R}_s \mathbf{A}^H + \sigma^2 \mathbf{I}, \quad (9)$$

\mathbf{R}_s is the covariance matrix of the signals. When the signals are uncorrelated, \mathbf{R}_s is a diagonal matrix. σ^2 is the power of the noise.

According to the MUSIC subspace method [18], the span of the eigenvectors corresponding to the $N-D$ small eigenvalues of \mathbf{R}_{xx} is the noise subspace \mathbf{E}_{KC} , and the span of the eigenvectors corresponding to the D large eigenvalues of \mathbf{R}_{xx} is the signal subspace.

Using the orthogonal principle of signal subspace and noise subspace, the entire signal subspace including polarized space is projected into the noise subspace. In the true direction of the signal, the following equation holds on:

$$\mathbf{u} \mathbf{a}^H \mathbf{E}_{KC} = 0. \quad (10)$$

Further,

$$\mathbf{u} \mathbf{a}^H \mathbf{E}_{KC} \mathbf{E}_{KC}^H \mathbf{a} \mathbf{u}^H = 0. \quad (11)$$

If DOA estimation is carried out directly using above equation, it is necessary to conduct a four-dimensional traversal searching in the whole polarization domain and spatial domain. In fact, this process can be simplified. For heterogeneous array, \mathbf{a} is a full rank matrix with dimension of $N \times 2$. Whatever the true polarization of the

signal is, making (11) holds on in the true direction of the signal, the matrix $\mathbf{a}^H \mathbf{E}_{KC} \mathbf{E}_{KC}^H \mathbf{a}$ whose dimension is 2×2 must be rank deficient. Namely,

$$\det\{\mathbf{a}^H \mathbf{E}_{KC} \mathbf{E}_{KC}^H \mathbf{a}\} = 0. \quad (12)$$

Operator symbol $\det\{\bullet\}$ represents the determinant of matrix.

Therefore, the spatial spectral function of the polarized MUSIC (Pol-MUSIC) can be constructed as below:

$$P(\vartheta, \varphi) = \frac{1}{\det\{\mathbf{a}^H(\vartheta, \varphi) \mathbf{E}_{KC} \mathbf{E}_{KC}^H \mathbf{a}(\vartheta, \varphi)\}}. \quad (13)$$

The DOA is obtained from the angle corresponding to the maximum spectral peak. Thus, the searching in polarization space can be avoided, and $\mathbf{a}(\vartheta, \varphi)$ is given by formula (4), which is the spatial response of the LPDA. The proposed method does not need to know the polarization state of incoming wave beforehand.

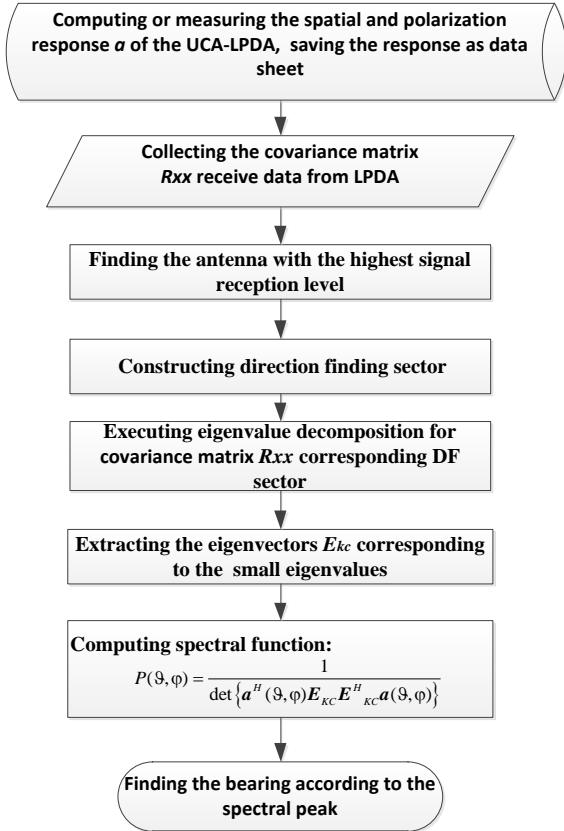


Fig. 3. Algorithm flow chart.

In (13), $\mathbf{a}(\vartheta, \varphi)$ is a vector composed of spatial response of LPDAs in the unified coordinate system. The spatial response contains $\hat{\theta}$ component and the $\hat{\phi}$

component. It can be obtained by electromagnetic calculation. Because of the directional pattern of the LPDA, spatial response should be normalized. $\mathbf{a}(\vartheta, \varphi)$ is replaced by $\mathbf{a}(\vartheta, \varphi) / \|\mathbf{a}(\vartheta, \varphi)\|_2$.

If ignoring the polarization in the spatial response of the LPDA, only consider the amplitude and phase, then,

$$\mathbf{a}_\phi(\vartheta, \varphi) = f(\vartheta, \varphi) e^{i\zeta(\vartheta, \varphi)}.$$

The spatial spectral function is:

$$P(\vartheta, \varphi) = \frac{1}{\mathbf{a}_\phi^H(\vartheta, \varphi) \mathbf{E}_{KC} \mathbf{E}_{KC}^H \mathbf{a}_\phi(\vartheta, \varphi)}. \quad (14)$$

This is the traditional MUSIC method. In fact, only when the polarization of the incoming wave signal is horizontal polarization or all elements in the array are same, $\mathbf{U}_1 = \mathbf{U}_2 = \dots \mathbf{U}_N$ (homogeneous array), formula (14) holds on. Direction of arrival estimation for unknown polarization signal using UCA-LPDA, the polarization states of the antennas must be included in the manifold.

Because the phase center of LPDA only exists in main beam [19]. When DF array employs UCA-LPDA, not all LPDAs can be used. There is a DF sector in the array. The DF sector employs a LPDA with highest signal reception level.

The proposed Pol-MUSIC applying to UCA-LPDA algorithm flow chart is shown in Fig. 3.

III. SIMULATION AND EXPERIMENTAL RESULTS

In order to illustrate the previous method, three simulation examples using UCA-LPDA are conducted for HF direction finding. The circular array is composed of 24 horizontal elements with an interval of 15 degrees which are disposed in XOY plane. The total number of the dipoles is 40 in each LPDA. The diameter of the UCA-LPDA is 340 meters. Because HF antenna is affected by the ground, the LPDA needs to have an angle of inclination to ensure that the electric height of the antenna above the ground doesn't change drastically in a wide frequency band. The projected length of the LPDA is 136.9m. The model of the UCA-LPDA is shown in Fig. 4. The parameters of the LPDA is shown in Table 1.

Table 1: The parameters of the LPDA

Parameter	Value	Parameter	Value
N	40	l_1	44.9m
τ	0.92	l_{40}	2.9m
σ	0.077	H1	41m
Projected length	136.9m	H2	15m

N : the total number of the dipoles in LPDA. τ is the scale factor and the σ is spacing factor. l_1 is the length of the longest dipole and l_{40} is the length of shortest dipole.

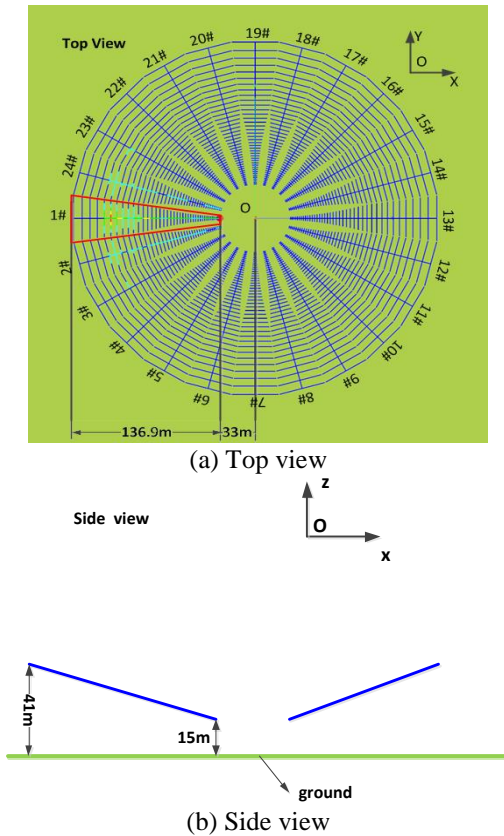


Fig. 4. The model of UCA-LPDA.

The spatial responses of the LPDA are calculated by FEKO. In order to take account of the mutual coupling between the antennas, the simulated element is excited while other elements are connected to standard loads.

In the first example, only one incident signal is received by the UCA-LPDA. The azimuth angle of the signal is 153° and elevation angle is 30° . The polarization parameter γ changes continuously from 0° to 90° with a step of 2° and η is -120° . In the simulation process, it is assumed that the noise power of each element is the same and independently distributed. The max signal-to-noise ratio (SNR) is set to be 20dB and the noise bandwidth is set to be 3 KHz. The frequency of signal is 6MHz. The total number of samples is 1024. We conduct 300 times Monte-Carlo simulations to estimate the azimuth and the pitch. Figure 5 shows the estimation results of Pol-MUSIC method using formula (13) compared with the general MUSIC method ignoring the polarization of the LPDA using formula (14).

The DF results show that the Pol-MUSIC can obtain accurate result whatever the incoming polarization varies. The proposed Pol-MUSIC method is effective. The accuracy of estimation is less than 1 degree. However the general MUSIC estimates wrong result, especially when polarization of incoming wave is close to vertical polarization. If only the polarization state of the signal

is close horizontal polarization, the general MUSIC method can obtain accurate result. This is because the general MUSIC method does not take into account the wave polarization effect. And the UCA-LPDA is a heterogeneous array, which is a polarization-sensitive array. Because of the ionosphere, the polarization state of incoming wave is often elliptical polarization. So the polarization of the DF antenna should be contained in the DF processing. The Pol-MUSIC method should be employed.

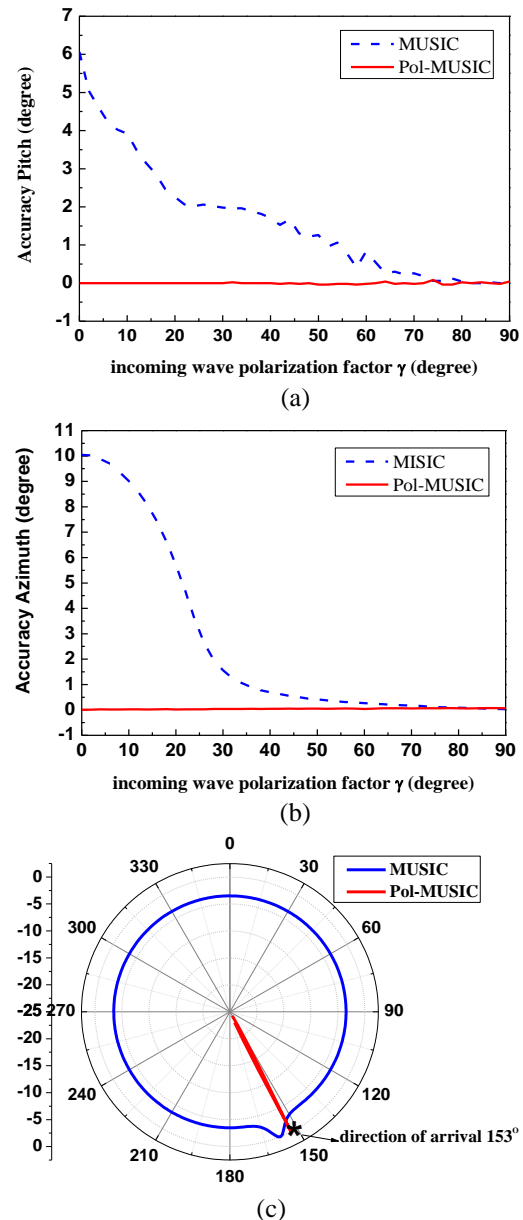


Fig. 5. The DF precision varies with the polarization using UCA-LPDA. SNR=20dB, in the noise bandwidth of 3 kHz, 1024 samples. Operating frequency is 6MHz. (a) Pitch estimation, (b) azimuth estimation, and (c) the beam tracking of direction finding, $\gamma=30^\circ$.

In the second example, the DF precision of full HF band is simulated. Incoming wave polarization state is elliptical polarization, $\gamma=30^\circ$, and $\eta=-120^\circ$. Figure 6 shows the DF precision of general MUSIC method and Pol-MUSIC method with 20dB of SNR. It is obvious that Pol-MUSIC method is superior to general MUSIC method in the full frequency band.

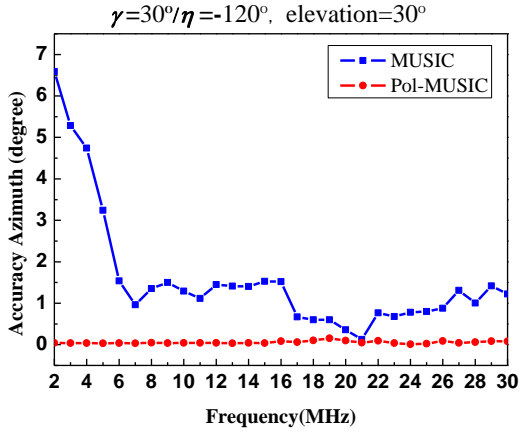


Fig. 6. DF precision varies with operation frequency in all HF frequency band. SNR=20dB.

Figure 7 shows the DF precision with different SNR in all HF bands. With the improvement of signal-to-noise ratio, the direction finding accuracy is improved. Figure 8 shows the variation curve of the estimation accuracy of Pol-MUSIC method with the SNR at 6MHz. The estimation results are close to the CRLB.

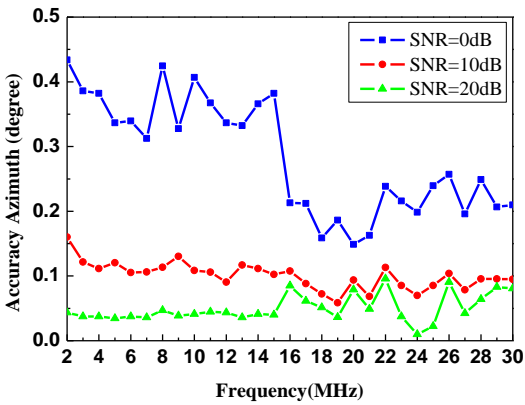


Fig. 7. The DF precision varies with operation frequency with different SNR.

In the third example, the angle resolution of two non-correlated signals with a small angular were simulated using uniform circular array composed of LPDAs, isotropic antennas, and orthogonal dipole antennas. The two signals are different polarization state. To make a

fair comparison, the electrical effective radiuses of the three arrays are same as 1.25λ . Because the equivalent diameter of the UCA-LPDA varies with operating frequency, we choose the operating frequency at 6MHz. Its effective radius (the distance from phase center to the center of the circle) is 62.5m (1.25λ). The effective radius of the LPDA is as show in Fig. 9.

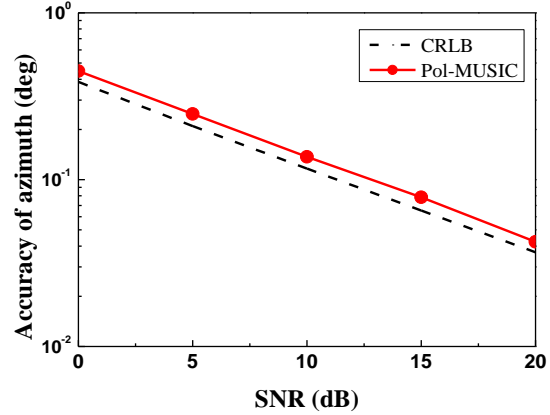


Fig. 8. Precision of DOA estimation of Pol-MUSIC.

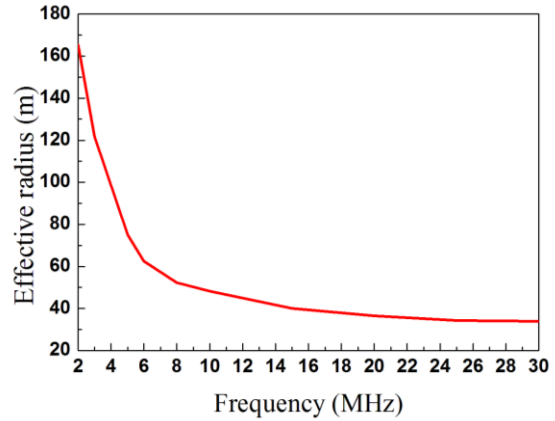


Fig. 9. The effective radius of the LPDA.

The parameters of the two simulation signals are presented in Table 2. The SNR is of 10dB. The orthogonal dipole antennas are composed of X antenna and Y antenna. The orientations of all elements in the array are parallel to the X-axis and Y-axis. The uniform circular arrays composed of isotropic antennas and orthogonal dipole antennas are indicated in Fig. 10.

Table 2: The simulation parameters of two signals

Parameters	Signal 1	Signal 2
Elevation	30°	36°
Azimuth	153°	157°
Polarization	$\gamma=30^\circ, \eta=120^\circ$	$\gamma=60^\circ, \eta=-60^\circ$

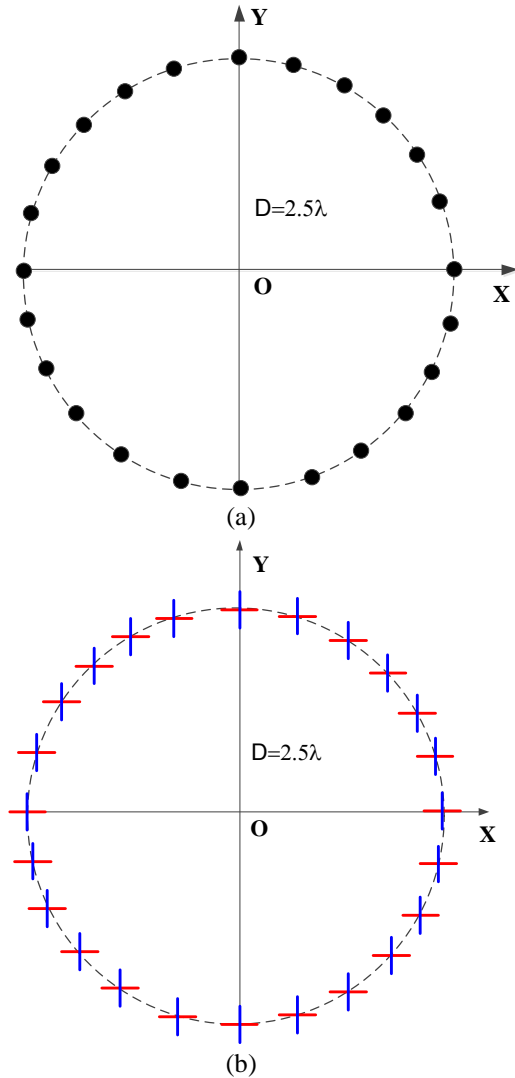


Fig. 10. (a) 24-element isotropic antennas UCA. (b) 24-element orthogonal antennas.

Figure 11 displays the MUSIC spectrums of the three arrays. The UCA-LPDA can accurately distinguish the angles of two signals with a small angular separation in the space, but the isotropic antennas cannot. DF results have higher angular resolution while using UCA-LPDA than isotropic antenna. The spatial correlation of UCA-LPDA is decreased with the use of polarization information of two signals. This feature is good for distinguishing signals from two approaching angles. However, the isotropic antennas have no polarization information, the spatial correlation is close to 1 (see formula (7)). So the isotropic array cannot distinguish signals from two approaching angles. Because of polarization sensitivity, the orthogonal dipoles can also distinguish two different polarized signals. However, the numbers of the required DF channels of the orthogonal dipole antennas are doubled, and its gain is lower than LPDA.

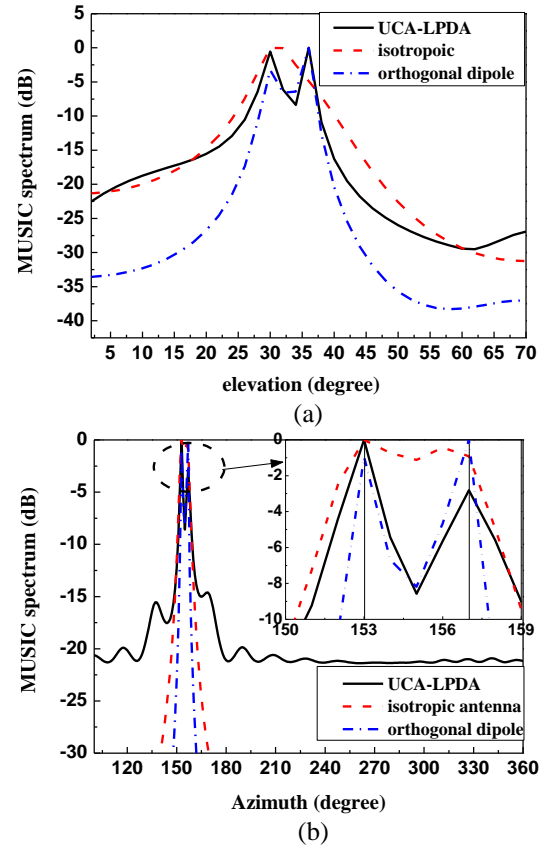


Fig. 11. Comparison of spatial spectrums for the three uniform circular array: LPDAs, isotropic antennas, and orthogonal dipole. SNR=10dB, in the noise bandwidth of 3 kHz, 1024 samples. (a) MUSIC spectrum of elevation, and (b) MUSIC spectrum of azimuth.

On the basis of simulations, one UCA-LPDA was fabricated for DF experiments. The array consists of 24 elements, with an angle of 15° . The parameters of the fabricated UCA-LPDA are the same as the simulated ones. The UCA-LPDA is connected to a 24 channel direction-finding receiver through the exchange matrix. The UCA-LPDA is shown as Fig. 12.



Fig. 12. The UCA-LPDA for direction finding.

The magnitude and phase spatial response of the element in the array are measured at 10° of elevation. The test results show a good agreement between the measured and simulated, as shown in Fig. 13. Because of the good agreement, the spatial response of full space adopts the theoretical calculation value in FEKO and saved into the DF receiver.

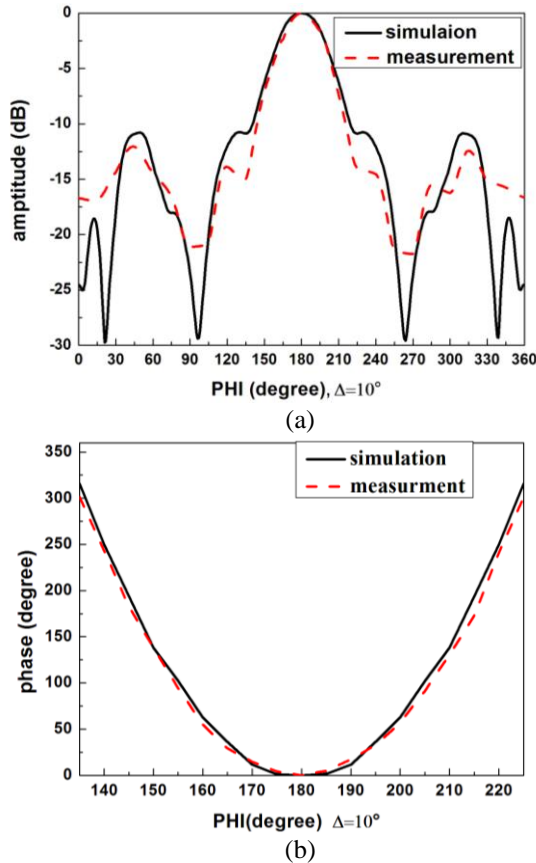
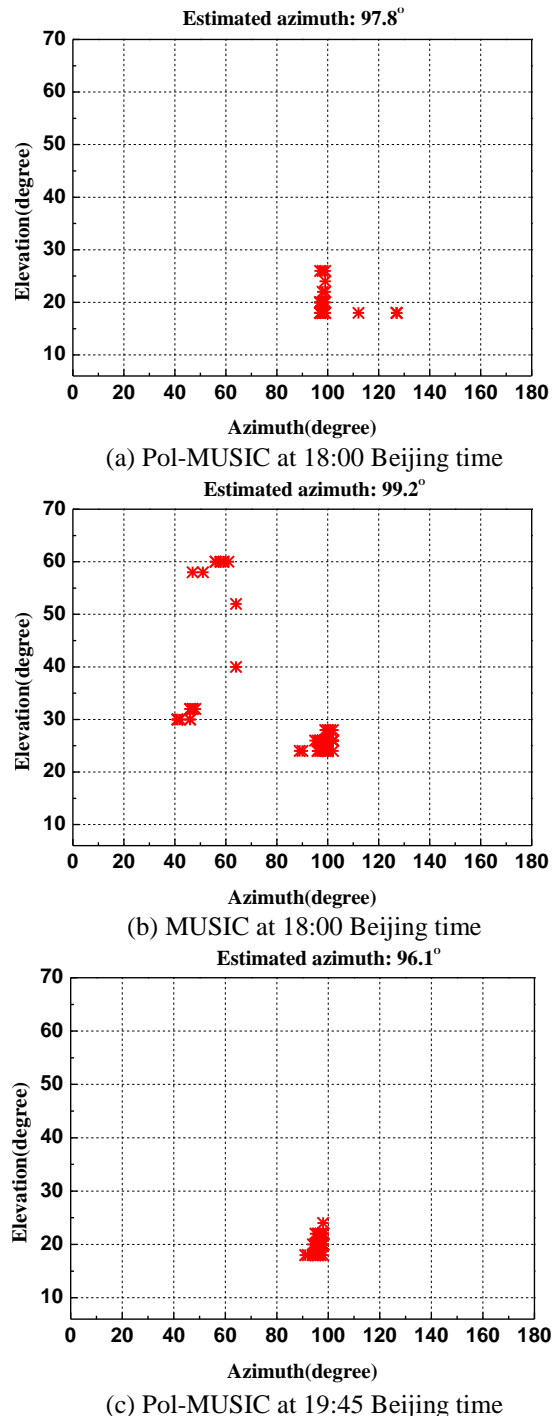


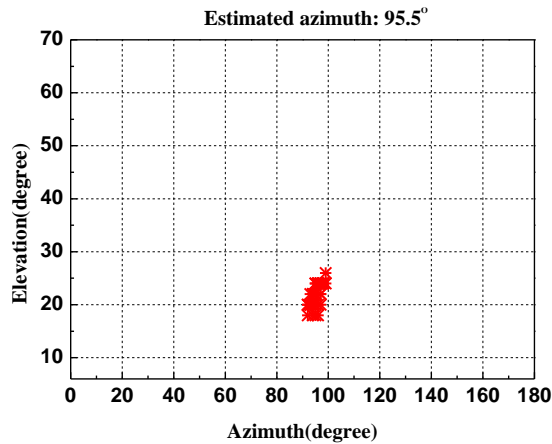
Fig. 13. Spatial response measured of the LPDA in the circular array at 6MHz: (a) the magnitude response, and (b) the phase response.

The DOA was estimated by 1024 sampling data of HF signal at 6.03MHz in 24 July, 2017. Due to the influence of the instrumental errors and actual non-ideal channel of the propagation, the DOA was estimated 100 times. The final direction finding result is given by the statistical median. The actual signal was at the azimuth of 96° with unknown polarization state. For HF signals, because of the Faraday rotational properties, after ionosphere reflection, the polarization characteristic of received signals is usually elliptical polarization. However, its polarization parameters are unknown [20].

The DF experiments are conducted at 18:00 and 19:45 Beijing time, respectively. We estimate the DOA of actual HF signal using Pol-MUSIC method and general MUSIC method. Figure 14 illustrates the DF

results of the signal. We can obviously see that the DOAs estimated are drifting at 18:00 from Fig. 14. This is caused by the ionosphere. When Pol-MUSIC method is used, the DF result is robust. This is because the Pol-MUSIC method takes into account the polarization characteristics of the signal. The direction of incoming wave is easier to identify and capture. DF experiments demonstrate the effectiveness and robustness using UCA-LPDA with Pol-MUSIC method.





(d) MUSIC at 19:45 Beijing time

Fig. 14. DF result using LPDA-UCA at 6030KHz in 24 July, 2017: (a) DF with Pol-MUSIC method at 18:00, (b) DF with MUSIC method at 18:00, (c) DF with Pol-MUSIC method at 19:45, and (d) DF with MUSIC method at 19:45

IV. CONCLUSION

In conclusion, a circular array composed of log-periodic dipole antennas is studied in this paper. The UCA-LPDA has higher gain and polarization-sensitivity though it employs to only one sensor at each point of the spatial sampling. For the UCA-LPDA, a new Pol-MUSIC method for unknown polarizations is derived. The proposed method does not need to search the polarization state of incoming wave. Using the polarization of the antennas, UCA-LPDA has a higher angular resolution for the DOA estimating than isotropic antennas. Simulations and actual signals DF experiments demonstrate the effectiveness and accuracy of using UCA-LPDA with Pol-MUSIC method. Because of the high gain, the UCA-LPDA can be used to estimate DOA for weak unknown polarized signals in the practical application.

ACKNOWLEDGMENTS

This work was supported by National Natural Science Foundation of China (no. 61601350), China Postdoctoral Science Foundation (no. 2015M580813), Natural Science Basic Research Plan in Shaanxi Province of China (no. 2015JQ6217), the Fundamental Research Funds for the Central Universities of China under Grant JB170208, and the China Research Institute of Radiowave Propagation. The authors would like to thank Dr. Cui and Associate Prof. Yanwen Wang with the 54th Institute of the CETC for useful discussions and DF measurement data.

REFERENCES

- [1] J.-H. Lee and J.-M. Woo, "Interferometer direction-finding system with improved DF accuracy using

two different array configurations," *IEEE Antennas and Wireless Propagation Letters*, vol. 14, pp. 719-722, 2015.

- [2] M. Wang, X. Ma, S. Yan, and C. Hao, "An auto-calibration algorithm for uniform circular array with unknown mutual coupling," *IEEE Antennas and Wireless Propagation Letters*, vol. 15, pp. 12-15, 2016.
- [3] S. Searle, "Disambiguation of interferometric DOA estimates in vehicular passive radar," *Iet Radar Sonar & Navigation*, vol. 12, pp. 64-73, 2018.
- [4] C. Chang, T. Cheng, and H. Lin, "Fast direction finding algorithm for circular array based on directional antenna," in *The 2012 International Workshop on Microwave and Millimeter Wave Circuits and System Technology*, pp. 1-4, 2012.
- [5] M. Pesavento and J. F. Bohme, "Direction of arrival estimation in uniform circular arrays composed of directional elements," in *Sensor Array and Multi-channel Signal Processing Workshop Proceedings, 2002*, pp. 503-507, 2002.
- [6] B. R. Jackson, S. Rajan, B. J. Liao, and S. Wang, "Direction of arrival estimation using directive antennas in uniform circular arrays," *IEEE Transactions on Antennas and Propagation*, vol. 63, pp. 736-747, 2015.
- [7] M. Yang, D. Jin, B. Chen, and Y. Xin, "A multiscale sparse array of spatially-spread electromagnetic-vector-sensors for direction finding and polarization estimation," *IEEE Access*, vol. 6, pp. 9807-9818, 2018.
- [8] J. He, Z. Zhang, T. Shu, and W. Yu, "Direction finding of multiple partially polarized signals with a nested cross-dipole array," *IEEE Antennas and Wireless Propagation Letters*, vol. 16, pp. 1679-1682, 2017.
- [9] K. T. Wong, Y. Song, C. J. Fulton, S. Khan, and W.-Y. Tam, "Electrically "long" dipoles in a collocated/orthogonal triad—For direction finding and polarization estimation," *IEEE Transactions on Antennas and Propagation*, vol. 65, pp. 6057-6067, 2017.
- [10] Y. Erhel, D. Lemur, L. Bertel, and F. Marie, "HF radio direction finding operating on a heterogeneous array: Principles and experimental validation," *Radio Science*, vol. 39, pp. 1-14, 2004.
- [11] R. Mueller, S. Lutz, and R. Lorch, "A novel circular direction finding antenna array for unknown polarizations," in *Eur.Conf. Antennas Propag. (EuCAP)*, Gothenburg, Sweden, pp. 1514-1518, 2013.
- [12] C. Bares, C. Brousseau, L. L. Coq, and A. Bourdillon, "Effect of antenna phase centre displacement on FM-CW measurements: Application to radar system," *Electronics Letters*, vol. 39, pp. 867-868, 2003.

- [13] E. Kornaros, S. Kabiri, and F. De Flaviis, "A novel model for direction finding and phase center with practical considerations," *IEEE Transactions on Antennas and Propagation*, vol. 65, pp. 5475-5491, 2017.
- [14] L. T and L. S. W, *Antenna Handbook*. New York: Chapman & Hall, 1993.
- [15] A. J. Weiss and B. Friedlander, "Analysis of a signal estimation algorithm for diversely polarized arrays," *IEEE Transactions on Signal Processing*, vol. 41, pp. 2628-2638, 1993.
- [16] R. O. Schmidt, "A *Signal Subspace Approach to Multiple Emitter Location Spectral Estimation*," Ph.D., Stanford University, CA, USA, 1981.
- [17] B. Friedlander, "Antenna array manifolds for high-resolution direction finding," *IEEE Transactions on Signal Processing*, vol. 66, pp. 923-932, 2018.
- [18] R. Schmidt, "Multiple emitter location and signal parameter estimation," *IEEE Transactions on Antennas and Propagation*, vol. 34, pp. 276-280, 1986.
- [19] Y. Jin, X. Ren, H. Ji, and S. He, "Variable phase center of log-periodic dipole antenna in full space," *Chinese Journal of Radio Science*, vol. 22, pp. 229-233, 2007.
- [20] F. Arikian, N. Yilmaz, O. Arikian, and M. K. B. H. Miled, "Mode separation and direction of arrival estimation in HF links," *Radio Science*, vol. 38, pp. 7-1-7-14, 2003.



Xiaofei Ren was born in Shaanxi, China, in 1981. He received M.S. degree from the China Research Institution of Radiowave Propagation (CRIRP) in 2006. He is currently working towards the Ph.D. degree at Xidian University, China. From 2006 to 2013, He worked in CRIRP engaged in the research and development of antenna theory and technology. His research interests include HF antenna, direction-finding techniques and reconfigurable antenna.



Shuai Zhang was born in Hubei province, China. He received the B.S. and doctorate degrees in Electromagnetic Field and Microwave Technique from Xidian University, Xi'an, in 2007 and 2012, respectively. He is currently working as Lecturer at National Key Laboratory of Antennas and Microwave Technology, Xidian University. His current research interests include antenna design, analysis, calculation and control techniques of the radiation and scattering characteristics of array antennas, and optimization methods in electromagnetics.

On the Approximate Calculation of Half-Power Beam Width for Uniform Circular Arrays

Hua Tang*, Xianzheng Zong*, and Zaiping Nie

School of Electronic Science and Engineering
University of Electronic Science and Technology of China (UESTC), Chengdu, Sichuan 610054, P.R.C.
tungh@foxmail.com

Abstract — In this paper, the approximate calculations of the half-power beam width (HPBW) of a uniform circular array (UCA) in azimuth and elevation are investigated by numerical calculations and data analysis methodology. Two corresponding formulas are proposed to approximately estimate the HPBW of UCA in azimuth and elevation under different pointing directions of the main lobe. The proposed formulas' validities are examined by comparing the results with the ones directly calculated from the array factor. Besides, the accuracies of the proposed approximate formulas are evaluated in both absolute error and error rate. The calculation speed is assessed in time as well. Numerical simulation results are provided to show the proposed formulas' performances.

Index Terms — Approximate calculation, estimation formulas, half-power beam width (HPBW), uniform circular array (UCA).

I. INTRODUCTION

Uniform circular arrays (UCAs), also known as uniform ring array, have some special characteristics compared with uniform linear arrays (ULAs) and uniform planar arrays (URAs). It can be known from the antenna theory that UCAs can provide a 2-dimension (2D) angular scan, namely angular scan in azimuth and elevation. Moreover, UCAs can scan in azimuth plane from 0° to 360° almost without distortion for the radiation pattern, since the mutual coupling effect is the same for each element. The applications of UCAs hence can be found in many fields, such as source localization [1], the direction of arrival (DoA) estimation [2], wireless communications [3], smart antennas [4], and so on.

Lots of studies have been reported on UCAs. The authors in [5] investigate the DoA estimation via moving a UCA in predefined path under multipath environments. 2D DoA estimations are studied for UCAs [6-8]. The phase-mode-decomposition-based and optimization-based methods are investigated to suppress the side lobe of UCA [9]. The effect of mutual coupling is studied for UCA from the electromagnetic aspect [10]. Only a few of researches pay attention to the fast calculation of

UCA's HPBW which is very complicated to compute from the definition. Though the calculation of HPBW for UCA is investigated in [11], it is only available for the main lobe pointing at the azimuth plane and still very complicated. A simple formula with only two parameters, wavelength and array radius, is proposed to estimate the HPBW of UCA roughly [12, 13], yet it is only applicable under the zenith angle of main beam being 90° .

It is necessary to figure out an easy and quick solution on calculating the HPBW of UCA, because fast HPBW estimation is an important and meaningful job in the pre-design of UCA. For example, before designing an UCA for 2D DoA estimation application, the HPBW of the UCA's main lobe needs a quick and rough evaluation. Estimating the HPBW of UCA is an energy-consuming and time-consuming task due to no formula with a simple form like that of the one for ULA [14].

Accordingly, the study of this paper focuses on finding out a simple method to estimate the HPBW for UCA. Based on numerical computation and data analysis, a formula is proposed to approximately calculate the azimuth HPBW for UCA under different zenith angles of the main lobe. Compared to the formula in [12, 13] which only can calculate the azimuth HPBW under the zenith angle of 90° , the proposed formula is more applicable. Considering the situation that the two main beams, which are symmetric about the azimuth plane (xy -plane in Fig. 1), of the UCA can be identified definitely, a formula with simple form is also proposed to estimate the elevation HPBW roughly. The proposed formulas not only can estimate the HPBW of UCA correctly, but also achieve the good calculation accuracy, especially for azimuth HPBW. More importantly, the proposed formulas far surpass the definition method in calculation speed.

The remainder of this paper is organized as follows. Section II describes the general geometry of UCA. The approximate estimations of HPBWs in azimuth and elevation are investigated in Section III where two corresponding estimation formulas are also proposed. The proposed formulas' performances in validity,

accuracy and speed are studied via numerical simulations in Section IV. Finally, conclusions are drawn in Section V.

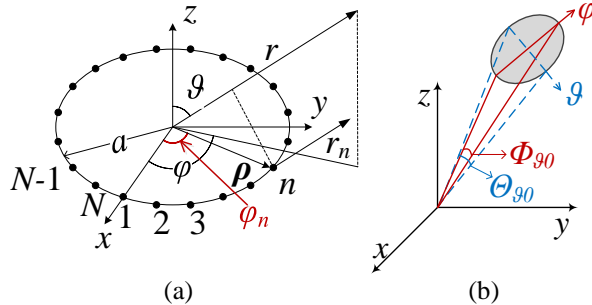


Fig. 1. (a) Configuration of UCA with N -element, and (b) definition of HPBW in azimuth and elevation.

II. GEOMETRY OF UCA

A configuration of UCA with N elements located in xy -plane is illustrated in Fig. 1 (a) [15]. The array radius is a , and the n th element is located at the phase angle of φ_n where $n=1, 2, \dots, N$. Each element has an associated weight I_n and phase α_n , meaning the amplitude and phase of excitation current. The array factor (AF) can be written as [14, 15]:

$$AF(\varphi, \vartheta) = \sum_{n=1}^N I_n e^{j(ka \sin(\vartheta) \cos(\varphi - \varphi_n) + \alpha_n)}, \quad (1)$$

$$\alpha_n = -ka \sin(\vartheta_0) \cos(\varphi_0 - \varphi_n),$$

where k , φ , ϑ are the wavenumber, azimuth angle, zenith angle, respectively, φ_n is the angular location in azimuth plane and given by:

$$\varphi_n = 2\pi \frac{n-1}{N}. \quad (2)$$

The element spacing of the UCA can be obtained as:

$$d = \frac{2\pi}{N} a. \quad (3)$$

Letting $d = \lambda/2$ and substituting it into (3), we have:

$$\frac{a}{\lambda} = \frac{N}{4\pi}. \quad (4)$$

The left term of (4) is usually named electrical length. Equation (4) reveals the proportional relationship between the electrical length of array radius and the number of array elements.

III. ANALYSIS OF THE APPROXIMATE CALCULATION OF HPBW

In order to define the HPBW for UCA clearly, the HPBWs in azimuth and elevation, Φ_{ϑ_0} and θ_{ϑ_0} , are used to describe the HPBW of UCA under the zenith angle of ϑ_0 , illustrated in Fig. 1 (b). Letting $\varphi = \varphi_0$ and $\vartheta = \vartheta_0$ in the AF in (1), we have:

$$AF(\varphi) = \sum_{n=1}^N I_n e^{j(ka \sin(\vartheta_0) \cos(\varphi - \varphi_n) + \alpha_n)}, \quad (5)$$

$$\alpha_n = -ka \sin(\vartheta_0) \cos(\varphi_0 - \varphi_n),$$

and

$$AF(\vartheta) = \sum_{n=1}^N I_n e^{j(ka \sin(\vartheta) \cos(\varphi_0 - \varphi_n) + \alpha_n)}, \quad (6)$$

$$\alpha_n = -ka \sin(\vartheta_0) \cos(\varphi_0 - \varphi_n).$$

In order to attain the common results, we assume

that the isotropic radiators are employed as the elements of the UCA in this paper. Considering a UCA model with uniform excitation amplitude, I_n in (5) and (6) can be set to 1, and the HPBWs in azimuth and elevation can be directly computed via (5) and (6) respectively at the half-power points. Although computing the HPBWs from (5) and (6) is the most accurate approach, it is obviously a tough job.

The azimuth HPBW of UCA under $d = \lambda/2$ can be approximately calculated by [12, 13]:

$$\Phi \approx 21^\circ \cdot \frac{\lambda}{a}. \quad (7)$$

However, (7) only can be used to calculate the azimuth HPBW under $\vartheta = 90^\circ$, namely (7) is not available under $\vartheta \neq 90^\circ$. It is also demonstrated in Table 1.

Table 1: Azimuth HPBW under different ϑ_0

ϑ_0 (deg.)	Φ_{ϑ_0} (deg.)	$\Phi_{\vartheta_0}/\Phi_{90}$
10	49.948	5.803
20	25.210	2.929
30	17.226	2.001
40	13.394	1.556
50	11.237	1.306
60	9.939	1.155
70	9.160	1.064
80	8.740	1.015
90	8.607	1.000

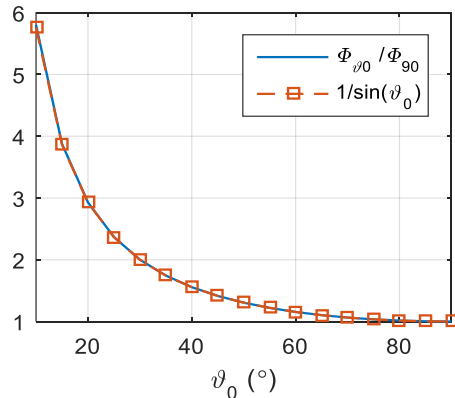


Fig. 2. Trend of Φ_{ϑ_0} normalized by Φ_{90} .

According to (5), we can find that both components of the main lobe direction, azimuth angle and zenith angle, are contained in the AF besides the electrical length of array radius. It implies that the azimuth HPBW should be affected by the direction of the main lobe. According to the knowledge of array antenna, it is known that the azimuth HPBW remains unchanging with the azimuth angle of the main lobe. It suggests that the azimuth HPBW must have a relationship with the zenith angle. Based on (5), it is easy and reasonable to deduce that Φ_{ϑ_0} has a relationship with the sine or cosine of the

zenith angle. To further investigate the relationship, the azimuth HPBWs of UCA are directly calculated from (5) under different values of ϑ_0 , and recorded in Table 1.

In Table 1, the zenith angles and the corresponding azimuth HPBWs, namely ϑ_0 and Φ_{ϑ_0} , are depicted on the first and second columns in degree respectively, and the ratios of the azimuth HPBWs corresponding to different ϑ_0 to azimuth HPBW under $\vartheta_0 = 90^\circ$, i.e., Φ_{90} , are presented on the third column. The data on the second and third columns indicate that the azimuth HPBW decreases with the increasing of ϑ_0 until $\vartheta_0 = 90^\circ$. In addition, the results of $\Phi_{\vartheta_0}/\Phi_{90}$ show a minimum ratio of 1 at $\vartheta_0 = 90^\circ$. It is easy to know that the property is coincident with that of $1/\sin(\vartheta_0)$. To observe the trend of the data clearly, the ratio of $\Phi_{\vartheta_0}/\Phi_{90}$ and $1/\sin(\vartheta_0)$ are plotted in Fig. 2. It can be seen that the curve of $\Phi_{\vartheta_0}/\Phi_{90}$ highly agrees with that of $1/\sin(\vartheta_0)$.

Therefore, the azimuth HPBW of UCA can be summarized as:

$$\Phi_{\vartheta_0} \approx \Phi_{90} \times \frac{1}{\sin(\vartheta_0)}, \quad (8)$$

where Φ_{90} is the HPBW under $\vartheta_0 = 90^\circ$ and given by (7). Substituting (7) into (8), an estimation formula for the azimuth HPBW of a UCA can be obtained as:

$$\Phi_{\vartheta_0} \approx 21^\circ \cdot \frac{\lambda}{a \sin(\vartheta_0)}, \quad (9)$$

where $\vartheta_0 \in (0^\circ, 180^\circ)$. Note that the absolute value of Φ_{ϑ_0} in (9) is approaching to infinity when ϑ_0 is closing to 0° and 180° . This apparently do not happen in reality. Under such situation, it is meaningless to consider the azimuth HPBW. Consequently, to avoid the two singular points and ensure the validity of (9), the value of ϑ_0 is limited in $(10^\circ, 170^\circ)$.

According to the antenna theory, the variation of elevation HPBW is too complicated to be described by a simple function for $\vartheta_0 \in (0^\circ, 180^\circ)$, since the array has two symmetric main beams with respect to the plane the array located in and the beams cannot be definitely separated when the element number is too small or the value of ϑ_0 is close to 90° . To estimate the elevation HPBW in a simple way, we only consider the situation that the two main beams of a UCA can be separated definitely. Thus, only $\vartheta_0 \in (10^\circ, 70^\circ) \cup (110^\circ, 170^\circ)$ are considered in the elevation HPBW's investigation in this paper.

Similarly, the elevation HPBWs under different values of ϑ_0 are computed via (6), as recorded in Table 2. The data on the second and third columns show that with the growing of ϑ_0 , the elevation HPBWs, θ_{ϑ_0} , increase gradually, as well as the normalized θ_{ϑ_0} . According to the AF in (6), the elevation HPBW must have a connection with the sine or cosine of ϑ_0 . It is easily to deduce that the elevation HPBW is related to $1/\cos(\vartheta_0)$. To observe the variations more clearly, the normalized θ_{ϑ_0} and $1/\cos(\vartheta_0)$ are plotted in Fig. 3.

Table 2: Elevation HPBW under different of ϑ_0

ϑ_0 (deg.)	θ_{ϑ_0} (deg.)	Normalized θ_{ϑ_0}
10	2.622	0.341
20	2.748	0.358
30	2.982	0.388
40	3.371	0.439
50	4.021	0.523
60	5.181	0.674
70	7.685	1.000

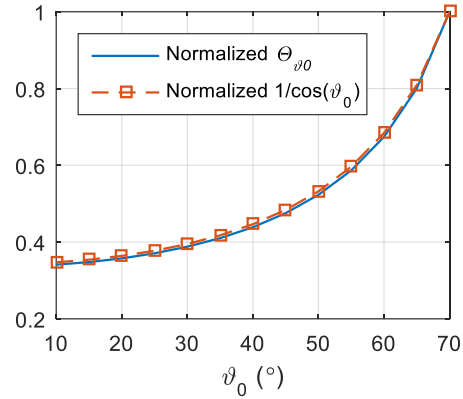


Fig. 3. Trend of the normalized θ_{ϑ_0} .

Based on the results in Table 2 and Fig. 3, the approximate formula for estimating the elevation HPBW of a UCA can be summarized as below:

$$\theta_{\vartheta_0} \approx 21^\circ \cdot \frac{\lambda}{a \cos(\vartheta_0)}, \quad (10)$$

where $\vartheta_0 \in (10^\circ, 70^\circ)$ and $\vartheta_0 \in (110^\circ, 170^\circ)$.

The proposed formulas, (9) and (10), depict the simple relations that the azimuth HPBW of UCA is inversely proportional to the sine of zenith angle of the main lobe and the electrical length of array radius, and the elevation HPBW is inversely proportional to the cosine of zenith angle of the main lobe and the electrical length of array radius. The overall computational costs of (5) and (6) are given by $O(N)$, while those of the proposed approximate formulas only require $O(1)$. Apparently, the computational complexities of (5) and (6) that increase with the growing of n are higher than those of the proposed approximate formulas, especially for a large UCA.

IV. RESULTS

In this section, the validities and accuracies of the proposed formulas are studied in numerical simulations as well as the calculation speed in time. Since the results validities and accuracies are symmetric about $\vartheta_0 = 90^\circ$, for the sake of brevity, only those for $\vartheta_0 \leq 90^\circ$ are provided in this paper.

A. Validity verification

According to proposed formulas, the HPBW of the

UCA in azimuth and elevation are only affected by λ/a and ϑ_0 . To examine the validities, the results of the HPBW obtained from (9) and (10) are compared with those computed via the AF in (5) and (6) under different values of λ/a and ϑ_0 respectively. As aforementioned, the study of paper focuses on the uniform tapering case. Accordingly, we can set $I_n = 1$ in (5) and (6).

The verification of (9) under different values of ϑ_0 is provided in Fig. 4 where the curves labeled “via (5)” and “via (9)” represent the results obtained by (5) and (9) respectively. Two array radii examples, $a = 3.18\lambda$ and $a = 4.77\lambda$, are presented in this simulation. It can be seen that the results obtained from the proposed formula (9) are highly in agreement with those computed by the AF in (5) under different zenith angles. It suggests that the proposed approximate formula (9) can not only get correct results, but also be applicable under different zenith angles of the main lobe for UCA. In addition, it also suggests that the proposed approximate formula is suitable for different array radii.

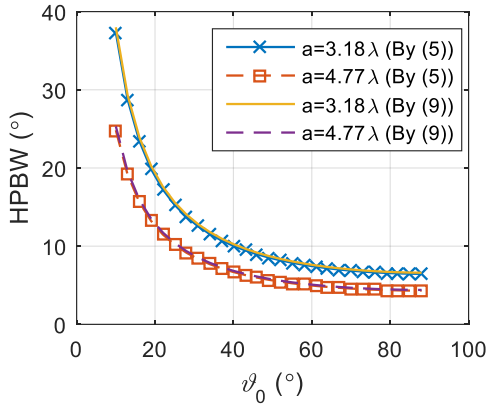


Fig. 4. Azimuth HPBWs under different zenith angles.

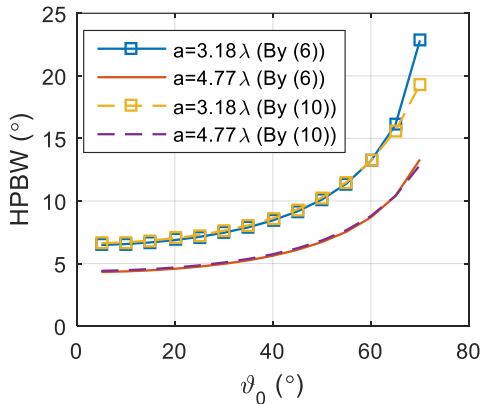


Fig. 5. Elevation HPBWs under different zenith angles.

The elevation HPBWs under different zenith angles for $a = 3.18\lambda$ and $a = 4.77\lambda$ are presented in Fig. 5. It can be seen that the results computed from (10) agree

with the ones calculated by (6) well, especially for $a = 4.77\lambda$. The results also indicate that (10) can obtain a correct elevation HPBW with an acceptable error, if the two main beams of a UCA can be definitely identified. Besides, the proposed estimation formula (10) is not only suitable for different zenith angles of the main lobe, but also applicable under different array radii.

Therefore, the proposed approximate formulas, (9) and (10), can be used to estimate the HPBWs of UCA in azimuth and elevation under different array radii and zenith angles of the main lobe.

B. Calculation error

Since the proposed formulas attain approximate results, the calculation error is a very important characteristic, which directly affects the accuracy of the results and leads to a limitation for the formulas' application. Consequently, the accuracies of the proposed formulas should be evaluated.

To investigate the accuracy of the proposed approximate formula (9), taking the results computed by (5) as a reference, the azimuth HPBWs of UCA are calculated by (9) under different zenith angles and array radii. The comparisons are presented in both absolute error and error rate, as depicted in Fig. 6 and Fig. 7.

It is clear from the results in Fig. 6 that the differences between the results calculated by (5) and (9) are very small. The absolute errors decrease with the growing of ϑ_0 , and reach the minimums at $\vartheta_0 = 90^\circ$. Besides, the errors decline with the growing of array radii in general, though the decreased calculation errors are smaller and smaller with the array radius growing. Moreover, the trends of the calculation errors for different array radii are almost the same, which implies the good agreements of the calculation errors under different array radii.

Figure 7 shows the contrary trends that the maximum error rates occur at $\vartheta_0 = 90^\circ$, and the error rates grow as ϑ_0 increases till 90° . The results also show that the maximum calculation error rates under different radii are almost the same, and their upper limits are around 2.2% at $\vartheta = 90^\circ$. In addition, as the array radius grows, the error rates decline slower and slower and tend to stay steady at the maximums when ϑ_0 is approaching to 90° . It means that the growing of array radius weakens the influence of the elevation component of the main lobe's direction to the calculation error rate. Both absolute error and error rate in Fig. 6 and Fig. 7 reflect that the proposed approximate formula (9) gets a good accuracy.

The accuracy of the proposed estimation formula (10) for the elevation HPBW is also evaluated in absolute error and error rate, as depicted in Fig. 8 and Fig. 9. It can be seen from Fig. 8 that the calculation errors are very small, except for the case of $a = 3.18\lambda$ under $\vartheta_0 > 65^\circ$. The calculation errors gradually increase as ϑ_0 is approaching to 90° , especially for the small array radius

cases, since it is harder and harder to distinguish the two main beams of the UCA. Generally, the calculation errors remain unchanging till $\vartheta_0 = 50^\circ$, and then begin to decline and bound. The results indicate that with the increasing of array radii, the calculation errors decrease and the values of ϑ_0 at bounding points increase.

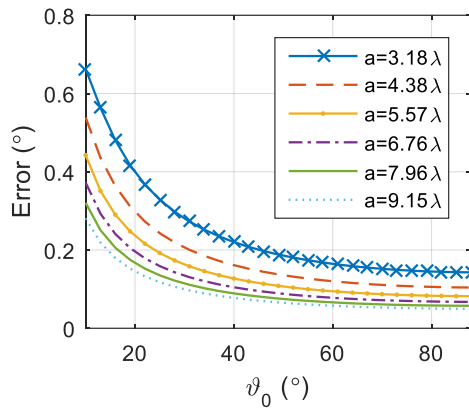


Fig. 6. Absolute error of (9).

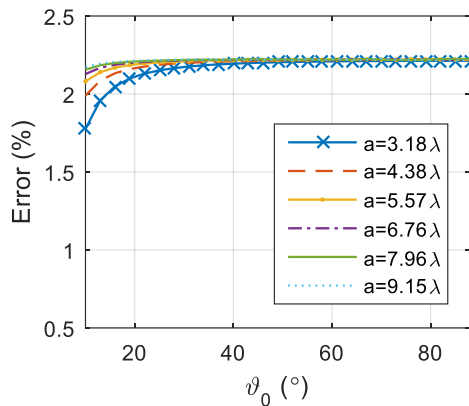


Fig. 7. Error rate of (9).

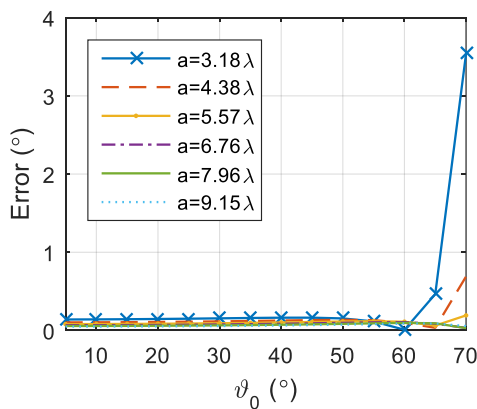


Fig. 8. Absolute error of (10).

The simulation results in Fig. 9 show that the error rates begin with around 2.2%, and with the growing of

ϑ_0 , they decrease gradually. The error rates bound at a certain ϑ_0 which grows as the array radius increases. The reason of the error rates grows quickly when $\vartheta_0 > 65^\circ$ for the case of $a = 3.18\lambda$ is mentioned before. In general, the larger the array radius is, the steadier the error rates are. Meanwhile, the general trends of error rate are coincident with those of the absolute errors in Fig. 8.

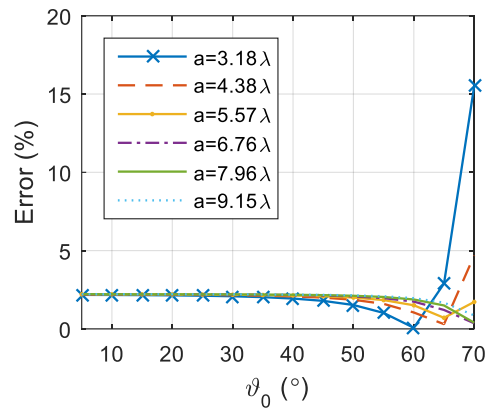


Fig. 9. Error rate of (10).

C. Calculation speed

To further show the proposed formulas' advantage, the computational speeds are evaluated based on the calculation time. Due to the same calculation speed of (5) and (6) and the same calculation speed of (9) and (10), for the sake of brevity, only the calculation times of (5) and (9) are presented. The results based on 10,000 iterations are depicted in Fig. 10. It shows that the calculation time of (9) remains constant even if N increases, yet the computational time of (5) grows with the increasing of N . Moreover, the calculation time of (9) is at least 2,000 times less than that of (5) in this example, and this ratio grows with the increasing of N . It implies that the proposed formulas can approximately estimate the HPBW of a UCA at a very high speed, compared with the involuted and time-consuming conventional method, i.e., by (5) and (6).

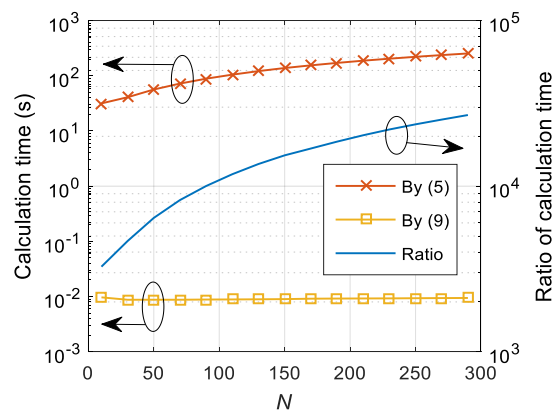


Fig. 10. Calculation times based on 10,000 iterations.

V. CONCLUSION

In this paper, two very simple formulas are proposed to estimate the HPBW of UCA in azimuth and elevation roughly under different main lobe directions. In contrast with computing the HPBW directly from definition, the proposed approximate formulas provide an easy and fast approach to estimate the HPBW of UCA in azimuth and elevation. The proposed formula for azimuth HPBW can get not only a correct result but also a good accuracy with a maximum error rate of 2.2%. The formula for elevation HPBW also can estimate the elevation HPBW correctly with an acceptable accuracy. Moreover, the proposed formulas attain an extremely high calculation speed. Therefore, the study in this paper provides a simple and quick method to estimate the HPBW of UCA.

REFERENCES

- [1] Y. Wu, H. Wang, Y. Zhang, and Y. Wang, "Multiple near-field source localization with uniform circular array," *IET Electronics Letters*, vol. 49, no. 24, pp. 1509-1510, Nov. 2013.
- [2] J. J. Fuchs, "On the application of the global matched filter to DOA estimation with uniform circular arrays," *IEEE Transactions on Signal Processing*, vol. 49, no. 4, pp. 702-709, Apr. 2001.
- [3] P. Wang, Y. Li, and B. Vucetic, "Millimeter wave communications with symmetric uniform circular antenna arrays," *IEEE Communications Letters*, vol. 18, no. 8, pp. 1307-1310, Aug. 2014.
- [4] P. Ioannides and C. A. Balanis, "Uniform circular arrays for smart antennas," *IEEE Antennas and Propagation Magazine*, vol. 47, no. 4, pp. 192-206, Aug. 2005.
- [5] V. L. Do, T. B. Nguyen, V. K. Dao, and C. H. Nguyen, "Direction finding in multipath environments using moving uniform circular arrays," *2017 3rd International Conference on Frontiers of Signal Processing (ICFSP)*, Paris, pp. 50-54, 2017.
- [6] X. Lian and J. Zhou, "2-D DOA Estimation for Uniform Circular Arrays with PM," *2006 7th International Symposium on Antennas, Propagation & EM Theory*, Guilin, pp. 1-4, 2006.
- [7] Y. Wu and H. C. So, "Simple and accurate two-dimensional angle estimation for a single source with uniform circular array," *IEEE Antennas and Wireless Propagation Letters*, vol. 7, pp. 78-80, 2008.
- [8] B. Liao, Y. T. Wu, and S. C. Chan, "A generalized algorithm for fast two-dimensional angle estimation of a single source with uniform circular arrays," *IEEE Antennas and Wireless Propagation Letters*, vol. 11, pp. 984-986, 2012.
- [9] F. Belfiori, S. Monni, W. Van Rossum, and P. Hoogeboom, "Side-lobe suppression techniques for a uniform circular array," *The 7th European Radar Conference*, Paris, pp. 113-116, 2010.
- [10] W. Jeon, J. H. Kim, and S. Y. Chung, "Effect of mutual coupling on uniform circular arrays with vector antenna elements," *IEEE Antennas and Wireless Propagation Letters*, vol. 16, pp. 1703-1706, 2017.
- [11] J. H. Kim, W. Jeon, and S. Y. Chung, "Asymptotic analysis on directivity and beamwidth of uniform circular array," *IEEE Antennas and Wireless Propagation Letters*, vol. 16, pp. 3092-3095, 2017.
- [12] H. G. Urban, *Handbook of Underwater Acoustic Engineering*. STN, Atlas Elektronik, 2002.
- [13] X. Lurton, *An Introduction to Underwater Acoustics: Principles and Applications*. Springer Science & Business Media, Berlin, 2002.
- [14] C. A. Balanis, *Antenna Theory Analysis and Design*. 3rd ed., John Wiley & Sons, Inc.: New Jersey, USA, 2005.
- [15] F. Gross, *Smart Antennas for Wireless Communications with MATLAB*. McGraw-Hill, New York, 2005.



Hua Tang received the B.S. degree in Electronic Information Engineering from the Southwest University of Science and Technology, Mianyang, China, in 2010. He is currently working towards the Ph.D degree with the School of Electronic Science and Engineering, University of Electronic Science and Technology of China, Chengdu, China. His research interests include antenna selection and signal processing in MIMO and massive MIMO, and antenna theory and technology in mobile communications.



Xianzheng Zong received the B.S., and Ph.D. degrees in Electromagnetic Field and Microwave Technique from the University of Electronic Science and Technology of China (UESTC), Chengdu, in 2002, and 2008, respectively. He was a Lecturer with UESTC, from 2008 to 2011. Since 2011, he has been an Associate Professor with UESTC. His current research interests include antenna theory and technology, computational electromagnetics, and electromagnetic compatibility (EMC).



Zaiping Nie received the B.S. degree in Radio Engineering and the M.S. degree in Electromagnetic Field and Microwave Technology from the University of Electronic Science and Technology of China, Chengdu, China, in 1968 and 1981, respectively.

He is currently a Professor with the Department of Microwave Engineering, UESTC. From 1987 to 1989, he was a Visiting Scholar with the Electromagnetics Laboratory, University of Illinois, Urbana, IL, USA. His current research interests include computational electromagnetics and its applications, antenna theory and techniques, electromagnetic scattering and inverse scattering, and field and waves in inhomogeneous media.

Dual-polarized Grid-slotted Microstrip Antenna with Enhanced Bandwidth and Low Profile

Wangyu Sun and Yue Li

Department of Electronic Engineering
Tsinghua University, Beijing, 100084, China
sunwy16@mails.tsinghua.edu.cn, lyee@tsinghua.edu.cn

Abstract — In this paper, a wideband dual-polarized microstrip antenna is proposed inspired by the concept of the periodic grid-slotted surface. Inherited the merit of low profile from microstrip antenna, a relatively wide bandwidth, i.e., up to 43% with reflection coefficient less than -10 dB, is achieved for both orthogonal polarizations. Multiple modes are excited due to the periodic slot-loaded structure and well matched using crossed aperture-coupled Y-shaped feeding. The overall height of the proposed antenna is only $0.06 \lambda_0$, λ_0 is the free-space wavelength at the centre frequency of 5.5 GHz. The proposed antenna is systematically studied in the numerical simulation and experiment, and results agree well. The proposed dual-polarized antenna provides an effective choice for wideband low profile antenna for the applications of base station.

Index Terms — Antenna feeds, microstrip antennas, polarization diversity, wideband antennas.

I. INTRODUCTION

Dual polarized antennas are widely used in modern wireless communication systems, especially for the applications of base stations. Conventional dual polarized antennas applied in base stations are cross-dipoles [1-2] or magneto-electric dipoles [3], which achieve a broad bandwidth around 45%. However, these designs are usually with a high profile above $0.2 \lambda_0$. Therefore, how to decrease the profile (less than $0.1 \lambda_0$) of the dual polarized base station antenna and maintain the broad bandwidth (around 45%) is still a challenge. Microstrip antennas may be a suitable choice to achieve this target due to these obvious advantages of low profile, light weight, low cost and easy integration [4]. Nevertheless, typical microstrip antennas usually suffer from narrow impedance bandwidth, e.g., less than 10% because of the high quality factor [5].

Several methods have been proposed to enhance the bandwidth of microstrip antennas. For example, the bandwidth as high as 20% can be achieved by using thick substrate with low dielectric constant for a low quality

factor [6]. Reference [7] presents a microstrip antenna with the impedance bandwidth greater than 20% by embedding a U-shaped slot. E-shaped microstrip antenna fed by a probe is given in [8], demonstrating that the bandwidth could reach up to 30.3%. And the stacked structures have been utilized to provide broadband property, knowing as the stacked microstrip antennas [9]. However, the profiles of these designs are usually higher than $0.1 \lambda_0$. To maintain the low profile performance and improve the bandwidth, multimode coupling theory [10-11] becomes an available method recently. By coupling TM_{10} and TM_{30} modes, the bandwidth of 15.5% is achieved with a profile of $0.03 \lambda_0$ [10]. Nevertheless, not all above techniques are suitable to be applied in dual-polarized applications due to asymmetrical radiating patches or complex feeding networks [11].

In our previous work [12], a microstrip antenna with strip-slotted hybrid patch and aperture-coupling feeding structure is presented. By adding three periodic slots on the radiating aperture, TM_{10} and antiphase TM_{20} modes are excited and coupled to achieve a broadband of 41% with a low profile of $0.06 \lambda_0$. But it can only support one polarization. Inspired from the periodic radiating structure in [12], a dual-polarized microstrip antenna with grid-slotted radiating aperture is proposed to realize the broad bandwidth and low profile. As this design is with a symmetrical radiating aperture, dual polarizations can be excited through the cross coupling-apertures and the cross Y-shaped feeding lines, which also help to realize the wideband characteristic. The antenna sample is fabricated for experiment, exhibiting good agreement with simulation results. The relative bandwidth around 43% for two polarizations and the profile of $0.06 \lambda_0$ indicate the proposed dual-polarized antenna has the potential to be applied in the design of low profile base stations.

II. ANTENNA DESIGN AND ANALYSIS

Figure 1 illustrates the configuration of the proposed dual-polarized grid-slotted microstrip antenna. The grid-

slotted radiating patch is above the ground and the crossed Y-shaped feeding lines is underneath the ground. Two dielectric layers ($\epsilon_r=3.38$, $\mu_r=1$ and $\tan \delta=0.0027$) with different thicknesses are utilized to support the antenna. The detailed geometry and dimensions are plotted in Figs. 2 (a)-(c) with the optimized parameters listed in Table 1. The proposed antenna is composed of 4×4 small square patch units with identical size and fed through a pair of orthogonal Y-shaped feeding lines. This structure can be regarded as a combination of two orthogonal 1×4 strip-slotted hybrid structures in [12]. Therefore, orthogonal polarizations are excited along x - and y -axis, respectively. For each Y-shaped feeding line, the distance between the two arms (W) and the vertical distance (s) are tuned for wideband impedance matching. The widths of these sections (W_{ms} , W_{ms2}) are selected to the intrinsic impedance of 50Ω . To avoid the intersection, four crossover structures with the same dimensions are introduced, and the detailed view is shown in Fig. 2 (c). The vias in the crossover are applied to connect the upper and bottom parts of Microstrip 1 or Microstrip 2. Therefore, the orthogonal Y-shaped feeding lines are separated at the intersecting points.

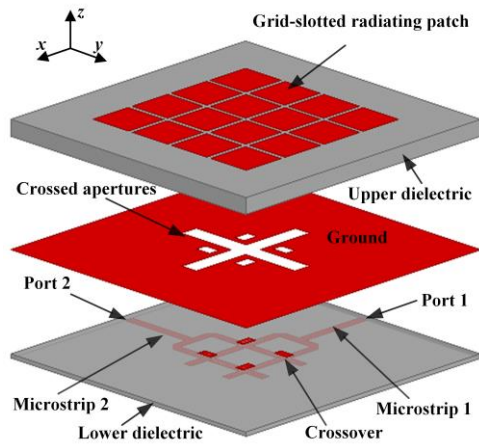


Fig. 1. Perspective view of the proposed dual-polarized grid-slotted microstrip antenna.

The proposed antenna applies the Y-shaped feeding line, instead of the typical straight feeding line. It has two benefits: (1) Improvement on impedance matching; (2) Easy realization of dual polarizations. To validate the design strategy, the evolution processes (Ant. 1, Ant. 2 and Proposed Ant.) are illustrated in Fig. 3, with the comparisons on reflection coefficients. Firstly, extra tuning parameters, i.e., W and s , are provided for impedance matching and lead to a remarkable improvement for impedance bandwidth. For Ant. 1, the simulated impedance bandwidth with $|S_{11}| < -10$ dB is

4.50-5.92 GHz (27.3%). For Ant. 2, the impedance bandwidth is 4.26-6.54 GHz (42%). The introduction of this Y-shaped microstrip feeding line greatly enhances the relative bandwidth with an increment of 15%. Secondly, the Y-shaped geometry is indispensable to achieve a dual-polarized performance. Supposing two straight microstrip lines are used to create a cross feeding structure, just as shown in Fig. 4 (a), the intersection of two orthogonal straight lines is right underneath the centre of cross apertures. Thus, it is difficult to avoid the intersection, even using the crossover mentioned in Fig. 2 (c). In Fig. 4 (b), two orthogonal Y-shaped microstrip lines are applied and the four intersections move outwards and are away from the cross-coupling apertures. Thus, with the Y-shaped feeding structure and crossovers, the two cross microstrip lines can be separated in the same layer to further excite two orthogonal polarizations. Besides, in Fig. 3, the proposed dual-polarized antenna (Proposed Ant.) can also realize a much wider simulated impedance bandwidth of 4.29-6.40 GHz (39.5%) than Ant. 1 (27.3%).

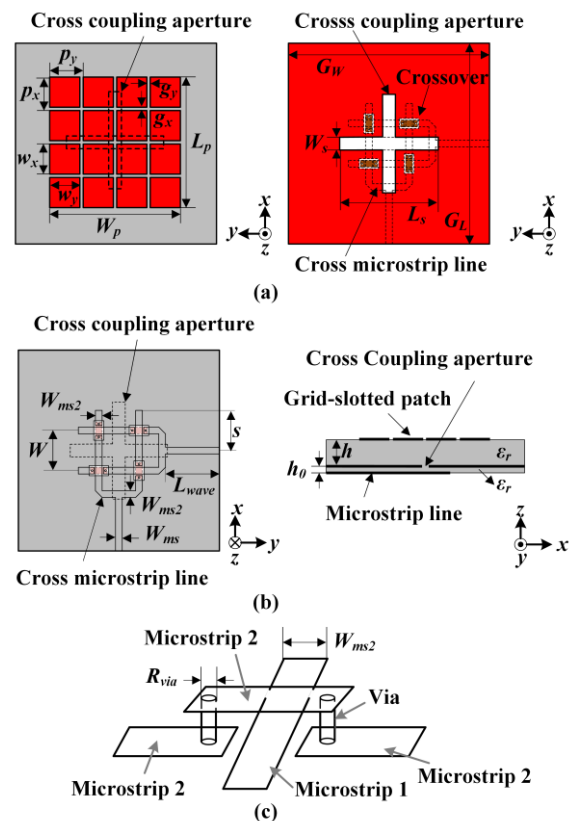


Fig. 2. Geometry of the proposed grid-slotted microstrip antenna: (a) top view of the radiating patch and GND, (b) bottom view of the feeding structure and side view of the overall structure, and (c) stereograph of the crossover.

Table 1: Optimized dimension of the proposed antenna (Unit: mm)

p_x	p_y	g_x	g_y	W_p	L_p	G_L	G_W	W_s
10	10	1	1	39	39	60	60	3.8
W	s	W_{ms}	W_{ms2}	L_{wave}	h	h_0	L_s	R_{via}
8	10	1.85	1.75	15.5	3.25	0.813	30	0.17

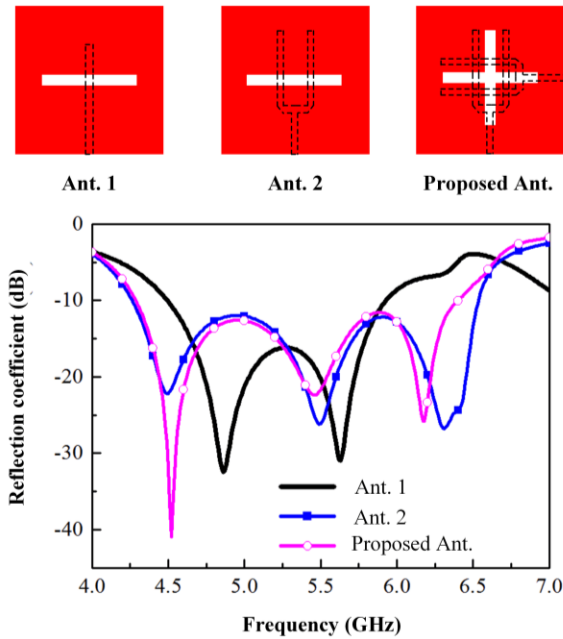


Fig. 3. Design evolution and simulated reflection coefficients.

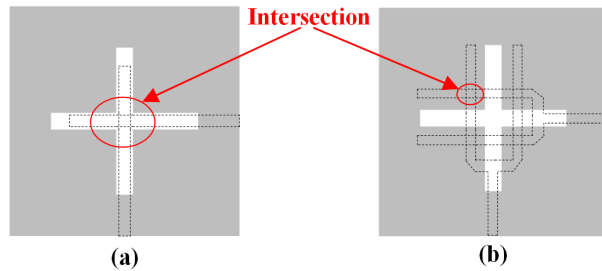


Fig. 4. Cross feeding structure: (a) with two orthogonal straight microstrip lines, and (b) with two orthogonal Y-shaped microstrip lines.

In the curve of Fig. 5 (a), three resonances appear at the frequencies of 4.5 GHz, 5.5 GHz, and 6.3 GHz. Snapshots of the vector electric field distributions at these three resonances are depicted in Figs. 5 (b)-(d). In Fig. 5 (b), it can be clearly seen that the E-field distribution is the TM_{10} mode of conventional patch antenna and meanwhile, there are very strong E-fields in

the grid slots along y-axis between two adjacent small square units. There are two resonances for the higher order mode. The resonances at 5.5 GHz and 6.3 GHz have almost the same electric field distributions (Figs. 5 (c)-(d)), named as antiphase TM_{20} mode. The directions of the E-field of the coupled aperture are antiparallel. The mode sketches at different resonance frequencies are inserted in Fig. 5 (a).

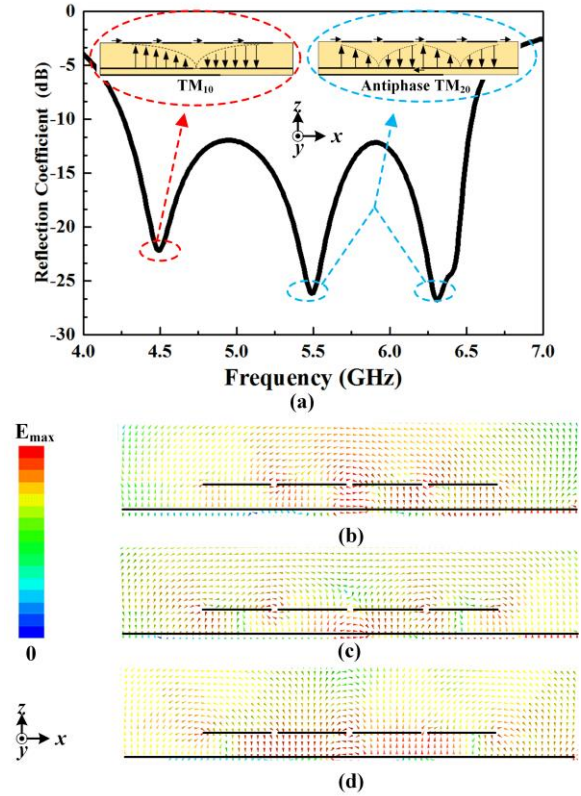


Fig. 5. Simulated reflection coefficient and E-field distribution of the proposed antenna. (a) Simulated reflection coefficient and sketches of the resonant modes. The vector electric field distributions at (b) 4.5 GHz, (c) 5.5 GHz, and (d) 6.3 GHz.

III. PROTOTYPE AND MEASUREMENTS

The numerical results illustrated in this study are obtained using the commercial software High Frequency Structure Simulator V15 (HFSS 15.0). Specifically, the frequency-domain solver with a Finite Element Method (FEM) algorithm is selected. During the simulation procedure, the solution frequency is 5.5 GHz and minimum converged passes is 2 with the converged precision of 0.02. For measurement, the Agilent E5071B vector network analyzer is used to measure the reflection and transmission coefficients. The ETS-LindgrenAMS8500 anechoic chamber is used to test the radiation performance.

A prototype of the proposed dual-polarized grid-slotted microstrip antenna (Proposed Ant.) is fabricated and measured, and Figs. 6 (a)-(c) show the photographs. The antenna prototype has the same dimensions with those listed in Table 1. The measured reflection and transmission coefficients at two ports are illustrated in Fig. 6 (d), also agreeing well with the simulated ones. The deviations may be mainly caused by manufacturing error, especially the thin air gap between upper and lower dielectrics. The achieved -10-dB impedance bandwidths are 4.23-6.62 GHz (44.1%) for port 1 and 4.26-6.61 GHz (43.2%) for port 2. The measured transmission coefficient between two ports is lower than -16 dB in the whole band.

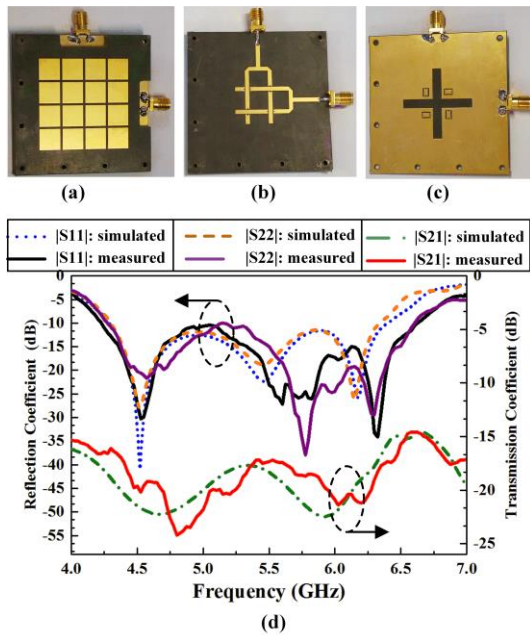


Fig. 6. Photographs and measured results of the fabricated Proposed Ant. (a) Top view, (b) bottom view, (c) the ground plane and cross coupling apertures in the GND layer, and (d) simulated and measured reflection and transmission coefficients.

Figures 7 and 8 show the simulated and measured normalized radiating patterns at 4.5 GHz, 5.5 GHz, and 6.3 GHz at two ports. The measured cross-polarization levels are less than -18 dB in the E-plane and -20 dB in the H-plane for port 1; -19 dB in the E-plane and -18 dB in the H-plane for port 2. Figure 9 (a) shows the simulated and measured gain and efficiency. For port 1, the simulated gain ranges from 6.9 to 10.4 dBi and the efficiency is higher than 89%, and the measured gain ranges from 6.4 to 10.1 dBi. For port 2, the simulated gain ranges from 6.9 to 10.5 dBi and the efficiency is

higher than 80%, and the measured gain ranges from 6.5 to 10.3 dBi. The differences between the maximum gain and minimum gain are 3.7 dBi and 3.8 dBi, respectively. The gain variations are accepted (less than 4 dB) in the whole operating impedance bandwidth. The proposed antenna can be regarded as a binary array when operating at antiphase TM_{20} mode. Therefore, the gain at TM_{10} mode is lower than the gain at antiphase TM_{20} mode. In Fig. 9 (b), the envelope correlation coefficients (ECC) between the two ports is also presented, which can quantitatively evaluate the MIMO performance. The ECC of two ports can be calculated by the complex radiation far field and the formulation is given in equations (1) and (2) [13]. The ECC is less than 0.07 in the whole operating bandwidth. Comparing with the benchmark value of ECC less than 0.5 [14-15], the proposed dual-polarized antenna achieves an excellent MIMO performance:

$$\rho_e \approx |\rho_c|^2 = \left| \frac{\iint A_{12}(\theta, \varphi) \sin \theta d\theta d\varphi}{\iint A_{11}(\theta, \varphi) \sin \theta d\theta d\varphi \cdot \iint A_{22}(\theta, \varphi) \sin \theta d\theta d\varphi} \right|^2, \quad (1)$$

where

$$A_{ij} = E_{\theta,i}(\theta, \varphi) \cdot E_{\theta,j}^*(\theta, \varphi) + E_{\varphi,i}(\theta, \varphi) \cdot E_{\varphi,j}^*(\theta, \varphi). \quad (2)$$

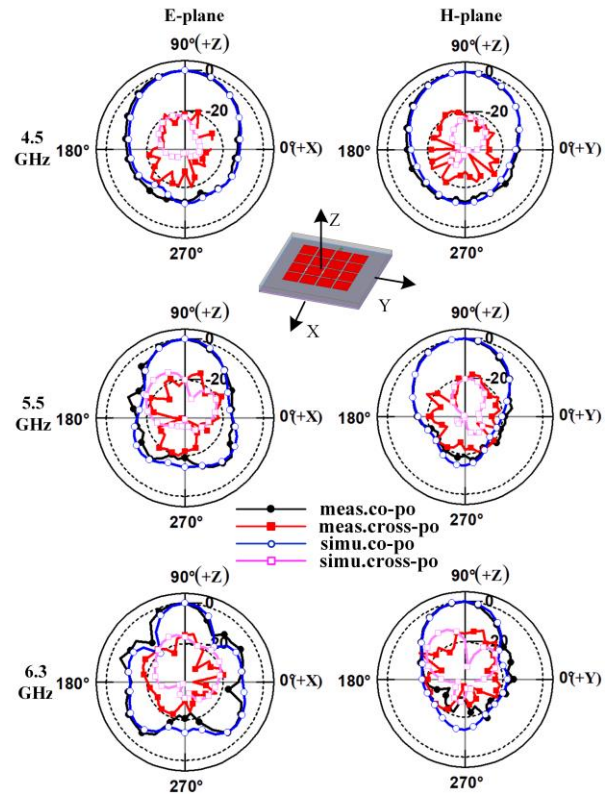


Fig. 7. Simulated and measured normalized radiating patterns at port 1 of the Proposed Ant. at 4.5 GHz, 5.5 GHz and 6.3 GHz.

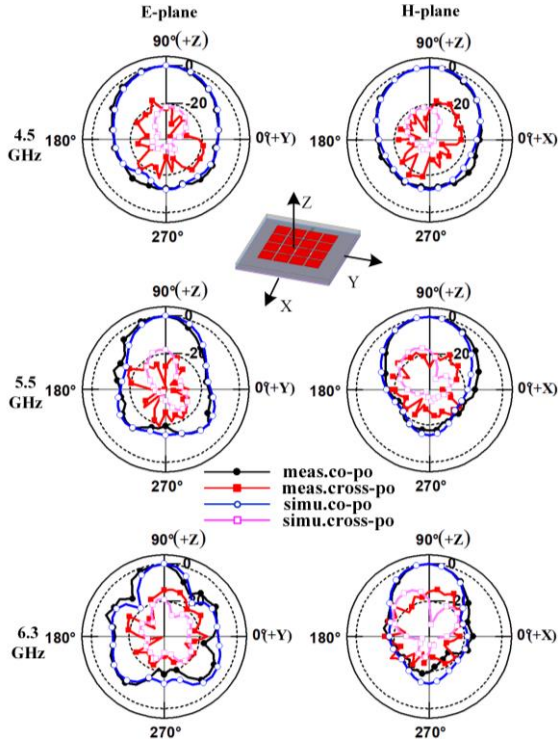


Fig. 8. Simulated and measured normalized radiating patterns at port 2 of the Proposed Ant. at 4.5 GHz, 5.5 GHz and 6.3 GHz.

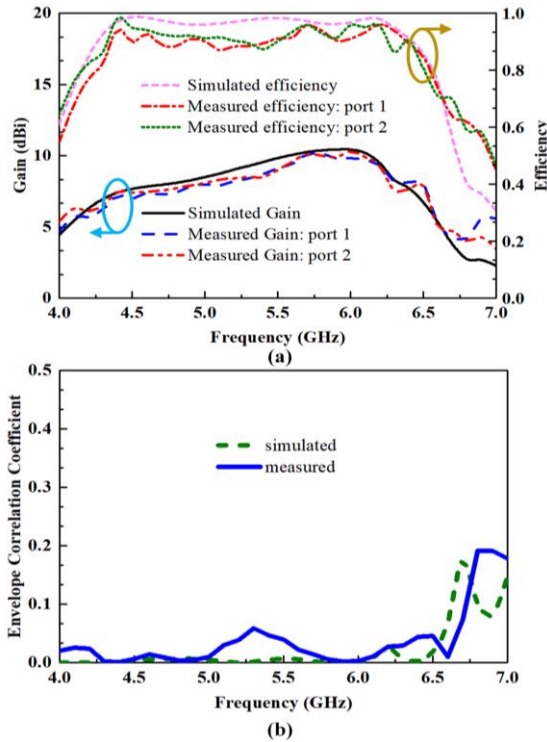


Fig. 9. Simulated and measured radiating performances of the Proposed Antenna. (a) Gain and efficiency, and (b) envelop correlation coefficients.

IV. CONCLUSION

In this paper, a dual-polarized grid-slotted microstrip antenna with enhanced bandwidth and low profile is proposed. The ingenious combination of the Y-shaped feeding structure and periodic radiating aperture is presented to enhance the bandwidth of the microstrip antenna significantly. The obtained results provide a guideline to design wideband microstrip antennas. Prototype of the proposed antenna is fabricated and measured. As shown in Table 2, compared with the existing broadband microstrip antennas [8,9,12], the proposed antenna can achieve wider bandwidth with low profile and meanwhile realize dual polarization. Compared with the existing dual-polarized antenna units [16-17] applied for base station, lower profile is observable. Up to 43% -10-dB bandwidth is obtained in our design, exhibiting possibilities to design dual-polarization low profile base station in wireless communication systems.

Table 2: Comparison of performances for various antennas (λ_0 is the centre operating wavelength in free space)

Antenna	Profile	BW	Polarization	Centre Frequency
Ref. [8]	$0.07 \lambda_0$	30.3%	Single	2.25 GHz
Ref. [9]	$0.1 \lambda_0$	36.8%	Single	30 GHz
Ref. [12]	$0.06 \lambda_0$	41%	Single	5.5 GHz
Ref. [16]	$0.25 \lambda_0$	54.5%	Dual	2.31 GHz
Ref. [17]	$0.24 \lambda_0$	45%	Dual	2.22 GHz
Proposed	$0.06 \lambda_0$	43%	Dual	5.50 GHz

ACKNOWLEDGMENT

This work was supported by the National Natural Science Foundation of China 61771280, and in part by Natural Science Foundation of Beijing Manipulate under Contract 4182029.

REFERENCES

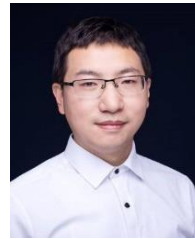
- [1] Q.-X. Chu, D. L. Wen, and Y. Luo, "A broadband $\pm 45^\circ$ dual-polarized antenna with Y-shaped feeding structure," *IEEE Trans. Antennas Propag.*, vol. 63, no. 2, pp. 483-490, Feb. 2015.
- [2] Z. Bao, Z. Nie, and X. Zong, "A broadband dual-polarization antenna element for wireless communication base station," in *Proc. IEEE Asia Pacific Conf. Antennas and Propagation*, pp. 144-146, 2012.
- [3] K. M. Luk and H. Wong, "A new wideband unidirectional antenna element," *Int. J. Microw. Opt. Technol.*, vol. 1, no. 1, pp. 2098-2101, July 2006.
- [4] O. Amjad, S. W. Munir, S. T. Imeci, and A. O. Ercan, "Design and implementation of dual band microstrip patch antenna for WLAN energy harvesting system," *Applied Computational Electromagnetic Society (ACES) Journal*, vol. 33, no. 7,

- pp. 746-751, July 2018.
- [5] R. Garg, P. Bhartia, I. Bahl, and A. Ittipiboon, *Microstrip Antenna Design Handbook*. Boston, MA, USA: Artech House, 2001.
 - [6] E. Chang, S. A. Long, and W. F. Richards, "An experimental investigation of electrically thick rectangular microstrip antennas," *IEEE Trans. Antennas Propag.*, vol. 34, no. 6, pp. 767-772, June 1986.
 - [7] T. Huynh and K. F. Lee, "Single-layer single-patch wideband microstrip antenna," *Electron. Lett.*, vol. 31, no. 16, pp. 1310-1312, Aug. 1995.
 - [8] F. Yang, X. X. Zhang, X. Ye, and Y. Rahmat-Samii, "Wide-band E-shaped patch antennas for wireless communications," *IEEE Trans. Antennas Propag.*, vol. 49, no. 7, pp. 1094-1100, July 2001.
 - [9] S. Mestdagh, W. De Raedt, and G. A. E. Vandenbosch, "CPW-fed stacked microstrip antennas," *IEEE Trans. Antennas Propag.*, vol. 52, no. 1, pp. 74-83, Jan. 2004.
 - [10] N.-W. Liu, L. Zhu, W.-W. Choi, and X. Zhang, "A low-profile aperture-coupled microstrip antenna with enhanced bandwidth under dual resonance," *IEEE Trans. Antennas Propag.*, vol. 65, no. 3, pp. 1055-1062, Mar. 2017.
 - [11] A. U. Zaman, L. Manholm, and A. Derneryd, "Dual polarised microstrip patch antenna with high port isolation," *Electron. Lett.*, vol. 43, no. 10, pp. 551-552, Sep. 2007.
 - [12] W. Y. Sun, Y. Li, Z. Z. Zhang, and Z. H. Feng, "Broadband and low-profile microstrip antenna using strip-slot hybrid structure," *IEEE Antennas Wireless Propag. Lett.*, vol. 16, pp. 3118-3121, 2017.
 - [13] Z. Zhang, *Antenna Design for Mobile Devices*, 2nd Edition, Hoboken, NJ, USA: Wiley, 2017.
 - [14] J. M. Lee, K. B. Kim, H. K. Ryu, and J. M. Woo, "A compact ultrawideband MIMO antenna with WLAN band-rejected operation for mobile devices," *IEEE Antennas Wireless Propag. Lett.*, vol. 11, pp. 990-993, 2012.
 - [15] H. Minseok and C. Jaehoon, "Small-size printed strip MIMO antenna for next generation mobile handset application," *Microw. Opt. Technol. Lett.*, vol. 53, no. 2, pp. 48-52, 2011.
 - [16] D.-Z. Zheng and Q.-X. Chu, "A wideband dual-polarized antenna with two independently controllable resonant modes and its array for base-station applications," *IEEE Antennas Wireless Propag. Lett.*, vol. 16, pp. 2014-2017, 2017.
 - [17] Y. Y. Jin and Z. W. Du, "Broadband dual-polarized F-probe fed stacked patch antenna for base stations," *IEEE Antennas Wireless Propag. Lett.*, vol. 14, pp. 1121-1124, 2015.



dual polarized antennas.

Wangyu Sun received the B.S. degrees from Tsinghua University, in 2016. He is currently working toward the Master degree in Electrical Engineering at Tsinghua University. His current research interests include broadband antennas, low profile antennas and



Yue Li received the B.S. degree in Telecommunication Engineering from the Zhejiang University, Zhejiang, China, in 2007, and the Ph.D. degree in Electronic Engineering from Tsinghua University, Beijing, China, in 2012. He is currently an Associate Professor in the Department of Electronic Engineering at Tsinghua University. In June 2012, he was a Postdoctoral Fellow in the Department of Electronic Engineering, Tsinghua University. In December 2013, he was a Research Scholar in the Department of Electrical and Systems Engineering, University of Pennsylvania. He was also a Visiting Scholar in Institute for Infocomm Research (I2R), A*STAR, Singapore, in 2010, and Hawaii Center of Advanced Communication (HCAC), University of Hawaii at Manoa, Honolulu, HI, USA, in 2012. Since January 2016, he has been with Tsinghua University, where he is an Assistant Professor. He has authored and coauthored over 90 journal papers and 45 international conference papers, and holds 15 granted Chinese patents. His current research interests include metamaterials, plasmonics, electromagnetics, nanocircuits, mobile and handset antennas, MIMO and diversity antennas, and millimeter-wave antennas and arrays. He was the recipient of the Issac Koga Gold Medal from URSI General Assembly in 2017; the Second Prize of Science and Technology Award of China Institute of Communications in 2017; the Young Scientist Awards from the conferences of ACES 2018, AT-RASC 2018, AP-RASC 2016, EMTS 2016, URSI GASS 2014; the Best Paper Awards from the conferences of CSQRWC 2018, NCMMW 2018 and 2017, APCAP 2017, NCANT 2017, ISAPE 2016, and ICMMT 2016; the Outstanding Doctoral Dissertation of Beijing Municipality in 2013, and the Principal Scholarship of Tsinghua University in 2011. He is serving as the Associate Editor of IEEE Transactions on Antennas and Propagation, IEEE Antennas and Wireless Propagation Letters and Computer Applications in Engineering Education, also as the Editorial Board of Scientific Report.

Mm-wave Radar Based Micro-Deformation Monitoring for Highway and Freight Railway Bridges

Yingsong Li^{1,2}, Zelong Shao^{1,3}, Xiangkun Zhang^{1,3,*}, and Jingshan Jiang¹

¹ Key Laboratory of National Microwave Remote Sensing
National Space Science Center, Chinese Academy of Sciences, Beijing 100190, China
*zhangxiangkun@mirslab.cn

² College of Information and Communication Engineering
Harbin Engineering University, Harbin, 150001, China
liyingsong@ieee.org

³ School of Electronic, Electrical and Communication Engineering
University of Chinese Academy of Sciences, Beijing, 100490, China

Abstract — In this paper, a mm-wave radar is devised to monitor the micro-deformation of bridges and its performance is verified via monitoring a highway and a freight railway bridges. The radar interferometry technology is utilized to develop the compact and portable mm-wave radar. Experiments are set up to monitor a highway bridge around Beijing-Tianjin expressway which is near the sixth ring roads of Beijing and a Daqin freight railway bridge in Yanqing, Beijing. The experimental results demonstrate that the devised radar can detect the micro-deformation of the bridge vibration with a super-resolution and high precision, making the mm-wave radar promising for bridge monitoring, dam monitoring, debris flow monitoring applications.

Index Terms — Micro-deformation monitoring, millimeter (mm) wave radar, super-resolution and high precision.

I. INTRODUCTION

The status of the bridges is very important, which can help to check and repair the bridge damages [1]. In particular, the bridges are increased rapidly for constructing the modern highway, high-speed railway and roads [2-3]. Thus, it is useful to monitor the status of these bridges to understand the bridge healthy status [4-5]. Moreover, these bridges should be monitored in real-time and repaired on time.

Recently, several methods or devices have been presented to monitor the status of the bridges, such as gauges, accelerometers, total stations, digital levels, global position system [4-5]. Although these devices or methods, including the sensors, can well detect the status of the bridges, the installations of these devices are difficult since they should contact with the bridges,

which are dangerous, time-consuming, and they are sensitive to the weather and the environments [6-8]. In addition, the installation of these devices might give unnecessary to the transportation and the economy. It is a best way to find out a solution to monitor the status of the bridges using non-contacting method, which can also provide a real-time and online monitoring. To overcome the drawbacks of these devices and meet the practical requirements, radar interferometry technique has been studied for providing an all-weather and non-contact method for monitoring the status of the bridges [9-12]. In comparison with the above mentioned techniques, the radar can overcome the disadvantages, and it has been used for detecting the civil structures. An IBIS radar is designed by Italy and it has been used for monitoring the simple bridges [13]. However, there is no comparison with the different bridges. Moreover, there is no radar-based micro-deformation monitoring for highway and freight railway bridges.

In this paper, a mm-wave radar is devised for monitoring the micro-deformation of the bridges. The radar is designed in our laboratory and its performance is verified for monitoring a highway and a freight railway bridges. In the designed mm-wave radar, interferometry technique is considered for improving the precision of the measurement. The measurement results are presented to prove that the devised radar can well monitor the micro-deformation of the bridge vibration with a super-resolution and high precision. The proposed mm-wave micro-deformation monitoring method can detect the displacement with a distance from the targets and it also is easy to install in the practical engineering. In our paper, we mainly discuss the micro-deformation monitoring based on our design mm-wave radar to detect the bridges vibrations of highway and freight railway.

II. THEORY AND STRUCTURE OF THE MM-WAVE RADAR

In the mm-wave radar design, frequency-modulated continuous wave (FMCW) mode is considered to make the radar compact and simple [14-15]. Additionally, it also has many advantages in comparison with traditional radars, such as high resolution and low transmitting power [14]. Thus, the radar can be used to monitor the bridges since the vibrations from the bridges are very small, which is always smaller than 5mm. As for the FMCW radar, the range resolution is described as [14-16]:

$$\Delta r = \frac{c}{2B}, \quad (1)$$

where B denotes the bandwidth of the radar while c represents the speed of light. The interferometric technique is used for improving the micro-deformation detection ability by taking echo phase difference into consideration [17]. The micro-deformation and the echo phase difference has a relationship which is given by:

$$\Delta R = \frac{\lambda}{4\pi} \Delta\varphi, \quad (2)$$

where ΔR is the change of the bridge, $\Delta\varphi$ is the echo phase shift, λ is the wavelength of the center frequency. Since the radar is designed at mm-wave, its wavelength is very small, and hence, the minimum deformation of the bridge vibration can be detected. In addition, phase unwrapping and phase calibrated methods are also utilized to guarantee the phase accuracy which can accurately measure the micro-deformation of the bridges [17]. The monitoring installation is illustrated in Fig. 1 to get the micro-deformation of the bridges [19-25].

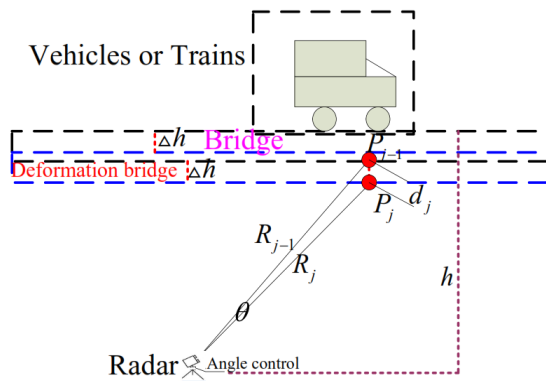


Fig. 1. Correction scheme of radar bridge monitoring.

In Fig. 1, the radar is always under the bridge to get the accurate deformation. If the mm-wave is installed with an angle to the bridge. The micro-deformation measurement results should be corrected by using the correction scheme listed in Fig. 1 and the computations are given in [20]. In Fig. 1, the deformation on the direction of sight is [20]:

$$d_j = R_{j-1} - R_j \quad (j=1,2,3\dots), \quad (3)$$

and we have

$$\Delta h^2 = d_j^2 + (R_{j-1}\theta)^2 - 2R_{j-1}\theta \cdot d_j \cdot \cos\left(\frac{\pi-\theta}{2}\right), \quad (4)$$

when θ is very small. Herein,

$$(R_{j-1}\theta) - 2 \cdot d_j \cdot \sin\left(\frac{\theta}{2}\right) \approx (R_{j-1} - d_j)\theta. \quad (5)$$

Thus, we can get the micro-deformation:

$$\Delta h = \sqrt{d_j^2 + (R_{j-1}\theta)^2 (R_{j-1} - d_j)}. \quad (6)$$

In fact, the micro-deformation is very small obtained from the vibration of the bridges in comparison with the distance between the radar and the bridges. And the micro-deformation is gotten from the measurement, which will be affected by position of the radar and the monitoring angle. To well get the measurement accuracy of the bridge vibrations, many experiments have been done and compared with the ANSYS simulations [20]. As we know, the highway bridge and the freight railway bridges are so wide that we should consider the monitoring position and the angle of the radar installation [19].

On the basis of the bridge micro-deformation monitoring applications, an mm-wave radar is designed, which is comprised of slot antennas, transmitter, receiver, data processing module, and power supplies. In this design, the two slot antenna arrays with high isolation of 60dB are used for transmitting antenna and receiving antenna, which are connected via the cable-to-waveguide transformer to the transmitter and receiver. Herein, the antenna array has a beam width of $4^\circ \times 10^\circ$. In the antenna design, we use the simple slot antenna to form an array, which is based on the experience in our lab. In the data processing, control and signal sampling units are utilized and integrated into the radar system to provide a data sequence control. Additionally, a battery and a voltage regulator are used for providing a stable voltage in the out bridge monitor testing. For the transceiver, the radio frequency signals are generated at the same time. Mixing the received signal with a local replica of the transmitting signal maintains coherence and makes the system compact. In the transmitter, a linear frequency-modulated chirp signal is generated by a direct digital synthesizer, which has a bandwidth of 300MHz, and then it is modulated to intermediate frequency (IF) of $3750\text{MHz} \pm 150\text{MHz}$. The IF chirp signal conveys to the transmitter and is up-converted to a signal with a center frequency of 36.05 GHz. Thus, the signal with a center frequency of 36.05 GHz and bandwidth of 300MHz is transmitted to the air. Then, the signal is received by the receiving antenna for processing by the receiver. The receiver is comprised of low noise amplifier (LNA), a mixer and an IF amplifier, where the LNA is used for amplifying the received echo signal. After that, the amplified signal is down-converted

to IF. Then, the IF amplifier further boosts the IF signal and conveys it to a 16-bit ADC with 10MHz sampling rate. A high-speed Compact Flash (CF) card is used to store the data. The FPGA is used as the controller of the designed radar system. All the radar is designed by us, including the software and the hardware.

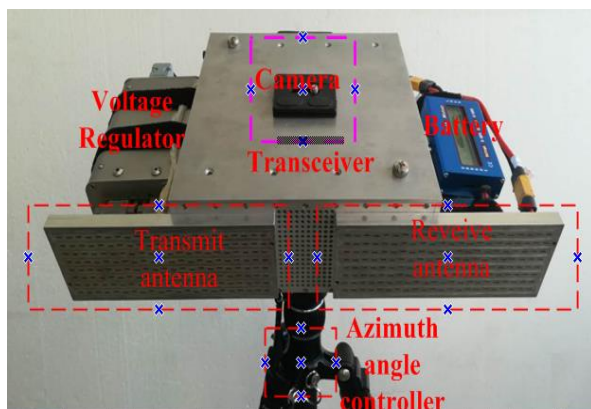


Fig. 2. Photograph of the designed mm-wave radar.

For the outside testing, the data is copied from the CF card and processed by using a laptop. In addition, a camera is installed on the top of the mm-wave radar to give a comparison between the monitoring and the practical scenarios. The designed mm-wave radar is shown in Fig. 2.

III. EXPERIMENT

To verify the effectiveness and the stability of the devised mm-wave radar system, two experiments have been constructed to monitor the micro-deformation of highway and the freight railway bridges. Based on the previous studies for monitoring the micro-deformations of the corner reflectors and the city railway bridges in Beijing, a highway bridge around Beijing-Tianjin expressway which is near the sixth ring roads of Beijing is monitored by using our developed mm-wave radar. The setup of the experiment is given in Fig. 3, where the radar is setup under the bridge. This is to say that the antenna array of the radar is pointed to the bridges directly. If the antenna array is installed and pointed to the bridge with an angle, the correction method should be adopted to ensure the accuracy of the monitoring. As we know, the health condition of the bridge is related the magnitude of the vibration. In the monitoring, the micro-deformation is given in continuous magnitude, which is to illustrate the displacement of the vibration. The monitored micro-deformation can give a reference to the health condition detection of the bridges.

The monitoring scenario is described in Fig. 4, where there is a truck passing through the monitored bridge. The monitored result is illustrated in Fig. 5. It is

found that there is no vibration when there are no vehicles passing across the bridge. The status of the bridge changes quickly when there are vehicles running through the bridge.



Fig. 3. Setup of the bridge vibration monitoring.



Fig. 4. Scenario of highway bridge monitoring.

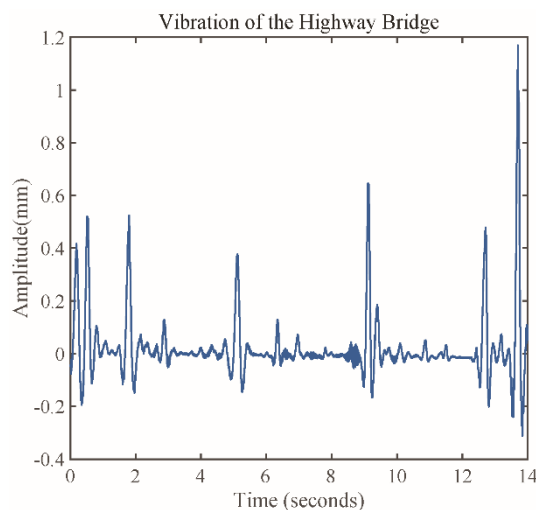


Fig. 5. Experiment result on vertical vibration of the highway bridge

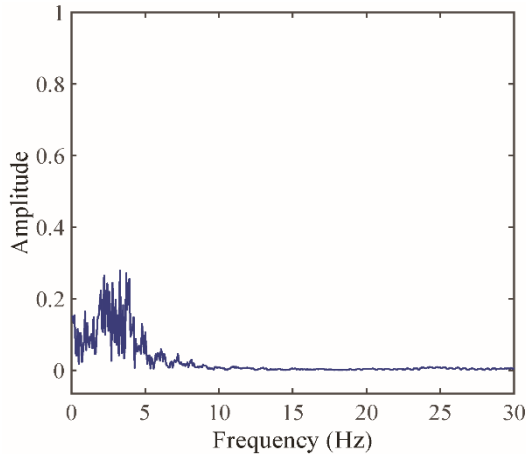


Fig. 6. Spectrum of the vertical vibration of the highway bridge w/o filter (Normalized amplitude in millimeter).

From the bridge monitoring experiments and the monitoring results of the highway bridge vibration monitoring, we found that the calculation method for loading vibration of highway bridge is similar with calculation method for loading vibration of light-railway bridge in [20]. At the same time, there are several trucks and cars running on the bridges. These vehicles hit the bridge to produce the strong vibrations during the different time at 0.5s, 0.8s, 2s, 5s, 9s, 12.3s and 13.8s. When the vehicles leave the bridge, the vibrations disappear quickly. There is some residual in the monitoring period, which might be caused by the radar installation position which is set under the bridge. Since the highway bridge is wide, the vibration is different at each side, which also depends on types of the vehicles. From the results, we can see that truck gives a strong hit to the bridge, and hence, an obvious vibration is appeared around 13.8s. Also, the vibrating frequency is considered to provide a reference for avoiding the self-resonance of the bridges.



Fig. 7. Setup and scenario of freight railway bridge monitoring.

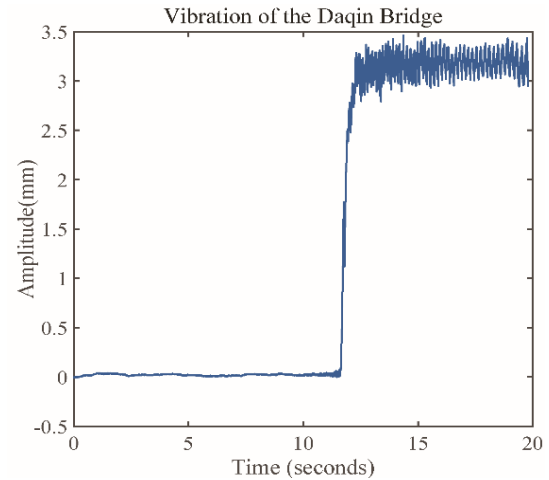


Fig. 8. Experiment result on vertical vibration of the freight railway bridge.

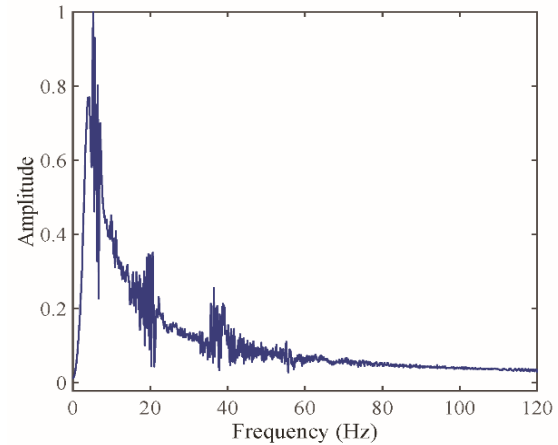


Fig. 9. Spectrum of the vertical vibration of the freight railway bridge with filter (Normalized amplitude in millimeter).

The spectrum of the highway bridge vibration can be gotten, which is illustrated in Fig. 6. From Fig. 6, it is clearly seen that the bridge vibration during the monitoring period is comprised of several different vibration frequencies which are focus on 0-5Hz. Based on the analysis and comparison with the optical picture, we found that the loading vibration frequency of the bridge is caused by the truck at 13.8s, while the vibration appeared at 12.8s is caused by the smaller truck. The bridge is a prestressed continuous concrete bridge made of several spans, which is supported by box girders [26]. The loading frequencies of the box girder caused by different vehicles are approximately 3Hz, which have relationship to the length of these vehicles. Herein, the relationship is given by [20]:

$$f = \frac{v}{L}, \quad (7)$$

In this experiment, the velocity of the truck is 110km/h. The length of the truck and the car is around 15m. Thus, the vibration frequency happened at 2-3Hz, and the complex vibration frequencies may be caused by the other vehicles passing though the bridge.

The vibration of the bridge will be affected by the material and the structure of the blocks and the boxes [22], which can be calculated by the following equation [20, 27]:

$$f_s = \frac{1}{2\pi} \sqrt{\frac{\frac{1}{2}EI_b \left(\frac{\pi}{L_b}\right)^4 L_b}{\frac{1}{2}m_b L_b}}, \quad (8)$$

where EI_b denotes the stiffness of the vertical bending of the bridge, L_b represents the length of bridge span, and m_b is the weight of the bridge per unit length. Thus, if we can get the accurate parameters of the bridges, we can also get the natural frequency of the bridge vibration.

The natural frequency of the bridge vibration is about 2-3Hz, which is approximately equal to the vibration frequency of the bridge obtained at 13.8s. Moreover, the vibration of the highway bridge is complex since there are many vehicles running on the bridge, and the structure, material and geographical positions are complex, making it difficult to select a good position to install the designed mm-wave radar. However, our designed mm-wave radar can get the accurate vibration of the bridge.

As for freight railway bridge monitoring, a freight railway bridge on the Daqin freight railway around Yanqing is monitored. The setup of the railway bridge monitoring and monitoring scenario for freight railway bridge vibration are presented in Fig. 7, where the radar is still installed under the bridge and a train has more than 100 boxes which are full with mines, is passing though the bridge. The monitored result is presented in Fig. 8. We can see that the bridge is static when there are no trains. When a train reaches the bridge, there is a strong vibration whose magnitude is large. Then, the vibration magnitude is invariable when the train is passing though the bridge in about 3 minutes. Thus, we found that the vibration of the freight railway bridge is different with the highway bridge and high-speed railway bridge. The spectrum of the freight railway bridge vibration is analyzed and is given in Fig. 9. It can be seen that the bridge has a strong vibration as the train arrive the bridge, and the vibration frequency is about 6Hz. There is a resonance at 20Hz and 40Hz which might be caused by the head of the train lying at the middle of the train and the leaving of the train from the bridge. Also, the free vibration of the monitoring freight railway bridge is complex since it is near a highway and crosses on a river. From the above monitoring results, we found that the vibrations from the freight railway bridge

and highway bridge are mainly determined by the changes of the bridge structure. The dominant vibrations of such bridges are symmetry with vertical bending of the main girder when the interferometry radar is fixed. From the experiments and discussions, it is worth noting that the vibrations of the bridges can be well monitored. To get the fast and accurate monitoring, the antenna array should be pointed to the bridge directing.

VI. CONCLUSION

A mm-wave radar has been designed and used for bridge micro-deformation monitoring. Two experiments have been setup to monitor a highway and freight railway bridges. The monitoring results showed that the proposed mm-wave can well monitor the vibrations of the highway and freight railway bridges with a high resolution and a good precision. In addition, the proposed mm-wave radar can also well detect the coming of the train in the freight railway bridge, which makes the radar very useful for bridge micro-deformation and the rail vibrations. In the future, we will develop reconfigurable and MIMO antennas based on defected ground plane to make the designed radar light [28-31].

ACKNOWLEDGMENT

This paper is supported by the National Key Research and Development Program of China (2016YFE0111100), Key Research and Development Program of Heilongjiang (GX17A016), the Science and Technology innovative Talents Foundation of Harbin (2016RAXXJ044), the Natural Science Foundation of Beijing (4182077), China Postdoctoral Science Foundation (2017M620918), the Fundamental Research Funds for the Central Universities (HEUCFM180806).

REFERENCES

- [1] Z. Li, T. Chan, and J. Ko "Evaluation of typhoon induced fatigue damage for Tsing Ma Bridge." *Engineering Structures*, vol. 24, no. 8, pp. 1035-1047, 2002.
- [2] X. He, W. Teng, Z. Yu, et al., "Recent developments of high-speed railway bridges in China," *Struct. Infrastruct. Eng.*, vol. 13, no. 12, pp. 1584-1595, 2017.
- [3] X. He, Z. Yu, and S. Hu, "Main achievements and technical challenges of high-speed railway bridges in China," in *Proc. IABSE Conf.*, 2016.
- [4] M. R. Chowdhury, et al., "Accelerometers for bridge load testing," *NDT E Int.*, vol. 36, no. 4, pp. 237-244, 2003.
- [5] Z. Zhang and Q. Liu, "Research of bridge health monitoring data acquisition system," *Boletín Técnico.*, vol. 55, no. 10, pp. 411-418, 2017.
- [6] C. Gentile, "Application of microwave remote sensing to dynamic testing of stay-cables," *Remote Sens.*, vol. 2, no. 1, pp. 36-51, 2010.

- [7] G. Luzi, M. Crosetto, and E. Fernández, "Radar interferometry for monitoring the vibration characteristics of buildings and civil structures: recent case studies in Spain," *Sensors*, vol. 17, no. 4, 2017.
- [8] C. Li, W. Chen, G. Liu, et al., "A noncontact FMCW radar sensor for displacement measurement in structural health monitoring," *Sensors*, vol. 15, no. 4, pp. 7412-7433, 2015.
- [9] M. Pieraccini, F. Parrini, M. Fratini, et al., "Static and dynamic testing of bridges through microwave interferometry," *NDT E Int.*, vol. 40, no. 3, pp. 208-214, 2007.
- [10] C. Gentile and G. Luzi, "Radar-based dynamic testing of the cable-suspended bridge crossing the Ebro River at Amposta, Spain," in *Proc. 11th Int. VMLC*, 2014.
- [11] M. Pieraccini, M. Fratini, F. Parrini, et al., "High-speed CW step-frequency coherent radar for dynamic monitoring of civil engineering structures," *Electron. Lett.*, vol. 40, no. 14, pp. 907-908, 2004.
- [12] S. Hensley, D. Moller, S. Oveisgharan, et al., "Ka-band mapping and measurements of interferometric penetration of the greenland ice sheets by the GLISTIN radar," *IEEE J. Sel. Topics Appl. Earth Observ.*, vol. 9, no. 6, pp. 2436-2450, 2016.
- [13] L. Mayer, B. S. Yanev, L. D. Olson, and A. W. Smyth, "Monitoring of Manhattan bridge for vertical and torsional performance with GPS and interferometric radar systems," *Transportation Research Board 89th Annual Meeting*, Washington DC, 2010.
- [14] H. Ko1, K. Cheng, H. Su, et al., "Range resolution improvement for FMCW radars," in *Proc. 5th Euro. Radar Conf.*, 2008.
- [15] H. Wang, M. Jiang, and S. Zheng, "Airborne Ka FMCW MiSAR system and real data processing," in *Proc. 17th Int. Radar Symp.*, 2016.
- [16] C. Wang, H. Zhang, and Z. Liu, *Spaceborne Synthetic Aperture Radar Interferometry Measurement*, Science Press, Beijing, 2002.
- [17] K. Hsu, C. Cheng, and C. Chiang, "Long-term monitoring of two highway bridges using microwave interferometer-case studies," in *Proc. 16th Int. Conf. GPR*, 2016.
- [18] X. Liu, X. Tong, K. Ding, et al., "Measurement of long-term periodic and dynamic deflection of the long-span railway bridge using microwave interferometry," *IEEE J. Sel. Topics Appl. Earth Observ.*, vol. 8, no. 9, pp. 4531-4538, 2015.
- [19] Z. Shao, X. Zhang, and Y. Li, "Analysis and validation of super-resolution micro-deformation monitoring radar," *Progress In Electromagnetics Research (PIER) M*, vol. 62, no. 12, pp. 41-50, 2017.
- [20] Z. Shao, X. Zhang, Y. Li, and J. Jiang, "A comparative study on radar interferometry for vibrations monitoring on different types of bridges," *IEEE Access*, vol. 6, pp. 29677-29684, 2018.
- [21] Z. Shao, X. Zhang, J. Ren, and Y. Li, "High-speed railway bridge vibration measurement and analysis with radar interferometry," *2018 International Geoscience and Remote Sensing Symposium*, Valencia, Spain, 23-27 July, 2018.
- [22] Z. Shao, X. Zhang, J. Ren, and Y. Li, "Short range SAR imaging for 2-D micro-deformation detection," *2018 IEEE International Symposium on Antennas and Propagation*, Boston, MA, USA 14-21 July 2018.
- [23] X. Zhang, J. Ren, Z. Shao, J. Jiang, and Y. Li, "Vehicles detection experiments with Ka band FMCW ISAR," *The 39th Progress In Electromagnetics Research Symposium*, Singapore, 19-22 Nov. 2017.
- [24] X. Zhang, Z. Shao, J. Ren, J. Jiang, and Y. Li, "Performance verification and testing for micro deformation detection radar," *The 39th Progress In Electromagnetics Research Symposium*, Singapore, 19-22 Nov. 2017.
- [25] Y. Li, Z. Shao, X. Zhang, and J. Jiang, "Vibrations monitoring for highway bridge using mm-wave radar," *IEEE 7th Asia-Pacific Conference on Antennas and Propagation*, Auckland, New Zealand, 5-8 Aug. 2018.
- [26] J. Li and M. Su, "The resonant vibration for a simply supported girder bridge under high speed trains," *J. Sound Vib.*, vol. 224, no. 5, pp. 897-915, 1999.
- [27] W. Wang, Y. Yang, P. Liu, et al., "Analysis of influence of MTMD on the vertical vibration character of high-speed railway 32m prestressed concrete simply supported box beam," *Environ. Eng.*, vol. 30, no. 4, pp. 153-155, 2016.
- [28] Y. Li, S. Luo, and W. Yu, "A triple stop-band filter based on defected microstrip line structures," *Applied Computational Electromagnetics Society Journal*, vol. 33, no. 7, pp. 752-757, 2018.
- [29] K. Yu, Y. Li, and X. Liu, "Mutual coupling reduction of a MIMO antenna array using 3-D novel meta-material structures," *Applied Computational Electromagnetics Society Journal*, vol. 33, no. 7, pp. 758-763, 2018.
- [30] T. Jiang, T. Jiao, Y. Li, and W. Yu, "A low mutual coupling MIMO antenna using periodic multi-layered electromagnetic band gap structures," *Applied Computational Electromagnetics Society Journal*, vol. 33, no. 3, pp. 305-311, 2018.
- [31] L. Zhao, F. Liu, X. Shen, G. Jing, Y. Cai, and Y. Li, "A high-pass antenna interference cancellation chip for mutual coupling reduction of antennas in contiguous frequency bands," *IEEE Access*, vol. 6, pp. 38097-38105, 2018.

Ungrounded Lightning Surge Protection Device for Wireless Sensor Networks Node in the Wilderness

Qinghua Cao, Lixia Yang, and Shu Yan

School of Computer Science and Communication Engineering
Jiangsu University, Zhenjiang, 212013, China
cqh@ujs.edu.cn, lixiayang@yeah.net, yanshu@ujs.edu.cn

Abstract — In the wilderness, the use of wireless sensor network (WSN) nodes because of their maintenance-free remote-monitoring characteristic demands ungrounded lightning surge protection. This paper proposes a design of a protection device with functions of low-frequency surge cutting off and radio-frequency (RF) signal passing. In this device, the discharge circuit consists of a three-level surge by-pass circuit, an outer conductor antenna, and a copper-clad circuit board. The current capacity, start time, and output voltage meet the requirements of surge protection for a weak current device. Discrete components that provide the protective feature were involved in calculating impedance matching, and the parameters of these components were estimated and adjusted constantly at the test stage to ensure that the impedance of the inserted protection device matches with those of the node RF transceiver module and antenna. The experimental results show that the node with the ungrounded protection device can pass fourth-level surge immunity experiments and run for 49 months at the outdoor monitoring site in the Xinjiang coal fire area.

Index Terms — Impedance matching, lightning surge protection, ungrounded, wireless sensor networks.

I. INTRODUCTION

Lightning protection is an important topic of concern in the electromagnetic compatibility (EMC) research, and has a long history of developments made in heavy electricity-protection devices, with introduction of more mature technology [1–4]. In addition, many scholars have studied the different lightning characteristics [5–8]. With the development of large-scale integrated electronic systems, researchers began focusing on lightning protection related to weak electricity devices, and different protective devices and various application specifications were devised [9–12]. The WSN node deployed in the wilderness, with low voltage, low power, and high frequency, is a very special weak-electricity device, which requires a protection device with quick response, low output voltage, and large current capacity.

The communications and free-maintenance characteristics of the WSN node require that the protection device does not affect the transmission of signals and does not include a grounded device that must be maintained. To date, most existing protection devices are grounded [13], and some ungrounded protection circuits that have been devised have an applicable scope in the aspects of starting voltage, response speed, and current capacity [14]. In this study, the authors designed an ungrounded lightning protection device, which consists of a series circuit and three-level shunt circuit. The transfinite surge energy passed through the discharge circuit formed by a three-level discharge passage, copper-clad circuit board, and an outer conductor antenna, neutralizing the induced charge. The characteristic and import impedances matched with those of the antenna and radio-frequency (RF) transceiver module of a 2.4GHz WSN node. The minimum return loss, voltage standing wave ratio (VSWR) fit the requirements specified in the IEC Standard 62305-1 [11]. The results of a surge immunity test and field test show that an ungrounded protection device for the WSN node can defend against kilovolt/kilo-ampere lightning surges.

II. PERFORMANCE REQUIREMENTS

The lightning effects include direct and induction lightning, where the former shows strong damage ability and a small occurrence probability, whereas the latter shows a high occurrence probability and large impact scope [15]. According to the international standard of IEC 61000-4-5 [16], the time waveform of surge caused by induction lightning can be simulated using a combined wave of 1.2/50–8/20 μ s, which increases to the withstand value of weak electricity device about several nanosecond. The frequency spectrum and energy concentration are in the low-frequency range of 0–100 kHz, and the peak is ranked in kV/kA.

The antenna of WSN nodes deployed in wilderness areas, when exposed to air, can receive signal and easily be at the risk of a lightning surge. Therefore, the protection device is mainly focused on the antenna feeder system.

A general WSN node is a low-voltage and low-current device, for example, the JN5139 node, with a working frequency of 2.4 GHz, working voltage of 2.2–3.6 V, and withstand current of 150 mA. The surge waveform rises at the withstand voltage of the node for about a few milliseconds. Overall, the surge-protection circuit should have many technical indicators to meet the industry standards [12], such as response speed in nanoseconds, withstand voltage/current in kilovolts/kilo-ampere, an output clamping voltage between the node working voltage and maximum withstand voltage, a maximum continuous working voltage greater than 1.2 times the antenna feeder signal voltage, and a by-pass low-frequency surge. Impedance characteristics of the input and output ports should respectively match the impedance characteristics of the antenna and node, and the insertion loss and voltage standing wave ratio should meet the industry standards. All of these technical indicators are listed in Table 1.

Table 1: Technical indicators of surge protection device

Parameter	Requirement
Operating frequency	2.4 GHz
Current impulse withstand capability	kA
Voltage impulse withstanding capability	kV
Response time	ns
Transmission power	$\geq 1.5 \times \text{node power}$
Voltage standing wave ratio	≤ 1.2
Insertion loss	≥ -1 dB
Impedance characteristic	50 Ω

III. LIGHTNING SURGE PROTECTION CIRCUIT

The designed surge protection circuit for the antenna feeder system of WSN consists of a series circuit with a shunt part, as shown in Fig. 1.

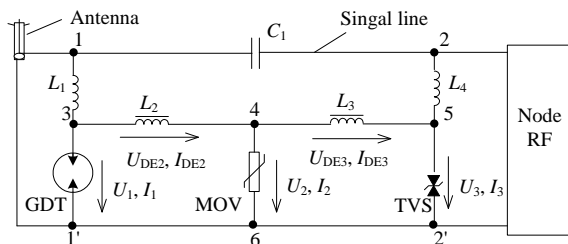


Fig. 1. Principle diagram of the antenna feeder surge protection circuit.

The series circuit comprises a signal line with capacitance C_1 placed between the antenna and node RF module, a cutoff low-frequency surge, and transit RF signal. Further, the shunt part comprises a discharge

channel, and is composed of a gas discharge tube (GDT), metal-oxide varistor (MOV), and transient voltage suppressor (TVS). The output voltage, current capacity, and startup time of the three levels decline in turn. Based on these three channels, the signal line and outer conductor of the antenna form a discharge circuit. Inductances L_1 and L_4 separate the signal line from the surge discharge channel.

A. Operating principle of circuit

Under normal conditions, the discharge channel closes. For the low-frequency surge wave, capacitor C_1 is equivalent to an open circuit and inductance L_1 is equivalent to a short circuit; thus, the voltage of port 1–1' is approximately equal to that of port 3–1'. When the surge approaches, the voltage at port 1–1', consisting of the work and surge voltages, rises quickly and takes approximately 3.5 ns to reach the node withstandable voltage. Then, the TVS with a small starting voltage and fast startup time, is the first to perform conduction, and the resulting output voltage is less than the tolerance voltage of the WSN node. The conduction path between ports 1–1' passes through 1–3–4–5–2'–1'. As the current of port 1–1' increases, induced dynamic voltage U_{DE3} by inductance L_3 also increases. If the superposition value of U_{DE3} and TVS clamp voltage U_3 is greater than the open voltage of MOV, the secondary channel starts to discharge. In addition, if induced dynamic voltage U_{DE2} with the addition of MOV clamping voltage U_2 is greater than the starting voltage of GDT, the first main discharge channel discharges current to the copper-clad board and forms a loop with the outer conductor of the antenna line. As the clamp voltages of GDT, MOV, and TVS decrease progressively, the voltage difference between the stages is undertaken by inductances L_2 and L_3 .

The three-level circuit requires coordinated work. The initial voltage, withstand current, and energy should abide by the following rules:

- 1) Before a subsequent level approaches the maximum tolerance energy, the following level starts functioning.
- 2) Before the following level is initiated, the subsequent level can withstand the surge current.
- 3) The startup voltage of the following level should be less than the withstand voltage of the subsequent level.

B. Determination of component types and parameters

According to the working principle of the protection circuit, coordination principle at all levels, and electrical characteristics of the node, the ESD5B5.0ST1G-type TVS, 20D180K-type MOV, and A81-C90X-type GDT [17–19] were selected.

1) Inductances L_2 and L_3

When the surge current increases rapidly, the induced electromotive force of the interstage inductance

pushes the first level of the protection component to start; this avoids excessive surge damage to the subsequent level. Figure 1 shows that the GDT discharge depends on whether the sum of U_2 and U_{DE2} is greater than GDT discharge voltage U_S :

$$U_1 = U_2 + U_{DE2} > U_S, \quad (1)$$

where

$$U_{DE2} = L_2 \cdot \frac{dI_{DE2}}{dt}. \quad (2)$$

From (1) and (2), the value of inductance L_2 can be derived as follows:

$$L_2 > \frac{U_S - U_2}{dI_{DE2}/dt}. \quad (3)$$

For the 8/20- μ s surge waveform with a 1-kA peak, $dI_{DE2}/dt \cong 0.1$ kA/ μ s. Further, $U_2 = 36$ V for the MOV clamp voltage [18], and GDT discharge voltage, $U_S = 600$ V [19]. When $L_2 > 5.64$ μ H, the GDT can be pushed; therefore, inductance L_2 was set at 10 μ H to leave some margin. By using the same method, the value of inductance L_3 that could push MOV to start was set at $L_3 > 1.08$ μ H. To leave some margin, L_3 was set at 1.2 μ H.

2) Capacitance C_1

In the RF band, inductances L_1 and L_4 segregate the signal line from the discharge channel, as shown in Fig. 1. In addition, capacitance C_1 and resistance R (50 Ω) of the WSN node constitute the RC high-pass filter. The voltage ratio between output and input is obtained as:

$$\dot{A} = \frac{R}{R + 1/j\omega C_1} = \frac{1}{1 + 1/j2\pi f RC_1}, \quad (4)$$

and the cutoff frequency is defined as:

$$f_L = 1/2\pi RC_1. \quad (5)$$

To transmit the RF signal (2.4–2.4835 GHz), cutoff frequency f_L should be less than 2.4 GHz so that C_1 should be larger than 1.3 pF.

Table 2: Maximum transmission distance of the WSN node with a protection broad with different C_1

Capacitor Value (pF)	Transmission Distance (m)					
	Sunny, Empty Area	Sunny, 0.5 m Grass	Cloudy, Empty Area	Cloudy, 0.5 m Grass	Rainy Day, Empty Area	Rainy Day, 0.5 m Grass
1	200	120	208	95	190	83
3	240	135	220	105	196	88
5	272	142	225	103	198	89
10	233	117	193	94	175	84
15	220	103	186	90	169	82

Considering the influence of the distributed capacitance, inductance, and resistance in the RF circuit, the test method was used to determine the final value of C_1 . As the transmission distance between two nodes can directly reflect the communication quality under the premise of no packet loss, the test method measures the

maximum transmission distance with different C_1 values. Multiple test results under six conditions were averaged and are listed in Table 2. As shown, following a change in the capacitance value, the transmission distances are similar in all six environments. When C_1 increases from 1 to 5 pF, the transmission distance gradually increased, and then began to decrease when C_1 increased to 15 pF. Therefore, the final determination of C_1 is 5 pF.

C. Impedance matching

In this study, the discrete component of the protection device also undertakes impedance matching. For the RF signal, L_2 and L_3 are equivalent to an open circuit, and GDT and TVS have stray capacitance; thus, the protection circuit of Fig. 1 can be equivalent to Fig. 2.

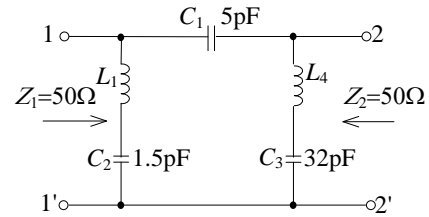


Fig. 2. Impedance-matching equivalent circuit of the protection circuit. Equivalent impedances Z_1 and Z_2 of port 1–1' and 2–2', respectively (Fig. 1).

In Fig. 2, C_2 and C_3 are the stray capacitances of GDT and TVS. Equivalent impedances Z_1 and Z_2 of ports 1–1' and 2–2', respectively, are equal to the characteristic impedances of the antenna and WSN node, and are defined as [20]:

$$Z_1 = \sqrt{Z_{oc1} Z_{sc1}}, \quad Z_2 = \sqrt{Z_{oc2} Z_{sc2}}, \quad (6)$$

where Z_{oc1} or Z_{sc1} is the equivalent impedance of port 1–1' when port 2–2' is an open- or a short-circuit; Z_{oc2} or Z_{sc2} is the equivalent impedance of port 2–2' when port 1–1' is the open- or a short-circuit:

$$Z_{oc1} = \left(j\omega L_1 + \frac{1}{j\omega C_2} \right) // \left(\frac{1}{j\omega C_1} + j\omega L_4 + \frac{1}{j\omega C_3} \right), \quad (7)$$

$$Z_{sc1} = \left(j\omega L_1 + \frac{1}{j\omega C_2} \right) // \left(\frac{1}{j\omega C_1} \right), \quad (8)$$

$$Z_{oc2} = \left(j\omega L_4 + \frac{1}{j\omega C_3} \right) // \left(\frac{1}{j\omega C_1} + j\omega L_1 + \frac{1}{j\omega C_2} \right), \quad (9)$$

$$Z_{sc2} = \left(j\omega L_4 + \frac{1}{j\omega C_3} \right) // \left(\frac{1}{j\omega C_1} \right), \quad (10)$$

where $Z_1 = 50$ Ω , $Z_2 = 50$ Ω , $C_1 = 5$ pF, $C_2 = 1.5$ pF [19], $C_3 = 32$ pF [17], and $\omega = 2\pi \times 2.4$ GHz. All of these parameters are substituted into (6)–(10) to compute L_4 and L_1 as follows: $L_4 \approx 5.4$ nH and $L_1 \approx 151$ nH. At this point, all discrete element models and parameters of the protection circuit have been established.

D. Ungrounded design

This device was designed for handling a low-grade lightning surge. The printed circuit board (PCB) of the protection device, excluding the signal lines and RF-signal channel area, is copper clad on both sides, which are connected via holes to an array to increase the volume. The thickness of the 140- μm copper foil is 4 times that of the ordinary PCB, thus improving the capacity of holding the electric charge as a buffer pool. The designed protection board is shown in Fig. 3.

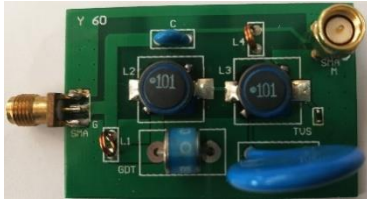


Fig. 3. The proposed surge-protection-device board.

IV. PERFORMANCE TEST

Based on the above-mentioned analysis, the ungrounded lightning surge-protection device was developed and tested according to the performance indicators in Table 1.

A. Return loss

Figure 4 shows the S_{11} curve of the surge-protection boards measured using a vector network analyzer.

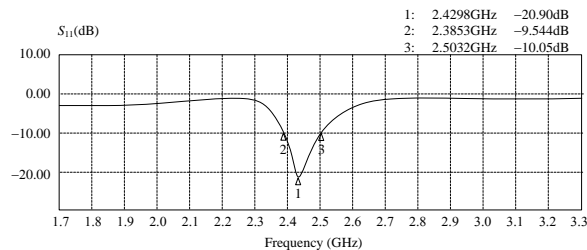


Fig. 4. S_{11} parameter curve of the surge protection device.

The center frequency in the frequency band of WSN node was 2.43 GHz; the minimum value of S_{11} was -20.9 dB, which approached the minimum value of the antenna. In addition, a -10 -dB bandwidth (2.39–2.50 GHz) covers the frequency band of the WSN node (2.4–2.4835 GHz). According to the minimum S_{11} , the VSWR is calculated as 1.198.

B. (VSWR)

The relation of VSWR, S_{11} and reflection coefficient Γ is given as:

$$S_{11} = 20 \lg(\Gamma), \quad (11)$$

$$\text{VSWR} = \frac{(1 + \Gamma)}{(1 - \Gamma)}. \quad (12)$$

The minimum S_{11} value, as shown in Fig. 4, was substituted into (11) and reflection coefficient Γ at the center frequency point was obtained as 0.09, which was substituted into (12) to obtain VSWR of 1.198; this is less than the indicator value of VSWR in Table 1.

C. Insertion loss

Under the impedance-matching conditions of the port, the S_{21} parameter can represent insertion loss, and was measured using the vector network analyzer. Accordingly, the insertion loss at 2.43 GHz was obtained as -0.9 dB, which is greater than the value in Table 1.

D. Packet-loss probability test

The monitoring density of the WSN nodes that are deployed in reality is less than 100 m; therefore, the packet-loss probability was measured within this distance. Over a period of seven days, one node sent one data package per second. The number of packets received per hour was then counted and the average packet loss rate per hour was computed. The test result in Fig. 5 shows that the packet-loss probability does not show any obvious change before and after the addition of the surge protection device to the nodes.

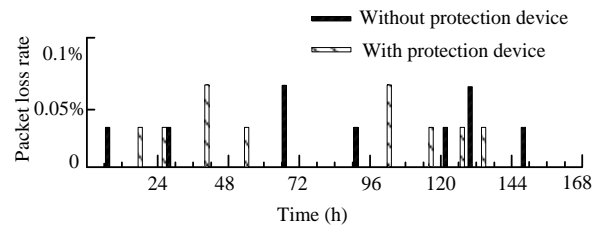


Fig. 5. Packet-loss rate of nodes with and without a surge-protection device.

E. Surge immunity test

The experimental conditions and test procedure were set as stipulated by the international standard of IEC 61000-4-5.

Experimental conditions: The test was conducted under standard climatic and electromagnetic environment conditions specified by the IEC 61000-4-5 standard. The environment temperature was 26 $^{\circ}\text{C}$, relative humidity was 45%, and atmospheric pressure was 98 kPa. The lab environment was without electromagnetic interference.

Connection: As shown in Fig. 6, the antenna and another port of the protection device were separately connected through a combined-wave-signal generator and an RF port of the protected node. A 3.7V lithium iron phosphate battery was used to supply power to the node.

Testing program:

- 1) A four-level test was conducted with voltages from low to high: 0.5, 1, 2, and 4 kV.
- 2) The source impedance of the generator was 2 Ω.
- 3) The test surge wave numbers were calculated to obtain five each of positive and negative waveforms.
- 4) Repetitive rate: 1 time/min.

According to the test plan, we conducted the tests many times, as shown in Table 3.

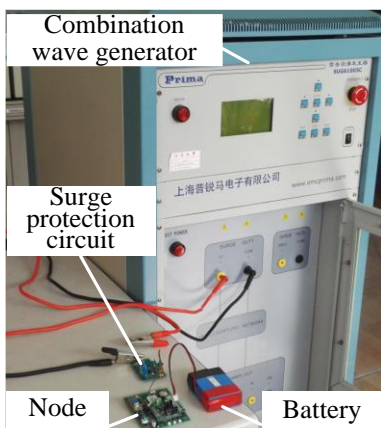


Fig. 6. Test connection diagram of the surge protection device.

Table 3: Experimental phenomena of surge immunity test

Test Level	Impulse Voltage (kV)	Surface Arc of GDT	Lines on PCB	Performance Character of Node	Peak Current of Node (mA)
1	0.5	Invisible	Intact	Normal	55
2	1	Visible	Intact	Normal	58
3	2	Clear	Intact	Normal	62
4	4	Bright	Intact	Normal	86

With the increase in test level, the GDT discharge intensity increased, and a dazzling arc gradually appeared on the GDT surface, indicating that a large amount of surge energy drains off through the GDT channel for protection. The line of the PCB is wider and thicker than that of a general board, and withstands the tests. During the testing, one node could continuously receive all the packets from another protected node, implying normal RF communication between the nodes. The performance characteristics, such as communication, distance, and packet loss, of the tested node are the same as those for an untested node. The peak current of the node increased with the increase in the test level, indicating that the surge affects the node’s working current. After the surge test, the node’s working current was measured again, and it was normal. Therefore, it can be concluded that the node with a protection device can pass the level-4 surge immunity test.

V. CONCLUSION

The protection circuit designed for WSN node bypasses the low-frequency surge and passes through the high-frequency signal. Protection components were installed at three levels of the bypass circuit and cooperated in start time and energy. When the bypass circuits are conducting successively, the RF signal line and outer conductor of the antenna form a closed loop through the TVS, MOV, and GDT. This loop can consume surge energy, and the thickness of the copper foil of the PCB can improve the capacity of holding the electric charge as a buffer pool. This helps the discharge circuit lines to withstand surge energy. The experimental results show that the node with the protection device can pass the standard level 4 of the surge immunity test. The proposed device was applied to the fire-monitoring network of the Xinjiang coalfield, and helped in the safe and continuous monitoring of the network for over four thunderstorm seasons. If we change the component types and parameters and adjust the working frequency and characteristic impedance, this ungrounded device could be used to protect other similar weak current devices.

ACKNOWLEDGMENT

This work was supported by the Natural Science Foundation of China (No. 41474095), the Science and Technology Aid Xinjiang Project (No. 201191210) and the College Graduate Research Innovation Projects of Jiangsu Province in (No. CXLX12_0654).

REFERENCES

- [1] M. A. Uman, *The Art and Science of Lightning Protection*. Cambridge University Press, Oxford, 2010.
- [2] M. O. Goni and M. S. I. Hossaini, “Numerical electromagnetic analysis of GSM tower under the influence of lightning over-voltage,” *ACES Journal*, vol. 24, no. 3, pp. 338-345, 2009.
- [3] B. Glushakow, “Effective lightning protection for wind turbine generators,” *IEEE Trans. Energy Convers.*, vol. 22, pp. 214-222, 2007.
- [4] V.A. Rakov and F. Rachidi, “IEEE overview of recent progress in lightning research and lightning protection,” *IEEE Trans. Electromagn. Compat.*, vol. 51, pp. 428-442, 2009.
- [5] M. O. Goni and A. Ametani, “Analysis and estimation of surge impedance of tower,” *ACES Journal*, vol. 24, no. 1, pp. 72-78, 2009.
- [6] D. H. Trout, J. E. Stanley, and P. F. Wahid, “Evaluation of lightning induced effects in a graphite composite fairing structure,” *ACES Journal*, vol. 26, no. 12, pp. 981-988, 2011.
- [7] M. Izadi, M. A. Ab Kadir, and M. Hajikhani, “Evaluation of lightning current and ground reflection factor using measured electromagnetic field,” *ACES Journal*, vol. 29, no. 1, pp. 107-115, 2014.

- [8] A. Karwowski, A. Noga, and T. Topa, "Computationally efficient technique for wide-band analysis of grid-like spatial shields for protection against LEMP effects," *ACES Journal*, vol. 32, no. 1, pp. 87-92, 2017.
- [9] P. Hasse, *Overvoltage Protection of low Voltage Systems*. 2nd ed., Institution of Electrical Engineers, United Kingdom, 2000.
- [10] M. O. Goni, E. Kaneko, and H. Takahashi, "Thin wire representation of the vertical conductor in surge simulation," *ACES Journal*, vol. 19, no. 1, pp. 55-64, 2004.
- [11] Protection against lightning - Part 1: General principles, *IEC Standard 62305-1*, 2010.
- [12] Protection against lightning electromagnetic impulse - Part 3: Requirements of surge protective devices, *IEC Standard 61312-3*, 2000.
- [13] S. Furukawa, A. Asakawa, and T. Hosokawa, "Experimental study on surge current to customer's facility owing to lightning stroke on television antenna," *2010 Asia-Pacific Symposium on Electromagnetic Compatibility*, Beijing, China, pp. 1181-1184, Apr. 2010.
- [14] C. F. Barbosa and F. E. Nallin, "Lightning protection of a smart grid sensor., *12th International Symposium on Lightning Protection*, Belo Horizonte, Brazil, pp. 273-277, Oct. 2013.
- [15] V. Cooray, *Lightning Protection*. Institution of Engineering and Technology, London, 2009.
- [16] Testing and measurement techniques – Surge immunity test, *IEC Standard 61000-4-5*, 2009.
- [17] ON Semiconductor Inc., *ESD5B5.0ST1G datasheet*, Available: <http://www.onsemi.com/pub/Collateral/ESD5B5.0ST1-D.PDF>, 2017.
- [18] World Products Inc., *20D180K datasheet*, June 8, 2011.
- [19] EPCOS, *A81-C90X datasheet*, Available: <https://en.tdk.eu/inf/100/ds/A81-C90X-X1380S102.pdf>, 2015.
- [20] D. M. Pozar, *Microwave Engineering*. Addison - Wesley Publishing Company, Boston, 1990.



Qinghua Cao received the B.S. degree in Information Engineering from Xi'an Jiangtong University, Xi'an, Shanxi, China, in 2000 and the M.S. degree in Communication and Information System from Lanzhou University, Lanzhou, Gansu, China, in 2004. She is currently pursuing the Ph.D. degree in Computer Application at Jiangsu University, Zhenjiang, Jiangsu, China. From July 2004 to now, she works at the School of Computer

Science and Communication Engineering, Jiangsu University as a Lecturer. Her main research interest is in Wireless Sensor Networks.



Lixia Yang received the Ph.D. in Electronics Engineering from Xidian University, China, in 2007. He was a Postdoctoral Fellow of Electro Science Laboratory, Ohio State University, USA and worked at Space Science Laboratory, Dallas University, Dezhou, USA, as a Visiting Scholar. He is a Professor with the School of Computer Science and Communication Engineering, Jiangsu University, China, the Member of National Expert Committee of Electromagnetic Scattering and Back-scattering, the Member of American Electromagnetic Research Institute, the Member of American Optical Society, the Senior Member of China Electronics Society. His research interests include electromagnetic scattering characteristics of complex targets (dielectric), antenna theory and design of communication system, RF microwave circuit design, time-domain computational electromagnetism.



Shu Yan received the B.S. degree in Physics, Nankai University, Tianjin, China, in 1978 and the Ph.D. degree from Department of Information and Communication Engineering of Xi'an Jiaotong University, Xi'an, Shanxi, China, in 2003. From October of 2005 to now, she works at the School of Computer Science and Communication Engineering, Jiangsu University, as a Professor, doctor adviser. Her research interests include Wireless Network, Computation Electromagnetics, Electromagnetic Field and Microwave Technology and Electric and Electromagnetic Exploration.

High Selectivity Bandpass Filter Using Three Pairs of Coupled Lines Loaded with Shorted Stubs

Kai-Da Xu^{1,2,3,*} and Fengyu Zhang^{1,2}

¹Department of Electronic Science, Xiamen University, Xiamen, 361005, China

²Shenzhen Research Institute of Xiamen University, Shenzhen 518057, China

³Department of Electrical and Computer Engineering, University of Wisconsin–Madison, Madison, WI 53706, USA
kaidaxu@ieee.org

Abstract — A high selectivity bandpass filter with multiple transmission poles (TPs) and transmission zeros (TZs) has been presented. By employing three pairs of parallel-coupled lines and two shorted stubs, sharp roll-off skirts and high stopband rejections can be achieved with five TPs and ten TZs. Theoretical analysis is explained and simulated results are illustrated on this high-performance filter. Finally, a bandpass filter example with center frequency of 2.15 GHz and 3-dB fractional bandwidth of 19% is designed, fabricated, and measured. It is shown that the measured transition band roll-off rates are better than 425 dB/GHz. Good agreement between the simulations and measurements validates the design method.

Index Terms — Bandpass filter, parallel-coupled lines, roll-off rates, shorted-circuit stubs, transmission poles, transmission zeros.

I. INTRODUCTION

Microstrip bandpass filters (BPFs) have drawn much attention to researchers due to their simple structure, small size, and easy fabrication. In recent years, BPFs using parallel-coupled lines are widely studied because the high accuracy and consistency of the filter circuit can be easily guaranteed [1-3]. Various structures using parallel-coupled lines loaded with stubs are designed for constructing high-performance filters, including open/shorted stubs [4-6], stepped-impedance stubs [7-9], and open/shorted coupled lines [10, 11]. Although wideband characteristics has been achieved in many filter designs, high frequency selectivity and excellent stopband suppression are facing the challenge due to lack of transmission zeros (TZs). In order to realize more pairs of TZs in the stopband, dual-mode ring resonators loaded with open stubs and open/shorted coupled lines have been proposed in [12]. However, this design method leads to large size of the filter circuit, which cannot meet the requirements of miniaturization.

In this paper, a high-selectivity BPF using three pairs of coupled lines loaded with two shorted stubs is

proposed. Compared with our previous work [13], this BPF can generate two more TZs in the stopband by employing two quarter-wavelength shorted stubs to the $3\lambda_g/4$ parallel coupled lines. Therefore, sharper roll-off skirts and high out-of-band rejection can be achieved with five TPs and ten TZs. For demonstration, a filter example with 3-dB fractional bandwidth (Δf) of 19% and operating center frequency at 2.15 GHz is fabricated, whose simulated and measured results are in good agreement.

II. BPF STRUCTURE AND DESIGN

Figure 1 shows the ideal circuit of the proposed BPF with three pairs of parallel-coupled lines and two shorted stubs, which can achieve high performance of ten TZs and five TPs. A pair of $\lambda_g/4$ parallel-coupled lines (even/odd-mode characteristic impedance Z_{0e2} , Z_{0o2} , electrical length θ , $\theta=90^\circ$ at the center frequency of f_0) in the middle are cascaded with two pairs of $3\lambda_g/4$ parallel-coupled lines (even/odd-mode characteristic impedance Z_{0e1} , Z_{0o1} , electrical length 3θ) at two sides. Two shorted stubs (characteristic impedance Z_1 , electrical length θ) are loaded on the end of two pairs of $3\lambda_g/4$ parallel-coupled lines, respectively. The characteristic impedances of the two feed lines at the input/output ports are both Z_0 . For further demonstration, theoretical analysis and design of the high selectivity BPF will be illustrated below.

The comparisons of the simulated transmission and reflection coefficients between the proposed BPF (i.e., BPF loaded with shorted stubs) and the BPF in [13] (i.e., BPF without shorted stubs) are shown in Figs. 2 (a) and (b), respectively. There are five TPs located at the two sides of the operating frequency $f_0=1$ GHz for generating a passband. Besides, ten TZs within the stopband are achieved. The impedance matrix deduction can be used for analyzing this BPF circuit. From Fig. 1, we can obtain that $V_2 = V_5$, $I_2 = -I_5$, $V_3 = V_8$, $I_3 = -I_8$, $V_6 = V_9$, $I_6 = -I_9$, $V_7 = V_{12}$, $I_7 = -I_{12}$, and $I_4 = I_{11} = -jV_4/(Z_1 \tan \theta)$. $[Z]^a$ and $[Z]^b$ denote the impedance matrix of the $3\lambda_g/4$ and $\lambda_g/4$ parallel-coupled lines, respectively. The overall impedance matrix Z' of the filter can be calculated as:

$$\begin{bmatrix} V_1 \\ V_{10} \end{bmatrix} = \begin{bmatrix} Z'_{11} & Z'_{12} \\ Z'_{21} & Z'_{22} \end{bmatrix} \begin{bmatrix} I_1 \\ I_{10} \end{bmatrix}. \quad (1)$$

The reflection coefficient S_{11} and transmission coefficient S_{21} can be expressed as:

$$S_{11} = \frac{(Z'_{11} - Z_0)(Z'_{22} + Z_0) - Z'_{12}Z'_{21}}{(Z'_{11} + Z_0)(Z'_{22} + Z_0) - Z'_{12}Z'_{21}},$$

and

$$S_{21} = \frac{2Z'_{21}Z_0}{(Z'_{11} + Z_0)(Z'_{22} + Z_0) - Z'_{12}Z'_{21}}. \quad (2)$$

Based on the impedance matrix deduction, TPs can be calculated by setting $S_{11}=0$. Through calculation, five TPs can be obtained and illustrated as below:

$$f_{p1} = \frac{2f_0}{\pi} \cos^{-1} \sqrt{\frac{Z_{0e1} - 2Z_{0o2} + Z_{0o1}}{2Z_{0e1} + 4Z_{0o2} + 2Z_{0o1}}}, \quad (3)$$

$$f_{p2} = \frac{2f_0}{\pi} \cos^{-1} \sqrt{\frac{Z_{0e1} - 2Z_{0e2} + Z_{0o1}}{2Z_{0e1} + 4Z_{0e2} + 2Z_{0o1}}}, \quad (4)$$

$$f_{p3} = f_0, \quad (5)$$

$$f_{p4} = \frac{2f_0}{\pi} (\pi - \cos^{-1} \sqrt{\frac{Z_{0e1} - 2Z_{0e2} + Z_{0o1}}{2Z_{0e1} + 4Z_{0e2} + 2Z_{0o1}}}), \quad (6)$$

$$f_{p5} = \frac{2f_0}{\pi} (\pi - \cos^{-1} \sqrt{\frac{Z_{0e1} - 2Z_{0o2} + Z_{0o1}}{2Z_{0e1} + 4Z_{0o2} + 2Z_{0o1}}}). \quad (7)$$

Compared with our previous work, i.e., BPF without shorted stubs, this proposed BPF can generate ten TZs, the four TZs f_{tz1} , f_{tz4} , f_{tz7} and f_{tz10} keep unchanged whose positions can be expressed as

$$f_{tz1} = 0, \quad f_{tz4} = \frac{2}{3}f_0, \quad f_{tz7} = \frac{4}{3}f_0, \quad f_{tz10} = 2f_0. \quad (8)$$

Another six TZs within the stopband at the frequency range from 0 to $2f_0$ can be obtained through calculation by setting transmission coefficient $S_{21}=0$. Moreover, the positions of the two TZs f_{tz5} and f_{tz6} are located more close to the passband than the BPF without shorted stubs, as seen in Fig. 2 (a). Thus, the roll-off skirts of the passband will become sharper to further improve frequency selectivity.

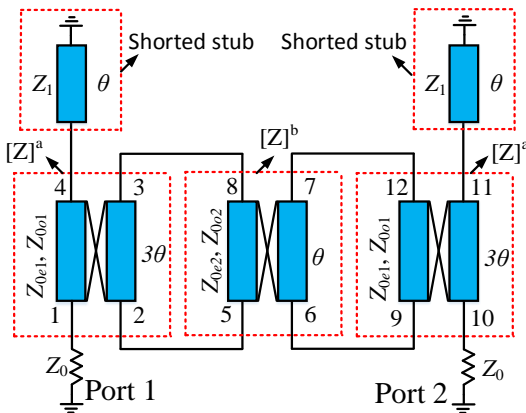


Fig. 1. Ideal circuit of the BPF with ten TZs.

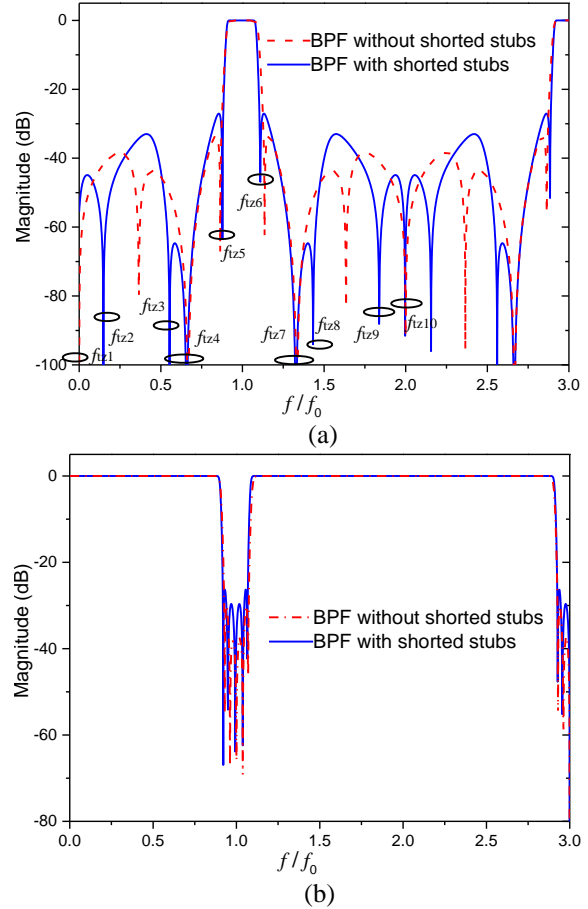


Fig. 2. Simulated results on ideal circuit of (a) S_{21} and (b) S_{11} with $\theta=90^\circ$, $Z_0=50 \Omega$, $Z_1=160 \Omega$, $Z_{0e1}=158 \Omega$, $Z_{0o1}=60 \Omega$, $Z_{0e2}=109 \Omega$, $Z_{0o2}=66 \Omega$.

Figure 3 illustrates the simulated $|S_{21}|$ against Z_1 and k_2 [$k_2 = (Z_{0e2} - Z_{0o2}) / (Z_{0e2} + Z_{0o2})$]. Seen from Figs. 3 (a) and (b), the four TZs f_{tz1} , f_{tz4} , f_{tz7} and f_{tz10} remain unchanged as the parameters Z_1 and k_2 shift, whereas the other six TZs f_{tz2} , f_{tz3} , f_{tz5} , f_{tz6} and f_{tz8} , and f_{tz9} will be adjusted. The 3-dB fractional bandwidth Δf almost keep unchanged as Z_1 varies, In contrast, when k_2 varies slightly, Δf will be changed very obviously.

Except for the TPs, TZs and Δf , the concerned characteristics of BPF mainly include maximal out-of-band $|S_{21}|$ (T_s), maximal in-band $|S_{11}|$ (T_p) [4] and transition band roll-off rate (ξ_{ROR}) [5]. Figures 4 (a), (b), (c) show the corresponding variations of Δf , T_s and T_p against the parameters Z_1 , k_1 and k_2 , respectively, where $k_1 = (Z_{0e1} - Z_{0o1}) / (Z_{0e1} + Z_{0o1})$, $k_2 = (Z_{0e2} - Z_{0o2}) / (Z_{0e2} + Z_{0o2})$. As seen in Fig. 4 (a), T_s and T_p will both decrease when Z_1 increases, which indicates that both of the in-band and out-of-band characteristics will be improved. When the parameter k_1 increases as seen in Fig. 4 (b), T_s will grow up slightly but T_p will decrease and then rise up, while the bandwidth Δf will fall down from 18.6% to 17.4% directly. In contrast, as k_2 increases, T_s will almost

remain unchanged but T_p will reduce and then go up, while Δf will rise up simultaneously as seen in Fig. 4 (c). Note that the Δf will be rise from 16% to 20% when k_2 increases under the return loss condition of over 10 dB within the passband. Consequently, it indicates that the 3-dB fractional bandwidth of the filter is mainly determined by the pair of $\lambda g/4$ coupled lines. In addition, due to the minimum dimension limitation of the fabrication, the width of the microstrip line and the gap of coupled lines must be no smaller than 0.1 mm on the substrate.

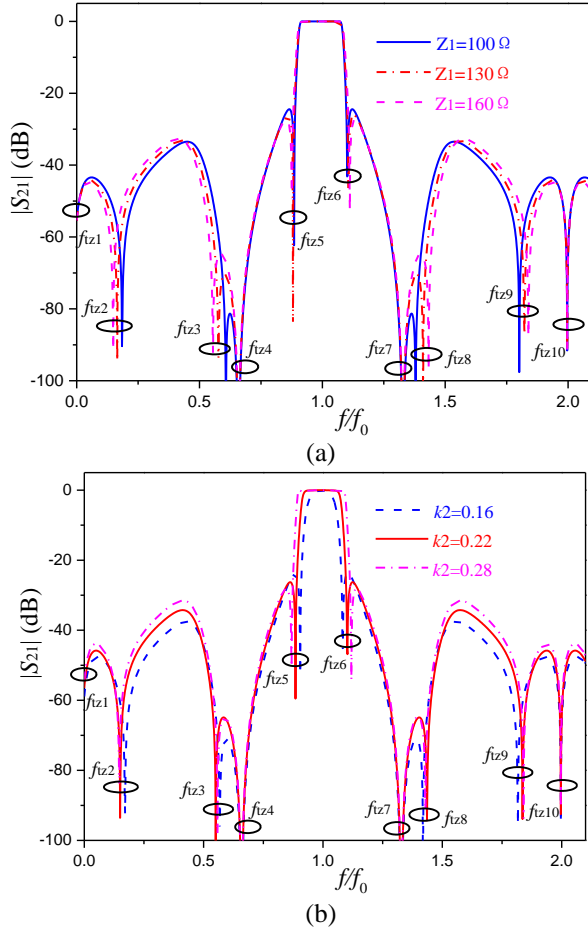


Fig. 3. Simulated $|S_{21}|$ (a) versus Z_1 , where $Z_{0e1}=158 \Omega$, $Z_{0o1}=60 \Omega$, $Z_{0e2}=109 \Omega$, $Z_{0o2}=66 \Omega$; and (b) versus k_2 , where $Z_1=160 \Omega$, $Z_{0e1}=158 \Omega$, $Z_{0o1}=60 \Omega$, $Z_{0e2}=109 \Omega$.

From the above analysis, it is observed that the parameter k_2 affects the Δf and T_p . On the other hand, it is also related to the coupling coefficient between the two one-wavelength ring resonators, thereby having impact on the in-band characteristics. The coupling coefficient can be expressed as [14]:

$$k = \frac{f_{ip5}^2 - f_{ip1}^2}{f_{ip5}^2 + f_{ip1}^2}. \quad (9)$$

where f_{ip1} and f_{ip5} denote the first and last transmission poles, respectively. Taking the layout in Fig. 5 (a) for instance, as shown in Fig. 5 (b), the coupling coefficient will increase slightly to the peak and then decrease when s_1 increases. Moreover, Fig. 5 (c) illustrates the external quality factor Q_e variation with the change of s_2 , where Q_e will increase gradually and become flat as s_2 increases.

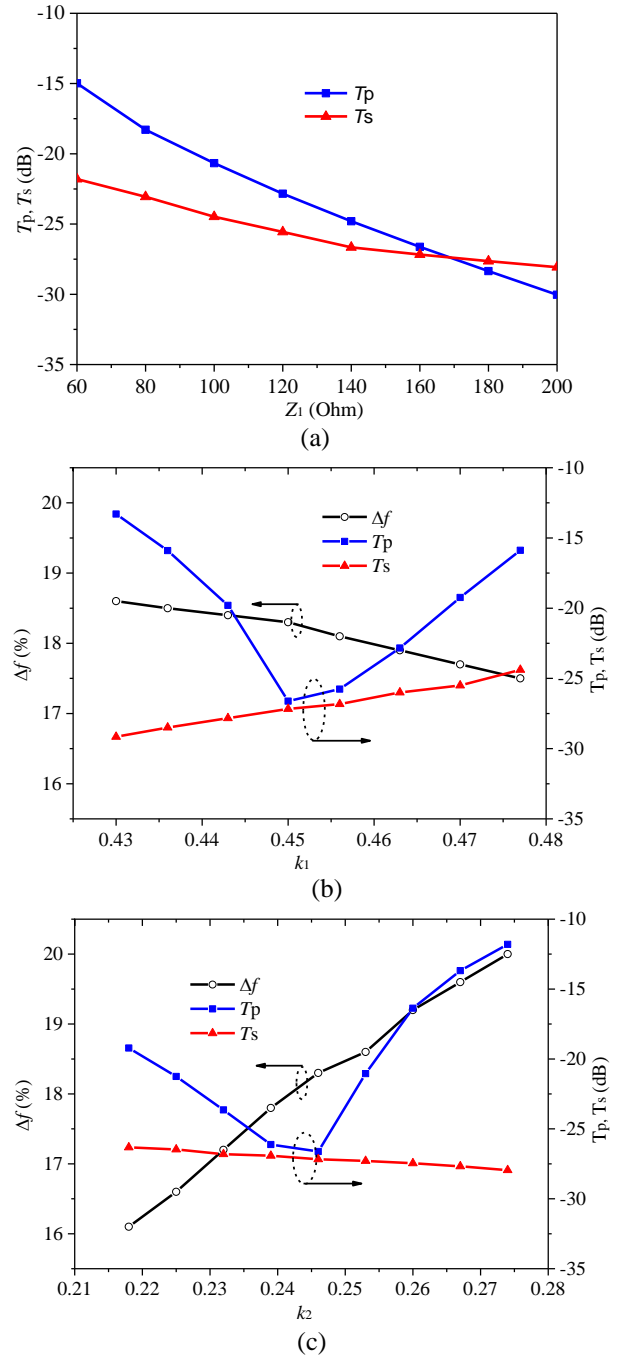


Fig. 4. Calculated Δf , T_s and T_p , (a) versus Z_1 , (b) versus k_1 , and (c) versus k_2 .

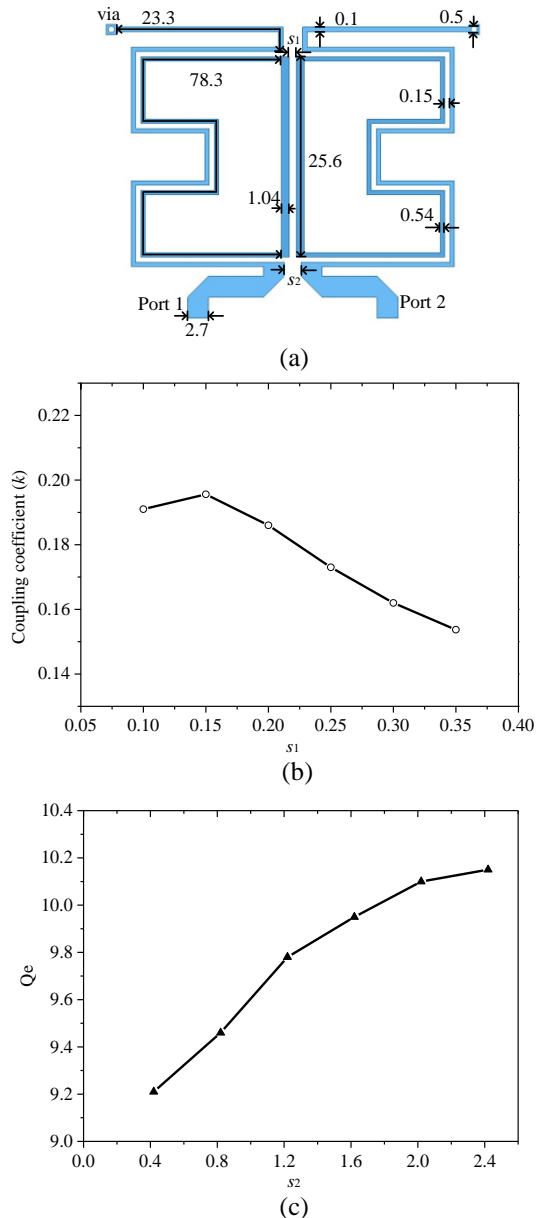


Fig. 5. (a) Layout of the proposed BPF (unit: mm, substrate: relative permittivity of 2.65, thickness of 1 mm), (b) coupling coefficient k changes with the value of s_1 , where $s_2=1.62$ mm, and (c) external quality factor Q_e changes with the value of s_2 , where $s_1=0.42$ mm.

III. EXPERIMENTAL RESULTS

According to the analysis and discussion above, a bandpass filter with center frequency at 2.15 GHz is designed. The final parameters for the filter circuit in Fig. 1 are: $Z_0=50 \Omega$, $Z_{0e1}=158 \Omega$, $Z_{0o1}=60 \Omega$, $Z_{0e2}=109 \Omega$, $Z_{0o2}=66 \Omega$, $Z_1=160 \Omega$ and $\theta=90^\circ$. Furthermore, the 3-dB bandwidth is chosen as 19%, and the printed bandpass filter prototype is fabricated on the substrate with relative permittivity of 2.65 and thickness of 1 mm as illustrated

in Fig. 5 (a), where $s_1=0.42$ mm and $s_2=1.62$ mm. Figure 6 shows the photograph of the fabricated filter.

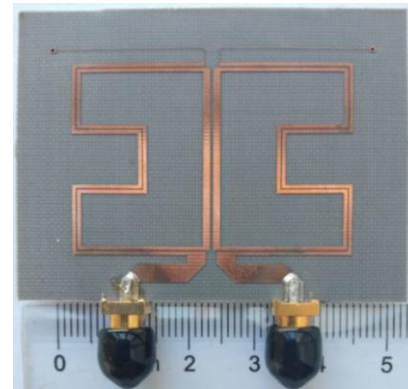


Fig. 6. Photograph of the fabricated BPF.

The simulated and measured results of Fig. 6 are shown in Fig. 7, which are in good agreement. The measured insertion losses are less than 1.8 dB while the return losses are greater than 11.5 dB within the passband (1.98–2.33 GHz). The simulated lower and upper transition band roll-off rates ζ_{ROR} are both better than 486 dB/GHz, while the measured counterparts are both over 425 dB/GHz. In addition, over 31 dB lower stopband can be achieved, while the upper stopband rejection is more than 23 dB from 2.41 to 4.24 GHz. Besides, due to the existing second harmonic around 4.49 GHz, the stopband rejection is over 13 dB from 2.41 to 6 GHz.

Table 1 tabulates the performance comparisons of the proposed BPF with some previous works, and it can be seen that the presented study has sharper roll-off skirts to realize high frequency selectivity with ten TZs. Compared with some previous BPFs, not only more TZs can be realized for improving stopband rejection, but also high transition band roll-off rates can be obtained in this BPF.

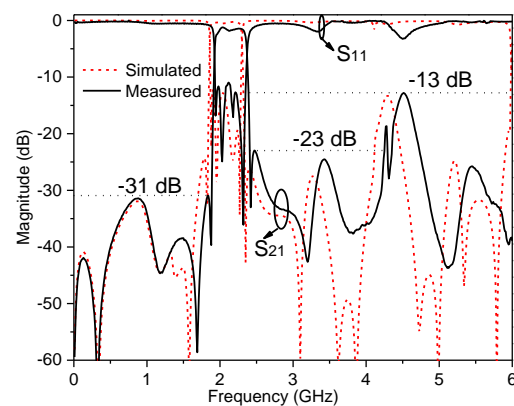


Fig. 7. Simulated and measured S-parameters of the BPF.

Table 1: Performance comparisons with some previous BPFs

	TPs	TZs	Δf	ξ_{ROR}^* (L/U) (dB/GHz)	Upper Stopband (dB)	Circuit Size $\lambda_g \times \lambda_g^{**}$
[4]-I	5	6	61.7%	175/213	>15 (2.7 f_0)	0.68×0.53
[5]	7	4	78%	288/175	>35.1 (2.6 f_0)	0.56×0.23
[7]-A	5	6	70%	81/121	>21 (2.6 f_0)	0.53×0.41
[7]-B	5	6	37%	94/120	>23 (2.8 f_0)	0.61×0.55
[12]	5	8	20.6%	175/340	>20 (2.9 f_0)	1.06×0.61
[13]	5	8	19%	340/425	>18 (3 f_0)	0.39×0.28
[15]	2	7	8.3%	130/215	>12 (2.6 f_0)	0.4×0.26
This work	5	10	19%	425/567	>23 (2.1f_0) >13 (3f_0)	0.49×0.28

Transition band roll-off rates $\xi_{\text{ROR}}^ = |\delta_{20\text{dB}} - \delta_{3\text{dB}}| / |f_{20\text{dB}} - f_{3\text{dB}}|$, where $\delta_{20\text{dB}}$ denotes the 20/3dB attenuation point, and $f_{20\text{dB}}$ is the 20/3dB passband frequency of $|S_{21}|$. L and U denote lower and upper transition band roll-off rates, respectively. ** λ_g : guided wavelength of the 50 Ω microstrip line at the center frequency.

IV. CONCLUSION

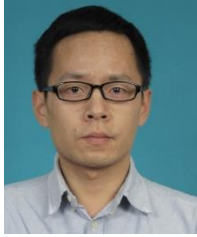
A high selectivity bandpass filter using three pairs of coupled lines loaded with shorted stubs has been presented in this paper. By employing three pairs of parallel-coupled lines and two shorted stubs, sharper roll-off skirts and good stopband rejections can be achieved with five TPs and ten TZs. Finally, the simulations and measurements of the demonstrative filter are in good agreement. The measured transition band roll-off rates can be up to 425 dB/GHz, which is much higher than those of the previous reported works.

ACKNOWLEDGMENT

This work was supported in part by the National Natural Science Foundation of China under Grant 61601390 and the Guangdong Natural Science Foundation under Grant 2016A030310375.

REFERENCES

- [1] T. Lopetegui, M. A. G. Laso, J. Hernandez, M. Bacaicoa, D. Benito, M. J. Garde, M. Sorolla, and M. Guglielmi, "New microstrip 'wiggly-line' filters with spurious passband suppression," *IEEE Trans. Microw. Theory Tech.*, vol. 49, pp. 1593-1598, 2001.
- [2] F. Karshenas, A. R. Mallahzadeh, and J. Rashed-Mohassel, "Size reduction and harmonic suppression of parallel coupled-line bandpass filters using defected ground structure," *ACES Journal*, vol. 25, pp. 149-155, 2010.
- [3] K. D. Xu, Y. Zhang, J. L. Li, W. T. Joines, and Q. H. Liu, "Miniaturized notch-band UWB bandpass filters using interdigital-coupled feed-line structure," *Microw. Opt. Technol. Lett.*, vol. 56, no. 10, pp. 2215-2217, Oct. 2014.
- [4] W. J. Feng, W. Q. Che, Y. M. Chang, S. Y. Shi, and Q. Xue, "High selectivity fifth-order wideband bandpass filters with multiple transmission zeros based on transversal signal-interaction concepts," *IEEE Trans. Microw. Theory Tech.*, vol. 61, no. 1, pp. 89-97, 2013.
- [5] K. D. Xu, F. Y. Zhang, Y. H. Liu, and W. Nie, "High selectivity seventh-order wideband bandpass filter using coupled lines and open/shorted stubs," *Electron. Lett.*, vol. 54, no. 4, pp. 223-225, 2018.
- [6] Y. J. Guo, X. H. Tang, and K. D. Xu, "Dual high-selectivity band-notched ultra-wideband filter with improved out-of-band rejection," *ACES Journal*, vol. 31, no. 9, pp. 1072-1078, 2016.
- [7] B. Zhang, Y. L. Wu, and Y. A. Liu, "Wideband single-ended and differential bandpass filters based on terminated coupled line structures," *IEEE Trans. Microw. Theory Tech.*, vol. 65, pp. 761-774, 2017.
- [8] Y. L. Wu, L. W. Cui, W. W. Zhang, L. X. Jiao, Z. Zhuang, and Y. Liu, "High performance single-ended wideband and balanced bandpass filters loaded with stepped-impedance stubs," *IEEE Access*, vol. 5, pp. 5972-5981, 2017.
- [9] X. Deng, K. D. Xu, Z. Wang, and B. Yan, "Novel microstrip ultra-wideband bandpass filter using radial-stub-loaded structure," *ACES Journal*, vol. 32, no. 12, pp. 1148-1151, 2017.
- [10] W. J. Feng, W. Q. Che, M. L. Hong, and Q. Xue, "Dual-band microstrip bandstop filter with multiple transmission poles using coupled lines," *IEEE Microw. Wireless Compon. Lett.*, vol. 27, no. 3, pp. 236-238, 2017.
- [11] K. D. Xu, D. Li, and Y. Liu, "High-selectivity wideband bandpass filter using simple coupled lines with multiple transmission poles and zeros," *IEEE Microw. Wireless Compon. Lett.*, vol. 29, no. 2, 2019. DOI: 10.1109/LMWC.2019.2891203
- [12] W. J. Feng, X. Gao, W. Q. Che, and Q. Xue, "Bandpass filter loaded with open stubs using dual-mode ring resonator," *IEEE Microw. Wireless Compon. Lett.*, vol. 25, pp. 295-297, 2015.
- [13] K. D. Xu, F. Zhang, Y. Liu, and Q. H. Liu, "Bandpass filter using three pairs of coupled lines with multiple transmission zeros," *IEEE Microw. Wireless Compon. Lett.*, vol. 28, no. 7, pp. 576-578, 2018.
- [14] J. S. Hong and M. J. Lancaster, *Microwave Filters for RF/Microwave Applications*. New York, NY, USA: Wiley, 2011.
- [15] K. Xu, Y. Zhang, Y. Fan, W. T. Joines, and Q. Liu, "Novel circular dual-mode filter with both capacitive and inductive source-load coupling for multiple transmission zeros," *J. Electromag. Waves Appl.*, vol. 26, pp. 1675-1684, 2012.



Kai-Da Xu received the B.S. and Ph.D. degrees in Electromagnetic Field and Microwave Technology from University of Electronic Science and Technology of China (UESTC), Chengdu, China, in 2009 and 2015, respectively.

From 2012 to 2014, he was a Visiting Researcher with the Department of Electrical and Computer Engineering, Duke University, Durham, NC, USA, under the financial support from the China Scholarship Council. From 2016 to 2017, he was a Postdoctoral Fellow with the State Key Laboratory of Terahertz and Millimeter Waves, City University of Hong Kong, Hong Kong. In 2015, he joined the Department of Electronic Science, Xiamen University, Xiamen, China as an Assistant Professor. Since 2018, he has been an Honorary Fellow with the Department of Electrical and Computer Engineering, University of Wisconsin–Madison, WI, USA. He has authored and coauthored over 100 papers in peer-reviewed journals and conference proceedings. He received the UESTC Outstanding Graduate Awards in 2009 and 2015,

respectively. He was the recipient of National Graduate Student Scholarship in 2012, 2013, and 2014 from Ministry of Education, China. Since 2014, he has served as a Reviewer for more than 30 journals including IEEE Transactions on Microwave Theory and Techniques, IEEE Transactions on Antennas and Propagation, IEEE Microwave and Wireless Components Letters and IEEE Antennas and Wireless Propagation Letters. Since 2017, he has served as an Associate Editor for both of the *IEEE Access* and *Electronics Letters*. He is also an Editorial Board Member of the *AEÜ-International Journal of Electronics and Communications*. His research interests include RF/microwave, mm-wave/THz devices and antenna arrays.



Fengyu Zhang was born in Fujian, China. He received the B.Sc. degree in Fuzhou University, Fujian, China, in 2016, and currently he is working toward the M.S. degree in Xiamen University. His research interests include RF/microwave components and circuits.

Three-Dimensional Spherical-Shaped UPML for FDTD with Cubic Lattices

Lu Wang¹, Mengjun Wang¹, Kanglong Zhang¹, Wenjie Cui¹,
Hongxing Zheng^{1*}, and Erping Li²

¹ School of Electronics and Information Engineering
Hebei University of Technology, Tianjin, TJ 22, China
wanglu_william@163.com, wangmengjun@hebut.edu.cn, zhangkanglong@yeah.net, wjcui_driver@163.com,
*hxzheng@hebut.edu.cn

² University of Illinois at Urbana-Champaign Institute
Zhejiang University, Haining, ZJ 573, China
liep@zju.edu.cn

Abstract — Spherical-shaped uniaxial perfectly matched layer (SS-UPML), an absorbing boundary for three-dimensional (3-D) finite-difference time-domain (FDTD) method with cubic cells, is proposed and applied to different objects. This boundary is used for truncating the computational domain to absorb outgoing electromagnetic waves, which has the advantages of higher efficiency and accuracy, compared with the conventional UPML. Update equations are transformed by coordinate rotation to better fit the Cartesian system. Different numerical experiments are implemented to verify the stability and practicability of the proposed boundary in 3-D case. Obtained results illustrate that about a half grid and computational time can be saved after SS-UPML is used, which is the foundation of a wider range of applications.

Index Terms — FDTD, Cartesian coordinate system, spherical boundary truncation, three-dimension, UPML.

I. INTRODUCTION

The finite-difference time-domain (FDTD) method is one of the most effective ideas in calculating radiation problems of electromagnetic waves, and has rapidly developed since it was introduced by Yee [1]. Finite computer memory, however, cannot meet the requirement of infinite problems. Thus, highly efficient absorbing boundary condition plays an important role in simulation. Uniaxial perfectly matched layer (UPML), a valid way for truncation without reflected wave, seems like a lossy media wall that surrounds the computing space. Sacks and Gedney described this method from the respect of uniaxial media with conductivity permeability and permittivity tensors [2], [3], and Chew implemented a similar one from another respect of Maxwell update equations with complex coordinate stretching along three directions in the Cartesian system [4]. In fact, the essence of these two derivations are the same, but reveal

the different characteristics of UPML. On the other hand, it avoids the nonphysical field splitting caused by Bérenger's PML, which was proposed and investigated in [5]-[9], whereas has the equally impressive In this paper, a spherical-shaped UPML (SS-UPML) strategy is discussed for FDTD in three-dimensional (3-D) condition. We establish the SS-UPML in the Cartesian coordinate system with cubic cells, as shown in Fig. 1. A continuous spherical-shaped boundary is used to truncate free space. After discretizing it, a two-dimensional section is obtained and placed on the right, which visibly avoids calculating unnecessary grids at corners and edges, and can absorb outgoing wave perfectly. The practicability and efficiency of the method are verified by simulating different radiation samples, and are compared with the conventional UPML. The results indicate that the proposed method obviously reduce the computational memory and time, and maintain at the same error level with the original UPML.

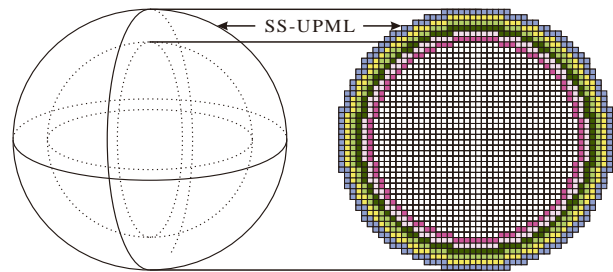


Fig. 1. SS-UPML in Cartesian coordinate system.

In Section II, we describe two advantages of this approach, *obvious reduction of memory and smaller incident angle*, that are the basis of successful application. Section III introduces the fundamental formulations of 3-D SS-UPML. Lastly, in Section IV, several numerical experiments are implemented to verify the performance

of our method.

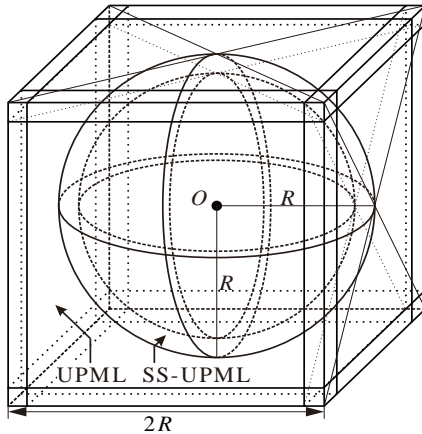


Fig. 2. Illustration of SS-UPML and UPML.

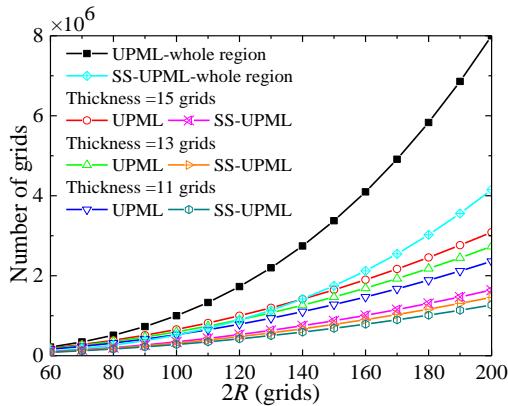


Fig. 3. The number of grids varies with R and thickness in two boundaries.

II. THREE-DIMENSIONAL SS-UPML

We are intending to introduce the features of 3-D SS-UPML, from which are where it differs the traditional methods. Pursuant to the previous description, we know that this boundary has less computer memory requirements than traditional methods; here we will carry out a quantitative analysis. Besides, it has another advantage of smaller incident angle, compared to the same source point in a cubic region. More details are given in the following.

A. Fewer computational memory

In order to clearly demonstrate the difference between the conventional cubic UPML and SS-UPML, we establish them with the size of $2R$ and the radius of R , respectively, and with a same centroid, as shown in Fig. 2. The thickness of these two boundaries is equal, thus, they are tangent at inside and outside.

It is clear that the volume of SS-UPML truncated region is $(4/3)\pi R^3$, and of UPML is $(2R)^3$, almost doubled to the former. This implies the FDTD cubic cells with

two boundaries may have the same relationship in quantity.

After dispersing these two regions in Cartesian coordinate system, the cubic UPML region is divided into a number of congruent cube-meshes. The curved SS-UPML boundary needs to approximate by groups of staircase lattices following the conformal condition [19]. Therefore, we can count the number of grids in both regions easily. The statistics of variations with different thickness and R (both units are grids, in order to illustrate the difference in the respect of quantity, and it has nothing to do with the size) are shown in Fig. 3. Apparently, an increasing number of grids are saved due to the use of our boundary with the edge length growth. Besides, the number of grids in SS-UPML region has always been about half of the UPML in not only the whole regions, but also the absorbers.

In our FDTD programs, the parameters of lattice are recorded by different variables, which means the computational memory will go forth and multiplying as the radius increases. On the other hand, the parameters of boundary are more complicated than free space, so it needs more memory to store and more time to calculate. Thus, fewer grids in both regions leads to considerable decline of memory in executing the programs. Further, this will bring the possibility to reduces computing time and enhance its efficiency.

B. Smaller incident angle

To plainly compare the difference of the incident angle of the same incident wave between SS-UPML and UPML, we define two computational regions, as we did in the last part. As clearly shown in Fig. 4, the point $O(x_0, y_0, z_0)$ is the geometric center of both region, the wave source is placed at an arbitrary point $S(x_s, y_s, z_s)$ in the region, and point $S'(x_s', y_s', z_s')$ is the projection of S on the right side of cubic region. After that, the wave will spread all around and eventually propagate to the interface of free space and absorption layer. For a more intuitive explanation of the relationship between the two, we assume that the wave propagates only to the right and the incident point is $P(x_p, y_p, z_p)$, which is on the right side of the region. The angle θ in the Fig. 4 is the angle of incidence on the boundary. According to the assumption above, the expressions of θ in different regions can be obtained by using the triangular relationship:

$$\theta_{\text{sph}} = \arccos\left(\frac{dis^2 - (x_s - x_0)^2 - (y_s - y_0)^2 - (z_s - z_0)^2 + R^2}{2R \cdot dis}\right), \quad (1)$$

$$\theta_{\text{cub}} = \arccos\left(\frac{dis^2 - (x_s' - x_p)^2 - (z_s - z_p)^2 + (y_s - y_s')^2}{2(y_s - y_s') \cdot dis}\right), \quad (2)$$

where dis represents the distance between point S and P , and can be expressed as:

$$dis = \sqrt{(x_s - x_p)^2 + (y_s - y_p)^2 + (z_s - z_p)^2}. \quad (3)$$

Now, we consider a special case, that is point S

coinciding with point O . Obviously, the wave propagates along the radius in the spherical region, which means that it always perpendicular to the boundary. In the square region, however, normal incidence can only be achieved when P is at the center of the right side, and the angle will become large when it is close to the border. This significant different trend is shown in Fig. 5. On the other hand, we mostly place the scatter at the center, which means the wave will always propagate from the region near the centroid, and have the similar incident angle pattern as mentioned. This feature is very helpful for improving calculation accuracy and reducing errors, which will be verified below.

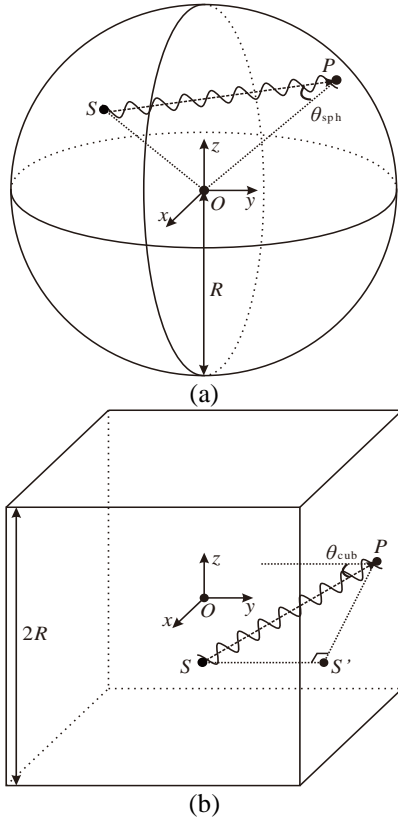


Fig. 4. Wave propagation in: (a) SS-UPML and (b) UPML.

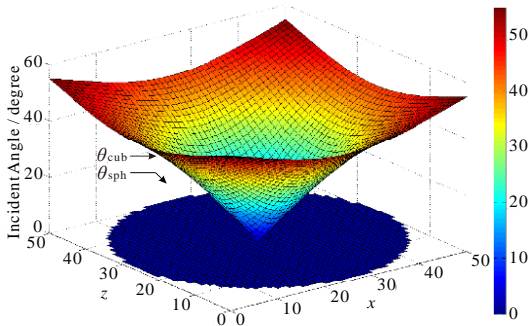


Fig. 5. Comparison of incident angle between two boundaries.

III. FORMULATIONS

The UPML, a physical model based on anisotropic perfectly matched medium, is one of the excellent absorbing boundaries of the FDTD method. It is derived from Maxwell equations with uniaxial media tensors, and does not have to split the field into sub-components. Therefore, it can calculate more complicated objects with different materials and structures. We use $\bar{\epsilon}$ and $\bar{\mu}$ diagonal matrix to represent the electric and magnetic permittivity tensor in absorbing region, respectively. These two parameters should meet the requirement of matching conditions, which are $\bar{\epsilon} = \epsilon_u \bar{s}$ and $\bar{\mu} = \mu_u \bar{s}$, where ϵ_u and μ_u are the relatively permittivity and permeability of the absorber, respectively, and \bar{s} is matching matrix, to ensure that the impedance of the medium and the free space are the same. Inserting them into Ampere and Faraday law, we have:

$$\nabla \times \mathbf{H} = j\omega \epsilon_u \bar{s} \mathbf{E}, \quad \nabla \times \mathbf{E} = -j\omega \mu_u \bar{s} \mathbf{H}. \quad (4)$$

The matrix \bar{s} has different expressions for different directions. For example, if the interface is perpendicular to x -axis, it can be written as $\bar{s}_x = \text{diag}[s_x^{-1}, s_x, s_x]$, where $s_x = \kappa_x + \sigma_x / j\omega \epsilon_0$, so does \bar{s}_y and \bar{s}_z . Inside the spherical boundary, it is obvious that the interface is perpendicular to the radius. Therefore, we should set the matching matrix as the product of \bar{s}_x , \bar{s}_y and \bar{s}_z to achieve the same purpose, which can be expressed as:

$$\bar{\zeta} = \zeta_u \bar{s}_x \cdot \bar{s}_y \cdot \bar{s}_z = \zeta_u \cdot \text{diag}[s_x^{-1} s_y s_z, s_x s_y^{-1} s_z, s_x s_y s_z^{-1}], \quad (5)$$

where ζ represents ϵ or μ . Directly inserting (5) into (4) and transforming them into time domain will lead to a convolution between coefficients and \mathbf{E} -field, which are not advisable, since implementing it would be computationally intensive. A more efficient approach is to define a proper constitutive relationship to decouple the frequency-dependent terms as follow:

$$D_x = \epsilon(s_x/s_x) \cdot E_x, \quad D_y = \epsilon(s_y/s_y) \cdot E_y, \quad D_z = \epsilon(s_z/s_z) \cdot E_z. \quad (6)$$

After simplify these relations, we obtain a two-step update cycle likes $\mathbf{D-E-B-H-D}$. Obviously, it is more complicated than the standard FDTD time domain update equations, and costs more computational time and memory. While, we can use radial subcomponents in SS-UPML to overcome this defect, which is expressed by using subscript 'r' in the following. Therefore, (4) can be transformed into time domain and rewritten as:

$$\kappa_r \frac{\partial D_{xr}}{\partial t} + \frac{\sigma_r}{\epsilon_0} D_{xr} = \frac{\partial H_{yr}}{\partial y} - \frac{\partial H_{yr}}{\partial z}, \quad (7a)$$

$$\kappa_r \frac{\partial D_{yr}}{\partial t} + \frac{\sigma_r}{\epsilon_0} D_{yr} = \frac{\partial H_{xr}}{\partial z} - \frac{\partial H_{xr}}{\partial x}, \quad (7b)$$

$$\kappa_r \frac{\partial D_{zr}}{\partial t} + \frac{\sigma_r}{\epsilon_0} D_{zr} = \frac{\partial H_{yr}}{\partial x} - \frac{\partial H_{xr}}{\partial y}, \quad (7c)$$

$$-\kappa_r \frac{\partial B_{xr}}{\partial t} - \frac{\sigma_r}{\epsilon_0} B_{xr} = \frac{\partial E_{zr}}{\partial y} - \frac{\partial E_{yr}}{\partial z}, \quad (8a)$$

$$-\kappa_r \frac{\partial B_{yr}}{\partial t} - \frac{\sigma_r}{\varepsilon_0} B_{zr} = \frac{\partial E_{xr}}{\partial z} - \frac{\partial E_{zr}}{\partial x}, \quad (8b)$$

$$-\kappa_r \frac{\partial B_{zr}}{\partial t} - \frac{\sigma_r}{\varepsilon_0} B_{zr} = \frac{\partial E_{yr}}{\partial x} - \frac{\partial E_{xr}}{\partial y}. \quad (8c)$$

In order to make these equations to better fit the Cartesian coordinates, resolution of these variables in each direction is needed. We should decompose each radial component along x-, y- and z-axis through the rotation relationship, and then calculate them according to the relative position. Fortunately, this method can also overcome the problem of different update coefficient forms caused by different permittivity and permeability between free space and absorbing region. Therefore, we can obtain uniform equations throughout the entire computational region, which ensure the global consistency of updating and highly efficient of programing.

In 3-D condition, the angle between the wave vector \mathbf{r} and the z-axis is θ , and the angle between \mathbf{r} and the x-axis is φ . Thus, each radial component's position can be identified, and its update equations (7) and (8) can be rewritten as:

$$D_{xr}|_{\xi+1/2,\psi,\gamma}^{n+1} = CA \cdot D_{xr}|_{\xi+1/2,\psi,\gamma}^n + CB \cdot (H_{zr}|_{\xi+1/2,\psi+1/2,\gamma}^{n+1/2} - H_{zr}|_{\xi+1/2,\psi-1/2,\gamma}^{n+1/2} - H_{yr}|_{\xi+1/2,\psi,\gamma+1/2}^{n+1/2} + H_{yr}|_{\xi+1/2,\psi,\gamma-1/2}^{n+1/2}), \quad (9a)$$

$$D_{yr}|_{\xi,\psi+1/2,\gamma}^{n+1} = CA \cdot D_{yr}|_{\xi,\psi+1/2,\gamma}^n + CB \cdot (H_{xr}|_{\xi,\psi+1/2,\gamma+1/2}^{n+1/2} - H_{xr}|_{\xi,\psi+1/2,\gamma-1/2}^{n+1/2} - H_{zr}|_{\xi+1/2,\psi+1/2,\gamma}^{n+1/2} + H_{zr}|_{\xi-1/2,\psi+1/2,\gamma}^{n+1/2}), \quad (9b)$$

$$D_{zr}|_{\xi,\psi,\gamma+1/2}^{n+1} = CA \cdot D_{zr}|_{\xi,\psi,\gamma+1/2}^n + CB \cdot (H_{yr}|_{\xi+1/2,\psi,\gamma+1/2}^{n+1/2} - H_{yr}|_{\xi-1/2,\psi,\gamma+1/2}^{n+1/2} - H_{xr}|_{\xi,\psi+1/2,\gamma+1/2}^{n+1/2} + H_{xr}|_{\xi,\psi-1/2,\gamma+1/2}^{n+1/2}), \quad (9c)$$

$$B_{xr}|_{\xi,\psi+1/2,\gamma+1/2}^{n+3/2} = CA \cdot B_{xr}|_{\xi,\psi+1/2,\gamma+1/2}^{n+1/2} - CB \cdot (E_{zr}|_{\xi,\psi+1,\gamma+1/2}^{n+1} - E_{zr}|_{\xi,\psi,\gamma+1/2}^{n+1} - E_{yr}|_{\xi,\psi+1/2,\gamma+1}^{n+1} + E_{yr}|_{\xi,\psi+1/2,\gamma}^{n+1}), \quad (10a)$$

$$B_{yr}|_{\xi+1/2,\psi,\gamma+1/2}^{n+3/2} = CA \cdot B_{yr}|_{\xi+1/2,\psi,\gamma+1/2}^{n+1/2} - CB \cdot (E_{xr}|_{\xi+1/2,\psi,\gamma+1}^{n+1} - E_{xr}|_{\xi+1/2,\psi,\gamma}^{n+1} - E_{zr}|_{\xi+1,\psi,\gamma+1/2}^{n+1} + E_{zr}|_{\xi,\psi,\gamma+1/2}^{n+1}), \quad (10b)$$

$$B_{zr}|_{\xi+1/2,\psi+1/2,\gamma}^{n+3/2} = CA \cdot B_{zr}|_{\xi+1/2,\psi+1/2,\gamma}^{n+1/2} - CB \cdot (E_{yr}|_{\xi+1,\psi+1/2,\gamma}^{n+1} - E_{yr}|_{\xi,\psi+1/2,\gamma}^{n+1} - E_{xr}|_{\xi+1/2,\psi+1,\gamma}^{n+1} + E_{xr}|_{\xi+1/2,\psi,\gamma}^{n+1}), \quad (10c)$$

where

$$\begin{cases} \xi = r \sin \theta \cos \varphi \\ \psi = r \sin \theta \sin \varphi, \\ \gamma = r \cos \theta \end{cases} \quad (11)$$

are the transform relationship between the Cartesian and spherical coordinate system, and

$$CA = \frac{2\varepsilon_u \varepsilon_0 \kappa_r - \sigma_r \Delta t}{2\varepsilon_u \varepsilon_0 \kappa_r + \sigma_r \Delta t}, \quad CB = \frac{2\varepsilon_u \varepsilon_0 \Delta t}{(2\varepsilon_u \varepsilon_0 \kappa_r + \sigma_r \Delta t) \delta}, \quad (12)$$

where δ is the size of cubic grids. Moreover, the feature is the same in $\mathbf{D-E}$ and $\mathbf{B-D}$ relationships:

$$E_{xr}|_{\xi+1/2,\psi,\gamma}^{n+1} = CA \cdot E_{xr}|_{\xi+1/2,\psi,\gamma}^n + CE \cdot (CP \cdot D_{xr}|_{\xi+1/2,\psi,\gamma}^{n+1} - CQ \cdot D_{xr}|_{\xi+1/2,\psi,\gamma}^n), \quad (13)$$

$$H_{xr}|_{\xi,\psi+1/2,\gamma+1/2}^{n+3/2} = CA \cdot H_{xr}|_{\xi,\psi+1/2,\gamma+1/2}^{n+1/2} + CF \cdot (CP \cdot B_{xr}|_{\xi,\psi+1/2,\gamma+1/2}^{n+3/2} - CQ \cdot B_{xr}|_{\xi,\psi+1/2,\gamma+1/2}^{n+1/2}), \quad (14)$$

where

$$CE = \frac{1}{(2\varepsilon_0 \kappa_r + \sigma_r \Delta t) \varepsilon_u \varepsilon_0}, \quad CF = \frac{1}{(2\varepsilon_0 \kappa_r + \sigma_r \Delta t) \mu_u \mu_0},$$

$$CP = 2\varepsilon_u \varepsilon_0 \kappa_r + \sigma_r \Delta t, \quad CQ = 2\varepsilon_u \varepsilon_0 \kappa_r - \sigma_r \Delta t. \quad (15)$$

Here, we only list the x-component as an example to illustrate the update process; the other two have similar forms of calculation. The two key parameters, σ_r and κ_r , are important factors to the absorption effect, which can be set by using a polynomial variation grading of the loss with depth of ρ in SS-UPML:

$$\sigma_r(\rho) = -\left(\frac{\rho}{\chi}\right)^m \frac{(m+1) \ln(R_0)}{2\eta_0 \rho}, \quad (16)$$

$$\kappa_r(\rho) = 1 + (\kappa_{r,\max} - 1) \cdot (\rho/\chi)^m, \quad (17)$$

where χ is the thickness of the SS-UPML, R_0 represents the desired reflection error which should be specified before computation, η_0 is wave impedance in free space, $\kappa_{r,\max}$ is an integer whose increase will result in an increase in the level of attenuation, and m determines the speed of parameter growth. A large m yields a σ_r distribution that is relatively flat near the SS-UPML surface. However, deeper within the boundary, σ_r increases more rapidly than for small m . In this way, σ_r increases from 0 at $\xi = 0$, the inner surface of the absorber, to the maximum value at $\xi = \gamma$, the outside of the boundary. Similarly, κ_r increases from 1 to $\kappa_{r,\max}$ at the same position. After finishing these preparations, different numerical experiments are implemented to verify its performance.

IV. NUMERICAL EXPERIMENTS

We have implemented several numerical experiments to verify the stability, accuracy and efficiency of the proposed SS-UPML with 3-D FDTD cubic lattice codes. The calculating process is shown as follow.

A. Dipole source excitation in spherical-shell

The proposed method is built in the Cartesian coordinate system, so the spherical-shaped boundary is

approximated by a series of cubic latticework, whose profile looks like staircase. In order to verify the stability of the SS-UPML, which is the most important performance for absorbing boundary, we excite a source in a spherical-shell-shaped region. It means that in traditional calculation space, we use SS-UPML to truncate the outer boundary, so the computational space becomes spherical. Then we define an anti-SS-UPML ball, which has identical parameters with truncated boundary, whereas the value increasing direction is from the outer to the inner. After we put this ball in the middle of the calculation area, the shape of free space will like a spherical-shell, with two absorbing regions on both sides. As comparison, we define a similar region surrounded by conventional UPML and a same inner ball in the middle, as shown in Fig. 6. There is one thing to be aware of is that the position of dipole is equivalent at anywhere inside the SS-UPML, because of the perfect symmetry of the region, whereas it is not in the cubic region. Therefore, we should place the dipole at different positions to compare the quality of the two.

In this simulation, we choose three representative positions as examples in cubic region, which are on the lower, lower left and upper left rear directions, corresponding to point A, B and C, respectively. In spherical region, these three points can be marked at the same position by converting (r, θ, φ) into (x, y, z) coordinates. The dimension of the cubic computational domain is set as $201 \times 201 \times 201$, which means there are 8.12 million grids in total. After truncated by SS-UPML with diameter 201 grids, however, the total number of mesh that need to be calculated are reduced to 4.15 million, which means that it saves 48.8% of memory, consistent with the previous predictions. The radius of the inner anti-SS-UPML ball is 20 grids. The positions of point A, B, and C are $(0, 0, -55)$, $(0, -50, -50)$, and $(-40, -40, 40)$, and the view points of them are $(0, 0, -45)$, $(0, -40, -40)$, and $(-30, -30, 30)$, respectively. Moreover, 15 layers of absorber are used to absorb the outgoing wave in both two cases. The edge length of the cubic cell is 5cm, and the time step is 83.33ps. We set the program to run 10000 steps, which is a long enough time to test its stability. The dipole is placed parallel to the z -axis at three points, whose radiation field in free space in time domain can be expressed as:

$$\begin{aligned} \mathbf{E}(\mathbf{r}, t) = \frac{\mu_0}{4\pi r} \left\{ \mathbf{e}_r \left[\frac{c_0}{r} \frac{\partial}{\partial t} + \left(\frac{c_0}{r} \right)^2 \right] 2 \cos \theta + \right. \\ \left. \mathbf{e}_\theta \left[\frac{\partial^2}{\partial t^2} + \frac{c_0}{r} \frac{\partial}{\partial t} + \left(\frac{c_0}{r} \right)^2 \right] \sin \theta \right\} p \left(t - \frac{r}{c_0} \right), \end{aligned} \quad (18)$$

where, c_0 is the speed of light in vacuum, r is the distance between dipole and view point. It is clearly that the electric field is only related to the angle and distance, due to the pose of dipole. In this sample, we use Gaussian

pulse as an excitation, which is expressed as:

$$p(t) = 10^{-10} e^{-(t-3T)/T]^2} \quad (T = 2\text{ns}). \quad (19)$$

At first, we simulate the dipole at different positions in Cartesian FDTD region truncated by two boundaries, with no inner objects. These results can be considered as reference values. Then place the anti-SS-UPML ball into the space, we can obtain another set of results. Actually, because the absorbing material is set on both sides of the observers, the reflection caused by the absorber will be overlapped. Relative errors at these three points can be calculated and are shown in Fig. 7. Due to the huge amount of original data in the period of simulation time, we sample every 100 points and plot in the figure. Obviously, the SS-UPML performs very well in absorbing, its error of each point is similar to the original UPML. Besides, there is another interesting phenomenon in the cubic region we should care about, that the errors at three points have tiny differences as the reflections caused by the corner, edge and face are different, while a same level is maintained in spherical region because of the perfect symmetry of SS-UPML. This is the fundamental guarantee for SS-UPML to simulate larger scale and complex structural scatters.

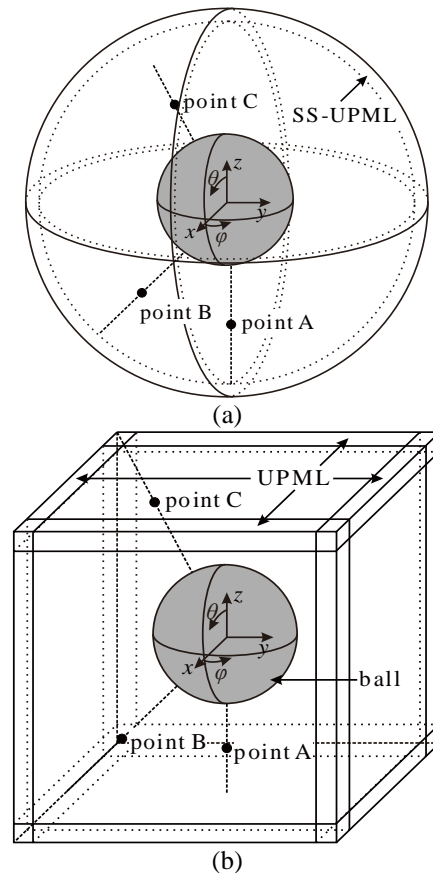


Fig. 6. Dipole in: (a) SS-UPML and (b) UPML truncated region with absorb object.

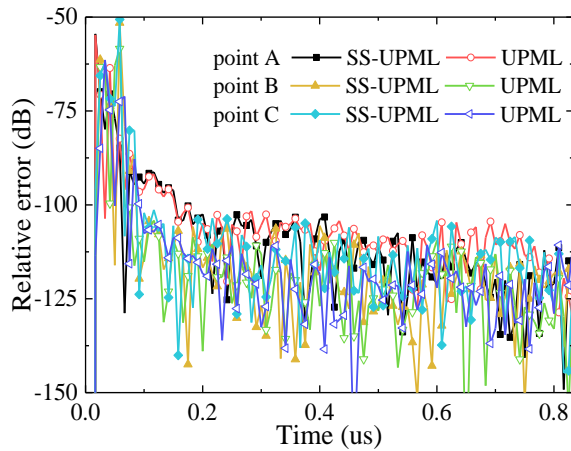


Fig. 7. Relative error of dipole radiation in different boundaries at different points.

B. Antenna simulation in SS-UPML

An inverted-F antenna is designed and calculated inside the SS-UPML. Its FDTD simulation result with different PMLs are presented and compared with finite element method (FEM). The structure and dimension of the antenna are shown in Fig. 8. The radiation element is designed on the top layer, and the ground is printed at the bottom layer. The plate thickness is 0.8mm, and has 2.2 dielectric constant. We use SS-UPML and UPML with 15 cells thickness as termination boundaries, and set at least 20 cells air gap in each direction between the antenna and the boundary. In this example, the FDTD problem space is composed of cells with 0.4mm in each direction. After we consider all these parts, the computational region is $161 \times 161 \times 161$ in cubic boundary, and the radius of the spherical region is 161 cells, which makes the probability of 49.15% memory reduction.

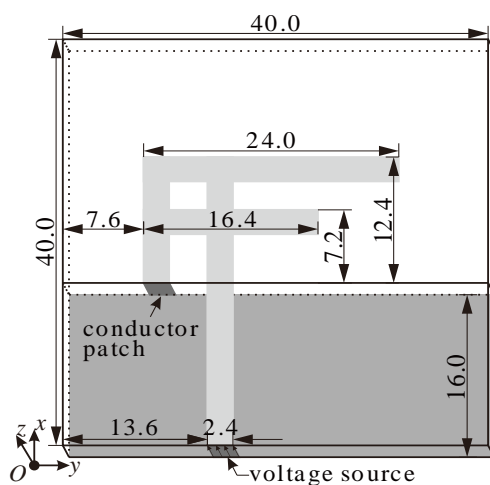


Fig. 8. Inverted-F antenna structure (unit: mm).

The antenna is excited by a voltage source, and its far-field frequencies are 2.4 and 5.8 GHz. The FDTD

simulation of the antenna is performed with 7000 time steps, and a key parameter of the input port, return loss, is calculated. The results of S_{11} calculated by different algorithms are plotted in Fig. 9. Results of two FDTD boundaries show a good agreement with each other, and have a little difference to the FEM at low frequency domain, which is negligible effect on the final result. Most importantly, in the UPML boundary, 144.1MB memories are used and 1846.98s are cost for simulating the program. In our SS-UPML boundary, however, 76.7MB and 1067.65s are needed. This means 46.77% memory and 42.19% are saved, which coincide with the previous analysis, but keeps perfect accuracy.

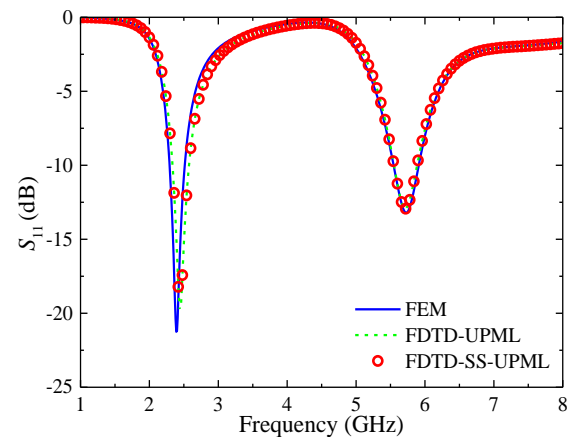


Fig. 9. Comparison of return loss calculated by different methods.

V. CONCLUSION

The SS-UPML strategy is applied for Cartesian FDTD in 3-D condition. We use this truncation boundary to calculate the different samples to test its performance. Due to the rotation of radial components in the Cartesian system, the equations in FDTD scheme can be simplified, which brings a huge convenience in programming. It reduces roughly half of the computational memory and time. In addition, it maintains high accuracy at different locations, even if the source is very close to the boundary. This is the foundation of future simulation for those objects with complex structures and material parameters. Our prospective study will pay much attention to appropriate parameters of SS-UPML for better absorbing performance, and more applications for 3-D cases.

ACKNOWLEDGMENT

This work is supported by the National Natural Science Foundation of China, under Grant 61671200, and the Key Project of Hebei Natural Science Foundation under grant F2017202283.

REFERENCES

- [1] K. S. Yee, "Numerical solution of initial boundary

- value problems involving Maxwell's equations in isotropic media," *IEEE Trans. Antennas Propag.*, vol. 14, no. 3, pp. 302-307, 1966.
- [2] Z. S. Sacks, D. M. Kingsland, R. Lee, and J. Lee, "A perfectly matched anisotropic absorber for use as an absorbing boundary condition," *IEEE Trans. Antennas Propag.*, vol. 43, no. 12, pp. 1460-1463, 1995.
- [3] S. D. Gedney, "An anisotropic perfectly matched layer absorbing media for the truncation of FDTD lattices," *IEEE Trans. Antennas Propag.*, vol. 44, no. 12, pp. 1630-1639, 1996.
- [4] W. C. Chew and W. H. Weedon, "A 3D perfectly matched medium from modified Maxwell's equations with stretched coordinates," *Microw. Opt. Technol. Lett.*, vol. 7, no. 13, pp. 599-604, 1994.
- [5] J. P. Bérenger, "A perfectly matched layer for the absorption of electromagnetic waves," *J. Comput. Phys.*, vol. 114, no. 2, pp. 185-200, 1994.
- [6] J. P. Bérenger, "Three-dimensional perfectly matched layer for the absorption of electromagnetic waves," *J. Comput. Phys.*, vol. 127, no. 2, pp. 363-379, 1996.
- [7] J. P. Bérenger, "Perfectly matched layer for the FDTD solution of wave-structure interaction problems," *IEEE Trans. Antennas Propag.*, vol. 44, no. 1, pp. 110-117, 1996.
- [8] N. V. Kantartzis, "Generalised higher-order FDTD-PML algorithm for enhanced analysis of 3D waveguiding EMC structures in curvilinear coordinates," *IEE Proc.-Microw. Antennas Propag.*, vol. 150, no. 5, pp. 351-359, 2003.
- [9] J. Wang, Z. Chen, J. Liang, Y. Wu, C. Peng, S. Tao, et al., "The split-field PML absorbing boundary condition for the unconditionally stable node-based LOD-RPIM method," *IEEE Antennas Wirel. Propag. Lett.*, vol. 17, no. 10, pp. 1920-1924, 2018.
- [10] F. L. Teixeira, "On aspects of the physical reliability of perfectly matched absorbers for electromagnetic waves," *Radio Sci.*, vol. 38, no. 2, pp. 15-1-15-10, 2003.
- [11] A. Taflove and S. C. Hagness, *Computational Electrodynamics: The Finite-Difference Time-Domain Method*. 3rd ed., Boston, USA: Artech House, 2005.
- [12] A. Taflove, A. Oskooi, and S. G. Johnson, *Advances in FDTD Computational Electrodynamics*. Boston, USA: Artech House, 2013.
- [13] J. F. Liu, Y. R. Pu, J. S. Zhang, and X. L. Xi, "An effective CFD-PML implementation for the cylindrical ADI-FDTD method," *IEEE Microw. Wirel. Compon. Lett.*, vol. 24, no. 12, pp. 824-826, 2014.
- [14] W. Bao and F. L. Teixeira, "Performance analysis of perfectly matched layers applied to spherical FDTD grids," *IEEE Trans. Antennas Propag.*, vol. 66, no. 2, pp. 1035-1039, 2018.
- [15] A. P. Smull, A. B. Manić, S. B. Manić, and B. M. Notaroš, "Anisotropic locally conformal perfectly matched layer for higher order curvilinear finite-element modeling," *IEEE Trans. Antennas Propag.*, vol. 65, no. 12, pp. 7157-7165, 2017.
- [16] H. X. Zheng and K. W. Leung, "Radial perfectly matched layer for the ADI-FDTD method," *IEEE Microw. Wirel. Compon. Lett.*, vol. 19, no. 7, pp. 425-427, 2009.
- [17] L. Wang, H. X. Zheng, M. J. Wang, and E. P. Li, "A circular-shaped perfectly matched layer strategy for rectangular FDTD grids," *Asia-Pacific Conference on Antennas and Propagation*, Xi'an, China, Oct. 2017.
- [18] L. Wang and H. X. Zheng, "Circular-shaped uniaxial perfectly matched layer for the FDTD method in Cartesian system," *International Applied Computational Electromagnetics Society Symposium*, Beijing, China, July 2018.
- [19] S. Dey and R. Mittra, "A locally conformal finite-difference time-domain (FDTD) algorithm for modeling three-dimensional perfectly conducting objects," *IEEE Microw. Guided Wave Lett.*, vol. 7, no. 9, pp. 273-275, 1997.



Lu Wang received the B.S. and M.S. degrees from Tianjin University of Technology and Education, Tianjin, China, in 2014 and 2017, respectively. He currently works toward the Ph.D. degree in the Hebei University of Technology, Tianjin, China. His current research interest is computational electromagnetics, especially in the FDTD method. He has published more than 20 papers in refereed journals and conference proceedings. He received the Chinese National Scholarship in 2016 and participated in the Chinese Graduate Mathematical Contest in Modeling for three times since 2014 with national third prize.



Mengjun Wang was born in Hebei, China, in 1978. He received the B.S. in Information Engineering and M.S. in Physical Electronics from Hebei University of Technology, Tianjin, China, in 1999 and 2005, respectively, and Ph.D. degree from Tianjin University, Tianjin, China, in 2008.

He is working as an Associate Professor with School of Electronics and Information Engineering, Hebei University of Technology, Tianjin, China. His research

interests include microwave radio frequency technology, flexible electronics devices and electromagnetic compatibility.



Kanglong Zhang received the B.E. degree in Communication Engineering from Zheng-zhou University of Aeronautics, Zhengzhou, China, in 2016. He currently works toward his Ph.D. degree in Hebei University of Technology, Tianjin, China. His current research interest is computational electromagnetics, especially in the FDTD method.



Wenjie Cui received the B.S. degrees from Tianjin University of Technology and Education, Tianjin, China, in 2017. He currently works toward his M.S. degree in Hebei University of Technology, Tianjin, China. His current interest is the design and fabrication of implantable medical antennas.



Hongxing Zheng received his Ph.D. degree in Electronic Engineering from Xidian University, Xi'an, in 2002. He is currently a Professor at School of Electronics and Information Engineering, Hebei University of Technology, Tianjin, China. He has authored six books and book chapters and more than 200 journal papers and 100 conference papers. He holds 40 China patents, issued in 2017. His recent research interests include wireless communication, design of microwave circuit and antenna, and computational electromagnetics.

Zheng is a Senior Member of the Chinese Institute of Electronics (CIE). He received the Young Scientists Award, in 2008, presented by the Tianjin Municipality, China.



Erping Li received the Ph.D. degree in Electrical Engineering from Sheffield Hallam University, Sheffield, U.K., in 1992. From 1993 to 1999, he was a Senior Research Fellow, Principal Research Engineer, Associate Professor, and the Technical Director at the Singapore Research Institute and Industry. In 2000, he joined the Singapore National Research Institute of High Performance Computing as a Principal Scientist and the Director of the Department of the Electronic and Photonics. He also holds the Distinguished Professor at Zhejiang University. He authored or coauthored more than 400 papers published in the referred international journals and conferences, authored two books. His research interests include electrical modeling and design of micro/nano-scale integrated circuits, 3-D electronic package integration, and nano-plasmonic technology.

Li is a Fellow of the MIT Electromagnetics Academy, USA. He has received numerous awards including the IEEE Electromagnetic Compatibility (EMC) Richard Stoddard Award for outstanding performance. He has served as an Associate Editor for number of IEEE Transactions and Letters. He has served as a General Chair and Technical Chair, for many international conferences. He was the founding General Chair for the 2008, 2010, and 2012 Asia-Pacific EMC Symposium. He has been invited to give numerous invited talks and plenary speeches at various international conferences and forums.

Double-layer Metal Wire Based Artificial Electromagnetic Surface and its Application to Bessel Beam Microwave Lens

He Yu¹, Guo-Hui Yang^{1,*}, Kuang Zhang¹, Fan-Yi Meng¹, and Yingsong Li²

¹Department of Electrical and Information Engineering
Harbin Institute of Technology, Harbin, 150001, China
yuhe@stu.hit.edu.cn, *gh.yang@hit.edu.cn, blade@hit.edu.cn

²College of Information and Communication Engineering
Harbin Engineering University, Harbin 150001, China
liyingsong@ieee.org

Abstract — In this paper, a transmissive periodic metasurface based on double-layer metal wire structure is designed by combining gradient phase theory with Pancharatnam-Berry (P-B) phase theory to control scattering phase of electromagnetic wave. The proposed artificial electromagnetic medium lens can improve the cross-polarized wave conversion efficiency of the phase discontinuous metasurface and ensure the thickness of the lens is ultrathin relative to the working wavelength.

Index Terms — Metasurface, microwave lens, P-B phase, phase discontinuity.

I. INTRODUCTION

Metasurface derived from the concept of metamaterials. It is array structure with a thickness of sub wavelength and a periodic structure in a plane, which can be used to modify the electromagnetic characteristics (phase, amplitude, polarization, beam shape) of reflected or transmitted electromagnetic waves. In 2011, the concept of metasurface was first proposed by Yu [1]. They obtained abrupt changes in the amplitude and phase of transmission field through V-shaped metal resonant structure arrays of sub-wavelength size. The law of phase modulation was obtained to construct phase gradient metasurface in the optical band for abnormal refraction [2-5]. In the metal sub-wavelength V-shaped antenna, the phase change of incident wave is based on the surface plasmon resonance effect, not on the accumulation of optical path. Besides, they realized polarization wave plate [6], plane lens [7] and vortex wave front [8] through the spatial arrangement of the unit structure. Other research groups proposed new structures to construct metasurfaces for electromagnetic wave control. Nathaniel et al. realized highly efficient transmission-type anomalous refraction metasurface based on highly efficient transmission-type linear polarized rotating metamaterials [9]. Huang et al. achieved abnormal

refraction under circularly polarized incident conditions through the spatial arrangement of short metal wire structural elements with different rotational directions [10].

In recent years, optical whirlpool wave plate based on metasurface, spherical aberration elimination, infinitely thin flat lens and axicon on communication wavelength have been studied. The research results of artificial electromagnetic metasurface in microwave band mainly focus on abnormal reflection, that is, one side of artificial electromagnetic surface is phase control unit, the other side is metal floor [11]. The focusing reflector was proposed with phase matching parabola distribution. The reflective phase gradient metasurface was realized by using the "H" structure design, which couples the vertical incident electromagnetic wave to the surface electromagnetic wave [12]. Based on the method of active device loading, a controllable $0-2\pi$ reflective phase artificial electromagnetic medium impedance surface was proposed [13]. It has been discovered that when the phase gradient of artificial electromagnetic surface can provide tangential wave vectors required by surface-like plasmon (SSP), the propagating wave and SSP can be efficiently coupled at specific frequencies in microwave band [14].

However, phase mutation is always accompanied by the change of polarization mode and most of the ultra-thin artificial electromagnetic surface can only affect the cross-polarization component. Therefore, the conversion efficiency of cross-polarization wave becomes the main factor restricting the practical application of ultra-thin artificial electromagnetic surface.

In this paper, by introducing phase discontinuity into the electromagnetic wave propagation interface, we can control the beam and realize reflection and transmission in any direction. The Pancharatnam-Berry (P-B) phase provides a theoretical basis to efficiently transform the circularly polarized wave. The cross-

polarization phase is twice the rotation angle when it rotates along the geometric center at a certain angle.

II. THEORY ANALYSIS

A. Pancharatnam-Berry phase

In order to realize phase discontinuity at the interface of metasurface, the theory of Pancharatnam-Berry (P-B) phase is considered for circularly polarized incident electromagnetic waves. In microwave region, metals are ideal conductors without surface plasmon effect, so phase discontinuity cannot be achieved by using cross-polarized resonance in optical frequency [15]. However, we can still achieve phase discontinuity by converting circularly polarized incident wave into its cross-polarized wave, which generates P-B geometric phase by changing spatial polarization [16].

Here, a phase factor (PF) is introduced. When the polarization mode is changed from the initial state to the final state, the process can be conveniently expressed in the Poincare Sphere by introducing the PF. As is shown in Fig. 1, the two poles of the sphere represent right-handed and left-handed circular polarized waves respectively, while the equator corresponds to the linear polarized state. In other words, when the polarization mode of incident wave changes through spatial variation, its spatial phase also changes, because this process is a purely geometric change process. Through the variable of phase factor, we can quantify the relationship between the change of space-varying polarization mode and the change of phase.

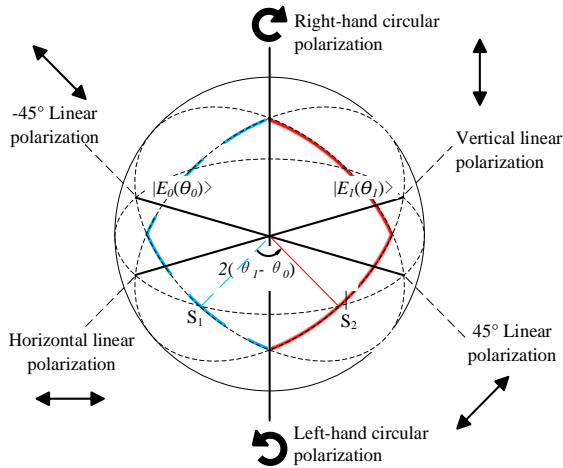


Fig. 1. Polarization representation on Poincare Sphere.

Assuming that the polarization mode varies between the poles of Poincare Sphere, any desired phase change (from 0 to 2π) can be achieved for any polarization rotation. When the incident wave is a circularly polarized wave, the transmission field can be described as:

$$\vec{E}_{out} = \sqrt{\eta_E} \vec{E}_{in} + \left(\sqrt{\eta_R} e^{\pm i2\theta} \vec{R} + \sqrt{\eta_L} e^{\mp i2\theta} \vec{L} \right), \quad (1)$$

η_E , η_R and η_L represent the coupling efficiency of polarization order, R and L represent the right-handed and left-handed polarization states. t_x and t_y denote as the transmission factors of the two linear polarization components, respectively. φ is the phase difference between the two transmission factors. For circularly polarized incident wave, the transmitted electric field contains two components. One component keeps the original rotation direction and the other component is cross polarized field, which is the key to the construction of hyperlens by using phase discontinuity.

B. Bessel beam metasurface

For an axle prism with a beta angle, the phase delay must increase linearly with the increase of the distance from center point. The use of artificial electromagnetic metasurface instead of traditional phase control elements will make it possible to achieve high-performance convergent lens with light weight and small volume. In this method, the control of the incident wavefront will no longer depend on cumulative phase of electromagnetic wave propagation, but on the phase shift obtained by scattering on the sub-wavelength ultra-thin array.

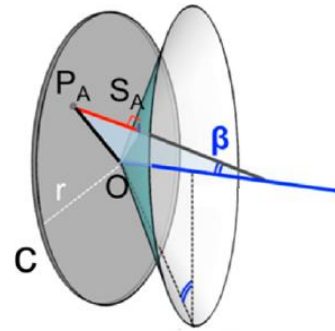


Fig. 2. Plane lens and its equivalent prism.

The plane lens and its equivalent prism is shown in Fig. 2. The phase shift of $P_A(x, y)$ at any point on the lens should satisfy the following equation:

$$\varphi_A(x, y) = \frac{2\pi}{\lambda} P_A S_A = \frac{2\pi}{\lambda} \sqrt{x^2 + y^2} \sin\beta \quad (2)$$

Based on the structure of split ring resonator (SRR) unit, we construct the phase profile of the lens and obtain a microwave lens with 25×25 unit by taking $\beta = 10^\circ$.

III. DESIGN AND RESULTS

A. Double-layer metal wire structure

The double-layer metal wire structure is shown in Fig. 3. Metal wires are arranged at the same position on both sides of the dielectric plate. The structure is used to simulate the silicon dielectric metasurface. When electromagnetic waves are irradiated on the structure, magnetic resonance will occur between the two metal.

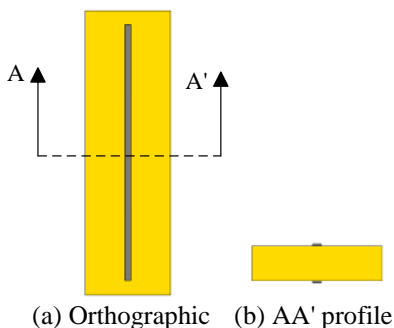


Fig. 3. Metal wire array unit from different perspectives.

The structure is periodically arranged horizontally and vertically, and the scattering parameters are obtained by irradiating the structure with left-handed circular polarization wave. From the results in Fig. 4, it can be seen that at 9.8 GHz, the cross-polarization transmission coefficient of the periodic structure is as high as 0.85, i.e., the cross-polarization conversion rate is 72%. At the same time, the co-polarization transmission coefficient is only 0.25, i.e., the co-polarization transmission rate is only 6.25%. Therefore, in the transmission wave, most of the energy transferred from the left circularly polarized wave is called the cross polarized wave. According to the principle of PB phase introduced above, the S_{21} phase value of the cross-polarized wave is the abrupt phase introduced by the structure to the incident electromagnetic wave.

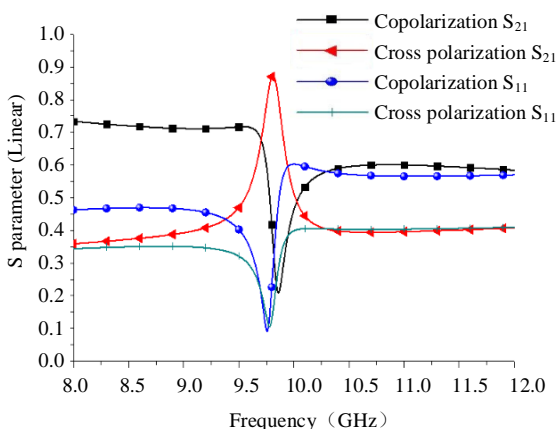


Fig. 4. S parameter simulation results of double-layer metal wire structure.

The unit size of the structure is only 3 mm×10 mm, which is insensitive to oblique incidence. Hence, when the electromagnetic wave was introduced as oblique incidence, the same results can be obtained. When the incident angle is changed from 0° to 60°, the cross polarization conversion coefficients are all above 0.85 (Fig. 5). This indicates that when the size of the unit is

much smaller than the wavelength, the electromagnetic response characteristics are insensitive to the incident angle, so the electromagnetic wave control process can be realized in a wide angle.

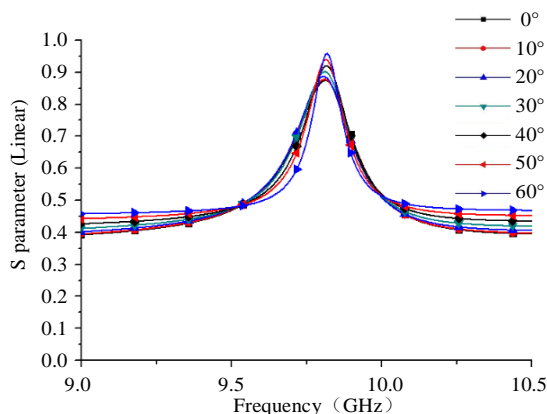


Fig. 5. Oblique incidence cross polarization conversion coefficient of double-layer metal wire structure.

If the right-handed circular polarization wave is used to irradiate, the parameters and simulation settings of the structure remain unchanged. The scattering parameters are obtained as shown in Fig. 6. It can be seen that the structure has the same polarization conversion effect for the left-handed circular polarization wave and the right-handed circular polarization wave.

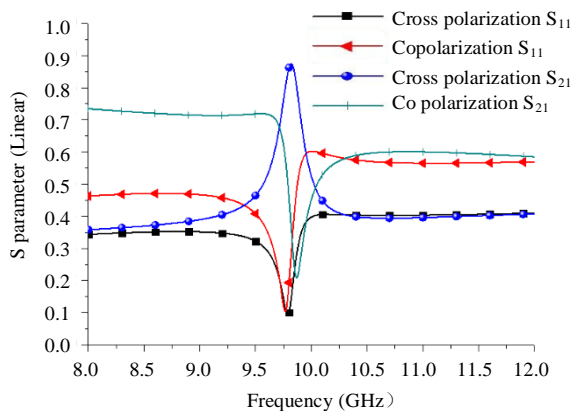


Fig. 6. S parameter simulation results of the structure irradiated by right-handed circularly polarized wave.

In the upper and lower metal structures, there are surface currents flowing in opposite directions. These two parts of the surface current and the displacement current between the two layers of metal will form a loop, which constitutes the magnetic response of the structure. A magnetic field monitor is applied around the structure to obtain the magnetic field distribution of the double-layer metal wire structure at 9.8 GHz. As is clearly seen

from Fig. 7, the section of the magnetic response generated by the structure under the irradiation of the left circularly polarized wave on z-o-y plane. It can be seen that at 9.8 GHz, there is a strong magnetic field in the position of the metal strip on the structure, and the magnetic field intensity takes the form of strong in the middle and weak at both ends. Figure 8 depicts the corresponding magnetic field distribution on the x-o-z plane when $y=0$ and $y=3$ mm. The results demonstrate that the magnetic field in the center of the structure is the strongest and extends gradually to both ends.

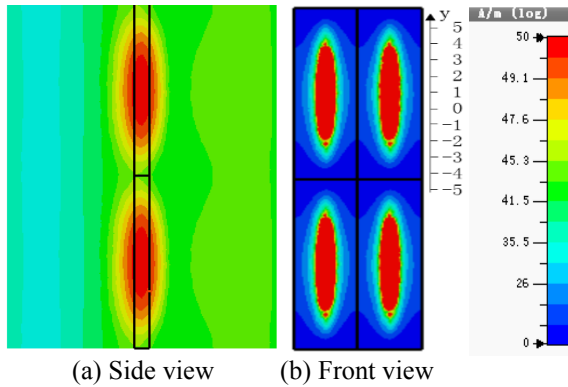


Fig. 7. Simulation of magnetic field distribution in double-layer metal wire structure.

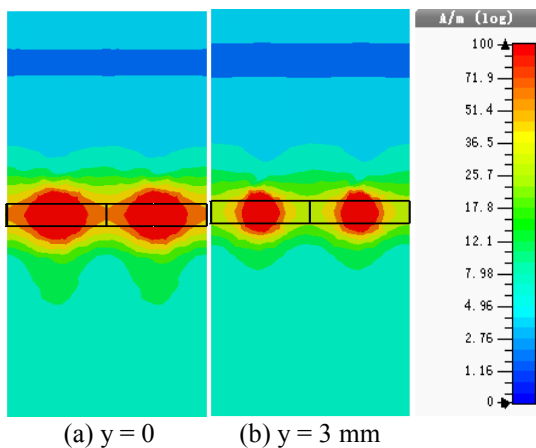


Fig. 8. Cross section of magnetic field distribution in double-layer metal wire structure.

B. Double-layer metal wire array metasurface

Eight rotating elements are combined to form a new unit, which is periodically arranged and irradiated by left-handed circular polarization wave. Metasurface with double-layer metal wire array structure and the SRR structure metasurface are depicted in Fig. 9. When the incident wave is perpendicular to the incident wave, the angle of the incident wave deflects. From the generalized refraction law formula, when the cell spacing is 10 mm,

the abrupt phase of the phase difference between adjacent elements is 45° , and the incident angle is 0° , the emission angle is 23° . The deflection of electromagnetic wave propagation direction was observed by an electric field monitor. The results of the electric field monitor show that when the structure is illuminated vertically by a left-handed circular polarized wave, the angle between the transmitted wave and the observed wave is 18.4° and the energy of the transmitted wave is high.

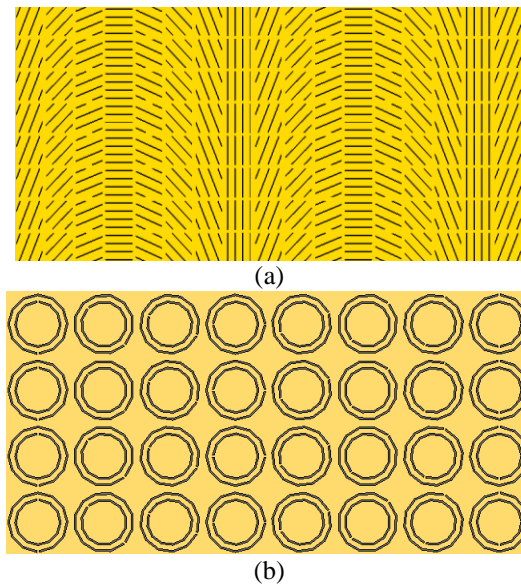


Fig. 9. (a) Metasurface with double-layer metal wire array structure. (b) SRR structure metasurface.

The performance comparison of single-layer metal wire array metasurface and the designed metasurface is demonstrated in Table 1. As can be concluded from the chart, the designed double-layer metal wire array metasurface can realize high transmittance efficiency of cross polarized waves by introduced magnetoresistance.

Table 1: Performance comparison of single-layer metal wire array metasurface and the designed metasurface

Structure	Efficiency
Single Layer	20%
Double Layer	72%

Full-wave simulation is carried out by using Lumerical FDTD (Fig. 10). Left-circular polarization wave is used to illuminate the lens, and its effect on electromagnetic wave convergence is studied. The near-field results of the convergent lens are obtained. According to the results, when the convergent lens is illuminated by the left-handed circular polarization wave, a non-diffracting Bessel beam with concentrated energy is generated on the other side of the lens. The maximum energy is achieved at $z=200$ mm, which means,

the focal length of the convergent lens is 200 mm.

The phase change of the structure is gradient change rather than uniform change, and the discrete phase change leads to the difference between the control effect and calculation of the final electromagnetic wave. When simulating metasurface, finite elements are selected to simulate the infinite periodic structure. For this structure, every element has been trimmed after rotation, so there is a small error between the simulation results and the calculation of the generalized refraction law formula.

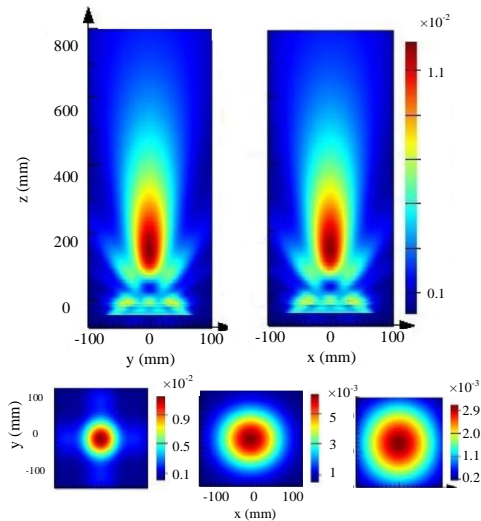


Fig. 10. FDTD results of double metal wire structure.

In the microwave anechoic chamber shown in Fig. 11, the circularly polarized horn is used as the transmitting antenna and the cross polarized horn is used as the receiving antenna. The metasurface is placed in front of the receiving horn and the receiving pattern is tested.

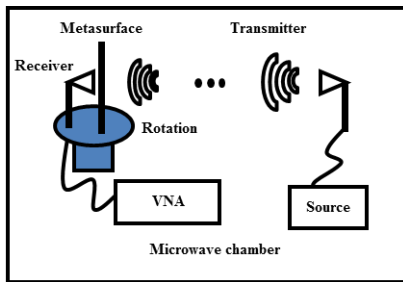


Fig. 11. Measurement setup of the designed metasurface.

In Fig. 12, when the incident wave is irradiated to the structure at 19° incidence angle, the receiving antenna obtains the maximum test level. In other words, when the incident wave is incident vertically, a transmission wave with an angle of 19° from the normal line will be generated, which is only slightly different from the calculated result of 23° .

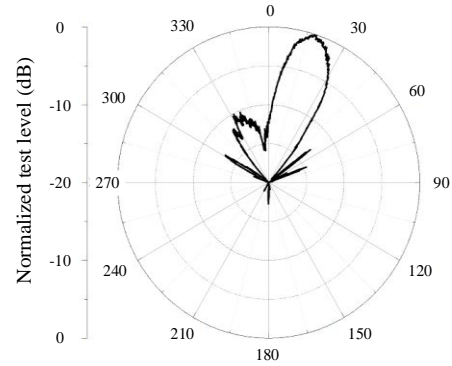


Fig. 12. Measurement results of double-layer metal wire array metasurface.

IV. CONCLUSION

In this paper, based on the generalized refraction law and P-B phase principle, an artificial electromagnetic surface with deflection effect and a Bessel beam theory for convergence of electromagnetic waves are designed by using the double-layer metal wire array unit structure. The unit used to form microwave lens has high efficiency in the X wave band to achieve efficient manual control of electromagnetic wave transmission, which will be a good candidate for electromagnetic wave regulating device application.

REFERENCES

- [1] X. Ni, N. K. Emani, A. V. Kildishev, et al., "Broadband light bending with plasmonic nano-antennas," *Science*, 335(6067): 427-427, 2012.
- [2] K. Yu, Y. Li, and X. Liu, "Mutual coupling reduction of a MIMO antenna array using 3-D novel meta-material structures [J]," *Applied Computational Electromagnetics Society Journal*, vol. 33, no. 7, pp. 758-763, 2018.
- [3] T. Jiang, T. Jiao, Y. Li, and W. Yu, "A low mutual coupling MIMO antenna using periodic multi-layered electromagnetic band gap structures," *Applied Computational Electromagnetics Society Journal*, vol. 33, no. 3, pp. 305-311, 2018.
- [4] L. Huang, X. Chen, H. Muhlenbernd, et al., "Dispersionless phase discontinuities for controlling light propagation," *Nano Letters*, 12(11): 5750-5755, 2012.
- [5] S. Luo, Y. Li, Y. Xia, and L. Zhang, "A high gain low mutual coupling antenna array with meta-material loading and neutralization line structure," *Applied Computational Electromagnetics Society Journal*, 2018, accepted.
- [6] R. Blanchard, G. Aoust, P. Genevet, et al., "Modeling nanoscale V-shaped antennas for the design of optical phased arrays," *Physical Review B*, 85(15): 155457, 2012.
- [7] M. A. Kats, P. Genevet, G. Aoust, et al., "Giant birefringence in optical antenna arrays with widely

tailorable optical anisotropy,” *Proceedings of the National Academy of Sciences*, 109(31): 12364-12368, 2012.

- [8] X. Ni, N. K. Emani, A. V. Kildishev, et al., “Broadband light bending with plasmonic nano-antennas,” *Science*, 335(6067): 427-427, 2012.
- [9] N. K. Grady, J. E. Heyes, D. R. Chowdhury, et al., “Terahertz metamaterials for linear polarization conversion and anomalous refraction,” *Science*, 340(6138): 1304-1307, 2013.
- [10] Y. Li, J. Zhang, S. Qu, et al., “Achieving wideband polarization-independent anomalous reflection for linearly polarized waves with dispersionless phase gradient metasurfaces,” *Journal of Physics D: Applied Physics*, 47(42): 425103, 2014.
- [11] X. Li, S. Xiao, B. Cai, et al., “Flat metasurfaces to focus electromagnetic waves in reflection geometry,” *Optics Letters*, 37(23): 4940-4942, 2012.
- [12] B. O. Zhu, J. Zhao, and Y. Feng, “Active impedance metasurface with full 360 reflection phase tuning,” *Scientific Reports*, 3: 3059, 2013.
- [13] T. J. Cui, M. Q. Qi, X. Wan, et al., “Coding metamaterials, digital metamaterials and programmable metamaterials,” *Light: Science & Applications*, 3(10): e218, 2014.
- [14] N. K. Grady, J. E. Heyes, D. R. Chowdhury, et al., “Terahertz metamaterials for linear polarization conversion and anomalous refraction,” *Science*, 340(6138): 1304-1307, 2013.
- [15] Y. Yao, M. A. Kats, P. Genevet, et al., “Broad electrical tuning of graphene-loaded plasmonic antennas,” *Nano Letters*, 13(3): 1257-1264, 2013.
- [16] L. Zhao, F. Liu, X. Shen, G. Jing, Y. Cai, and Y. Li, “A high-pass antenna interference cancellation chip for mutual coupling reduction of antennas in contiguous frequency bands,” *IEEE Access*, vol. 6, pp. 38097-38105, 2018.



He Yu received the B.S. degree in Electronic and Information Engineering from Dalian Maritime University, China in 2015, and the M.S. degree in Electronic and Communication Engineering from Harbin Institute of Technology, Harbin, China, in 2017.

She is currently pursuing the Ph.D. degree in Electromagnetic Field and Microwave Technology at Harbin Institute of Technology, Harbin, China. Her research interests include the study of nonlinear characterization, modeling, design and analysis of comb generators, RF devices measurement.



Guo-Hui Yang received his B.S. in Communication Engineering, M.S. in Instrument Science and Technology, and Ph.D. in Microelectronics and Solid State Electronics all at Harbin Institute of Technology (HIT), Harbin, China in 2003, 2006, and 2009, respectively. Since 2009, he has been with the Dept. of Microwave Engineering, School of Electronics and Information Engineering at HIT, China, where he is currently an Associate Professor of Harbin Institute of Technology.

His recent research interests are mainly in metamaterials and metasurface, frequency selective surface and RF microwave active and passive circuits.



Kuang Zhang received his B.Sc. in Electronics and information Engineering, M.Eng. in Electronics Engineering, and Ph.D. in Communication and Information Systems, all at Harbin Institute of Technology (HIT), Harbin, China in 2005, 2007, and 2011, respectively. He worked as a Visiting Professor at University of Wisconsin-Madison in U.S., from 2015 to 2016. Since 2010, he has been with the Dept. of Microwave Engineering, School of Electronics and Information Engineering at HIT, China, where he is currently an Associate Professor.



Fan-Yi Meng received the B.S., M.S., and Ph.D. degrees in Electromagnetics from the Harbin Institute of Technology, Harbin, China in 2002, 2004, and 2007, respectively. Since August 2007, he has been with the Department of Microwave Engineering, Harbin Institute of Technology, where he is currently a Professor. He has coauthored four books, 40 international refereed journal papers, over 20 regional refereed journal papers.

His current research interests include antennas, electromagnetic and optical metamaterials, plasmonics, and electromagnetic compatibility (EMC).



Yingsong Li received his B.S. degree in Electrical and Information Engineering in 2006, and M.S. degree in Electromagnetic Field and Microwave Technology from Harbin Engineering University, 2006 and 2011, respectively. He received his Ph.D degree from both Kochi University of Technology (KUT), Japan and Harbin Engineering University, China in 2014. Now, he

is a Full Professor of Harbin Engineering University from July 2014.

His current research interests are mainly in remote

sensing, underwater communications, signal processing, radar, SAR imaging, compressed sensing, and antennas.

A Novel Query Tree Anti-collision Algorithm for RFID

Fan Yang^{1,2}, Lei Zhao³, Hu Chen¹, and Shuixia Hao¹

¹ Jiangsu Key Lab of Education Big Data Science and Engineering
Jiangsu Normal University, Xuzhou, Jiangsu 221116, China
yangfan@jsnu.edu.cn

² College of Engineering
Nanjing Agricultural University, Nanjing, Jiangsu 210031, China

³ School of Information and Control Engineering
China University of Mining and Technology, Xuzhou, Jiangsu 221116, China
leizhao@cumt.edu.cn

Abstract — In order to further decrease the probability of the collision and reduce communication complexity, a new low complexity anti-collision algorithm for RFID is proposed using Query Tree. The proposed algorithm can reduce the probability of collision and the traffic of data communication by using tag grouping and setting rules, respectively. The simulation results show that the proposed scheme consumes fewer slots and has lower communication complexity.

Index Terms — Anti-collision algorithm, data clipping, Query tree, RFID.

I. INTRODUCTION

The Radio Frequency Identification (RFID) is an automatic identification system where the reader identifies the tags by radio waves [1]. In light of high-speed, feasible, convenient and contactless, RFID is one of the key technologies of the Internet of things (IoT) and is widely used in many fields, such as medical treatment, supply-chain management, transportation and item tracking. However, the rapid development of RFID technology gives rise to several problems, including data security, transmission distance, electromagnetic interference (EMI), antenna failure and tag collision etc. The last three issues seriously restrict the development of RFID [2,3]. In a frequency band such as 125kHz, 13.56MHz, and 2.45GHz, a large amount of electromagnetic radiation is generated due to the simultaneous operation of many electronic devices. RFID system will interfere with adjacent electronic devices. Similarly, radiation from other electronic devices interferes with RFID systems as well. Thus, the performance of communication quality between reader and tag can be severely affected by EMI, which significantly increasing bit error rate of RFID system

[4,5]. Moreover, the reader cannot receive data normally due to antenna failure, the failed antenna may cause deterioration of array performance [6]. But, an excellent anti-collision algorithm can alleviate the impact of EMI and antenna failure on the system. How to optimize anti-collision algorithm effectively is the key point of the research of RFID technology. To resolve this problem, many optimization anti-collision algorithms have been proposed, which are divided into two categories: Aloha-based probabilistic algorithms and tree-based deterministic algorithms.

Framed-Slotted Aloha (FSA) [7] method is a typical Aloha-based anti-collision algorithm and has been widely used in many RFID applications. In FSA, each unread tag randomly selects one slots in frame. Unless the reader receives the tag's information successfully, the tag will try again in the next frame. Aloha-based anti-collision algorithms work efficiently when the frame size matches with the number of tags. However, the performance of the algorithms becomes very poor when the number of tags changes in a wide range with the fixed size of frame. Therefore, many dynamic frame-slotted Aloha (DFSA) algorithms have been proposed to improve the system performance [8-11]. Since Aloha-based algorithms, however, cannot completely prevent collisions, they have a serious problem that a specific tag may not be identified for a long time, leading to tag starvation problem.

Tree-based algorithms including deterministic tree-based algorithm such as query tree algorithm (QT) [12,13], and probabilistic counter-based algorithm such as binary tree algorithm (BT) [14], repeatedly separate collided tags into two sets until each set has only one tag or no tag. BT adopts random binary numbers (0 or 1) to split the tag set while QT uses tag IDs. Although they have relatively long identification delay, they do

not cause the tag starvation problem. In QT, the reader provides the tags with a query and the tags must respond with their full ID as a result of a successful matching of the query with their corresponding ID part. Since using prefixes, the performance of QT is sensitive to the distribution of IDs of tags. Collision tracking tree algorithm (CTTA) [15], which is modified from QT, is used to reduce the number of collisions in QT using a tree traversal path. CCTA takes the advantage of grouping in QT and cuts off the useless bits in each grouping round. In this way, CCTA decreases total data exchange in QT. Bit tracking technology is commonly based on Manchester code, which is often used to detect collision bits. Optimal Query Tracking Tree (OQTT) algorithm [16], which used bit tracking technology, tries to separate all of the tags into smaller sets to reduce collisions at the beginning of identification. Although solving high collision rate at the initial stage, the random number generation module and bit modulating module are added to increase the hardware cost. According to the characteristics of tree-based anti-collision algorithm, scholars have proposed a lot of improved algorithms. However, those algorithms are still inevitably cause lots of unsuccessful slots [17,18].

In this paper, a query tree with low complexity anti-collision algorithm (QTLC) is proposed to further decrease the probability of the collision and reduce communication complexity, which divides the traditional identification into tag grouping stage and tag identification stage. In the first stage, using the bit tracking technology, the reader determines the grouping prefix by sending a prefix query command and the tags with the same grouping prefix are in the same branch, in which a large search tree is divided into several branches to reduce the probability of the collisions. In the second stage, using the set of reply rules, the data replied by tag is clipped to decrease the transmission quantity of invalid data and reduce the communication complexity of the system. Simulation results show that the proposed algorithm takes great advantage of identification delay and communication complexity.

The rest of this paper is organized as follows: Section II introduces the theory and method of a query tree with low complexity anti-collision algorithm (QTLC) in brief. Section III derives the mathematical analysis of QTLC. Section IV presents analytical and simulation results. Finally, the conclusions are presented in Section V.

II. THEORY AND METHOD

The core of QTLC is tag grouping and data clipping. By the regrouping of the tags, the collision probability of the tags is decreased; the transmission of the invalid data in the channel is reduced by data cutting, and the communication complexity of the system is further decrease.

A. Tag grouping

The purpose of grouping is to divide the mass tags into several groups with the same ID prefix sequence, and each tag is identified in the group, resulting in the reduction of the collision probability in the initial stage. The reader gets the grouping prefix sequence of all the tag ID by sending query command to unread tags, and the tags with the same prefix sequence are divided into one group.

The length of grouping prefix sequence is $n = \lfloor \log_2^g \rfloor$, where $\lfloor * \rfloor$ is a rounded down operation and g is the initial groups. In initial stage of grouping, the reader first sends the k bit query sequence (11. 1000.. 0), where the length of ID and the length of 1 are k and n , respectively. While obtaining the query sequence, all tags encoded the former n bit data of ID to the decimal number m , then a 2^n bit data is generated, in which the m_{th} bit of the sequence is 1, and the remaining bits are all 0. After receiving the tag reply, the reader counts the number of the non-repeating sequence and gets the number of the actual grouping.

For example, there are 8 tags with IDs 00110101 (T1), 00111010 (T2), 00100100 (T3), 10101000 (T4), 10101101 (T5), 10110001 (T6), 11001111 (T7) and 11010100 (T8), respectively and $g = 8$. While obtaining the query sequence of 11100000, all tags convert the first 3-bit binary number of ID to decimal number, then replying 8 bits of binary sequence to reader, in which the 1th, 5th, 6th bit of the sequence is “1” respectively, and the other are 0. At the same time, the reader determines the 1th, 5th, 6th bit in this sequence to be “1” and converts it into the corresponding binary sequence, namely, “001”, “101” and “110”. The prefix, such as “000”, “010”, “011”, “100”, “111”, is eliminated. As a result, the prefix sequence of each group of tag is determined. Table 1 shows an example of tag grouping.

Table 1: An example of tag grouping

No.	The Prefix	Coded Information	Grouping No.
T1	001	00000001	1
T2	001	00000001	1
T3	001	00000001	1
T4	101	00010000	5
T5	101	00010000	5
T6	101	00010000	5
T7	110	00100000	6
T8	110	00100000	6

B. Data clipping

For NEAA [19] and CTTA [15], when there is a collision, the reader still receives the remaining ID data sent by the tag and this invalid data increases the communication complexity of the system. According to the above problem, QTLC sets up a data clipping

mechanism. When the reader sends a query prefix sequence with h bits, if the former h bits of tag ID match this sequence and the $(h + 1)_{th}$ bit is 0, the tag will send the remaining $(k - h)$ bits to the reader; otherwise, it only replies 1 to reader. So the $(h + 1)_{th}$ bit can be defined as information bit. Using data clipping technology, QTLC can reduce the communication complexity of the system, and speeds up the identification.

For example, when the current query prefix is 001, T1, T2 and T3 will assigned to the same group. By detecting the information bit. T3 reply the remaining bits to the reader, it is "00100". T1 and T2, however, reply "1" to the reader. Figure 1 shows an example of data clipping.

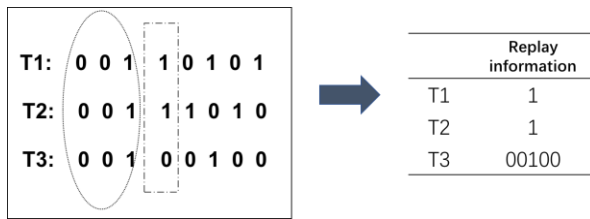


Fig. 1. Example of data clipping.

III. PERFORMACNE ANALYSIS

A. Identification delay

Being similar to the definition in [20], the identification delay of the anti-collision algorithm, denoted as W , is defined as the number of queries sent by the reader in order to identify tags. Given a distributed uniformly set of N tags, the initial group is g , since the tag ID is distributed uniformly, the tags are assigned to each group with the same probability. Thus,

$$p = 2^{-\lceil \log_2^g \rceil} = 2^{-n}. \quad (1)$$

So the probability of groups with idle, success and collision are:

$$P_I(0, N) = (1 - 2^{-n})^N, \quad (2)$$

$$P_S(1, N) = N \times 2^{-n} \times (1 - 2^{-n})^{N-1}, \quad (3)$$

$$P_C(m, N) = 1 - P_I(0, N) - P_S(1, N). \quad (4)$$

Therefore, the number of groups with idle, success and collision are:

$$Q_I(0, N) = 2^n \times (1 - 2^{-n})^N, \quad (5)$$

$$\begin{aligned} Q_S(1, N) &= 2^n \times N \times 2^{-n} \times (1 - 2^{-n})^{N-1} \\ &= N \times (1 - 2^{-n})^{N-1}, \end{aligned} \quad (6)$$

$$\begin{aligned} Q_C(m, N) &= 2^n \times (1 - P_I(0, N) - P_S(1, N)) \\ 1 &< 2^n \leq k. \end{aligned} \quad (7)$$

Obviously, the value of 2^n is affected by g and the minimum value of g is 2. With the increasing of g , the probability of grouping collision is decreases. However, g is not bigger is better. The larger value of g will increase the communication complexity of the system, which will affect the simulation experiment as well. So we assume that $1 < 2^n \leq k$, the exact value of g will be discussed at next section.

In the application of Internet of things, the number of tags is massive, namely, the value of N can be assumed to be infinite; while $N \gg g$,

$$\lim_{N \rightarrow +\infty} (1 - 2^{-n})^N = 0,$$

$$\lim_{N \rightarrow +\infty} (1 - 2^{-n})^{N-1} = 0.$$

By simplifying Equations (5-7) with the above two equations:

$$\lim_{N \rightarrow +\infty} Q_I(0, N) = \lim_{N \rightarrow +\infty} (1 - 2^{-n})^N = 0, \quad (8)$$

$$\lim_{N \rightarrow +\infty} Q_S(1, N) = \lim_{N \rightarrow +\infty} N \times (1 - 2^{-n})^{N-1} = 0, \quad (9)$$

$$\lim_{N \rightarrow +\infty} Q_C(m, N) = \quad (10)$$

$$\lim_{N \rightarrow +\infty} (2^n \times (1 - P_I(0, N) - P_S(1, N))) = 0.$$

In other words, when the number of tags is very large, there are almost all of groups are collided. So the number of tags of each group can be assumed to:

$$t = \frac{N}{2^n} = \frac{N}{2^{\lceil \log_2^g \rceil}}. \quad (11)$$

For QTLC, the number of nodes in BT, generated by the QTLC, represents the identification delay. Each node in QTLC represents query command send by the reader, the intermediate node represents a collision and the leaf node represents a tag.

In the grouping phase, the reader only needs to broadcast a grouping query command to obtain the grouping information. So the identification delay of this phase is 1. In the identification phase, when collision occurring, QTLC divides the collision node into two subsets. Because of the properties of BT, the degrees of nodes only are 0 and 2. Meanwhile, the number of nodes with degree 2 is one less than nodes with degree 0. So the number of nodes with degree 0 and 2 in each group are:

$$w_0 = t = \frac{N}{2^{\lceil \log_2^g \rceil}}, \quad (12)$$

$$w_2 = t - 1 = \frac{N}{2^{\lceil \log_2^g \rceil}} - 1. \quad (13)$$

Therefore, the number of nodes in this current group is:

$$\begin{aligned}
 W_g &= w_0 + w_2 = \frac{N}{2^{\lfloor \log_2^g \rfloor}} + \frac{N}{2^{\lfloor \log_2^g \rfloor}} - 1 \\
 &= \frac{N}{2^{\lfloor \log_2^g \rfloor - 1}} - 1.
 \end{aligned} \quad (14)$$

QTLC divides the tags into $2^{\lfloor \log_2^g \rfloor}$ groups and the number of node in each branch is W_g . So the identification delay is:

$$W = 2^{\lfloor \log_2^g \rfloor} \times w_g + 1 = 2 \times N - 2^{\lfloor \log_2^g \rfloor} + 1. \quad (15)$$

B. Communication complexity

For an anti-collision algorithm in RFID, the communication complexity is the number of bits transmitted between the reader and tags. The reader communication complexity and the tag communication complexity represent the number of bits send by reader and tags, respectively. The tag communication complexity is more important than the reader, because it is desirable to minimize the power consumption of the tags [20].

Let $D(N)$ be the communication complexity of QTLC. $D_G(N)$ and $D_I(N)$ represents the communication complexity in the grouping and identification phase respectively:

$$D(N) = D_G(N) + D_I(N). \quad (16)$$

In the grouping phase, the reader only sends k bits grouping query sequence. Then tags reply with 2^n bits, so $D_G(N)$ is:

$$D_G(N) = k + N \times 2^{\lfloor \log_2^g \rfloor}. \quad (17)$$

In the identification phase, let j be the number of "0" in the same bit of the tag ID, so j also obeys the binomial distribution:

$$V(j, N) = C_N^j p^j (1-p)^{N-j}. \quad (18)$$

Because each bit has the same probabilities with "0" and "1", so p in Equation (18) is 0.5. When the same bit of tag ID is all "0" or "1" in N tags, this bit will not collide:

$$\begin{aligned}
 V(j=0 | j=N, k, N) &= V(0, N) + V(N, N) \\
 &= 2^{1-N}.
 \end{aligned} \quad (19)$$

Otherwise, it will be occurring collision:

$$V(j \neq 0 | j \neq N, k, N) = 1 - 2^{1-N}. \quad (20)$$

$F_R(u)$ is defined as the length of u_{th} query prefix. $F_{T0}(u)$ and $F_{T1}(u)$ represents the length of u_{th} reply for tags when information bit is 0 and 1 respectively. p_0 and p_1 represent the probability when the information bit is 0 and 1 respectively. So $F_{T0}(u) + F_{T1}(u) = k$, $F_{T1}(u) = 1$.

According to Equations (18-20), the communication complexity in the tag identification phase is:

$$D_I(N) = \sum_{u=1}^T \left(F_R(u) + V(j \neq 0 | j \neq N, k, N) \right) \times (F_{T0}(u) \times p_0 + F_{T1}(u) \times p_0) \quad (21)$$

$$= \sum_{u=1}^T \left(F_R(u) + (0.5 + (0.5)^{-N}) \times (k - F_R(u) + 1) \right).$$

So $D(N)$ is:

$$\begin{aligned}
 D(N) &= k + N \times 2^{\lfloor \log_2^g \rfloor} \\
 &\quad \sum_{u=1}^T \left(F_R(u) + (0.5 + (0.5)^{-N}) \times (k - F_R(u) + 1) \right).
 \end{aligned} \quad (22)$$

IV. PERFORMACNE EVALUATION

In this section, theoretical analysis and simulation experiments were undertaken to validate QTLC algorithm. Compared with QT, NEAA and CTTA algorithm, QTLC is analyzed from aspects of identification delay and communication complexity. The simulation condition is as follows: the number of tags increases from 100 to 1000. The size of tag IDs is 96 bits. Tag IDs are distributed uniformly.

A. Selection of initial groups

The system efficiency represents the ratio of the readable slot to the identification delay, which is an important parameter to evaluate the performance of an anti-collision algorithm. In order to obtaining optimal g , the experiment was conducted. Fig.2 shows the system efficiency with different initial groups. The proposed algorithm gets a higher efficiency with a larger initial groups, and the cost will increase as well. Compared with $g = 4$, the system efficiency of $g = 8$ is about 0.5, this is still not ideal. The reason is that with the increasing number of tags in each group, the probability of collision in each group is high due to the small initial groups. Considering the cost of the tag with larger initial groups, the optimal initial group is $g = 16$.

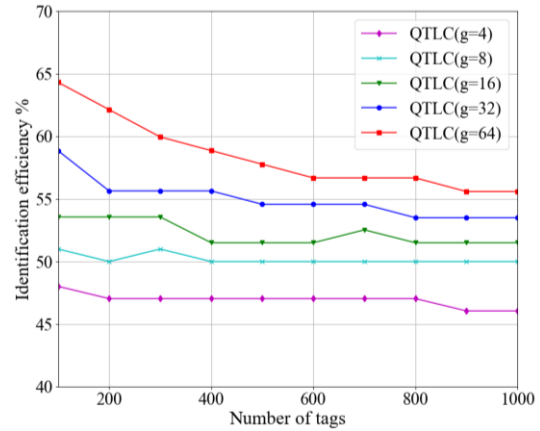


Fig. 2. The system efficiency of QTLC with different initial groups.

B. Communication complexity

(1) Reader communication complexity

Reader communication complexity refers to the total number of bits sent by the reader to all tags. Figure 3 shows the traffic of reader. The traffic of the four algorithms increases with the number of tags, and this pattern of growth is linear. QT algorithm has the fastest growth, CTTA is faster than NEAA, but all of them is slower than QT, and the proposed algorithm has slowest growth because it automatically generates valid query prefixes, which greatly reduces the number of queries sent by a reader. When $N = 1000$, the traffic of QT algorithm is 80968 bit, CTTA and NEAA is 59863 bit, 52469 bit respectively. However, QTLC is 49764 bit.

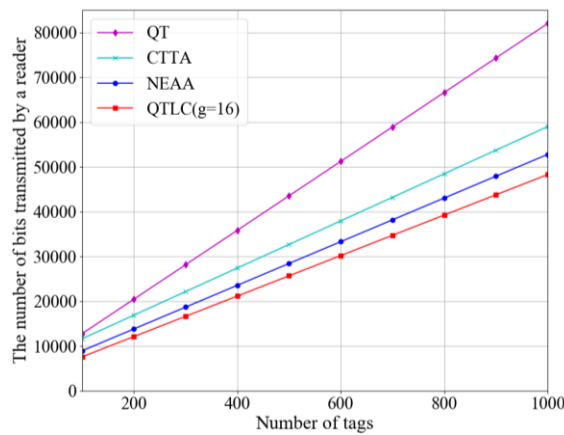


Fig. 3. The traffic of reader.

(2) Tag communication complexity

In the process of identification, the tag has a corresponding response to the different commands of the reader, and the sum of the bits sent by tags is called the traffic of tag, which is closely related to the power consumption. The larger traffic is, the more power will consume. However, for the traditional tag, the power consumption is limited. In addition, by reducing the amount of data returned from tags, the security of system will be improved. Therefore, the traffic of tag should be reduced as much as possible. QTLC algorithm inherits the advantages of QT algorithm. It not only simplifies the design of tag, but also reduces the traffic. From Fig. 4, it can be seen that the traffic growth of QTLC is the slowest, which is significantly lower than the other three algorithms. When $N = 1000$, the traffic of tag for QT algorithm is 120800 bit, CTTA and NEAA is 112003 bit, 92560 bit respectively, but QTLC is 61976 bit.

C. Identification delay

The identification delay is defined as the number of queries that identify all tags successfully by the reader, namely the total slots, and it is a key parameter to measure the performance of an anti-collision algorithm.

Figure 5 shows the identification delay. The total slots of four algorithms increases with the number of tags, but QTLC has slowest growth. As the number of tags increases, the advantages of QTLC algorithm are more obvious. When $N = 1000$, the total slots of QTLC algorithm is 1912, about 985 less than QT algorithm, 191 less than NEAA algorithm, and 159 less than CTTA algorithm.

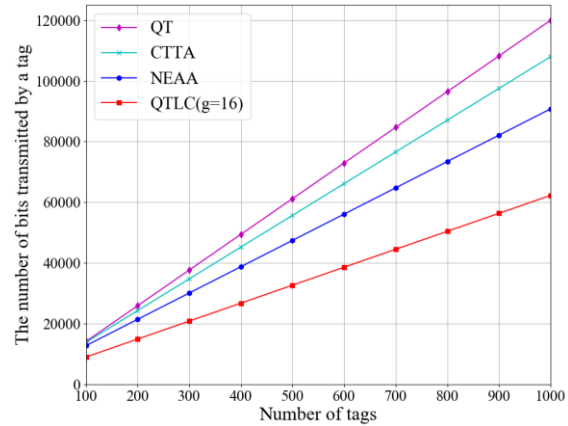


Fig. 4. The traffic of tag.

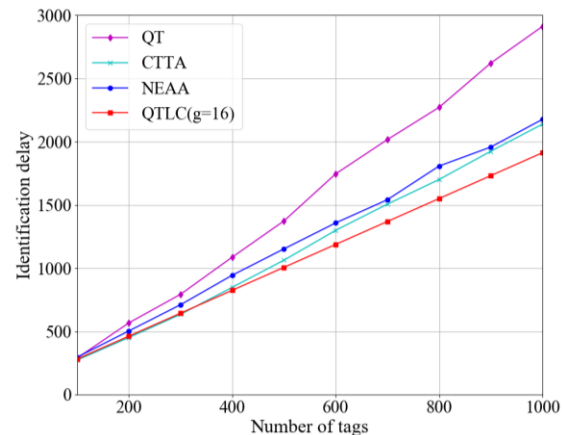


Fig. 5. The identification delay.

V. CONCLUSION

In this paper, a new anti-collision algorithm for RFID is proposed for decreasing the probability of the collision and reducing communication complexity by dividing the traditional identification stage into tag grouping and tag identification. Simulation results show that the proposed QTLC algorithm outperforms other existing algorithms, such as QT, CTTA and NEAA, regardless of the number of tags. QTLC is an efficient anti-collision algorithm for tag identification in an RFID system.

ACKNOWLEDGMENT

This work was supported in part by the National

Science Foundation of China under Grant No. 61771226, 61372057, and 61671223, in part by the Natural Science Foundation of the Jiangsu Higher Education Institutions of China under Grant No. 18KJA110001, and in part by the Science and Technology Innovation Project of Xuzhou in 2018 under Grant No. KC18004.

REFERENCES

- [1] G. Orecchini, L. Yang, A. Rida, F. Alimenti, M. M. Tentzeris, and L. Roselli, "Green technologies and RFID: Present and future," *Applied Computational Electromagnetics Society Journal*, vol. 25, no. 3, pp. 230-238, 2010.
- [2] K. Finkenzeller, "RFID handbook: Radio-frequency identification fundamentals and applications," 2003.
- [3] J. Banks, M. Pachano, L. Thompson, and D. Hanny, *RFID Applied*. Wiley Publishing, 2007.
- [4] S. P. Gao, H. Zhao, H. W. Deng, B. Wang, and W. J. Zhao, "Estimating interference to airborne patch antenna with limited information," *IEEE Transactions on Electromagnetic Compatibility*, vol. 58, no. 2, pp. 631-634, 2016.
- [5] H. Zhao, S. P. Gao, W. J. Zhao, Y. Zhang, J. Hu, and Z. Chen, "Fast prediction of coupling coefficient between monopole antennas on electrically large cylindrical platforms using a linear parametric model," *Applied Computational Electromagnetics Society Journal*, vol. 32, no. 5, pp. 418-423, 2017.
- [6] H. Zhao, Y. Zhang, J. Hu, and Z. Chen, "Hybrid sparse reconstruction-method of moments for diagnosis of wire antenna arrays," *Applied Computational Electromagnetics Society Journal*, vol. 32, no. 10, pp. 882-887, 2017.
- [7] W. T. Chen, "Optimal frame length analysis and an efficient anti-collision algorithm with early adjustment of frame length for RFID systems," *IEEE Transactions on Vehicular Technology*, vol. 65, no. 5, pp. 3342-3348, 2016.
- [8] F. U. Yu, Z. H. Qian, M. Jie, and W. Xue, "FSA anti-collision algorithm based on continuous slot prediction," *Acta Electronica Sinica*, pp. 0-0, 2016.
- [9] S. U. Jian, L. B. Xie, Y. Yang, G. J. Wen, and Q. W. Meng, "Idle slots elimination based anti-collision algorithm for UHF RFID," *Acta Electronica Sinica*, vol. 45, no. 2, pp. 307-314, 2017.
- [10] J. Vales-Alonso, V. Bueno-Delgado, E. Egea-Lopez, F. J. Gonzalez-Castano, and J. Alcaraz, "Multiframe maximum-likelihood tag estimation for RFID anticollision protocols," *IEEE Transactions on Industrial Informatics*, vol. 7, no. 3, pp. 487-496, 2011.
- [11] Y. Sun, P. J. Hawrylak, Z.-H. Mao, and M. H. Mickle, "Collision resolution in ISO 18000-6c passive RFID," *Applied Computational Electromagnetics Society Journal*, vol. 25, no. 3, pp. 239-262, 2010.
- [12] C. N. Yang and J. Y. He, "An effective 16-bit random number aided query tree algorithm for RFID tag anti-collision," *IEEE Communications Letters*, vol. 15, no. 5, pp. 539-541, 2011.
- [13] Y. C. Lai and C. C. Lin, "Two couple-resolution blocking protocols on adaptive query splitting for RFID tag identification," *IEEE Transactions on Mobile Computing*, vol. 11, no. 10, pp. 1450-1463, 2012.
- [14] Y. C. Lai and L. Y. Hsiao, "General binary tree protocol for coping with the capture effect in RFID tag identification," *IEEE Communications Letters*, vol. 14, no. 3, pp. 208-210, 2010.
- [15] F. Zhou, D. Jin, C. Huang, and M. Hao, "Optimize the power consumption of passive electronic tags for anti-collision schemes," in *International Conference on ASIC, 2003, Proceedings*, vol. 2, pp. 1213-1217, 2003.
- [16] Y. C. Lai, L. Y. Hsiao, H. J. Chen, C. N. Lai, and J. W. Lin, "A novel query tree protocol with bit tracking in RFID tag identification," *IEEE Transactions on Mobile Computing*, vol. 12, no. 10, pp. 2063-2075, 2013.
- [17] Y. Jiang, R. Zhang, W. Cheng, B. Li, and W. Sun, "An adaptive ternary query splitting based tag anti-collision protocol for mobile RFID systems," in *Vehicular Technology Conference*, pp. 1-6, 2017.
- [18] S. U. Jian, G. J. Wen, and J. L. Han, "An efficient RFID anti-collision algorithm for ISO18000-6b protocol," *Acta Electronica Sinica*, vol. 42, no. 12, pp. 2515-2519, 2014.
- [19] Y. H. Chen, S. J. Horng, R. S. Run, J. L. Lai, R. J. Chen, W. C. Chen, Y. Pan, and T. Takao, "A novel anti-collision algorithm in RFID systems for identifying passive tags," *IEEE Transactions on Industrial Informatics*, vol. 6, no. 1, pp. 105-121, 2010.
- [20] C. Law, K. Lee, and K. Y. Siu, "Efficient memoryless protocol for tag identification (extended abstract)," in *International Workshop on Discrete Algorithms and Methods for Mobile Computing and Communications*, pp. 75-84, 2000.



Fan Yang received the B.S. from Nanjing University of Posts and Telecommunications in 2011 and received the M.S. degrees from Nanjing Agricultural University in 2014. He is currently working toward the Ph.D. degree in the College of Engineering at Nanjing Agricultural University, China. His research interests

include performance analysis and protocol design on networks, Wireless Sensor Networks and IoT.



Lei Zhao received the B.S. degree in Mathematics from Jiangsu Normal University, China, 1997, the M.S. degree in Computational Mathematics, and the Ph.D. degree in Electromagnetic Fields and Microwave Technology from Southeast University, Nanjing, China, in 2004 and 2007, respectively.

He joined the Jiangsu Normal University, Xuzhou, China, in 2009, where he is currently the Professor and the Director of Center for Computational Science and Engineering. From Aug. 2007 to Aug. 2009, he worked in Department of Electronic Engineering, The Chinese University of Hong Kong as a Research Associate. From Feb. 2011 to Apr. 2011, he worked in Department of Electrical and Computer Engineering, National University of Singapore as a Research Fellow. From Sep. 2016 to Sep. 2017, he worked in Department of Electrical and Computer Engineering, University of Illinois at Urbana-Champaign, USA as a Visiting Scholar. He has authored and coauthored over 50 referred journal and conference papers. His current research interests include antennas design and its applications, computational electromagnetics, electromagnetic radiation to human's body, and spoof surface plasmon polaritons design and its applications.

He serves as an Associate Editor for IEEE Access, an Associate Editor-in-Chief for ACES Journal and a Reviewer for multiple journals and conferences including the IEEE Trans. Antennas and Propagation, IEEE Access, IEEE Antennas and Wireless Propagation Letters, Progress In Electromagnetics Research, ACES Journal, and other primary electromagnetics and micro-

wave related journals.

Zhao was the TPC Chair of the 2018 Cross Strait Quad-Regional Radio Science and Wireless Technology Conference. He was elected TPC Member of IEEE MTT-S International Microwave Workshop Series on RF and Wireless Technologies for Biomedical and Healthcare Applications since 2013, the TPC Member of 2010 International Conference on Microwave and Millimeter Wave Technology, the TPC Member of 2012 International Conference on Microwave and Millimeter Wave Technology, the TPC Member of 2013 Cross Strait Quad-Regional Radio Wireless Conference, the TPC Member of 2014 Cross Strait Quad-Regional Radio Wireless Conference..



Hu Chen was born in 1975. He received the Ph.D. degree from Xidian University in 2016. Now, he is an Associate Professor of Jiangsu Normal University. His main research interests include cryptography and information security.



Shuixia Hao is an Associate Professor in the School of Mathematics and Statistic, JiangSu Normal University. Her research interests include parallel computing, heterogeneous computing and big data. She received her B.S. degrees in Information Management and Science from Beijing Normal University in 1997; and received her M.S. degrees in Computer Department from Soochow University in 2004; received her D.S. degrees in Computer Department from Tongji University in 2014.

Design and Evaluation of Typical Antennas for Monitoring Vital Signs

Ramadhani Selemani Mpanda¹, Lin Qi^{1*}, Qiancheng Liang¹, Lisheng Xu¹, Jingjing Shi¹,
and Lei Zhao²

¹Sino-Dutch Biomedical and Information Engineering School
Northeastern University Shenyang, Liaoning Province, 110819, China
mpandamgimba@yahoo.com, *qilin@bmie.neu.edu.cn

²Center for Computational Science and Engineering
School of Mathematics and Statistics, Jiangsu Normal University, Xuzhou, China
leizhao@jsnu.edu.cn

Abstract — Non-contact method to monitor vital signs using radar-based sensor system is a more convenient way in comparison with the contact monitoring devices. Portable with a low profile and low-cost non-contact vital signs sensors system that are capable to monitor heart and respiration rates are presented and evaluated their performances. A printed 2x1 patch array antenna, Yagi-Uda antenna and dipole array antenna are designed and integrated with sensor system Tx/Rx module for their performances analysis. The gain of the designed antennas are 6.38 dBi, 7.7 dBi, and 10.5 dBi, VSWR are 1.1, 1.15, and 1.0, and return loss are -26.26 dB, -22.7 dB and -21.6 dB respectively at 2.4 GHz. The evaluations performances of these antennas were compared with a standard respiratory-rate measurement using a pulse sensor and respiratory sensor. The measurement results using the proposed non-contact sensor systems and the standard contact systems showed excellent performance with the printed dipole array antenna compared with other two antennas, the error between the average heart rate extracted by the non-contact systems and the reference systems are ± 1.1 beat/min for dipole array antenna, ± 1.5 beat/min for printed 2x1 patch array antenna and ± 1.9 beat/min for Yagi-Uda antenna.

Index Terms — Heartbeat rate, printed dipole array arrays, printed patch array antenna, printed Yagi-Uda antenna, respiration rate, vital signs.

I. INTRODUCTION

Due to the increase of healthcare costs, aging population and difficulties in getting access to healthcare, especially in physiological monitoring systems, telemedicine and continuous remote patient monitoring applications are urgently needed [1]. The conventional respiration measurement techniques that mostly based on contact methods, such as, ECG monitoring [2], and other wearable systems are still cost-fully [3]. The contact

nature of these devices makes the subject aware of being monitored, as the result it affects the spontaneous breathing patterns and may lead to inaccurate assessment of physical states. Wired connections for data acquisition of these conventional devices hinder patient mobility and normally measure only one specific vital sign, also they are not capable for long term continuous monitoring of vital signs especially when monitoring patients with disease that need long term treatment such as stroke [4].

A non-contact radio frequency (RF) radar sensor with low cost, comfortable, portable and low power consumption is very attractive for the healthcare applications. Using microwaves radar system to detect small physiological movements such as respiration and heartbeat dates back to the 1970s [5]. It is realized by detecting the phase information in the received radar signals, which is caused by Doppler shift due to the moving chest wall.

Radar physiological system play crucial role in our daily life application. It has wide applications, such as searching for human subjects under earthquake rubble or behind a barrier, security monitoring based on motion detection, and monitoring breathing conditions and identifying potential abnormality of sleeping people [6]. The radar sensor has also been used for indoor detection of human falls which allows timely and accurate reporting of fall incidents to avoid severe injuries. Recently, radar technology has been extended for accurate respiration measurement in motion adaptive cancer radiotherapy [7].

In detection process with radar system, there are basically two types of radars: continuous wave (CW) radar and ultrawideband (UWB) radar. The CW radar falls into three subcategories: single-tone, stepped frequency (SFCW), and frequency-modulated CW (FMCW). Each category of radars has its specific advantages. The single tone CW radar has a simple system architecture that allows high level chip integration. It also has high

accuracy in relative displacement measurement [8]. With the advantages of CW radar system our designed radar based-sensors will be based on CW architecture.

With simple structure, low profile and easy integrated with other systems of the printed antennas to detect and monitor vital signs, this paper focus on implementing three kind of antennas and make comparative analysis on their performances. Printed 2x1 patch array antenna, printed dipole array antenna and printed Yagi-Uda antenna are designed and evaluated their performances on vital signs detection. The antennas analysis and evaluation were based on radiation properties such as directivity, gain, S11 and VSWR of the antennas. Then various measurements were performed on heartbeat and respiration rate to compare their performances. The designs of these printed antennas are based on the ISM frequency band.

This paper starts with design process and simulation result of antennas in Section II. Section III describes result and discussion of the designed antennas. Evaluation of the antenna performances are described in Section IV. Conclusion of the paper is offered in Section V.

II. DESIGN PROCESS AND SIMULAION RESULTS OF ANTENNAS

Printed 2x1 patch array, printed dipole array, and Yagi-Uda antenna are described in this section. The proposed antennas are designed and simulated using HFSS software. FR4 substrate with relativity of $\epsilon_r = 4$ used as the dielectric constant of substrate in the designing of the antennas. The antennas are designed to work at resonating frequency of 2.4 GHz.

A. Printed 2x1 patch array antenna design

A micro-strip printed patch antenna consists of a radiating patch with an electrically large ground plane separated by a dielectric material as shown in Fig. 1 (a). The design of a 2x1 patch array antenna is done by first design a single micro-strip patch antenna. The design of a single patch antenna is designed according to the formula given below:

$$W = \frac{C}{2f} \left(\frac{\epsilon_r + 1}{2} \right)^{-\frac{1}{2}}, \quad (1)$$

$$\epsilon_r = \frac{\epsilon_r + 1}{2} + \frac{\epsilon_r - 1}{2} \left(1 + 12 \frac{h}{w} \right)^{-\frac{1}{2}}, \quad (2)$$

$$\Delta l = 0.412 \frac{(\epsilon_r + 0.3) \left(\frac{W}{h} + 0.064 \right)}{(\epsilon_r - 0.258) \left(\frac{W}{h} + 0.8 \right)}, \quad (3)$$

$$L = \frac{C}{2f} \frac{1}{\sqrt{\epsilon_r}} - 2\Delta l, \quad (4)$$

where W is the width of the rectangular radiating patch, L is the length of the radiation patch and h is the height of the substrate and FR4 substrate with relativity of

$\epsilon_r = 4.3$ used as the dielectric constant of substrate. To increase the gain of the patch antenna, the cascade patch is arranged in array as shown in Fig. 1 (b). Table 1 show the the optimized parameter of 2x1 patch array antenna.

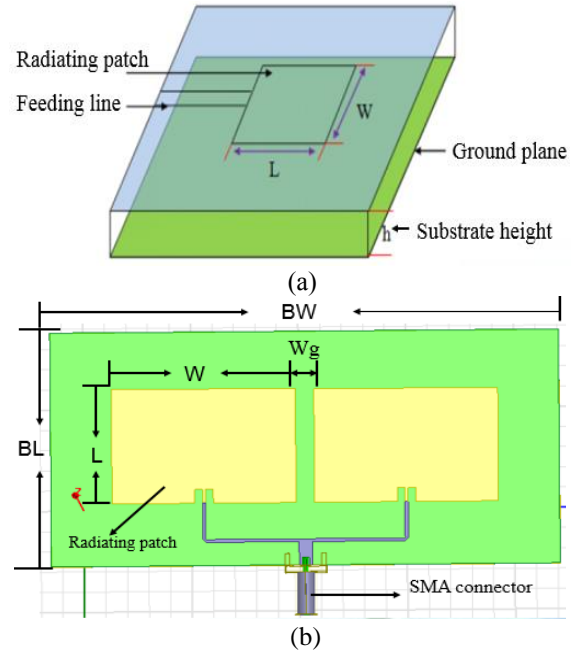


Fig. 1. (a) The structure of micro-strip patch antenna; (b) the structure of rectangular 2x1 patch array antenna.

Table 1: The optimized parameter of 2x1 patch array

Variable	BW	BL	W	L	W _g
Values (mm)	137.4	82.7	48.5	38	12

Figures 2 (a) and (c) show the simulation results of reflection coefficient and radiation pattern of proposed 2x1 patch array antenna. The simulation results indicate that the S11 of the designed patch array is -26.26 at resonating frequency of 2.4 GHz. In this working band, its radiation also satisfies directional radiation with gain of 6.38 dBi as indicated in Fig. 2 (b).

B. Printed dipole array antenna design

Printed dipole array antenna has a simple and novel structure with symmetrical array elements for attaining high antenna gain and a reflector to focus the radiation beam at a specific direction as shown in Figs. 3 (a) and (b). Each dipole array element has two arms in the same side of the substrate, and the length of each arm equals to $\lambda/4$, where λ indicates the wavelength at 2.4 GHz. The FR4 substrate with relativity of $\epsilon_r = 4$ and thickness of $h = 4$ mm was used in this antenna which can shorten the wavelength compared to free space. Therefore, the corresponding theoretical value of radiation element l_1 can be described as:

$$l_1 = \frac{1}{4} \lambda = \frac{c}{4f\sqrt{\epsilon_r}} \quad (5)$$

where, c is the velocity of light, f is the resonance frequency. A metal plate worked as antenna reflector is added to the back side of dipole array elements, with a distance of $h = \lambda/4$ from the FR4 substrate [9]. The calculated optimized parameters of the dipole array antenna shown in Table 2.

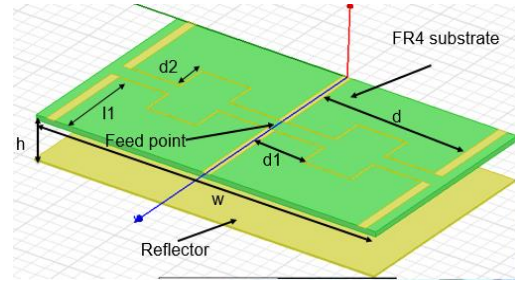


Fig. 3. Geometrical structure of the dipole array antenna.

The simulation result of the designed dipole array antenna is described below, Fig. 4 (a) show that the reflection coefficient of the design is -29.31 dBi at 2.4 GHz, with a gain of 10.5 dB and a directional lobe as shown in Figs. 4 (b) and (c), respectively.

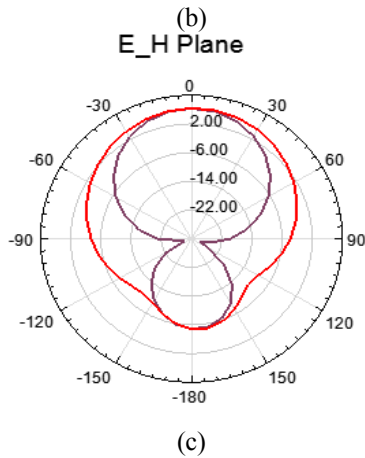
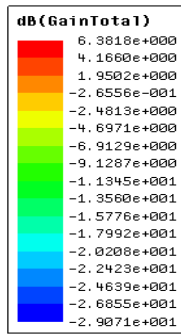
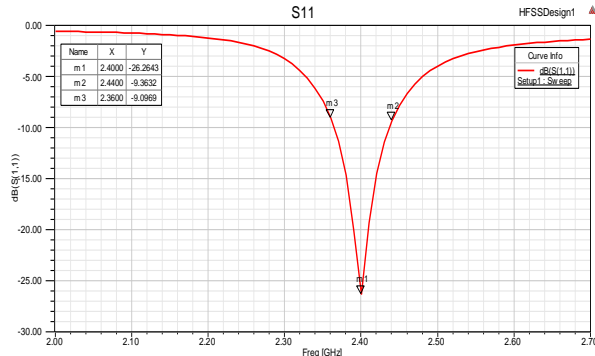


Fig. 2. (a) The S11 parameter of 2x1 patch array antenna; (b) the 3D radiation pattern of the designed 2x1 patch array antenna; (c) the radiation performance of EH plane of 2x1 patch array antenna.

Table 2: The optimize parameter of dipole array antenna

Variable	l_1	d	d_1	d_2	h	w	l
Values (mm)	35	51	17	12	12	120	78

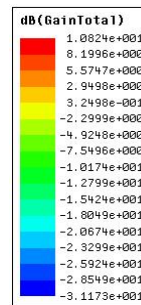
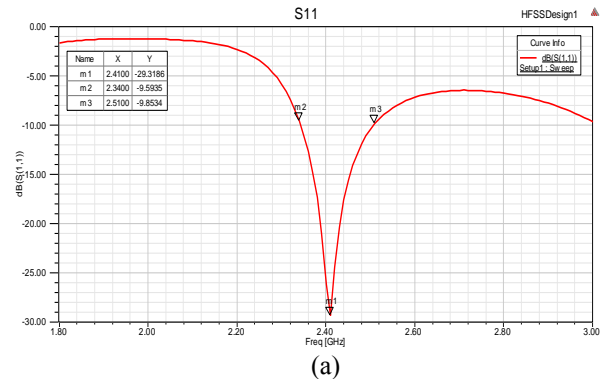


Fig. 4. (a) The S11 parameter of the designed Yagi-Uda antenna; (b) the 3D radiation pattern of the designed Yagi-Uda antenna; (c) the radiation performance of EH plane of the designed Yagi-Uda antenna.

Fig. 5. (a) The S11 parameter of the designed Yagi-Uda antenna; (b) the 3D radiation pattern of the designed Yagi-Uda antenna; (c) the radiation performance of EH plane of the designed Yagi-Uda antenna.

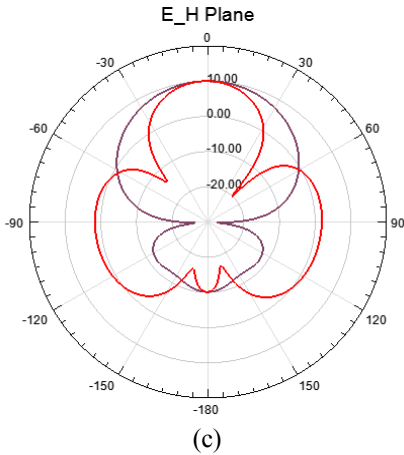


Fig. 4. (a) The S11 parameter of dipole array antenna at 2.4 GHz; (b) the 3D radiation pattern for the dipole array antenna; (c) the radiation performance of EH plane of dipole array antenna.

Table 3: The optimized parameter of Yagi-Uda antenna

Variable	d_r	d_1	g_1	g_2	W_1
Values (mm)	42.5	37.0	18.0	10.0	3.7

Figures 5 (b) and (d) show the simulation results of reflection coefficient and radiation pattern of proposed Yag-Uda antenna. The simulation results indicate that the S11 of the designed Yag-Uda is -20.86 at resonating frequency of 2.4 GHz. In this working band, its radiation also satisfies directional radiation with gain of 8.69 dBi as indicated in Fig. 5 (c).

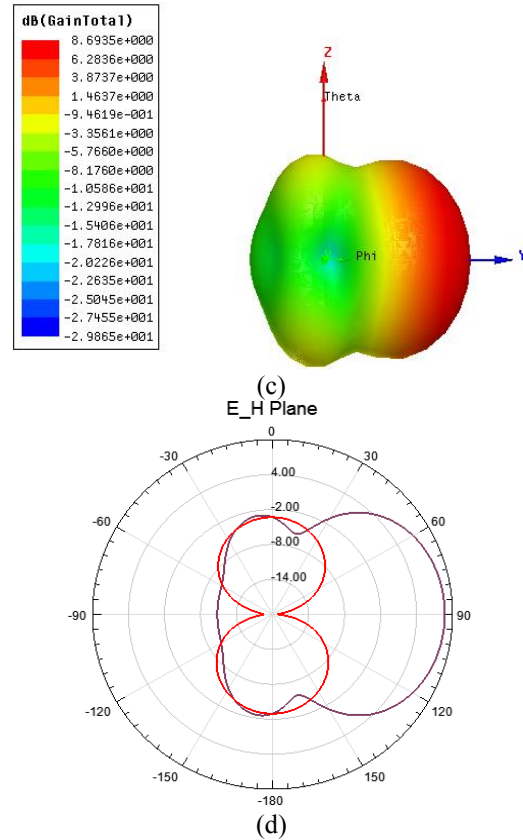


Fig. 5. (a) The configuration designed Yagi-Uda antenna; (b) the S11 parameter of Yag-Uda antenna at 2.4 GHz; (c) the 3D radiation pattern for the Yagi-Uda antenna; (d) the radiation performance of EH plane of Yag-Uda antenna.

III. RESULT AND DISCUSSION OF THE DESIGNED ANTENNAS

Figure 6 shows the fabricated antennas, the measurement of each antenna were carryout to compare the measurement and simulation result, different parameters such as reflection coefficient S11, antenna gain and VSWR of the antennas were compared. Table 4 lists the simulation and experimental measurement of each antenna.

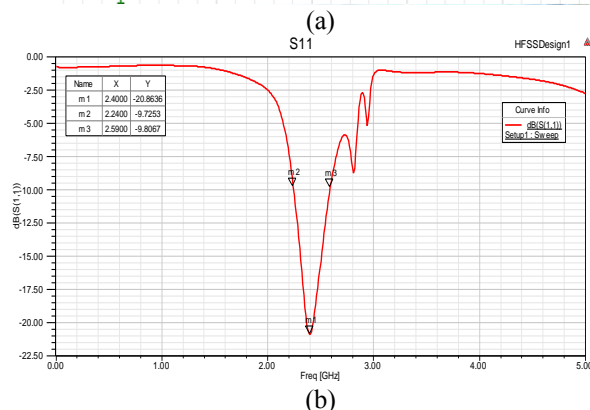
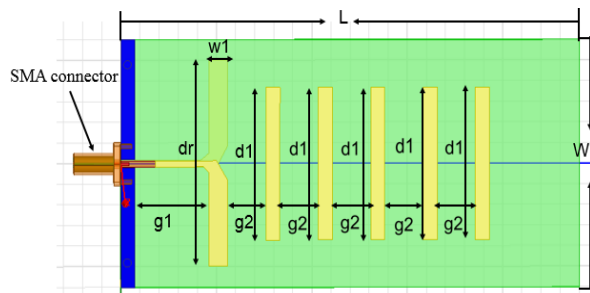


Table 4: The simulation and experimental results of S11, gain and VSWR of the designed antennas

Antenna		S11 dB	Gain dBi	VSWR
Patch array	Sim	-26.26	6.38	1.1
	Exp	-26.8	6.42	1.0
Yag-Uda	Sim	-20.86	7.7	1.15
	Exp	-21.8	7.62	1.2
Dipole array	Sim	-29.31	10.82	1.3
	Exp	-22.7	10.5	1.5

*Sim=Simulation results

*Exp=Experimental results

Table 4 lists the simulations and experimental measurement results of the designed antennas; the result shows that the simulation and the experimental measurement of the designed antennas have only slightly difference.

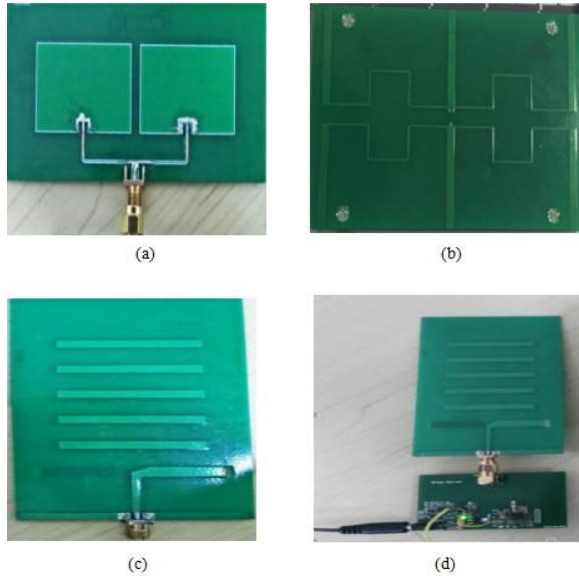


Fig. 6. (a) 2x1 fabricated patch array antenna; (b) fabricated dipole array antenna; (c) fabricated Yagi-Uda antenna; (d) fabricated Yagi-Uda together with the Tx/Rx module.

IV. EVALUATION OF THE ANTENNAS PERFORMANCES

In order to verify the feasibility of the antennas performances, the corresponding experimental scheme was conducted. The experimental devices includes a set of contact physiological signal acquisition devices, pulse sensor, respiratory sensor and the non-contact detection system was setup to evaluate our designed performances.

As shown in Fig. 7, during the experiment, the contact device and the non-contact detection device are used to collect the physiological signals of the human body. The pulse sensor is attached to the fingertip of the subject's finger, and the respiratory sensor is attached to the abdomen of the subject. The non-contact detection systems were placed 35 cm away from the human thoracic cavity and the experimental data was collected for 60s.

In order to increase accuracy of data collected by the non-contact sensors, it is necessary to avoid interference activities of other people around when collecting experimental data. Our designed antennas are directional, in order to obtain good signal detection, the antenna is placed to focus the human chest as shown in Fig. 7.

According to the experimental measurements described above, the physiological signals of 10 groups

of subjects were collected by the non-contact detection system based on our design, 2x1 patch array antenna, dipole array antenna and Yagi-Uda antenna, respectively. The contact reference system is also used for synchronous acquisition of signals.

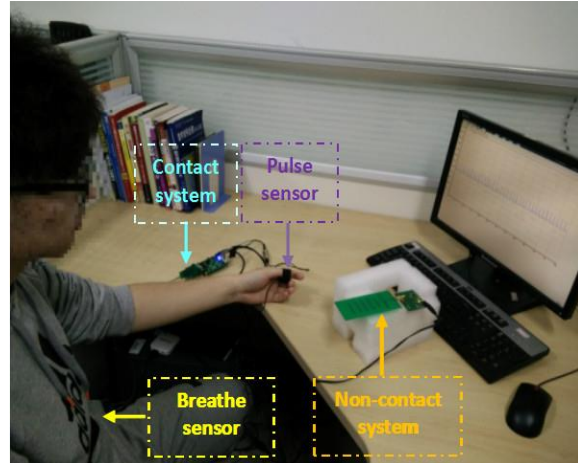


Fig. 7. The experimental setup to detect vital signs.

Table 5, Table 6 and Table 7 shows the average heart rate (AHR) calculation results of the 10 sets of samples data extracted by the printed 2x1 patch array antenna, dipole array antenna and Yagi-Uda antenna-based non-contact monitoring system respectively and the error with the reference system. AHR can be calculated by equation 6, where n is the length of time for each set of data samples and $IHR(i)$ is the heart rate:

$$AHR = \frac{\sum_{i=1}^n IHR(i)}{n} . \quad (6)$$

It can be seen from the tables that there are a certain error between the average heart rate extracted by the rectangular array antenna, dipole array antenna and Yagi-Uda antenna, based non-contact monitoring system and the average heart rate extracted based on the reference systems acquisition signal. The error between the average heart rate extracted by the non-contact systems and the reference systems are ± 1.1 beat/min for dipole array antenna, ± 1.5 beat/min for printed 2x1 patch array antenna and ± 1.9 beat/min for Yagi-Uda antenna.

In addition in order to compare the signals collected by the designed non-contact sensors with reference respiration sensors, the extraction of respiration signals collected by non-contact sensor are achieved by digital filter and wavelet transform to remove noise. Figure 8, Fig. 9 and Fig. 10 shows the respiration signals that collected by respiration sensor and that collected by the designed non-contact sensors.

Table 5: Averaged heart rate of non-contact monitoring system based on 2x1 patch array antenna

Experimental sample	1	2	3	4	5	6	7	8	9	10
Non-contact system based on 2x1 patch array	80	78	74	79	82	86	67	71	78	70
Reference system	82	76	74	77	84	88	67	70	80	72
Error (beat/min)	-2	2	0	2	-2	-2	0	1	-2	-2

Table 6: Averaged heart rate of non-contact monitoring system based on dipole array antenna

Experimental sample	1	2	3	4	5	6	7	8	9	10
Non-contact system based on dipole array	72	70	75	73	80	71	73	73	68	68
Reference system	73	71	75	71	78	71	75	75	68	69
Error (beat/min)	-1	1	0	2	2	0	-2	-2	0	-1

Table 7: Averaged heart rate of non-contact monitoring system based on Yagi-Uda antenna

Experimental sample	1	2	3	4	5	6	7	8	9	10
Non-contact system based on Yagi-Uda	76	68	79	76	78	75	74	80	71	69
Reference system	75	71	77	79	77	76	72	82	70	72
Error (beat/min)	1	-3	2	-3	1	-1	2	-2	1	-3

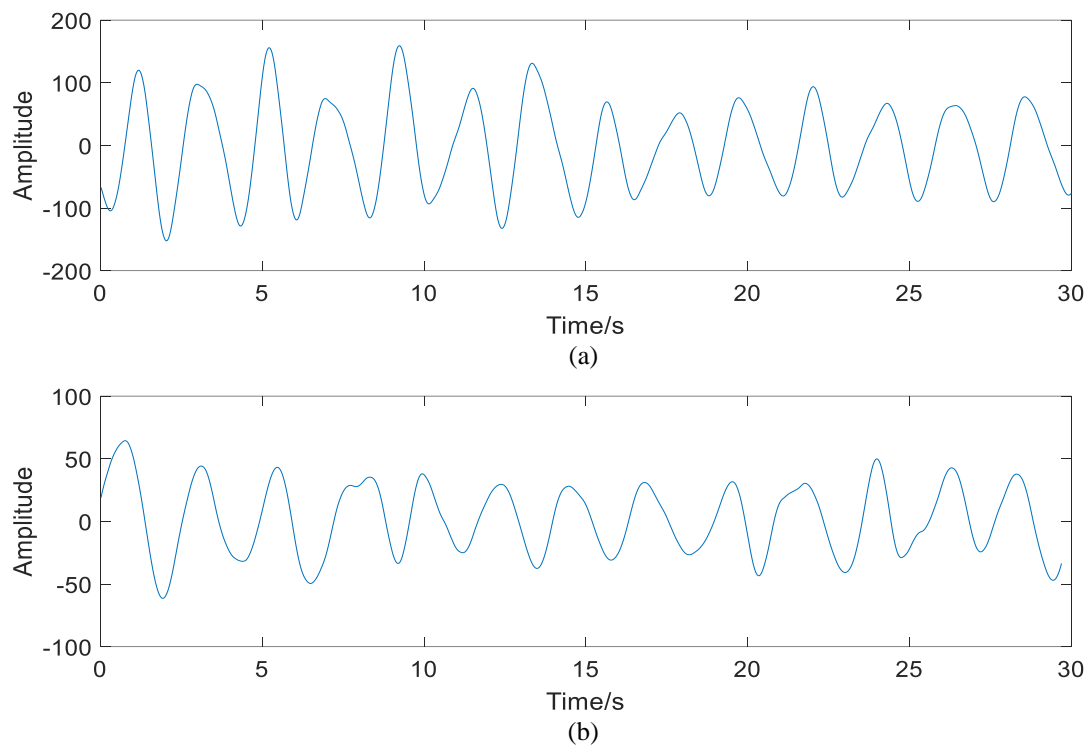


Fig. 8. Respiration signal: (a) signal from reference sensor (respiration belt sensor), and (b) signal from printed 2x1 patch array antenna.

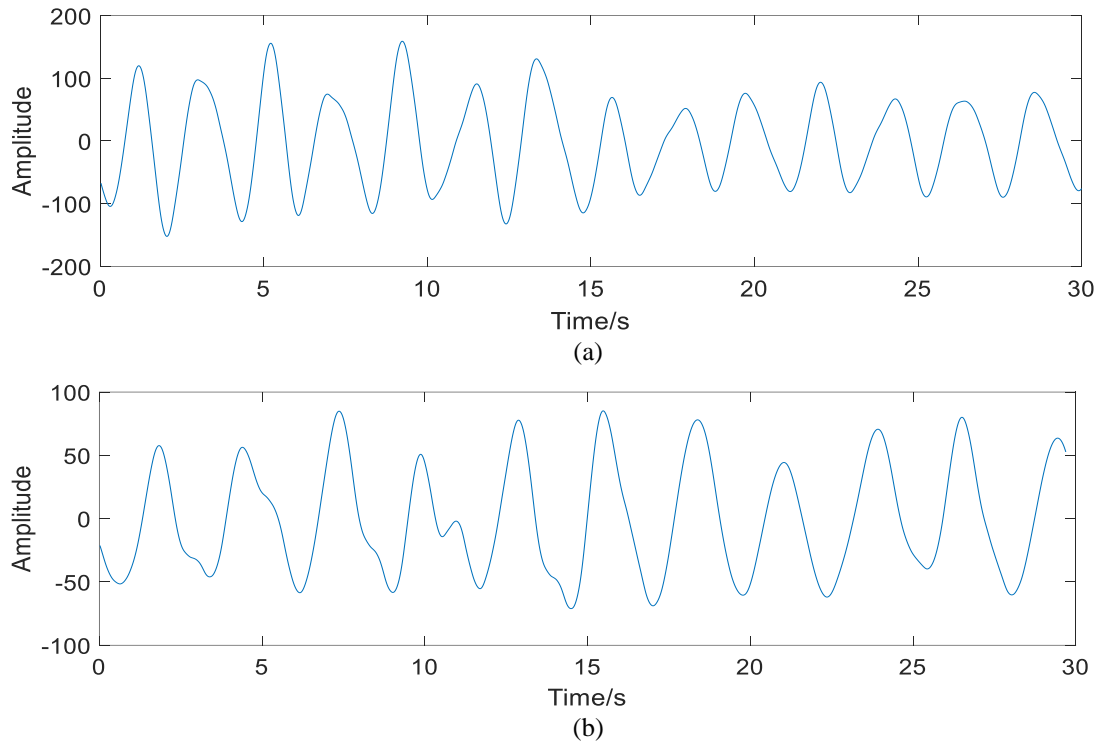


Fig. 9. Respiration signal: (a) signal from reference sensor (respiration belt sensor), and (b) signal from dipole array antenna.

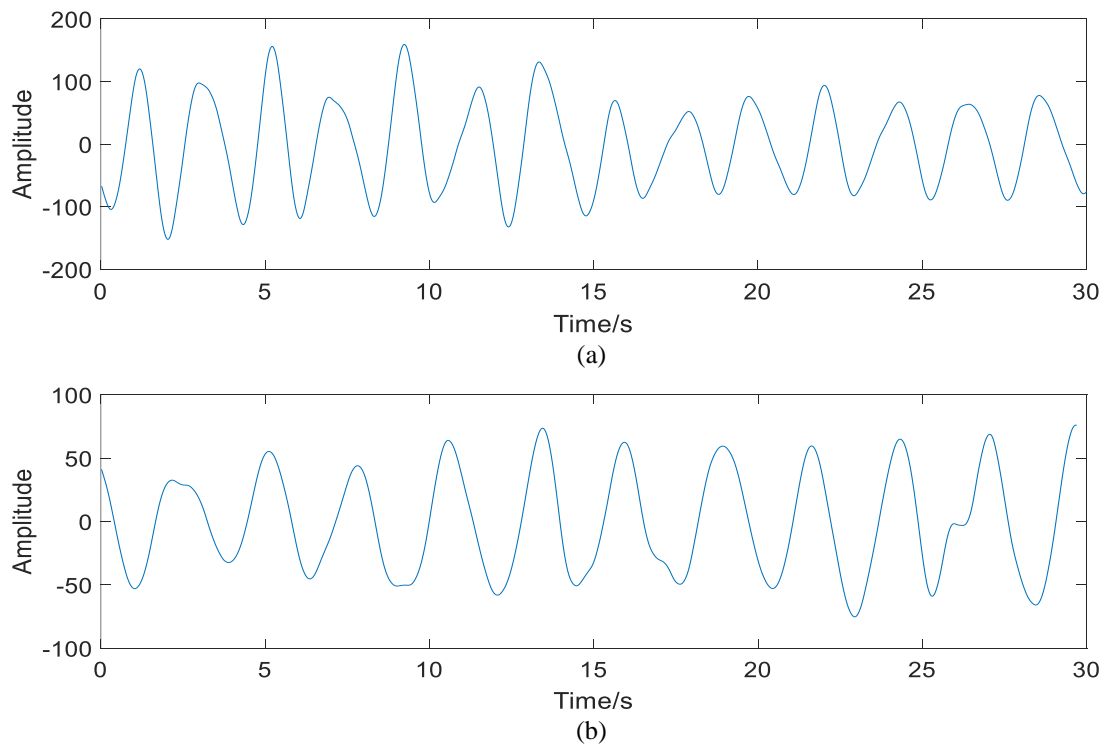


Fig. 10. Respiration signal: (a) signal from reference sensor (respiration belt sensor), and (b) signal from printed Yagi-Uda antenna.

It observed that the signal accuracy of the non-contact monitoring system based on the experimental data collected on the tables above and wave form signals of the non-contact sensors together with the reference monitoring systems, shows that the dipole array antenna has higher accuracy than that of the 2x1 patch array antenna and Yagi-Uda antenna non-contact monitoring system.

V. CONCLUSION

Portable with low profile and low cost Doppler-based non-contact vital signs monitoring system operating at 2.4 GHz were presented. With the advantages of CW radar system our designed radar system was based on CW architecture, the systems were assessed with other contact monitoring devices to analyze their performances. Focusing on the heart rate and respiration signal, a large amount of experimental data indicates that a dipole array antenna can significantly perform well as compared with 2x1 patch array antenna and Yagi-Uda antennas. Therefore dipole array antenna can be the best candidate antenna to be integrated with other medical device for vital signs detection due to its excellent features, such as low weight, profile, and cost, while maintaining good performances on detecting vital signs.

ACKNOWLEDGMENTS

This work was supported by the National Natural Science Foundation of China (Nos. 61773110, 61374015, and 61202258), Natural Science Fund Project of Liaoning Province (No. 20170540312), and the Fundamental Research Funds for the Central Universities (Nos. N161904002 and N161604006).

REFERENCES

- [1] M. Mahfouz and M. Kuhn, "No strings attached," *IEEE Microwave Magazine*, Dec. 2011.
- [2] J. Boyle, N. Bidargaddi, A. Sarela, and M. Karunanithi, "Automatic detection of respiration rate from ambulatory single-lead ECG," *IEEE Trans. Inform. Technol. Biomed.*, vol. 13, no. 6, pp. 890-896, Nov. 2009.
- [3] A. Lanata, E. P. Scilingo, E. Nardini, G. Loriga, R. Paradiso, and D. De-Rossi, "Comparative evaluation of susceptibility to motion artifact in different wearable systems for monitoring respiratory rate," *IEEE Trans. Inform. Technol. Biomed.*, vol. 14, no. 2, pp. 378-386, Mar. 2010.
- [4] A. Z. Elsherbeni, *FDTD Course Notes*, Department of Electrical Engineering, The University of Mississippi, MS, Spring 2001.
- [5] J. C. Lin, "Noninvasive microwave measurement of respiration," *Proc. IEEE*, vol. 63, no. 10, pp.

1530-1530, Oct. 1975.

- [6] C. Li, J. Cummings, J. Lam, E. Graves, and W. Wu, "Radar remote monitoring of vital signs," *IEEE Microwave Mag.*, vol. 10, no. 1, pp. 47-56, Feb. 2009.
- [7] C. Gu, R. Li, C. Li, and S. B. Jiang, "Doppler radar respiration measurement for gated lung cancer radiotherapy," in *Proc. IEEE Radio Wireless Week*, Phoenix, AZ, pp. 91-94, Jan. 2011.
- [8] S. Kim and C. Nguyen, "A displacement measurement technique using millimeter-wave interferometry," *IEEE Trans. Microwave Theory Tech.*, vol. 51, no. 6, pp. 1724-1728, 2003.
- [9] Q. Liang, R. S. Mpanda, X. Wang, J. Shi, and L. Xu, "A printed dipole array antenna for non-contact monitoring system," *IEEE In 2018 Cross Strait Quad-Regional Radio Science and Wireless Technology Conference (CSQRWC)*, pp. 1-3, July 2018.
- [10] H. Bo, L. Xu, L. Hao, Y. Dou, L. Zhao, and W. Yu, "A single-channel non-orthogonal I/Q RF sensor for non-contact monitoring of vital signs," *Applied Computational Electromagnetics Society Journal*, vol. 31, no. 6, June 2016.



R. S. Mpanda received the B.S. degree in Electronics Science and Communication from University of Dar es Salaam, Dar es Salaam, Tanzania, 2012. He is currently working toward the M.S. degree in Biomedical Engineering at the Northeastern University, Shenyang, China. His research interests include antenna structures design to monitor physiological signs, wearable sensor design, digital signal processing and electronic circuits design.



Lin Qi (M'08) received the Ph.D. degree in the Department of Electronic Engineering, the Chinese University of Hong Kong in 2013. He got the B.S. and M.S. degrees in Biomedical Engineering, School of Medicine, and Tsinghua University. He is now the Associate Professor in Sino-Dutch Biomedical and Information Engineering School, Northeastern University, China. His research interests include medical robotics and biomedical signal processing.



Lisheng Xu (SM'15) received the B.S. degree in Electrical Power System Automation, the M.S. degree in Mechanical Electronics, and the Ph.D. degree in Computer Science and Technology from Harbin Institute of Technology, Harbin, China, in 1998, 2000, and 2006, respectively.

He is currently a Full Professor in the Sino-Dutch Biomedical and Information Engineering School, Northeastern University, China. He has authored or coauthored more than 100 international research papers, and holds fifteen

patents and four pending patents. His current research interests include nonlinear medical signal processing, computational electromagnetic simulation, medical imaging, and pattern recognition.

Xu is the Director of Theory and Education Professional Committee of China Medical Informatics Association. He is Senior Member of IEEE and Chinese Society of Biomedical Engineering. He is the Member of the editor board for many international journals such as *Physiological Measurement*, *Biomedical Engineering Online*, *Computers in Biology and Medicine* and so on.